

https://dspace.org/

Towards teleporting quantum images

Sephton, Bereneice

2024
https://hdl.handle.net/10539/37433

Downloaded from a DSpace repository. https://dspace.org/

UNIVERSITY OF THE WITWATERSRAND

DOCTORAL THESIS

Towards Teleporting Quantum Images

Author:
Bereneice SEPHTON

Supervisor:
Prof. Andrew FORBES



A thesis submitted in fulfillment of the requirements
for the degree of Doctor of Philosophy

in the

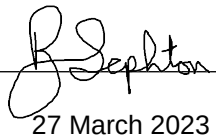
Structured Light Laboratory
School of Physics

March 27, 2023

Declaration of Authorship

I, Bereneice SEPHTON, declare that this thesis titled, "Towards Teleporting Quantum Images" and the work presented in it are my own. I confirm that:

- This work was done wholly or mainly while in candidature for a research degree at this University.
- Where any part of this thesis has previously been submitted for a degree or any other qualification at this University or any other institution, this has been clearly stated.
- Where I have consulted the published work of others, this is always clearly attributed.
- Where I have quoted from the work of others, the source is always given. With the exception of such quotations, this thesis is entirely my own work.
- I have acknowledged all main sources of help.
- Where the thesis is based on work done by myself jointly with others, I have made clear exactly what was done by others and what I have contributed myself.

Signed: 

Date: 27 March 2023

"If you think you understand quantum mechanics, you don't understand quantum mechanics."

Richard P. Feynman

UNIVERSITY OF THE WITWATERSRAND

Abstract

Doctor of Philosophy

Towards Teleporting Quantum Images

by Bereneice SEPHTON

Achieving higher dimensionality in quantum protocols is receiving increasing interest at the promise of a range of benefits, starting from increased information capacity to noise resilience. This also arises naturally in many quantum systems, from the multitude of photonic states in the temporal, frequency or spatial domains to many atomic levels in an atom. Generalising these to superpositions of states with unique amplitude and phases, we can call such encoded information quantum images. The ability to transfer, either the state of a system directly or information encoded as quantum images thus becomes a pressing frontier with teleportation an important building block. Bearing two distinct features, teleportation forms a fundamentally different way of communicating such that the information does not pass directly between communicating parties and when used with quantum carriers, can form the basis for a variety of quantum networks, starting from quantum repeaters to a type of quantum computing.

In this thesis, the over-arching goal involves physically implementing a high-dimensional system in an effort towards teleporting quantum images. To do so, Chapter 1 considers the basic language, protocol, characterising techniques and spatial states being used in this work.

We then consider bringing in nonlinear optical strategies to the physical implementation of both the generation and detection aspects in Chapter 2. Particular emphasis is made on orbital angular momentum (OAM) states as they are used as a test-bed for our spatial degree of freedom. For this property, the naturally generated states in spontaneous parametric down-conversion are considered where the amplitude structure is neglected and an in-depth investigation done. Here, we look at the radial modal purities in both the generational and detection aspects of such phase-only structuring and emphasise the general nature with experiments spanning from quantum to classical. Mitigating measures and corrective steps are also introduced which show the effects of maintaining the naturally-preserved eigenmode structures of the wave-equation.

Next, the time-reversed phenomenon, sum-frequency generation, was explored as a detection mechanism. We test this classically by interacting different modal structures and looking at the generated modes. In doing so, we showed that the phase-flattening nature of conjugate states in the interaction allows for modal detection that is not confined to the same wavelength. The measurement-conditioned process could then be modelled in quantum formalism as reverse SPDC and introduced as a projector for quantum teleportation.

Chapter 3 explores the full theoretical formalism of a non-linear detection-based teleportation system for spatial modes, which is numerically modelled for OAM and implemented as a test-bed. Here, the physical system was characterised and control explored by changing the generation and detection mode sizes. In doing so, we demonstrated a 15-dimensional teleportation system in OAM that exceeds the

classical limit and extended the implementation to include a variety of states across different bases, extending from polar to Cartesian coordinates. We achieved this by encoding the information on bright coherent laser light. Despite this protocol extending to quantum carriers, present inefficiencies in the non-linear interaction require many copies to to be present, stimulating the process and yielding what we call stimulated teleportation.

While the ability to develop efficiencies is both beyond the scope of this work and an active area of research, with promising advances in metasurfaces, we look towards how this system may be further applied and enhanced in Chapter 4. Notably, we numerically map out an optimisation space for pixel states and look at requirements for teleporting images of complex objects, directly. Here, we derive a technique for characterising such teleportation, based on single pixel quantum ghost imaging where signal at higher resolution is conserved, wavelength dependency is lessened and the ability to fully distinguish the complex spatial structure; the latter being is an active challenge in quantum imaging systems. Further applications are also discussed where pump engineering could lead to better fidelities, how a deterministic system could be implemented and how hybrid entanglement channels could lead to the teleportation of hybrid entangled states.

Acknowledgements

What a crazy journey its been with twists and turns I'd never have imagined! I'd like to express my sincerest gratitude for everyone that has been part of this undertaking, be it for a smaller moment or 'along for the ride'. Each input, experience and encounter has made this a truly valuable undertaking. Specifically, I'd like to thank the following:

Supervisors: First, I would like to thank my supervisor, Professor Andrew Forbes for his invaluable guidance, enthusiasm and expertise throughout this work. I have been afforded so many wonderful experiences and opportunities, both locally and abroad that I am thoroughly thankful for. Thank you for having time to discuss the strange things things I saw in the lab and always having more questions than I have answers. My gratitude also extends to Dr. Adam Vallés for being a strong voice of reason, great fun to both learn from and work with and everlasting patience as I explored the ropes of my first quantum experiments. I really appreciate every effort, video chat, update meeting and word of support.

Seniors: I'd like to thank the postdocs that have come and gone in my time here, who have come to feel like friends. Thank you, Valeria, for being an unbreakable source of strength, Najmeh, for the fun chats and coffee breaks, Wagner, for your interesting take on physics - your enthusiasm is inspiring. I'd like to thank Dr. Dudley for the quick chats and understanding when things were tough as well as the constant supply of recommendation letters. It has been a privilege learning from and working with all of you.

Colleagues and friends: I'd like to thank Hend, BV, Isaac and Chané for all the help and emotional support throughout this PhD. Hend, despite the travels overseas, you never felt too far off with the constant checkups, calls, cycles in the wild and 'backup' in every tricky situation. BV, thank you for your calm mindset and shroud of sureness always made the mountains molehills. Isaac, your passion for science and relentlessness persuit for the answer. Chané, the morbid jokes, looks of understanding, jokes only we seem to get and moments of feeling girly have made you the best fellow desk mate. To all the 'new' recruits: Ravin, Keshaan, Lehola, Pedro, Leerin, Cade and those too many to mention - thanks for the countless jokes, epic stories to be retold and fun moments that will be fond memories of the Structured Light Lab as I leave.

Family: Last, but not least, thank you to my family: Eline, Abigail and Kyle. Thank you for your understanding, fun holidays away from the lab and countless prayers, and support that has always been there. Without you all, I'd not have made it through.

Thank you, Lord, for being my refuge when I'd not had the strength and joy in every moment, good and bad.

Contents

Declaration of Authorship iii

Abstract vii

Acknowledgements ix

1 Introduction 1
- 1.1 The language of quantum states . . . 3
  - 1.1.1 Qubits and the Bloch sphere . . . 3
  - 1.1.2 Density matrices and purity . . . 5
  - 1.1.3 Qudits . . . 6
  - 1.1.4 Multi-particle states and entanglement . . . 7
  - 1.1.5 Schmidt decomposition and dimensionality . . . 10
- 1.2 Projectors and measurement . . . 10
- 1.3 Traditional teleportation . . . 11
- 1.4 Transverse spatial modes for high-dimensional encoding . . . 14
  - 1.4.1 Laguerre-Gaussian modes . . . 14
  - 1.4.2 Hermite-Gaussian modes . . . 16
  - 1.4.3 Pixel basis . . . 16
- 1.5 Interrogating the state . . . 17
  - 1.5.1 Quantum state tomography . . . 18
  - 1.5.2 Maximum likelihood estimation . . . 22
  - 1.5.3 Sampling dimensionality and purity . . . 24

2 Bringing in Non-linear Optics 27
- 2.1 Second-order nonlinear optics . . . 27
- 2.2 Spontaneous parametric down-conversion . . . 29
  - 2.2.1 Phase-matching . . . 29
  - 2.2.2 Wavefunction and efficiencies . . . 31
  - 2.2.3 Spatial entanglement in SPDC . . . 32
  - 2.2.4 Dimensional extent of OAM in SPDC . . . 33
- 2.3 Taking care: the modal purity of orbital angular momentum photons . 35
  - 2.3.1 Concept . . . 37
  - 2.3.2 Experimental implementation . . . 39
    - Dielectric metasurface . . . 39
    - Enhanced generation scheme . . . 40
    - Enhanced two photon detection scheme . . . 41
  - 2.3.3 Results . . . 41
    - Enhanced generation of OAM modes . . . 41
    - Enhanced quantum detection of OAM modes . . . 43
  - 2.3.4 Discussion and Conclusion . . . 45
- 2.4 Sum-frequency generation . . . 45
  - 2.4.1 Phase-matching and efficiencies . . . 46

2.4.2 Classical demonstration of upconversion for spatial mode detection . . . 47
Concept . . . 48
Experiment . . . 49
Results . . . 50
Conclusion . . . 53
2.4.3 A wavefunction description for a non-linear mode projector . . . 53

3 Stimulated high-dimensional spatial teleportation 55
3.1 Theoretical and numerical framework . . . 56
3.1.1 Teleportation with SFG . . . 56
3.1.2 The teleportation channel: physical limitations . . . 58
3.1.3 Numerically simulating teleportation for OAM . . . 60
3.2 Experimental implementation . . . 63
3.2.1 Working principle . . . 64
3.2.2 Experimental details . . . 66
3.2.3 Probing the limits . . . 68
3.2.4 Rotating states, reconstructing the channel and breaking the state of the art . . . 69
3.2.5 Changing the basis symmetry - a step towards pixel states . . . 71
3.2.6 Bringing it all together: A similarity comparison . . . 71
3.2.7 Challenges and errors . . . 72
3.2.8 Looking forward: From stimulated to quantum teleportation . . . 78
3.3 Discussion and conclusion . . . 80

4 Application, future work and conclusions 83
4.1 Towards teleporting phase objects . . . 83
4.1.1 Numerical simulation . . . 84
4.1.2 Retrieving phase images . . . 87
Method . . . 88
Results . . . 91
Conclusion . . . 94
4.1.3 Outlook and considerations . . . 95
4.2 Future Work . . . 95
4.2.1 Deterministic teleportation . . . 95
4.2.2 Hybrid entanglement state teleportation: Expanding degrees of freedom . . . 96
4.2.3 Tailoring the source for optimal teleportation . . . 97
4.3 Conclusion . . . 97

A Supplementary information for modal purity of OAM photons 101
A.1 OAM in the Laguerre-Gaussian basis . . . 101
A.2 Modal decomposition . . . 103
A.3 Holograms . . . 103

B Suplementary information for stimulated high-dimensional spatial teleportation 107
B.1 Suitable experimental conditions for teleportation with SFG . . . 107
B.2 Fidelity of the teleportation channel . . . 108
B.3 Procrustean filtering . . . 110
B.4 Background subtraction . . . 111

B.5 Qutrit teleportation 112
B.6 Unbalanced teleportation 115
B.7 Raw experimental measurements with uncertainties 115
B.8 Teleportation fidelity results 117

C Supplementary information for detecting phase images **121**
C.1 Revealing the embedded phase information 121

Bibliography **127**

List of Figures

1.1 **Bloch sphere.** The Bloch sphere with key qubit states and mapping parameters indicated. Poles contain the basis states with equal superpositions positioned on the equator. 4
1.2 **Pure and mixed quantum systems.** Exemplary particles for a mixed and pure quantum system which will always give a 50% outcome of measuring a $|0\rangle$ or a $|1\rangle$. Determination of the nature of the system can be made by finding the purity. 5
1.3 **Traditional teleportation protocol.** Initially, a pair of entangled photons (purple) is shared between Alice (particle A) and Bob (particle B), establishing an entanglement channel. A third particle C (green) containing an unknown or prepared quantum state to be teleported is then indirectly interacted with Alice's particle. Alice then performs a Bell state measurement on photons A and C. The Bell state projection collapses the entanglement between particles A and B, while simultaneously entangling photons A and C as well as destroying the state of photon C. Alice then transmits classical information to Bob about the Bell measurement projection (j), allowing him to correct for any unitary rotation on the state being teleported (U_j). The state has then been teleported. 12
1.4 **Laguerre-Gaussian mode family.** Intensity profiles for the spatial distributions described by LG modes, at the waist plane ($z = 0$), with indices $\ell = [-1, 2]$ and $p = [0, 2]$ with the phase profile given in the top-right inset. 15
1.5 **Hermite-Gaussian mode family.** Intensity profiles for the spatial distributions described by HG modes, at $z = 0$, with indices $n = [0, 2]$ and $m = [0, 2]$ with the phase profile given in the top-right inset. 16
1.6 **Pixel basis states.** An example of the discretised pixel basis states superimposed on an SPDC cone for (a) striaghtforward 1-to-1 images as well as a (b) tailored pixel basis for entanglement concentration. . . 17
1.7 **Concept of tomography.** Projective measurements (a) are made on an object which are then used to (b) 'work backwards' so that a picture of the object can be rebuilt. 18
1.8 **Tomographic MUB projection OAM states.** Projective OAM states for exemplary $d = 3$ tomographic measurements for an $\ell = \{-1, 0, 1\}$ quantum system based on the (a) d-dimensional MUB approach and (b) restricted two-dimensional MUB approach. S_j refers to the basis state indicated in Table 1.1 21

2.1 **Spontaneous parametric downconversion.** Diagrams of (a) the interaction geometry for spontaneous parametric downconversion with a $\chi^{(2)}$ non-linear crystal and interaction geometries for (b) collinear as well as (c) non-collinear phase matching scenarios. Inset shows the energy level diagram for such a process. 29
2.2 **Quasi-phase matching with periodic poling.** Example of (a) periodic poling in a non-linear crystal comprising alternating domains to compensate for the (b) wavevector mismatch. 31
2.3 **SPDC generational OAM bandwidth.** Example of an (a) SPDC OAM bandwidth marked in the (b) pump beam waist size w_p and the non-linear crystal length L parameter space determining the OAM Schmidt number. 34
2.4 **SPDC measurable OAM bandwidth.** Example of measurable bandwidth as a function of the pump and detection beamsizes for a (a) $L = 5$ mm crystal and (b) $L = 1$ mm crystal. Dotted line indicates the optimal ratio for maximum bandwidth between detection and signal beam waists. 35
2.5 (a) A Gaussian beam modulated by an azimuthal phase, shown here as a metasurface, results in an OAM mode with many radial orders, shown in (b) as the sum of beams with several intensity rings. By combining dynamic and geometric phase control using holograms and metasurfaces, high purity OAM modes can be produced, as seen in (c). For detection of the modal composition of a beam, conjugate modulation of the mode being evaluated is applied and the Fourier plane on-axis intensity measured, as shown in (d). 38
2.6 (a) Schematic of a J-plate design. The J-plate imprints two kinds of helical phase profiles for x- and y-incident polarization, resulting in output beams with orbital angular momentum $m\hbar$ and $n\hbar$, where m and n can be any independent integers. The metasurface elements are rectangular nano-posts made of amorphous TiO_2 with a fixed height $h = 600$ nm. By changing the width along x- and y-direction (w_x and w_y), the nano-posts impart phase delays given by δ_x and δ_y. (b-d) Optical micrographs (b) and Scanning electron micrographs (SEMs) (c and d) of a representative J-plate with OAM number (m, n) = (10, 100). The SEMs show a top view (c) and angled view (d) of the device center. 40
2.7 Illustrations of the (a) classical and (b) quantum experimental setups. SLM: spatial light modulator functioning in reflective mode but drawn here as transmissive; F,L: lens; CCD: charge-coupled device; NC: non-linear crystal; BS: beam splitter; M: mirror; SMF: single mode fibre; APD: avalanche photodiode; BPF: band-pass filter; s: signal; i: idler; C.C.: coincidence counter. Overhead insets show representative phase maps for the respective beam manipulations carried out at each point. 41

2.8 Normalised detection probabilities with variation in the p-mode index and $\alpha = w_\ell/w_0$ for (a) $\ell = 10$ and (b) $\ell = 1$. Measured p-mode spectra (blue bars) are given for detection with (i) the unadjusted mode size ($w_\ell = w_0$) and (ii) the optimal encoded mode size ($w_\ell = w_{\text{opt}}$) shown with the theoretical predictions (black bars). The normalisation was performed with respect to the p-mode distribution. False colour map images of an $\ell = 100$ generated beam with (c) phase-only modulation and (d) amplitude corrected phase modulation are shown. 42
2.9 The p-mode spectrum when full amplitude and phase control is applied for (a) $\ell = 10$ and (b) $\ell = 1$. The bars represent the theory while the points represent the experiment. Insets show the processed transverse spatial distributions. The small intensity oscillations are due to the discrete nature of the metasurface nano-posts. 43
2.10 (a) Experimental and (b) simulated coincidence measurements based on the detection probabilities of OAM photons measured with the encoded holograms. (c) The normalized coincidences as a function of $\alpha = w_\ell/w_0$ for (c) $\ell = 1$ (d) $\ell = 2$ (e) $\ell = 5$. The bars represent the experimental data while the points represent the simulation. (f) Spiral-bandwidth plots obtained from the diagonal of the inset mode projections for (left) w_0 and (right) w_{opt}. Insets are density plots representing measured coincidences for OAM projections on the SLMs when the encoded LG beam size is w_0 (black squares) and the optimal mode sizes (w_{opt}) (blue triangles). Each data point was measured over a 5 seconds time interval. 44
2.11 **Sum-frequency generation.** Diagram of the interaction geometry for sum-frequency generation with a $\chi^{(2)}$ non-linear crystal. Top right inset shows the energy level diagram. 46
2.12 (a) In a traditional quantum experiment, a Gaussian mode pumps a nonlinear crystal (NLC) mediating the generation of two entangled photons with OAM values of ℓ and $-\ell$. (b) Example of flat and anti-correlated modal spiral spectrum of the paired down-converted photons. (c) In the frequency up-conversion process, two incoming signals are engineered to be in specific states. The up-converted signal is detected in the far field, so that there is a non-zero signal only when the phases are conjugate. 48
2.13 Schematic of the experimental up-conversion spatial mode detection setup. 806nm laser: high-power single frequency diode laser (Roithner); 1565 nm laser: single mode fiber pigtailed laser diode (Thorlabs); FL: Fourier lens; PH: pin hole; SLM: spatial light modulator (Holoeye); HWP: half-wave plate; DM: dichroic mirror; PPKTP: 5-mm-long nonlinear periodically-poled potassium titanyl phosphate crystal (Raicol); SPF: short-pass filter; CCD: CCD camera (Spiricon). . . 50
2.14 Cross-talk expressed in dB relative to the power in an input OAM mode with a particular helical charge for the 1565 nm ($\ell_A = [-3, 3]$) and performing a modal decomposition by varying the helical charge of the input OAM mode for the 806 nm ($\ell_B = [-5, 5]$). We have obviated the cross-talk values below -60 dB. The inset rightmost column shows the captured intensities for the OAM input mode $\ell_A = 1$, marked with a dotted white rectangle, to indicate where the central pixels are extracted. 51

2.15 HG modal cross-talk given in dB for two different input $HG_{m,n}$ modes. The 1565 nm laser beam is encoded with (a) $HG_{0,0}$ and (c) $HG_{1,1}$, performing a modal decomposition with the 806 nm input laser beam such as $HG_{n,m}$, with the m, n indexes ranging within [0,3]. We show the captures obtained in the right indicating the weightings of the detected modes in the left, by extracting the center pixel value in the intensity plots for (b) $HG_{0,0}$ and (d) $HG_{1,1}$. Dotted cross-hairs indicate the central coordinate. 51
2.16 Up-converted images measured as M_C with M_A (1565 nm) as a Gaussian, shown in (a), and M_B (806 nm) set to be (b) lambda, (c) yin yang and (d) jay symbols. The insets show the applied amplitude modulated mask and the corresponding hologram to imprint the image onto mode M_B. The emerging fringes are the Moiré pattern due to the finite resolution of the SLM screen. 52

3.1 **Teleportation channel scheme with optimisation parameters.** A pump photon with a waist size of w_p impinges on a nonlinear crystal, generating two photons, photon B and photon C. Photon C is transmitted to a second crystal for SFG where it is absorbed with another independent photon encoded with the mode $|\Theta_A\rangle$, corresponding to a mode field with a waist size of w_0. We will call this independent photon, photon A. To recover the spatial information of photon A, we scan the spatial mode of photon B with spatial projections mapping onto the state $|\Phi_B\rangle$ with a corresponding mode field that also has a waist size of w_D. ℓ_A and ℓ_B refer to the encoded and projected vortex states displayed on the spatial light modulators (SLMs). 60
3.2 **Simulated spiral bandwidths and dimensionalities from measurements of photon B relating to encoded states of photon A.** Example renormalised teleported spiral bandwidths for vortex modes when (a) $\alpha = w_p/w_0 = 1$ and (b) $\alpha = 5$, using a fixed $\beta = w_p/w_D = 1$. These are marked as dashed lines in a wider (c) density plot of the spiral spectrum diagonal ($\ell_A = \ell_B$) as a function of α and (d) the calculated dimensionality (K), measured from the Schmidt number as a function of α. 61
3.3 **Generalised OAM teleportation channel capacity analysis.** Contour plot of the dimensionality (K) as a function of β and α. For higher dimensionality we need a small $\beta < 1$ and large α. The blue single dash line corresponds to the minimum $\alpha = \alpha_0$ for teleporting a spatial mode through the setup. The red double dashed line corresponds to the minimum $\alpha = \alpha_5$ for teleporting OAM modes with $\ell = [-2, 2]$ giving access to no more than $K = 5$ dimensions. 61

3.4 **Realising a teleportation channel based on nonlinear optical detection.** (a) A pump photon ($\lambda_p = 532$ nm) undergoes spontaneous parametric downconversion (SPDC) in a nonlinear crystal (NLC_1), producing a pair of entangled photons (signal B and idler C), at wavelengths of $\lambda_B = 1565$ nm and $\lambda_C = 808$ nm, respectively. Photon B is directed to a spatial mode detector comprising a spatial light modulator (SLM_B) and a single mode fibre coupled avalanche photo-diode detector (APD). The state to be teleported is prepared as photon A using SLM_A ($\lambda_A = 1565$ nm), and is overlapped in a second nonlinear crystal (NLC_2) with photon C, resulting in an upconverted photon D which is sent to a single mode fibre coupled APD. Photons B and D are measured in coincidence to find the joint probability of the prepared and measured states using the two SLMs. (b) The teleportation channel's theoretical modal bandwidth (K) as a function of the pump (w_p) and detected photons' (w_0 and w_D) radii, with experimental confirmation shown in (c) through (e) corresponding to parameter positions C, D and E in (b). K_{th} and K_{ex} are the theoretical and experimental teleportation channel capacities, respectively. The cross-talk plots are shown as orbital angular momentum (OAM) modes prepared and teleported. The raw data is reported with no noise suppression or background subtraction, and considering the same pump power conditions in all three configurations. 65

3.5 Detailed experimental setup description for high-dimensional spatial teleportation without ancillary photons. Ap: Aperture; BPF: Bandpass filter; DM: Dichroic mirror; f: Lens focal length; LPF: Lowpass filter; HWP: Half-waveplate; NLC: $\chi^{(2)}$ Non-linear crystal; SLM: Spatial light modulator (phase-only). 67

3.6 **Quality of the teleportation process.** Experimental fidelities (points) for teleportation channel dimensions up to the maximum achievable channel capacity of $K = 15 \pm 1$, all well above the classical limit (dashed line). The solid line forms a maximum fidelity for the measured teleported state. The inset shows the measured OAM modal spectrum of the optimised teleportation channel with maximum coincidences of 320 per second for a 5 minute integration time. The raw data is reported with no noise suppression or background subtraction. Error bars are produced from error propagation of Poissonian statistics and uncertainties the analysis method. 68

3.7 **Visibilities and quantum state tomography.** (a) Measured coincidences (points) and fitted curve (solid) as a function of the phase angle (θ) of the corresponding detection analyser for the state $|\phi\rangle = |\ell\rangle + \exp\{(i\theta)\}|-\ell\rangle$, for three OAM subspaces of $\ell = \pm1$, ±2, and ±3 (further details in Appendix B.4). (b) The real (Re[ρ]) and imaginary (Im[ρ]) parts of the density matrix (ρ) for the qutrit state $|\Psi\rangle = |-1\rangle + |0\rangle + |1\rangle$ as reconstructed by quantum state tomography. The inset shows the raw coincidences with maximum coincidences of 220 detected per second from the tomographic projections (full details in the Appendix B.3 and B.7). (c) Measurements for the teleportation of a 4-dimensional state, constructed from the states $\ell = \{\pm1, \pm3\}$, with the inset graph showing the detection (solid bars) of all the prepared (transparent bars) OAM states comprising one of the MUB states. The raw data is reported with no noise suppression or background subtraction and error bars produced from multiple measurements. 70

3.8 **Teleportation in the Hermite-Gaussian basis**. Coincidence measurements for teleportation of a (a) 3-dimensional and (b) 9-dimensional $HG_{n,m}$ state, constructed from the states $(n,m) = \{(0,1),(1,0),(1,1)\}$ and $(n,m) = \{(0,0),(2,0),(0,2),(2,2),(2,4),(4,2),(4,4)\}$, respectively. The teleported state (solid bars) is in good agreement with the prepared state (transparent bars). The raw data is reported with no noise suppression or background subtraction. 71

3.9 **Summary of teleported states**. Similarities for teleportation of a 2,3,4 and 9-dimensional superposition states in the OAM (represented as $|\varphi\rangle$) and HG (represented as $|\gamma\rangle$) bases shown and labelled to the left. Raw data are reported without noise suppression or background subtraction Teleported states are $|\varphi_1\rangle = |0\rangle + |1\rangle$, $|\varphi_2\rangle = |-1\rangle + |1\rangle$, $|\varphi_3\rangle = |0\rangle + |-1\rangle$, $|\varphi_4\rangle = |-2\rangle + |0\rangle + |2\rangle$, $|\gamma_1\rangle = |HG_{1,0}\rangle + |HG_{1,1}\rangle + |HG_{0,1}\rangle$, $|\varphi_5\rangle = |-3\rangle - i|-1\rangle + |1\rangle + i|3\rangle$, $|\gamma_2\rangle = |HG_{0,0}\rangle + |HG_{1,0}\rangle + |HG_{1,1}\rangle + |HG_{0,1}\rangle$ and $|\gamma_3\rangle = |HG_{0,0}\rangle + |HG_{2,0}\rangle + |HG_{0,2}\rangle + |HG_{2,2}\rangle + |HG_{4,0}\rangle + |HG_{0,4}\rangle + |HG_{4,2}\rangle + |HG_{2,4}\rangle + |HG_{4,4}\rangle$. Error bars given are from multiple measurements 72

3.10 **Modal detection efficiencies with experimental parameters.** Numerical simulation of the change in detection efficiency for $\ell = 0$ as the experimental parameters are optimised for higher dimensionality. Points C-E indicated correspond to experimental parameters tested in Fig. 3.4. 73

3.11 **Mode dependent detected noise.** Spiral bandwidth plot spanning $\ell = [-8,8]$ showing the measured background noise indicating higher noise for lower order modes. 74

3.12 **Visibilities with detection parameters.** Experimental visibility curves obtained by rotating $\theta = [0,2\pi]$ in the detection mode $(|-1\rangle + e^{i\theta}|1\rangle)$ for teleported state $|\psi\rangle = |-1\rangle + |1\rangle$ for (a) 1 μs deadtime and 1.5 ns coincidence window, (b) 5 μs deadtime and 1.5 ns coincidence window as well as (c) 1 μs deadtime and 0.5 ns coincidence window. Error bars given are from multiple measurements. 75

3.13 **Channel SPDC characterisation.** Experimental (a) spiral bandwidth of the channel SPDC and (b) visibility curve obtained by rotating phase angle, $\theta = [0, 2\pi]$, in the detection mode ($|-1\rangle + e^{i\theta}|1\rangle$) in Bob's arm for the state $|\psi\rangle = |-1\rangle + |1\rangle$ in the arm used for teleportation. No noise subtraction or error correction was performed on the data. Error bars given are from multiple measurements 77
3.14 **Nonlinear efficiency vs quantumness of the teleportation**. Conceptual plot showing the convergence of the number of copies carrying the d-dimensional teleportee state as the SFG is increased. Red dots help to identify the different examples of commercial nonlinear crystals (ppKTP type-0 being our case), and the *all-dielectric* metasurface of Ref. [298] with a notably increased nonlinear coefficient. The plot in the inset shows an example of the amount of extra ancillary photons required to teleport the same d-dimensional teleportee state using linear optics. 79

4.1 **Simulated pixel bandwidths and dimensionalities from measurements of photon B relating to encoded states of photon A.** Example renormalised teleported pixel bandwidths for a 5×5 discretised position space when (a) $\alpha = w_p/w_0 = 1$ and (b) $\alpha = 10$, using a fixed $\beta = w_p/w_D = 1$. These are marked as dashed lines in a wider (c) density plot of the spiral spectrum diagonal ($j_A = j_B$) as a function of α and (d) the calculated dimensionality (K), measured from the Schmidt number as a function of α. The pixel order in the space is indicated in the top-right inset of (a). 85
4.2 **Generalised pixel teleportation channel capacity analysis.** Contour plot of the dimensionality (K) as a function of β and α. For higher dimensionality we need a larger $\beta > 5$ and large α. The white dash line corresponds to the general value of $\beta = 5$, which indicates parameter values in which close to maximal dimensionality ($K = 25$) is achievable. 86
4.3 A schematic diagram of the implemented quantum ghost imaging setup. (a) Entangled bi-photons are produced via spontaneous parametric down-conversion (SPDC) at the NLC. The entangled photons are spatially separated and each imaged onto a SLM. Required holograms are displayed on each SLM. Coincidence measurements are done between both paths and the coincidences are used to reconstruct an image of the object. For each object two measurements are taken, as numerically simulated in (b). These two images are then combined such that the argument reveals the total phase. (c) Shows the digital phase-only objects used in the experiment, while the simulated image reconstructions are shown in (d) showing how the digital objects are expected to perform. L_1 = 50 mm, L_2 = 750 mm, L_3 = 750 mm, L_4 = 2 mm. 89
4.4 Reconstructed amplitude-only images using the Walsh-Hadamard masks for (a) an intensity slit, and (b) an intensity ring. The outer area of the dashed white circle indicates the region in which noise was suppressed due to lack of SPDC signal. The amplitude-only objects are shown as insets. 91

4.5 Numerical simulations (Sim) showing excellent agreement with the Experimental reconstructions (Exp) for the *pi*-phase slit and the azimuthal gradient ring using (a) Walsh-Hadamard and (b) random masks. Experimental images were denoised with image processing tools and contrast adjustment after reconstruction. The outer area of the dashed white circle indicates the region in which noise was suppressed due to lack of SPDC signal. Insets show the corresponding cosine and sine components of the experimental reconstructions. 92
4.6 Phase image cross-sections showing the phase value per pixel for the numerically simulated reconstruction given by the grey dotted line and experimental reconstructions for both the Walsh-Hadamard (blue diamonds) and random masks (red dots) for (a) the π-phase slit in the horizontal direction, and (b) phase ring in the azimuth direction for a radius set inside the ring. Error bars shown are from error propagation of Poissonian statistics. 93
4.7 Experimental ghost image of a (a) pure phase and (b) complex amplitude gradient spiral flower using Walsh-Hadamard masks. The full phase profile was denoised after reconstruction by image processing tools and contrast adjustment. The cosine (middle) and sine (right) components are shown for completeness in (a). The complex aplitude object (left) was reconstructed to give phase (middle) and threshold amplitude (right) in (b). Three-dimensional renders of the raw reconstruction data are shown below. 94

A.1 Diagram of the holograms and field structure for holographic analysis of the meta-surface generated modes. Grating, amplitude and phase components are combined to form the holograms shown for the 3 cases evaluated in this paper. (a) Detection of the modes in the azimuthal and radial bases with varying encoded beam waists. (b) Correction of the modal amplitude to generate OAM modes with pure radial profiles. We believe that the residual rings observed in the farfield are due to pixelation from the nano-posts and possibly due to no aperturing before the CCD. (c) Traditional phase-only OAM generation with Gaussian input onto the meta-surface. Far-field images shown in (b) and (c) were post-processed to remove a central intensity spot, resulting from the presence of the unmodulated Gaussian remaining after the meta-surface. This was achieved by setting the central values to 0 and thus allows one to see only the amplitude correction and modulation effects of the meta-surface as well as demonstrating what one would see in detection for a 100% efficient device. . 104

B.1 **Procrustean filtering of the OAM modes.** (a) Unflattened and (b) flattened spiral bandwidths by decreasing the grating depth for lower ℓ-values. Here (i) gives the density plot, (ii) shows the diagonal of (i) and (iii) renders the data in 3D where the diagonal values are highlighted. Error bars are calculated from multiple measurements. 110
B.2 **Illustration of background measurement.** Histogram showing the arm delays with the coincidence windows for a 3s integration time, demonstrating the measured background values for noise correction. . 111

B.3 **Effects of applying noise correction to the results.** Plots showing the (a) raw measured coincidences and (b) coincidences corrected by subtracting the background measured in an uncorrelated time-bin for the (i) spiral bandwidth with a (ii) 3D rendering and (iii) the visibility measurable for rotating the projected state for the $\ell = \pm 1$ teleported state. Error bars are calculated from multiple measurements. 112
B.4 **Teleported MUB states.** Experimental fidelities measured for state tomography performed on all 12 teleported MUB states for a $d = 3$ space comprised OAM modes ℓ = {-1,0,1}. Dashed (solid) lines indicate the classical (genuine qutrit) limit and phase insets along the x-axis show the MUB state phase profiles. The data is raw and not background subtracted. Error bars are calculated from multiple measurements. . . 114
B.5 **Teleportation of unevenly weighted states.** Experimental measurements (filled bars) of uneven encoded superposition states (bar outlines) for (a) $|\psi\rangle = 2|-1\rangle + 3|0\rangle + |1\rangle$, (b) $|\psi\rangle = 2|-2\rangle + 3|0\rangle + |2\rangle$, (c) $|\psi\rangle = |-2\rangle + 2|0\rangle + |2\rangle$ and (d) $|\psi\rangle = 2|-3\rangle + |-1\rangle + |1\rangle + 2|4\rangle$. Uncertainties are calculated from multiple measurements. 116
B.6 **Channel tomography measurements with uncertainties.** Experimental measurement plot shown with the detected coincidences given by the false colormap and the associated uncertainties, calculated from multiple measurements, printed in each measurement block. $\theta = 0, \frac{\pi}{2}, \pi$ and $\frac{3\pi}{2}$ as indicated for each of the bracketed superposition subspaces. 117
B.7 **Four-dimensional MUB measurements with uncertainties.** Experimental measurement plot shown with the detected coincidences given by the false colormap and the associated uncertainties, calculated from multiple measurements, printed in each measurement block. 117
B.8 **Teleported MUB states tomography.** Experimental state tomography measurements measured with an integration with of 120s performed on the 12 MUB states for a $d = 3$ space comprised OAM modes ℓ = {-1,0,1}. Numbers printed on the measurement blocks indicate the associated standard deviations measured from multiple measurements. . 118
B.9 **Spiral bandwidth measured for high dimensionally tuned setup.** Experimental measurements with standard deviations, calculated from multiple rounds, printed on the average coincidences shown by the false colormap for the spiral bandwidth of an optimally tuned system where $K \approx 15$. 118
B.10 **Teleportation Fidelities.** The measured teleportation fidelities for the channel ($F_{channel}$) for states that bob receives (F_{Bob}). The classical ($F_{classic}$) and cloning bounds (F_{clone}) are also shown. Our system shows the possibility of teleporting up to $d = 4$ dimensions. Moreover, since our spectrum for the OAM basis was not flat (maximal correlations), we show how a flat spectrum would improve the teleportation fidelities (F_{max}) under the same experimental conditions. 119
B.11 **Size-matched flattened modes.** Example of the experimentally measured teleported spectrum diagonal for the lowest three modes used to comprise the twelve $d = 3$ MUB teleported states. Error bars are calculated from multiple measurements. 119

C.1 Examples of the computed terms in the ghost imaging protocol. Here the labels $t_{1,2,3}$ correspond to the first, second and third term in $\mathbf{GI}_{\cos}$. The inset in the firs column corresponds to the ghost image obtained from the algorithm in Eq C.1. The insets in the fourth column show the DC component to be subtracted. 122
C.2 Example theoretical phase reconstruction from the ghost images. . . . 124
C.3 Uncropped experimentally measured ghost images. 125

List of Tables

1.1 **Mutually unbiased basis states.** Mutually unbiased basis state sets for $d = 2$ and $d = 3$, calculated using Hadamard constructions. S_j refers to the basis state in each indicated MUB and $\omega = e^{i\frac{2\pi}{3}}$. 20

2.1 **Phase matching types.** Summary of various phase-matching regimes for second order non-liner interactions which differ for input and output field polarisation with respect to parallel orientation to the crystal ordinary (o) or extraordinary (e) axes. 30

3.1 **Experimentally tested parameters.** Parameters values used experimentally to test the numerically simulated dimensionality trends. . . . 66

3.2 **Visibilities for different parameters.** Comparison of the visibility and maximum detected coincidences with different detector dead-times and coincidence windows for results obtained by rotating $\theta = [0, 2\pi]$ in the detection mode $(|-1\rangle + e^{i\theta}|1\rangle)$ for teleported state $|\psi\rangle = |-1\rangle + |1\rangle$. Uncertainties are calculated from multiple measurements . 76

B.1 **Results summary of background subtracted and raw data.** Experimental visibilities, fidelities and similarities calculated for the teleportation channel and teleported states comparing raw and background subtracted (B. Sub.) outcomes. Abbreviated states are: $|\varphi_1\rangle = |0\rangle + |-1\rangle$, $|\varphi_2\rangle = |-1\rangle + |1\rangle$, $|\varphi_3\rangle = |0\rangle - |1\rangle$, $|\varphi_4\rangle = |-2\rangle + |0\rangle + |2\rangle$, $|\gamma_1\rangle = |HG_{1,0}\rangle + |HG_{1,1}\rangle + |HG_{0,1}\rangle$, $|\varphi_5\rangle = |-3\rangle - i|-1\rangle + |1\rangle + i|3\rangle$, $|\gamma_2\rangle = |HG_{0,0}\rangle + |HG_{1,0}\rangle + |HG_{1,1}\rangle + |HG_{0,1}\rangle$ and $|\gamma_3\rangle = |HG_{0,0}\rangle + |HG_{2,0}\rangle + |HG_{0,2}\rangle + |HG_{2,2}\rangle + |HG_{4,0}\rangle + |HG_{0,4}\rangle + |HG_{4,2}\rangle + |HG_{2,4}\rangle + |HG_{4,4}\rangle$, as given in Section 3.9. Slightly better similarities may be noted in some cases for the raw values of the superposition on states as the Procrustean filtering applied was optimised for the raw data. Uncertainties are calculated from multiple measurements. 113

B.2 **Comparison of d = 3 teleported MUB states.** Comparison of the teleported fidelities calculated from raw (not background subtracted) data. for all 12 MUB states with those in reported in existing literature for high-dimensional teleportation. Values estimated from the graphs presented in the respective publications are labelled (app.). 115

List of Publications

1. **B. Sephton**, Nape, I., A. Vallés, M.A. Cox, F. Steinlechner, T. Konrad, J.P. Torres, F.S. Roux and A. Forbes, "Stimulated teleportation of high-dimensional information with a nonlinear spatial mode detector", *arXiv:2111.13624v2 [quant-ph]*, (under review at Nature Photonics, 2022)

2. **B. Sephton**, C. Moodley, J. Francis and A. Forbes, "Revealing the embedded phase in single pixel quantum ghost imaging", *Optica*, **10** 2(2023), 286-291

3. I. Nape, **B. Sephton**, Y-W. Huang, A. Ambrosio, C-W. Qui, A. Vallés, F. Capasso and A. Forbes, "Enhancing the modal purity of orbital angular momentum photons", *APL Photonics* **5** 7(2020), 070802

4. **B. Sephton**, A. Vallés, F. Steinlechner, T. Konrad, J. P. Torres, F. S. Roux and A. Forbes, "Spatial mode detection by frequency upconversion", *Optics Letters* **44** 3(2019), 586-589

Dedicated to my family. Eline, Kyle and Abigail: thank you for always being there. Lucius: I miss you, always.

Chapter 1

Introduction

With the reference "Beam me up Scotty", the idea of being able to move an object from one position in space to another without having to physically traverse the distance has become commonplace in science fiction. This, after first being proposed by H. Forte [1] in the 1970s and then made popular by Star Trek. In this sense, the classical format may be considered as moving all the particles comprising the object and so moving the 'baking ingredients' between two positions. Quantum mechanically, however, Vaidman [2] discussed an interesting view of teleportation where an object may be rather considered as the quantum state of the elementary particles of which it is made and thus rather the 'recipe' that combines the ingredients into making the object. Accordingly, reconstruction of this state on other such elementary particles at another location can be thought of as actually teleporting a quantum mechanical object [2]. More formally, however, we can describe quantum teleportation as a way to broadcast unknown information between two distant locations without using a physical carrier in between. A key feature here is that the state forms on the other side without needing to know what it is and does not travel directly between the two positions as in traditional methods of communication, be it classical or quantum. This formed the basis of the protocol proposed by Bennett *et al.* [3] some 20 years later in 1993 which coined the term *quantum teleportation*. In doing so, the state need not be intercepted as it does not exist between the communicating parties and does not necessarily need to suffer the distortion effects of the communication channel as it uses a pre-shared resource. As there is no direct observation of the state being sent, the superposition as well as all the correlations are maintained, preserving the quantum nature.

In order to achieve this, the protocol relies on the quantum mechanical property of entanglement to first form a channel between two distant parties. Each party then possesses one of a pair of entangled entities and, as such, shares the quantum mechanical correlations existing between them. Information may then be transferred to within a unitary rotation between them by manipulating the state of one of the entangled particles such that it becomes entangled with a secondary entity that carries an unknown quantum state that one wishes to be sent. It thus follows that information is sent between parties without that actual information being transmitted physically between them i.e. the particle with the unknown state is never sent directly to the other party, but stays with the one sending it. A measurement is then required to determine the unitary rotation that needs to be applied in order to retrieve the state on the other side. This is communicated classically and results in excluding the protocol from communication faster than the speed of light and thus remains in the bounds of physics.

Quantum teleportation thus forms a unique method for sending states which utilises quantum entanglement at its core and can be exploited as a quantum information protocol where inherent advantages can be exploited due to its properties.

As such, it is an active component in the development of quantum information science [4–7]. Here the conceptual scheme forms a fundamental step in many formal quantum information theories and its physical process forms a basic building block towards the development of many quantum technologies, allowing information exchange protected against eavesdropping [8]. For instance, quantum technologies such as quantum repeaters [9], measurement-based quantum computing [10] as well as quantum gate teleportation [11] all derive from the quantum teleportation protocol and extend to the idea of a quantum network [12]. Additionally, the scheme has been shown useful for exploring 'extreme' scenarios such as closed timelike curves [13].

It follows that many avenues are being actively explored in order to develop physical systems that can easily and accurately implement quantum teleportation with systems ranging from nuclear magnetic resonance [14], atomic ensembles [15–18], solid state systems [19–22] and trapped atoms [23–27] to optical modes [28–36] and discrete photonic states. Here, optical mode teleportation occurs in a continuous variable regime [37, 38] adapted from the originally proposed discrete variable case by Bennett *et al.* In this case, the information is carried in the electric field that is described by phase and amplitude or position and momentum-like quadrature operators [6, 7]. For discrete photonic states, the many degrees of freedom possessed by the particles have been utilised to form qubits, including the spin or polarisation states [39–45], time-binning [46–48], single- [49, 50] and dual- [51, 52] rail states and as well as spatial structures [53].

Much focus has been given to extending the distance and fidelities [54] at which the protocols may be executed across both fibre [40, 46, 48, 55, 56] and free-space [44, 45, 57] with efforts extending to a low orbit satellite [58]. These advances bring the practicality of implementing large quantum networks which can then form a quantum internet [12, 59, 60].

All of these, however, remain at the fundamental two-dimensional or qubit state space, which limits the bandwidth of the communication link to one bit of information per photon and thus limiting the communication link to how fast the signal can be sent, measured and corrected. Quantum systems at the core are also generally multi-dimensional and so, either full reconstruction of one or extending the bandwidth of the information that can be sent at a given time would be a limiting factor on the practicality of implementing and using such a technique in quantum networks. Extension of this limitation then lies in increasing the dimensions that can be teleported by the physical system from qubits (two-dimensions) to qudits (d-dimensional). This has already gained attention in the broad quantum information field where advantages of using higher dimensional systems extend past increasing information capacity to offer protection against optimal quantum cloning machines [61–63], higher information security [64–66] and possible noise resilience [67].

In lieu of this, recent research has also begun to focus on experimentally extending the degrees of freedom [53] and dimensions [68, 69] of the states being sent, bringing the current state of the art to three-dimensions or qutrit teleportation. Theoretical protocols for qudit teleportation using linear optics have already been put forward [70, 71], however, much of the limitation lies in the physical implementation of a system that can support and entangle the higher dimensional states in a scalable manner. For instance, in the qutrit implementation schemes [68, 69], the protocols can be extended past the demonstrated dimensions, however, each additional dimension requires another (ancillary) pair of entangled photons which involves additional optics and and nonlinear crystals that makes implementation for higher dimensions increasingly difficult. Here the scheme relies on a linear optical

approach which has a fundamental limitation in the entanglement step that restricts the ability to discriminate all of the teleportation variations.

A method to side-step this involves a nonlinear approach [72–74] where the entanglement step involves up-conversion of the channel and prepared state photon, rather than an interaction with a beamsplitter. Studies show that the quantum properties such as squeezing are conserved in up-conversion [75], allowing the state up-converted with the interacting channel photon to be transferred to the entangled partner. Here the approach has been used to demonstrate a complete Bell-state measurement for discrete-variables [43] as well as multiplexed teleportation of orbital angular momentum spatial states with continuous variables [76], however, neither of the demonstrations extend beyond qubits.

With this nonlinear approach, it is possible to exploit the transverse spatial modes in structured light [77] such as orbital angular momentum (OAM) or pixel states as high-dimensional encoding bases. Higher dimensional spatial modes have been a topic of interest as a promising approach for increasing information capacity with experiments with other quantum information protocols demonstrating their potential in freespace [63, 78–84], optical fibres [85] and underwater [86] quantum communication channels. Using the pixel basis, one may achieve teleportation of quantum images, allowing compact, high bandwidth information to be securely teleported to another party and, with other bases like OAM, can introduce diversity for implementing versatile quantum networks.

In the sections that follow, we introduce how states can be represented and then extend the formalism to cover the basic concept of teleportation before exploring transverse spatial modes as a convenient encoding basis that scales easily. We then look at how choice measurements can be used to reconstruct the states of interest. These form the basics which will be taken further in order to develop, implement and characterise high-dimensional quantum teleportation with non-linear optics in a way that scales conveniently and can be extended towards the teleportation of complex images.

1.1 The language of quantum states

Due to the probabilistic nature of quantum entities, the outcome of a single-shot measurement is not directly predictable, but rather a picture of such is gained by the statistical outcomes of many choice single-shot measurements repeated on identically prepared systems. The collective outcomes then allows one to determine a probability distribution which can be used to describe the particles. Mathematically, quantum states are used to describe the behaviour of quantum entities and as such represent key building blocks of quantum processes. Here we cover the basic mathematical formalism used to describe and handle the quantum systems used to both understand the teleportation protocol as well as implement it in higher dimensions later on.

1.1.1 Qubits and the Bloch sphere

Wavefunctions such as ψ can be used to describe a quantum state. With Dirac formalism, this is can be represented as a vector, $|\psi\rangle$ in an inner product vector space, known as Hilbert space, $\mathcal{H}$. In the discrete case, where particles have quantised outcomes such as spin up or spin down, those form elements in a discrete Hilbert space, $\mathcal{H}^d$ where d represents the dimension of the space and as such is the number

of unique elements that span it for an orthonormal computational basis. Outside of

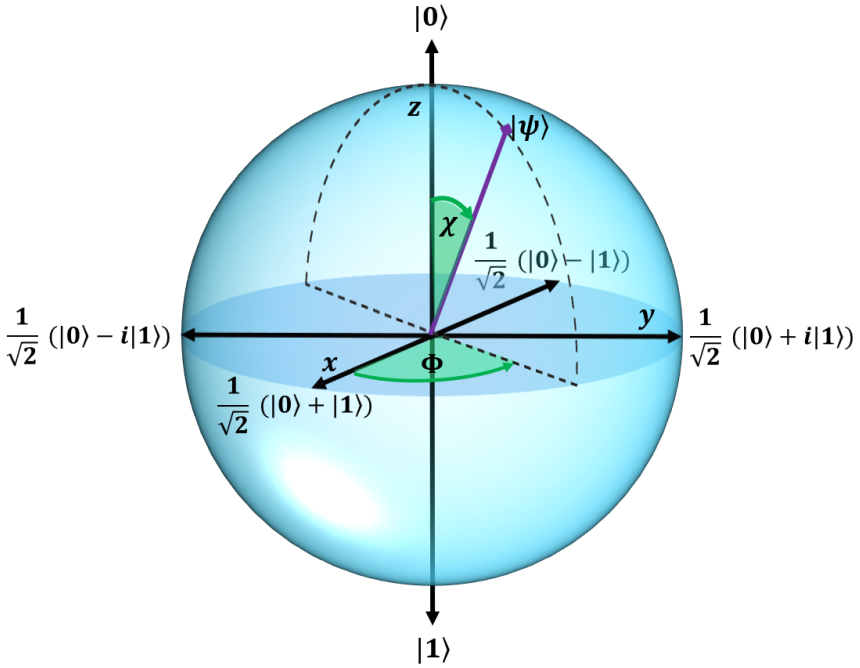


FIGURE 1.1: **Bloch sphere.** The Bloch sphere with key qubit states and mapping parameters indicated. Poles contain the basis states with equal superpositions positioned on the equator.

the trivial one-dimensional case, two-dimensions represent the simplest example of discrete quantum states spanning a Hilbert space. Here the basis vectors

$$|0\rangle = \begin{bmatrix} 1 \\ 0 \end{bmatrix}; \quad |1\rangle = \begin{bmatrix} 0 \\ 1 \end{bmatrix} \tag{1.1}$$

span the state space. A particle described by this space is called a qubit. It then follows that a general description of a pure qubit state $|\psi\rangle$ is made from a linear superposition of the basis vectors such that,

$$\begin{aligned} |\psi\rangle &= \alpha\,|0\rangle + \beta\,|1\rangle \\ &= \begin{bmatrix} \alpha \\ \beta \end{bmatrix} \end{aligned} \tag{1.2}$$

where α and β are complex coefficients weighting the contribution and phase between the basis vectors. $|\alpha|^2$ and $|\beta|^2$ thus give the probability of finding the qubit in the basis state $|0\rangle$ or $|1\rangle$, respectively. Additionally, $|\alpha|^2 + |\beta|^2 = 1$ as the probabilities should sum to unity i.e. $|\langle\psi|\,\psi\rangle|^2 = 1$. Traditionally, qubits are graphically visualised on a Bloch sphere [4], shown in Fig. 1.1 for an arbitrary state. Here the poles (z-axis) represent the basis states with the hemisphere (x- and y-axes) then giving equal superpositions of both with different relative phases. The pure qubit ($|\psi\rangle$) is mapped to the surface of the sphere with the relation,

$$|\psi\rangle = \cos\left(\frac{\chi}{2}\right)|0\rangle + e^{i\Phi}\sin\left(\frac{\chi}{2}\right)|1\rangle\,, \tag{1.3}$$

where $0 \leq \chi \leq \pi$ and $0 \leq \Phi < 2\pi$ and the radius of the sphere is 1. The parameter χ gives the polar angle and thus dictates the contribution of the basis state,laterally positioning the qubit. For instance, at $\chi = \frac{\pi}{2}$ an equal superposition of $|1\rangle$ and

$|0\rangle$ is specified. The second parameter Φ specifies the azimuthal angle, yielding the relative phase between the basis states and as such generates a rotation of the qubit vector about the z-axis. For example, $\Phi = \frac{\pi}{2}$ then gives results in the state $\frac{1}{\sqrt{2}}(|0\rangle + |1\rangle)$. In this case, the common phase value between the complex α and β in Eq. 1.2 is factored out as a global value that can be ignored, leaving only the relative phase between them.

1.1.2 Density matrices and purity

When describing a quantum system, however, using a wavefunction or state vector such as given in Eq. 1.2 is not always sufficient. For instance, what if the particles in the system are not all identically prepared, but rather different particles have different states with some accompanying probability? This would be different from a particle that is in a *superposition* of different basis states as in Eq. 1.2. Here the particle can be seen to be in both states at the same time and simply collapses into one of these states based on the measurement or observation being made. Rather the particle is in a specific state, but then the next particle being observed is in a different state, making the system a statistical ensemble of varying states. This latter case is known as a *mixed state*. This concept is illustrated in Fig. 1.2 for the two cases where three particles in such as ensemble are considered. Here measurements of the particles in either system will always give a 50% outcome of measuring a $|0\rangle$ or a $|1\rangle$. In the mixed case, the quantum system can no longer only be described by a single state vector that has a superposition of these outcomes as in the pure case. It follows that the state vector presented previously is no longer a viable way to describe the system being looked at. In order to extend the way we describe the quantum system, density matrices may be introduced along with another factor which is the purity. Purity in this case describes how 'identical' the system is that is being observed. Additionally, the question may arise as to how a system can be described where the states of different particles are correlated to each other. Density matrices are also integral to dealing with such entangled particles. This is explored further on in Section 1.1.4.

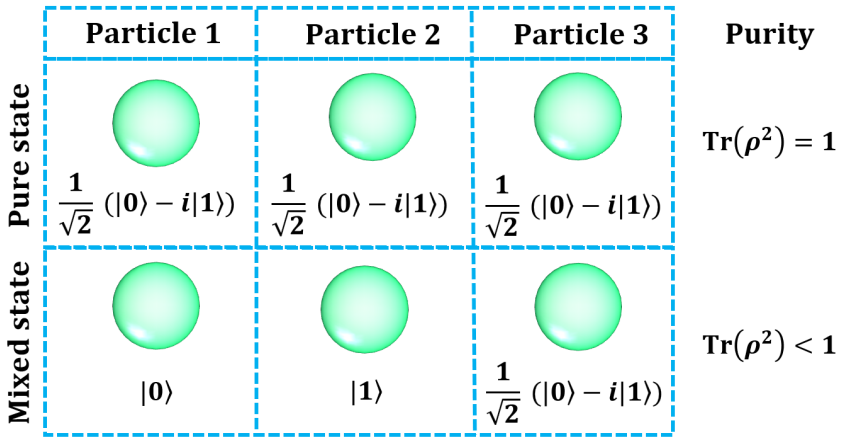


FIGURE 1.2: **Pure and mixed quantum systems.** Exemplary particles for a mixed and pure quantum system which will always give a 50% outcome of measuring a $|0\rangle$ or a $|1\rangle$. Determination of the nature of the system can be made by finding the purity.

More specifically, for a pure state, the density matrix can be obtained by taking the outer product of the state with itself. In terms of Eq. 1.2, the density matrix (ρ) is

then

$$\begin{aligned}\rho &= |\psi\rangle\langle\psi| \\ &= \begin{bmatrix}\alpha \\ \beta\end{bmatrix}\begin{bmatrix}\alpha^* & \beta^*\end{bmatrix} \\ &= \begin{matrix}\\ |0\rangle \\ |1\rangle\end{matrix}\begin{matrix}\langle 0| & \langle 1| \\ \end{matrix}\begin{bmatrix}|\alpha|^2 & \alpha\beta^* \\ \alpha^*\beta & |\beta|^2\end{bmatrix}\end{aligned} \tag{1.4}$$

with * indicating the complex conjugate. On the last line, the basis states are indicated outside the matrix to indicate the significance of each element. For instance. the first term ($|\alpha|^2$) yields the coefficient for the outer product, $|0\rangle\langle 0|$, in the pure state. It then follows that the density matrix of a mixed state is given by the weighted sum of pure matrices,

$$\begin{aligned}\rho &= \sum_j P_j |\psi_j\rangle\langle\psi_j| \\ &= \sum_j P_j \rho_j.\end{aligned} \tag{1.5}$$

Here the P_j is the probability of finding a particle in the state $|\psi_j\rangle$ with $\sum P_j = 1$. Due to its significance, the density matrix has several properties to note. Firstly, when taking the trace of the of the quantum state ρ with $Tr(\rho) = \sum_{j=0}^{d} \langle j|\rho|j\rangle$ for a d-dimensional state space with the basis $|0\rangle, |1\rangle, ..., |d\rangle$, it should equal to one. This is as the sum of all the possible measurements in a particular basis must equate to one. Secondly, it should be Hermitian and so equal to the complex conjugate, $\rho = \rho^*$. Lastly, any projective measurements should have a non-negative outcome, $\langle\psi|\rho|\psi\rangle \leq 0 \ \forall |\psi\rangle$. In other words, the density matrix should be positive semi-definite which also corresponds to all the eigenvalues of ρ being positive values.

Based on these restrictions, it is also possible to write a more generalised form of the density matrix with entries which satisfies these properties, but is not necessarily pure. In two-dimensions such a matrix takes on the form,

$$\rho = \begin{bmatrix} a & b+ic \\ b-ic & d \end{bmatrix}, \tag{1.6}$$

where $d = 1 - a$ as $Tr(\rho) = 1$ and a, b, c, d are real parameters.

As this form of the quantum state allows one to describe both pure and mixed states, it follows that one can harness the properties of such to extract a measure that allows one to determine the degree of 'pureness' or the purity of the system. This is achieved by taking the trace of ρ^2, or $Tr(\rho^2)$. The outcome of which ranges from 0 indicating maximally mixed to 1 for a completely pure state.

1.1.3 Qudits

Real particles are not only confined to two-dimensional states, however. Considering photons for instance, contrary to spin or polarisation, properties such as the temporal [87], frequency [88] and spatial [89–91] domains all have many modes and thus the photon can exist in a vast array of different states. Atomic levels offer another example with many different possible excited states in which an atom can exist [92]. Here we accommodate this by simply extending the dimension of the state space and

thus the number of possible basis states from $\{|0\rangle, |1\rangle\}$ spanning $\mathcal{H}^2$ in 2-dimensions to $\{|0\rangle, |1\rangle, ..., |d-1\rangle\}$ spanning $\mathcal{H}^d$ in d-dimensions. Here, the higher-dimensional particles are *qudits* and the mathematically, the pure states are described by the vector $|\psi\rangle = \sum_{j=0}^{d-1} c_j |j\rangle$. As before, c_j are complex coefficients giving the probability, $|c_j|^2$, of the particle being measured in the basis state $|j\rangle$ and $\sum_j c_j = 1$. Unpacking this using three dimensions (d=3) as an example, the basis states are now written as

$$|0\rangle = \begin{bmatrix} 1 \\ 0 \\ 0 \end{bmatrix}; \quad |1\rangle = \begin{bmatrix} 0 \\ 1 \\ 0 \end{bmatrix}; \quad |2\rangle = \begin{bmatrix} 0 \\ 0 \\ 1 \end{bmatrix} \tag{1.7}$$

with any pure state described as

$$|\psi\rangle = c_0 |0\rangle + c_1 |1\rangle + c_2 |2\rangle . \tag{1.8}$$

The density matrix describing Eq. 1.8 is then computed as follows:

$$\begin{aligned} \rho &= |\psi\rangle \langle\psi| \qquad (1.9) \\ &= \begin{bmatrix} c_0 \\ c_1 \\ c_2 \end{bmatrix} \begin{bmatrix} c_0^* & c_1^* & c_2^* \end{bmatrix} \\ &= \begin{array}{c} \\ |0\rangle \\ |1\rangle \\ |2\rangle \end{array} \begin{array}{c} \begin{array}{ccc} \langle 0| & \langle 1| & \langle 2| \end{array} \\ \begin{bmatrix} |c_0|^2 & c_0 c_1^* & c_0 c_2^* \\ c_1 c_0^* & |c_1|^2 & c_1 c_2^* \\ c_2 c_0^* & c_2 c_1^* & |c_2|^2 \end{bmatrix} \end{array} . \qquad (1.10) \end{aligned}$$

By expanding on this example, it can thus be seen that the for a qudit (d-dimensional), the denisty matrix can also be expressed as

$$\rho = \sum_{j,k}^{d-1} c_{jk} |j\rangle \langle k| , \tag{1.11}$$

where $\{j, k\} \in \{0, 1, \ ..., \ d-1\}$ are the row and column indices of the matrix and there are d^2 elements. For mixed states, the density matrix can then be described by d x d pure matrices as in Eq. 1.5. Furthermore, the corresponding generalised form of the density matrix in higher dimensions can thus be also be extended as show in the three-dimensional example,

$$\rho = \begin{bmatrix} a_1 & b_1 + ic_1 & b_2 + ic_2 \\ b_1 - ic_1 & a_2 & b_3 + ic_3 \\ b_2 - ic_2 & b_3 - ic_3 & a_3 \end{bmatrix} , \tag{1.12}$$

where $a_1 + a_2 + a_3 = 1$ and $\{a_j, b_j, c_j\}$ are real parameters for $j \in 1, 2, 3$.

1.1.4 Multi-particle states and entanglement

So far, only the states of single particles or one degree of freedom (DoF) have been described. A quantum system may entail more than a single particle, however, or we may way to look at more than one property (DoF). Furthermore, the state of a single particle may depend on that of another, resulting in a particular property known as entanglement, as will be seen further on. In order to incorporate this, we describe

how to write the state of more than one particle in this section and what it means in cases where there is non-separability present.

When considering the state of more than one particle such as two photons or even two DoFs such as the spin and path in a single photon, tensor products of each individual state is used. For instance, for a system comprised two d-dimensional pure particles or pure qudits with the individual states,

$$|\psi_1\rangle = \begin{bmatrix} a_0 \\ a_1 \\ \vdots \\ a_{d-1} \end{bmatrix}; \quad |\psi_2\rangle = \begin{bmatrix} c_0 \\ c_1 \\ \vdots \\ c_{d-1} \end{bmatrix}, \tag{1.13}$$

the quantum state of the system is given as

$$|\psi_1\rangle \otimes |\psi_2\rangle = \begin{bmatrix} a_0 \\ a_1 \\ \vdots \\ a_{d-1} \end{bmatrix} \otimes \begin{bmatrix} c_0 \\ c_1 \\ \vdots \\ c_{d-1} \end{bmatrix} = \begin{bmatrix} a_0 \begin{bmatrix} c_0 \\ c_1 \\ \vdots \\ c_{d-1} \end{bmatrix} \\ a_1 \begin{bmatrix} c_0 \\ c_1 \\ \vdots \\ c_{d-1} \end{bmatrix} \\ \vdots \\ a_{d-1} \begin{bmatrix} c_0 \\ c_1 \\ \vdots \\ c_{d-1} \end{bmatrix} \end{bmatrix} = \begin{bmatrix} a_0c_0 \\ a_0c_1 \\ \vdots \\ a_0c_{d-1} \\ a_1c_0 \\ a_1c_1 \\ \vdots \\ a_1c_{d-1} \\ a_{d-1}c_0 \\ a_{d-1}c_1 \\ \vdots \\ a_{d-1}c_{d-1} \end{bmatrix}. \tag{1.14}$$

Furthermore, the joint state ($|\psi_1\rangle \otimes |\psi_2\rangle$) forms an element in the corresponding Hilbert space that is the tensor product of the individual Hilbert spaces: $\mathcal{H}_{1,2}^{d^2} = \mathcal{H}_1^d \otimes \mathcal{H}_2^d$. The dimensions then scale as product of the two composite Hilbert spaces. In this example, both dimensions were d, making the dimensions of the system then d^2. Following the convention in Eq. 1.2, the basis states of the system then becomes the tensor product of all the individual basis states with each other. This can be seen from Eq. 1.14 where the coefficients for each basis states for particle 1 ($a_0, a_1, \ldots, a_{d-1}$) is multiplied with each of the coefficients of the basis states for particle 2 ($c_0, c_1, \ldots, c_{d-1}$). The new set of basis states then becomes $\{|0\rangle_1 \otimes |0\rangle_2,\ |0\rangle_1 \otimes |1\rangle_2,\ \ldots,\ |0\rangle_1 \otimes |d-1\rangle_2,\ |1\rangle_1 \otimes |0\rangle_2,\ |1\rangle_1 \otimes |1\rangle_2,\ \ldots,\ |1\rangle_1 \otimes |d-1\rangle_2,\ |d-1\rangle_1 \otimes |0\rangle_2,\ |d-1\rangle_1 \otimes |1\rangle_2,\ \ldots,\ |d-1\rangle_1 \otimes |d-1\rangle_2\}$. More generally, the composite basis, $\mathcal{M}_{1,2}$, resulting from the tensor product of two other bases, i.e. $\mathcal{M}_1$ spanning the Hilbert space $\mathcal{H}_1$ of dimension d_1 and $\mathcal{M}_2$ spanning the Hilbert space $\mathcal{H}_2$ of dimension d_2, is given by

$$\begin{aligned} \mathcal{M}_{1,2} &= \mathcal{M}_1 \otimes \mathcal{M}_2 \\ &= \{|j\rangle_1 \otimes |k\rangle_2\}_{j,k}. \end{aligned} \tag{1.15}$$

Here $\{\}_{j,k}$ denotes the set where $j \in \{0, 1, \ldots, d_1 - 1\}$ and $k \in \{0, 1, \ldots, d_2 - 1\}$. The dimension of the new basis is then d_1 x d_2. Accordingly, the arbitrary pure state of two particles can thus be written as

$$|\psi\rangle_{1,2} = \sum_{j=0}^{d_1-1} \sum_{k=0}^{d_2-1} b_{j,k} |j,k\rangle_{1,2} \tag{1.16}$$

with $|j\rangle \otimes |k\rangle$ is rewritten in shorthand notation as $|j,k\rangle_{1,2}$ and the position of the element in the combined ket indicates the composite basis (particle) being described. Following on from Eq. 1.11, the density matrix then takes on the form

$$\rho_{1,2} = \sum_{j,k,l,n=0} b_{j,k,l,n} |j,k\rangle_{1,2} \langle l,n|_{2,1} \tag{1.17}$$

where indices j, n correspond to basis states spanning the basis of particle 1 and k, l refer to those spanning the basis of particle 2. b is then the complex coefficient weighting each of the elements in the matrix.

An important aspect, integral to many quantum protocols being developed today, makes use of a specific type of two-particle state. Here, the two particle state cannot be written as a tensor product of the composing single-particle states, but instead must be described using the basis states in the combined Hilbert space ($\mathcal{H}_{1,2}$). For instance, we can consider a system comprised two qubit particles such as described in Eq. 1.2. The basis in which we can describe the particles is readily formed from the tensor product of the individual bases:

$$\mathcal{M}_{1,2} = \mathcal{M}_1 \otimes \mathcal{M}_2 = \{|00\rangle_{1,2}; |10\rangle_{1,2}; |01\rangle_{1,2}; |11\rangle_{1,2}\}. \tag{1.18}$$

If each individual particle was in a separate arbitrary superposition as given in Eq. 1.2, where the coefficients are non-zero, the state of the composite system is

$$\begin{aligned} |\psi\rangle_{1,2} &= \alpha_1\alpha_2 |00\rangle_{1,2} + \beta_1\alpha_2 |10\rangle_{1,2} + \alpha_1\beta_2 |01\rangle_{1,2} + \beta_1\beta_2 |11\rangle_{1,2} \\ &= (\alpha_1 |0\rangle_1 + \beta_1 |1\rangle_1) \otimes (\alpha_2 |0\rangle_2 + \beta_2 |1\rangle_1) \\ &= |\psi\rangle_1 \otimes |\psi\rangle_2 . \end{aligned} \tag{1.19}$$

As shown in Eq. 1.19, the composite state can be factorised and thus written as a product or tensor state of the individual particles. The state of each particle can thus be produced individually and does not show any specific interaction between them.

Interesting properties arise when this is no longer true. For example, we can consider the state

$$|\psi\rangle_{1,2} = b_0 |00\rangle_{1,2} + b_1 |11\rangle_{1,2} , \tag{1.20}$$

where the coefficients are non-zero. Here, it is clearly not possible to factor the state of either particle and so is said to be *non-separable*.

The implications of this is that one can no longer describe either particle individually (in each basis alone), but rather requires the both at the same time. Such a system holds correlations where the measurement of one particle results in the determination of the state of the other particle. This is due to the act of measurement collapsing the state. Accordingly, a common (Copenhagen) interpretation of this is that, if a $|0\rangle$ was measured on particle 1, particle 2 would then also be in the state $|0\rangle$, even though before measurement it was in a superposition of both. Similarly, a measurement of $|1\rangle$ ensures the other particle will also be in that state, despite any arbitrary distance of separation. This prompted Einstein questioning the reality [93],

calling this "spooky action at a distance" and has since been termed *quantum entanglement* [94]. It follows that this property is a direct consequence of the inability to factorise the state into its subsystems. As such, composite states for which one is not able to write as a product state i.e. $|\psi\rangle_{1,2} \neq |\psi\rangle_1 \otimes |\psi\rangle_2$ can be called entangled.

1.1.5 Schmidt decomposition and dimensionality

It may now be noted that there is a particular type of decomposition on pure state composite systems such as described in Section 1.1.4 which assist in the characterisation thereof. More specifically, it can be shown [4] that there exists a particular decomposition of a pure composite state, such as given in Eq. 1.15, where the sum of the basis state combinations no longer run over all possible indices. Instead, a particular basis can be found, known as the Schmidt basis, such that $b = 0$ for all $i \neq j$ with

$$|\psi\rangle^S_{1,2} = \sum_{j=0}^{d-1} b_j \, |j,j\rangle_{1,2} \, . \tag{1.21}$$

Here b_j now becomes the Schmidt coefficients where $b \geq 0$. They are also the square roots of the eigenvalues for partial traces with respect systems 1 and 2 across the composite density matrix in this basis,

$$\begin{aligned} \rho^S_1 &= \mathrm{Tr}_2 \left(\rho^S_{1,2} \right) = \sum_{j=0}^{d-1} |b|^2_j \, |j\rangle_1 \langle j|_1 \\ \rho^S_2 &= \mathrm{Tr}_1 \left(\rho^S_{1,2} \right) = \sum_{j=0}^{d-1} |b|^2_j \, |j\rangle_2 \langle j|_2 \, . \end{aligned} \tag{1.22}$$

These partial traces are thus diagonal matrices with the entries given by the squared Schmidt coefficients. It follows that several characteristics can be determined from the coefficients. If there is only one non-zero coefficient, the system is separable, if there is more than one, the system is entangled and if all the coefficients are non-zero and equal ($b_j = \frac{1}{\sqrt{d}}$), the system is said to be *maximally entangled*.

Furthermore, the value d in this case is the Schmidt number [95]. This is has a significant implication in high-dimensional entangled systems as this quantified the 'amount' of entanglement in these systems. For example, in a three-dimensional maximally entangled bipartite system, $d = 3$ and so the Schmidt number, K, is three which is indicative of maximal entanglement across thee states. Generalised to systems that are not necessarily maximally entangled, this number can instead be approximated by [96, 97]

$$K = \frac{1}{\sum_j |b_j|^4}, \tag{1.23}$$

where $0 < b_j \leq 1$ so that $K = 1$ dictates a separable system and $K > 1$ an entangled one. K thus provides an effective number of the contributing modes to the entangled state and thus refers to the *dimensionality* of the system.

1.2 Projectors and measurement

The crux of quantum information protocols and technology relies on the ability to perform various operations in order to manipulate quantum states and measure

them. To do so, we may consider the role of operators. More specifically, we consider the role of projector operators which forms a ubiquitous type of measurement in quantum mechanics. Once applied to a system, they project it onto a specific state. As such, these operators are take on the form $\mathcal{P}_n = |n\rangle\langle n|$ which results in the system being projected onto the state $|n\rangle$. Here it can be noted that the density matrix for a pure state is actually a projection operator of the pure state itself, acting on the Hilbert space of the quantum system. Mixed states are then simply formed from the sum of such pure state projectors.

The effect of such a projector on a quantum system, ρ can, thus be seen in the following [4]

$$\begin{aligned}\rho' &= \frac{\mathcal{P}_n \rho \mathcal{P}_n^\dagger}{\mathrm{Tr}(\mathcal{P}_n \rho \mathcal{P}_n^\dagger)} \\ &= \frac{|n\rangle\langle n|\,\rho\,|n\rangle\langle n|}{\mathrm{Tr}(\mathcal{P}_n^\dagger \mathcal{P}_n \rho)} \\ &= \frac{|n\rangle\,\mathrm{Tr}(\mathcal{P}_n\rho)\,\langle n|}{\mathrm{Tr}(\mathcal{P}_n\rho)} \\ &= |n\rangle\langle n| \end{aligned} \tag{1.24}$$

where ρ' is the resulting density matrix after performing the projection operation and is trace-preserved due to division by the trace of the operation. This is as a single operator is not always trace-preserving. It thus follows that the act of measurement on ρ' causes the quantum system to be projected onto the pure state, $|n\rangle$ as dictated by the projection operator. It can then be seen that the probability of obtaining the outcome, n, when doing such a measurement on a system with the state ρ is

$$P_n = \mathrm{Tr}(\mathcal{P}_n\rho) = \langle n|\,\rho\,|n\rangle\,, \tag{1.25}$$

which is known as Born's rule. When the density matrix is for a pure state ψ ($\rho = |\psi\rangle\langle\psi|$), the probability reduces to

$$P_n = \langle n|\psi\rangle\,\langle\psi|n\rangle = |\langle n|\psi\rangle|^2. \tag{1.26}$$

Using a variety of these projections and subsequent measurements, information on the quantum state can be gathered or, in the case of entangled systems, certain states can be heralded.

1.3 Traditional teleportation

Using the concepts covered so far, it is possible to consider how teleportation works following on from the seminal paper by Bennett *et al.* in 1993 where they considered the spin-$\frac{1}{2}$ states of particles [3]. Here, instead of spin states, we use the generic qubits states introduced previously.

In the traditional protocol, Alice wishes to send information in the form of an unknown qubit quantum state $|\Phi\rangle_C = \alpha\,|0\rangle_C + \beta\,|1\rangle_C$ to a second party, Bob, where $|\alpha|^2 + |\beta|^2 = 1$ are complex coefficients. Here $|0\rangle$ and $|1\rangle$ represent specific states such as the horizontal and vertical polarisations of a photon or spin-up and spin-down states of an electron. Figure 1.3 shows the overall protocol with each step broken down. In order to do so, a maximally entangled state between particles A and B such as $|\Psi_{00}\rangle_{AB} = \frac{1}{\sqrt{2}}(|00\rangle_{AB} + |11\rangle_{AB})$ is generated. The particles are then

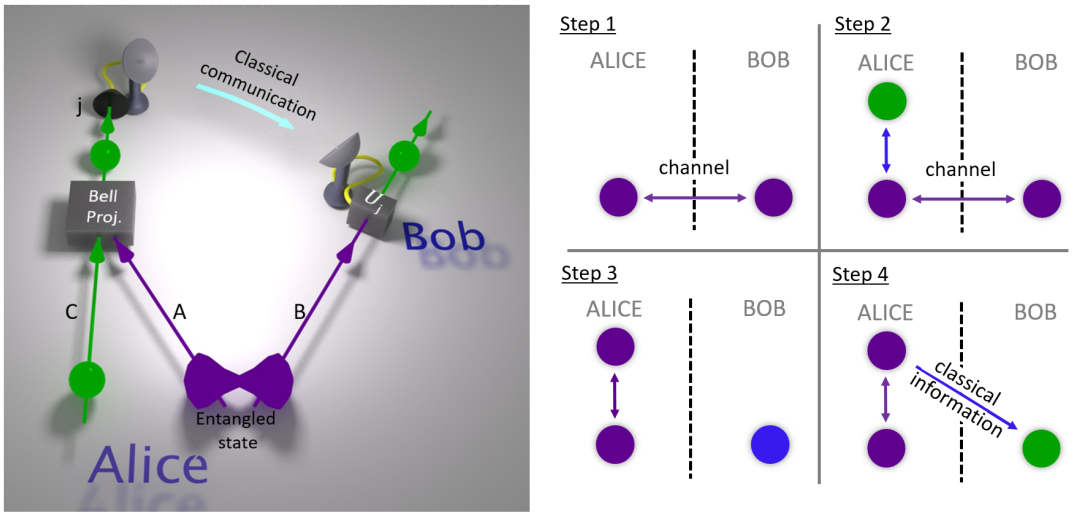


FIGURE 1.3: **Traditional teleportation protocol.** Initially, a pair of entangled photons (purple) is shared between Alice (particle A) and Bob (particle B), establishing an entanglement channel. A third particle C (green) containing an unknown or prepared quantum state to be teleported is then indirectly interacted with Alice's particle. Alice then performs a Bell state measurement on photons A and C. The Bell state projection collapses the entanglement between particles A and B, while simultaneously entangling photons A and C as well as destroying the state of photon C. Alice then transmits classical information to Bob about the Bell measurement projection (j), allowing him to correct for any unitary rotation on the state being teleported (U_j). The state has then been teleported.

shared between Alice and Bob to form a quantum channel such that particle A goes to Alice and particle B goes to Bob (Step 1). When describing this system where a third particle, C, possesses the unknown state Alice wishes to send, the initial total state of the system can be written as

$$|\Phi\rangle_C \otimes |\Psi_{00}\rangle_{AB} = [\alpha\,|0\rangle_C + \beta\,|1\rangle_C] \otimes [\frac{1}{\sqrt{2}}(|00\rangle_{AB} + |11\rangle_{AB})], \tag{1.27}$$

$$= \frac{1}{\sqrt{2}}(\alpha\,|000\rangle_{CAB} + \alpha\,|011\rangle_{CAB} + \beta\,|100\rangle_{CAB} + \beta\,|111\rangle_{CAB})$$

Here the initially shared maximally entangled state forms one of the four variations known as Bell states or EPR pairs [4] which are listed below:

$$|\Psi_{00}\rangle = \frac{1}{\sqrt{2}}(|00\rangle_{AB} + |11\rangle_{AB}), \tag{1.28}$$

$$|\Psi_{01}\rangle = \frac{1}{\sqrt{2}}(|00\rangle_{AB} - |11\rangle_{AB}), \tag{1.29}$$

$$|\Psi_{10}\rangle = \frac{1}{\sqrt{2}}(|01\rangle_{AB} + |10\rangle_{AB}), \tag{1.30}$$

$$|\Psi_{11}\rangle = \frac{1}{\sqrt{2}}(|01\rangle_{AB} - |10\rangle_{AB}). \tag{1.31}$$

It can be noted that choice of the initial maximally entangled state could be any of the Bell states as long as it is known between Alice and Bob. For simplicity the first state was chosen in this example.

In order to transfer the state carried by particle C to Bob, particle C must be indirectly interacted with her channel particle (A), such that the state of either particle is

not directly measured (Step 2). This is due to direct measurement of either particle's state results in collapse to a specific observable and, with this, destruction of the unknown state or loss of the entanglement channel. To see how one may achieve this, the state of the particles we wish to interact can be rewritten in the Bell basis such that their states remain undefined using the following relations:

$$|\Psi_{00}\rangle = \frac{1}{\sqrt{2}}(|00\rangle_{CA} + |11\rangle_{CA}), \tag{1.32}$$

$$|\Psi_{01}\rangle = \frac{1}{\sqrt{2}}(|00\rangle_{CA} - |11\rangle_{CA}), \tag{1.33}$$

$$|\Psi_{10}\rangle = \frac{1}{\sqrt{2}}(|01\rangle_{CA} + |10\rangle_{CA}), \tag{1.34}$$

$$|\Psi_{11}\rangle = \frac{1}{\sqrt{2}}(|01\rangle_{CA} - |10\rangle_{CA}). \tag{1.35}$$

Expanding Equation 1.28 and then substituting in the indirect Bell state relations between particles A and C gives

$$\begin{aligned}|\Phi\rangle_C \otimes |\Psi_{00}\rangle_{AB} = \frac{1}{2}[\,&|\Psi_{00}\rangle_{CA} \otimes (\alpha\,|0\rangle_B + \beta\,|1\rangle_B) + |\Psi_{01}\rangle_{CA} \otimes (\alpha\,|0\rangle_B - \beta\,|1\rangle_B) \\ &+ |\Psi_{10}\rangle_{CA} \otimes (\alpha\,|1\rangle_B + \beta\,|0\rangle_B) + |\Psi_{11}\rangle_{CA} \otimes (\alpha\,|1\rangle_B - \beta\,|0\rangle_B)].\end{aligned} \tag{1.36}$$

The total state here is still the same and thus there is not yet any teleportation as no operations have been done. It can clearly be seen, however, that should particles A and C be projected into one of the Bell states (Step 3), such as $|\Psi_{01}\rangle$, the relation collapses to one of the terms e.g. $|\Psi_{01}\rangle_{CA} \otimes (\alpha\,|0\rangle_B - \beta\,|1\rangle_B)$. Particle B then assumes the state that particle C carried to within some unitary rotation, say U_j, that can be described in terms of the Pauli matrices, σ [4],

$$\sigma_x = \begin{bmatrix}0 & 1\\ 1 & 0\end{bmatrix}; \quad \sigma_y = \begin{bmatrix}0 & -i\\ i & 0\end{bmatrix}; \quad \sigma_z = \begin{bmatrix}1 & 0\\ 0 & -1\end{bmatrix} \tag{1.37}$$

and the identity matrix,

$$\sigma_{\mathbb{I}} = \begin{bmatrix}1 & 0\\ 0 & 1\end{bmatrix}, \tag{1.38}$$

in the trivial case. For instance, Bell projection $|\Psi_{01}\rangle_{CA}$ results in particle B having the unitary rotation $U_j = \sigma_z$. It is upon this projection that a variation of the state transfer has occurred where the projection causes particles C and A to become entangled (the Bell state is a maximally entangled state), while the entanglement between particles A and B is broken such that B assumes a variation of the prepared state.

Here the unitary variation of the prepared state that Bob's particle is in can be determined from the Bell state that Alice projected onto. To complete the teleportation, recovery of the state requires Alice to then classically communicate to Bob which Bell state she projected onto. Bob then applies the corresponding unitary operation that undoes the variation and restores the original prepared state (Step 4). This classical communication limits the speed at which the information is transferred, causing the protocol to remain within the laws of relativity. Additionally, with the Bell state projection, the state of particle C becomes undefined as it is entangled with particle A which implies that the state is not cloned, adhering to the no-cloning theorem [98].

1.4 Transverse spatial modes for high-dimensional encoding

The transverse spatial distribution of photons constitute a high-dimensional state space contained in its internal degrees of freedom (DoF) [91, 99, 100] that spans higher dimensional Hilbert spaces. By structuring this DoF, it is then possible to encode in a qudit space that comprises a theoretically infinite number of orthonormal modes. It follows that a theoretically infinite-dimensional space in which to represent information is available, limited only by the physical constraints of the system being constructed. Here we briefly review the properties and structures of three such bases which can be used for high-dimensional state teleportation.

1.4.1 Laguerre-Gaussian modes

By considering the field functions, $A(r,z,t)$, describing the transverse oscillations of the electric field which satisfies the wave equation [101], a basis set of eigenmodes can be derived. Here r, z and t respectively represent the transverse, longitudinal and temporal coordinates. A paraxial approximation is taken where it is assumed that the transverse spatial components vary slowly with propagation (z) and as such satisfy the inequality [102]

$$|\frac{\partial^2}{\partial^2 z}A(r,z)| << k|\frac{\partial}{\partial z}A(r,z)|. \tag{1.39}$$

A differential equation, known as the paraxial Helmholtz equation, then governs the propagation of these fields and is written as [102]

$$(\nabla_\perp^2 + ik^2\frac{\partial}{\partial z})A(r,z) = 0, \tag{1.40}$$

where $\nabla_\perp^2$ is the transverse component of the Laplacian differential operator and $k = 2\pi/\lambda$ is the wavenumber corresponding to wavelength λ . By considering different coordinate spaces, such as the cylindrical and Cartesian, varying families of solutions can be found that correspond to different orthonormal mode sets or bases. In cylindrical coordinates, solving for the paraxial Helmholtz equation results in the Laguerre-Gaussian (LG) family of modes which has the complex amplitude [102]

$$A(r,\phi,z) = \mathrm{LG}_{\ell,p} = \sqrt{\frac{2p!}{w^2\pi(p+|l|)!}}(\frac{r\sqrt{2}}{w})^{|l|}L_p^{|l|}(\frac{2r^2}{w^2})e^{\frac{-r^2}{w^2}}e^{-il\phi}e^{\frac{-ikr^2}{2R}}e^{-i\vartheta_{p,l}} \tag{1.41}$$

where r retains the previous definition, ϕ is the azimuthal angle and $L_p^{|l|}(x) = (x^{-|l|}\frac{e^x}{p!})(\frac{d}{dx})^p(x^{|l|+p}e^{-x})$ is the generalized Laguerre polynomial of orders $p \geq 0 \in Z, l \in Z$. The parameters z_R, w and R govern how the field changes with propagation. Here $z_R = \pi w_0^2/\lambda$ determines the propagation distance at which the beam width is $\sqrt{2}$ larger than the fundamental, Gaussian beam waist at the $z = 0$ plane, w_0. $w = w_0\sqrt{1+(z/z_R)}$ is the size of the transverse mode as it propagates and radius of curvature, $R = z[1+(z_R/z)^2]$, represents the 'bending' of the wavefront and $\vartheta = (2p+|l|+1)\tan^{-1}(z/z_R)$ is the Gouy phase [102]. Figure 1.4 shows the intensity ($|\mathrm{LG}_{\ell,p}|^2$) and phase ($\mathrm{mod}[\arg(\mathrm{LG}_{\ell,p}), 2\pi]$) spatial distributions for the first few LG modes ($\ell = [-1,2]$ and $p = [0,2]$) at the waist plane (z=0). Here the significance of the ℓ and p indices can be seen. For instance, p dictates the radial profile where the field results in p concentric radial nulls in the intensity as well as a singularity in the phase profile such that a π-phase jump occurs between the ring phase profiles.

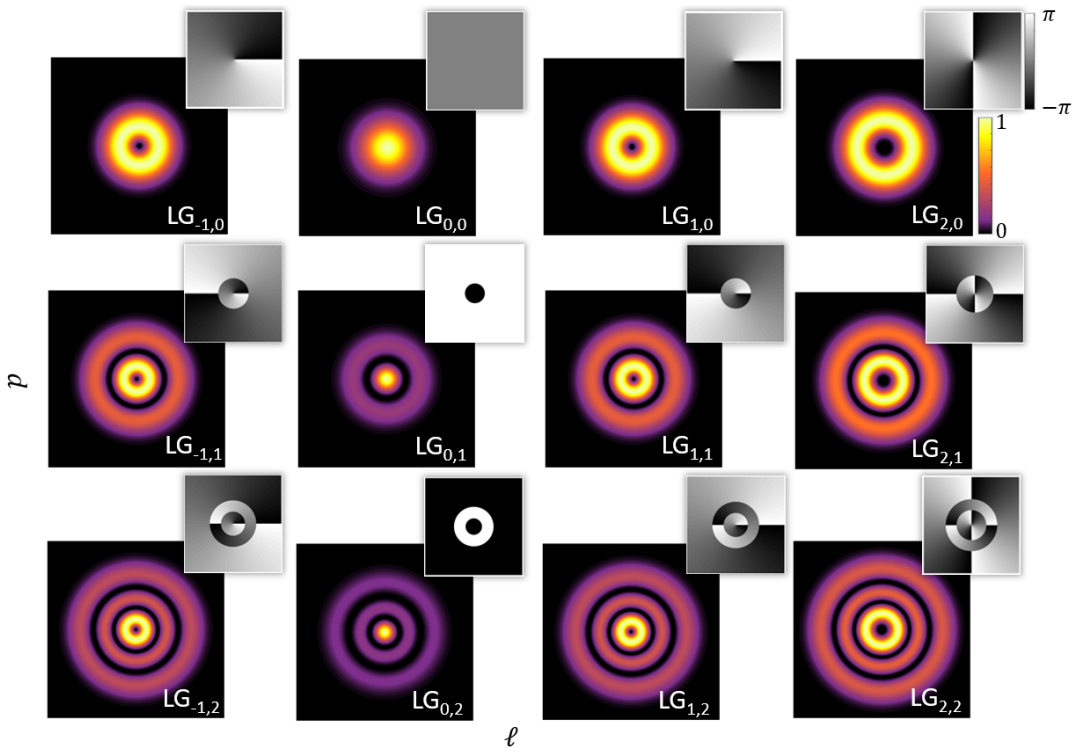


FIGURE 1.4: **Laguerre-Gaussian mode family.** Intensity profiles for the spatial distributions described by LG modes, at the waist plane ($z = 0$), with indices $\ell = [-1, 2]$ and $p = [0, 2]$ with the phase profile given in the top-right inset.

The index ℓ results in an azimuthal phase variation with a phase singularity at the centre of the beam and a central intensity null. This results in the phase-front of the beam 'twisting' about the axis of propagation with the number of intertwined twists per wavelength equal to the value of $|\ell|$. Additionally, the sign of ℓ indicates the handedness of the twist. This rotation of the wavefront corresponds to a significant physical property which can be attributed directly to the $e^{i\ell\phi}$ term. More specifically, light with this term carries orbital angular momentum (OAM) where each photon carries $\ell\hbar$ OAM [102, 103].

It follows that light carrying OAM can be generated with beams carrying the general form $A(r, \phi, z) = a(r, z)e^{i\ell\phi}$ which are known as vortex beams. Here, $a(r, z)$ need not be the remaining terms in Eq. 1.41. In fact, simplistic methods for generation of these OAM or vortex beams often do not involve modulation of the amplitude, but rather only a phase modulation of the fundamental Gaussian mode (LG_{00}). Such methods utilise phase control ranging from dynamic phase with spatial light modulators (SLM) [104] to geometric phase using birefringent liquid crystals [105–107] and metasurfaces [108]. The trade-off of this approach results the radial profile of the beam amplitude changing upon propagation as the distribution is no longer a solution to the paraxial Helmholtz equation. A shift to higher p-indices related to the OAM charge is seen as a result when decomposed into the LG basis [109]. It has been shown that these beams are accurately modelled as Hypergeometric-Gaussian modes [110].

1.4.2 Hermite-Gaussian modes

By considering a solution to Eq. 1.40 in the Cartesian coordinate system, the Hermite-Gaussian (HG) family of basis modes as found with the distribution given by [102]

$$A(x,y,z) = \mathrm{HG}_{n,m} = A_0 \frac{w_0}{w} H_n\left(\frac{\sqrt{2}x}{w}\right) H_m\left(\frac{\sqrt{2}y}{w}\right) e^{-\frac{x^2+y^2}{w^2}} e^{\frac{-ik(x^2+y^2)}{2R}} e^{-i\vartheta_{n,m}}. \tag{1.42}$$

Here w_0, w and R retain their definitions given for the LG modes with $\vartheta_{n,m} = (n + m + 1)\tan^{-1}(z/z_R)$ similarly giving the Gouy phase. A_0 is a normalisation factor and $H_j(x) = (-1)^j e^{x^2} \frac{d^j}{dx^j} e^{-x^2}$ is the Hermite polynomial of order j. It follows that the family of HG modes are characterised by two indices, $n \geq 0$ and $m \geq 0$. Figure 1.5 shows the intensity and phase distributions at the waist plane for the first few modes where $n = [0,2]$ and $m = [0,2]$.

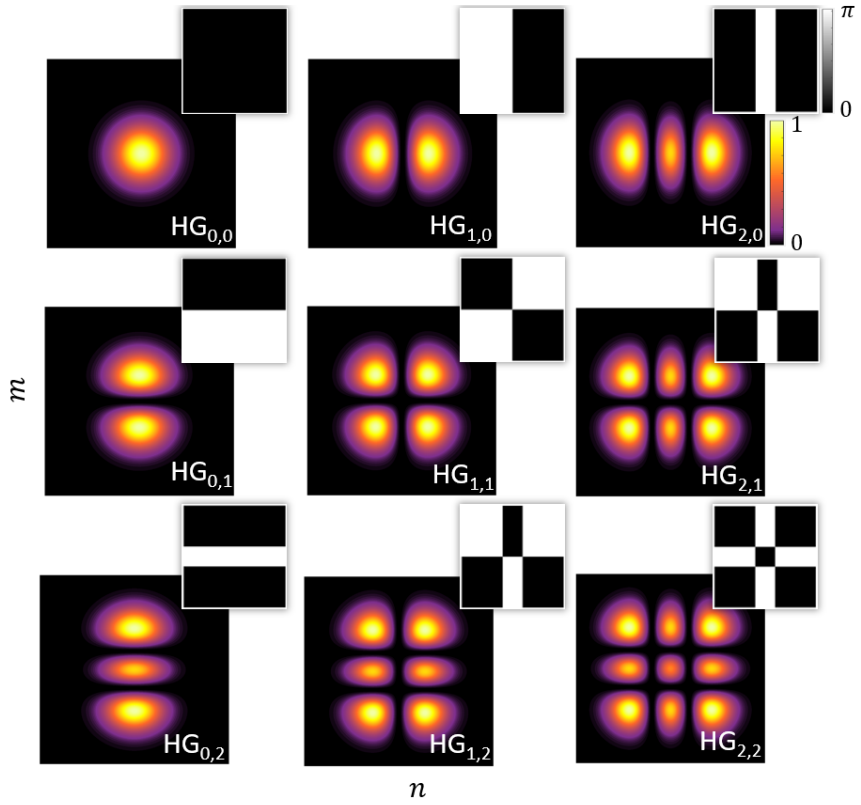


FIGURE 1.5: **Hermite-Gaussian mode family.** Intensity profiles for the spatial distributions described by HG modes, at $z = 0$, with indices $n = [0,2]$ and $m = [0,2]$ with the phase profile given in the top-right inset.

It is straightforward to see that due to the Hermite polynomials, indices n and m reflect a linear intensity null in the x and y coordinates, respectively. This corresponds to a π-phase jump in the phase. Here these modes reflect a rectangular symmetry and is another structurally sound basis which may be used as qudits for teleportation.

1.4.3 Pixel basis

Another mode set that may be exploited for encoding and teleporting information is the pixel basis. Conversely, however, this set of modes does not result from generating a solution to the paraxial Helmholtz wave equation as was the case for the

LG and HG modes. Subsequently, they do not form eigenmodes of free-space and change structure with propagation, akin to the phase-only vortex modes. They do however form orthogonal states that span the spatial distribution that they comprise. These states, arise out of the transverse position-momentum entanglement generated in the spontaneous parametric downconversion (SPDC) process [111]. Here the position plane in divided into a discretised grid of positions, akin to the Cartesian plane. This is illustrated in Fig 1.6(a).

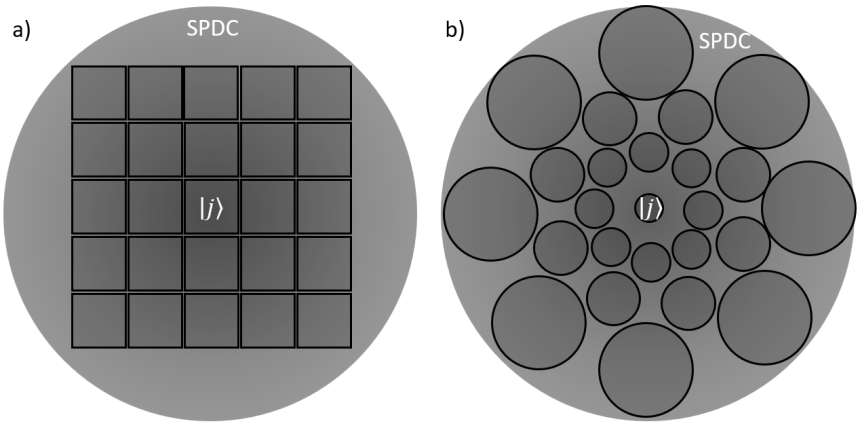


FIGURE 1.6: **Pixel basis states.** An example of the discretised pixel basis states superimposed on an SPDC cone for (a) striaghtforward 1-to-1 images as well as a (b) tailored pixel basis for entanglement concentration.

Here each position state ($|j\rangle$) has an associated phase and amplitude that constitute a complex coefficient, c_j,

$$|\Psi\rangle = N \sum_{j=0}^{d-1} c_j |j\rangle , \tag{1.43}$$

where N is the normalisation term. Similarly to the other basis, a theoretically infinite number of modes are possible. Realistically, however, the pixel size is limited by the resolution of the system in the same way the LG and HG modes are limited by the system apertures and angular resolution. If a 1-to-1 image-to-pixel ratio is used, it follows that complex optical images can be generated and teleported where each pixel holds an tailored amplitude and relative phase. An advantage of using this basis is that the size and shape of each state can be tailored to the system such that they achieve optimal detection [91]. This idea is illustrated in Fig. 1.6(b). Using this method, reports indicate fidelities of over 98% for dimensions exceeding 50 [91].

1.5 Interrogating the state

When using quantum states, it is imperative to be able to both read out the information that has been encoded in the states as well as determine if the system is working correctly. In order to do so, the quantum states must be interrogated. This has been, and remains, a topic of interest for over 80 years with questions on how one can obtain such an estimate tracing at least back to Pauli in 1933 [112]. Studies have become more intense, however, since the 1990s as the applications in quantum information and communications have become clearer due to the inherently quantum nature that is being exploited. One significant challenge is the estimation of systems

with higher dimensions as a result of increasing complexity. As such, there is an expanding toolbox with a growing collection of techniques to date such as [113–130] that can be characterised as quantum tomographic methods and, more recently, a technique which serves to obtain the bounds of a system [131]. In this section, the methods used in this thesis will be highlighted which allows one to determine the quantum state and dimensionality of the system of interest, given judiciously chosen measurements.

1.5.1 Quantum state tomography

The concept of tomography relies on the idea of projecting a quantum state onto observable basis states and measuring the relative probability that the particle is in the state. One then works backwards in order to determine what state would result in the outcomes measured. Tutorial references covering this topic may be found in Refs [132, 133] with a more brief overview tailored to this work detailed here. The concept is illustrated in Fig. 1.7. Here the projective measurements equate to using a light source to project the shadow of the object of interest onto a plane such as the x-, y- and z-axes shown in Fig. 1.7 (a). The shapes and dimensions of the projected profiles then allow one to reconstruct what the object was as indicated in Fig. 1.7 (b). It can be noted that here only three projective measurements were used which assumes a fairly simple and symmetric object. For more complex objects or measurements that introduce uncertainties, a larger number of projections onto different sets of planes can allow for a more accurate reconstruction.

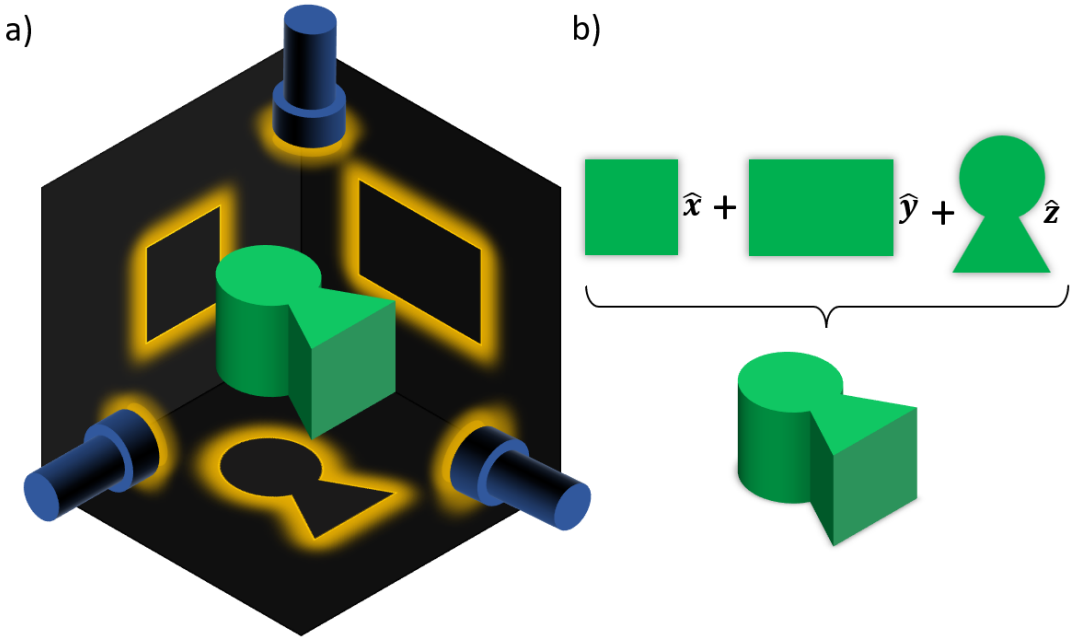


FIGURE 1.7: **Concept of tomography.** Projective measurements (a) are made on an object which are then used to (b) 'work backwards' so that a picture of the object can be rebuilt.

Quantum mechanically, we can carry out this reconstructive concept by performing various operations in order to manipulate the state and thus characterise it. To do so, we apply a variety of projections on many copies of the quantum system and with the subsequent measurements, information on the quantum state being interrogated is built up, analogous to the projections of the object shown in Fig. 1.7 (a).

The question now arises: what are the optimal projections necessary in order to accurately determine the quantum state?

Several types of approaches to such tomographic measurements have been put forward which allows one to extract the information needed to reconstruct the state. Here these range from generalised Bell tests [115–117] to using mutually unbiased bases [119–121] or incorporating self-guided approaches [129, 130], with each approach having certain merits. One may also ask how many measurements are enough to accurately reconstruct the state in methods chosen? The answer to this lies in uncertainties in the measurements being made. Initially one may consider the projections in the concept figure. Here, only three projective measurements are actually necessary in order to find the object. These would then form a tomographically complete set. If there is any uncertainty or 'blurriness' in the projection, the actual size and perhaps the fine structural details of the outlines may be in question. To improve this, one may consider making additional projections on the object where the planes are rotated to some degree. While these projections may not give additional information, they will allow the reconstructed object to be checked against this and adjusted as necessary. This results in the 'blurriness' or uncertainty being reduced. This then forms an overcomplete set of measurements, but allows a greater degree of accuracy in the reconstruction [134, 135].

In this work we made use of mutually unbiased bases (MUBs) and as such will explore it in more detail. Here, MUBs [113, 136] refer to basis states that are characterised by a minimal overlap with all other respective bases in the state space i.e. the overlap of any basis states between different MUBs gives a value of 1/d. That is to say, given two different bases: $\mathcal{M}_1$ with orthonormal bases $\{|j_1\rangle, ..., |j_d\rangle\}$ and $\mathcal{M}_2$ with orthonormal bases $\{|k_1\rangle, ..., |k_d\rangle\}$ in Hilbert space $\mathcal{H}^d$, they are mutually unbiased if

$$|\langle j_l|k_n\rangle|^2 = \frac{1}{d} \tag{1.44}$$

for all $l, n \in \{1, ..., d\}$. This implies that they form an optimal set in which to retrieve information as they are not biased to any one of the bases and so serve to maximise the amount of information that can be extracted for each measurement and minimise redundancy. Despite their usefulness, some uncertainties are associated with the formulation and existence of higher-dimensional MUBs and as such are noted here. Firstly, it is only known that there are exactly d+1 MUBs for dimensions which are prime or powers of prime [113, 137]. For arbitrary d-dimensions, however, such as $d = 6$, it can only be shown that the number of MUBs do not exceed d+1 [113, 138] with the exact number unknown [139–142]. Secondly, construction of these higher-dimensional MUBs is a problem of increasing difficulty as one needs to be able to define them [137]. Methods for constructing the known bases include using Weyl groups or Hadamard matricies [139], with Ref. [143] outlining the Hadamard constructions for $d = 2$ to 5 in detail. Table 1.1 gives such basis states for all the MUBs ($\mathcal{M}$) where $d = 2$ and $d = 3$ as an example.

An initial approach uses the full MUB construction using all d-modes as constituents for interrogating a d-dimensional system [144, 145]. This naturally is limited by the constraints of the construction noted above and thus would only be valid for a certain set of dimensional systems. Furthermore, if the quantum system is multi-particle, the dimensions to be measured over are d^N for an N-particle system which implies an increasingly large-dimensional MUB which needs to be constructed and measured as well as some measurements needed for entangled observables.

A way around this is to instead restrict the measurements to the localised space

MUB		$\mathcal{M}_1$	$\mathcal{M}_2$	$\mathcal{M}_3$	$\mathcal{M}_4$
$d=2$	S_1	$\|0\rangle$	$\frac{1}{\sqrt{2}}(\|0\rangle+\|1\rangle)$	$\frac{1}{\sqrt{2}}(\|0\rangle+i\|1\rangle)$	-
	S_2	$\|1\rangle$	$\frac{1}{\sqrt{2}}(\|0\rangle-\|1\rangle)$	$\frac{1}{\sqrt{2}}(\|0\rangle-i\|1\rangle)$	-
$d=3$	S_1	$\|0\rangle$	$\frac{1}{\sqrt{3}}(\|0\rangle+\|1\rangle+\|2\rangle)$	$\frac{1}{\sqrt{3}}(\omega\|0\rangle+\|1\rangle+\|2\rangle)$	$\frac{1}{\sqrt{3}}(\omega^2\|0\rangle+\|1\rangle+\|2\rangle)$
	S_2	$\|1\rangle$	$\frac{1}{\sqrt{3}}(\|0\rangle+\omega\|1\rangle+\omega^2\|2\rangle)$	$\frac{1}{\sqrt{3}}(\|0\rangle+\omega\|1\rangle+\|2\rangle)$	$\frac{1}{\sqrt{3}}(\|0\rangle+\omega^2\|1\rangle+\|2\rangle)$
	S_3	$\|2\rangle$	$\frac{1}{\sqrt{3}}(\|0\rangle+\omega^2\|1\rangle+\omega\|2\rangle)$	$\frac{1}{\sqrt{3}}(\|0\rangle+\|1\rangle+\omega\|2\rangle)$	$\frac{1}{\sqrt{3}}(\|0\rangle+\|1\rangle+\omega^2\|2\rangle)$

TABLE 1.1: **Mutually unbiased basis states.** Mutually unbiased basis state sets for $d=2$ and $d=3$, calculated using Hadamard constructions. S_j refers to the basis state in each indicated MUB and $\omega = e^{i\frac{2\pi}{3}}$.

of each particle. Despite the restriction, interrogation of this reduced subspace still adheres to the conditions for a complete set of tomographic measurements [120]. In doing this, the measurements are derived from MUBs defined in a Hilbert space of $d^{\frac{1}{N}}$, which reduces to a $(d(d+1)^2)$ number of measurements for a bipartite or two-particle system as not all of the d^N space of the quantum system is probed, but rather each particle's d-subspace. The dimension of the basis states comprising the MUBs then also reduce to d as well. It follows that the scaling of this approach, both with respect to the complexity of MUB construction as well as number and type of measurements required, is more favourable as higher dimensional systems are considered. It can be noted that while the number of measurements are greatly reduced, it is still susceptible to the shortcomings outlined for using MUBs, just at a slower rate and without the possibility of needing to consider entangled observables. As a result, there still exists a restriction on the dimensionality of the quantum system one wants to interrogate.

An alternate method, bypassing this, is to keep the dimensionality of the MUBs projections restricted to two [119] as the construction of such a basis is straightforward and simple to implement. The localised measurements for each particle is then spread across combinations of these two-dimensional subspaces within the d-dimensional system. This naturally results in the many more measurements as each two-dimensional subspace combination in the d-dimensions of each particle needs to be measured along with all the different MUBs therein. As such the number of measurements scale as $(4\mathcal{C}_2^d + d)^2$ with d for a two-particle system where $\mathcal{C}_2^d$ is a binomial coefficient. The trade-off for the lack of complexity here is thus an increase in the number of measurements sufficient for accurate state reconstruction. In this work, we made use of both the multiple qubit projections as well as the localised higher-dimensional MUBs in order to characterise our quantum states when appropriate.

One way to visualise this is to consider the projective states in terms of the LG basis from Section 1.4.1. More specifically, we will consider the OAM-only modes where $p=0$ and a system where $d=3$. By choosing $|0\rangle \rightarrow |\ell=1\rangle$, $|1\rangle \rightarrow |\ell=-1\rangle$ and $|2\rangle \rightarrow |\ell=0\rangle$ from Table 1.1, the MUB basis states and thus the modes projected onto are those shown in Fig. 1.8 (a) for the full MUB projection method. Here ℓ retains its parameter definition and refers to the OAM charge per photon. For the restricted MUB method, all the two dimensional subspaces must be considered and as such $|0\rangle$ and $|1\rangle$ take on the different combinations of the $\ell = \{-1, 0, 1\}$ states. This is shown in Fig. 1.8 (b) where $\ell_{|0\rangle} < \ell_{|1\rangle}$ in each superposition. It can be noted here that the projected states in the $\mathcal{M}_1$ basis have redundancy and thus measurements would be reduced to the three $\ell=-1$, $\ell=0$ and $\ell=1$ states.

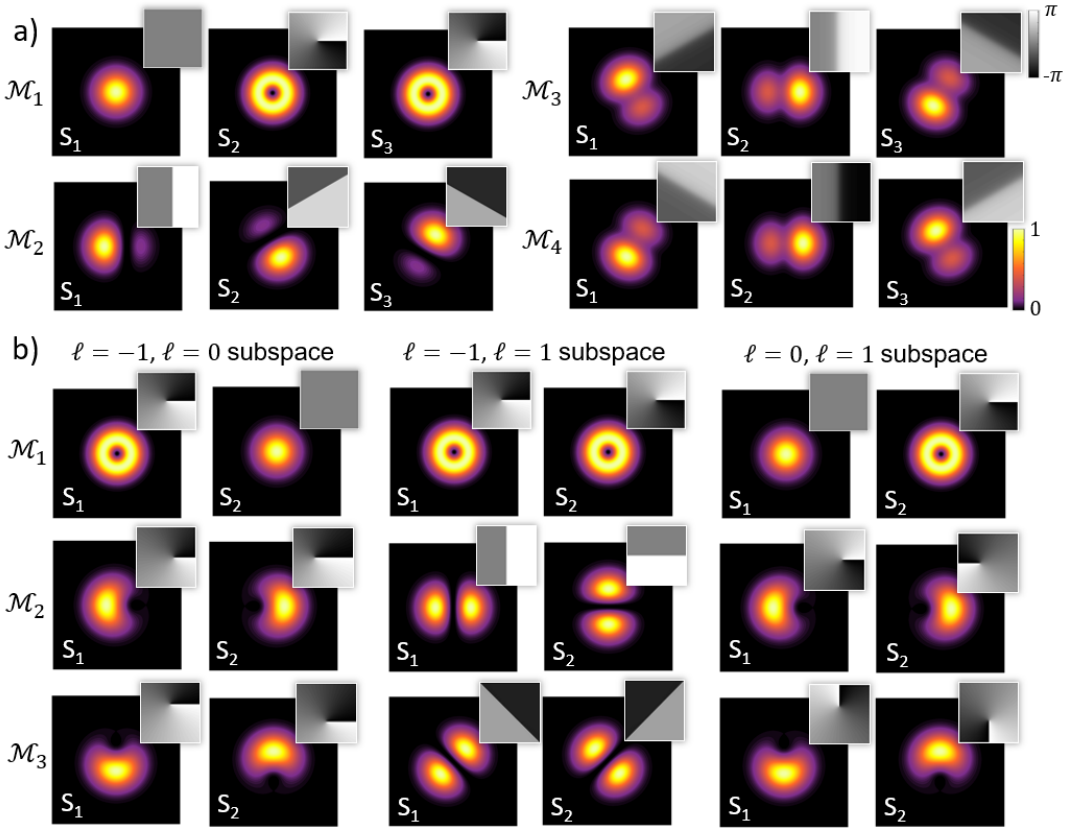


FIGURE 1.8: **Tomographic MUB projection OAM states.** Projective OAM states for exemplary $d = 3$ tomographic measurements for an $\ell = \{-1, 0, 1\}$ quantum system based on the (a) d-dimensional MUB approach and (b) restricted two-dimensional MUB approach. S_j refers to the basis state indicated in Table 1.1

Once such measurements are made, the question of how one may go about reversing the process to reconstruct the density matrix of the quantum state may be asked. The simplest and naive approach involves linear inversion. Here we may consider the generalised form of a density matrix as in Eq. 1.6 which does not assume purity,

$$\rho = \begin{bmatrix} a & b+ic \\ b-ic & 1-a \end{bmatrix}, \tag{1.45}$$

and the elements are as previously defined. By considering the outcome of different basis measurements and applying Eq. 1.25 or Born's rule, the variables may be determined. For example, in this two-dimensional case, a complete set of measurements involve projections onto three different MUB basis states, such as $|0\rangle$, $\frac{1}{\sqrt{2}}(|0\rangle + |1\rangle)$ and $\frac{1}{\sqrt{2}}(|0\rangle + i\,|1\rangle)$ given in Table 1.1, which are also points on the axes of the Bloch sphere in Fig. 1.1. Here, relations to the measurement outcomes, P_n are as follows:

$$P_{|0\rangle} = \begin{bmatrix} 1 & 0 \end{bmatrix} \begin{bmatrix} a & b+ic \\ b-ic & 1-a \end{bmatrix} \begin{bmatrix} 1 \\ 0 \end{bmatrix} = a \tag{1.46}$$

$$P_{\frac{1}{\sqrt{2}}(|0\rangle+|1\rangle)} = \frac{1}{2} \begin{bmatrix} 1 & 1 \end{bmatrix} \begin{bmatrix} a & b+ic \\ b-ic & 1-a \end{bmatrix} \begin{bmatrix} 1 \\ 1 \end{bmatrix} = \frac{1}{2} + b \tag{1.47}$$

$$P_{\frac{1}{\sqrt{2}}(|0\rangle-i|1\rangle)} = \frac{1}{2} \begin{bmatrix} 1 & i \end{bmatrix} \begin{bmatrix} a & b+ic \\ b-ic & 1-a \end{bmatrix} \begin{bmatrix} 1 \\ -i \end{bmatrix} = \frac{1}{2} + c. \tag{1.48}$$

Finding the variables that define the matrix is then the case of inverting the equation such the variables equate to the outcomes of the projective measurements taken (P_n). For the case of a pure quantum system with the wavefunction, $|\psi\rangle = \frac{1}{\sqrt{2}}(|0\rangle + i|1\rangle$, perfect measurements would yield values of $P_{|0\rangle} = 0.5$, $P_{\frac{1}{\sqrt{2}}(|0\rangle+|1\rangle)} = 0.5$ and $P_{\frac{1}{\sqrt{2}}(|0\rangle-i|1\rangle)} = 1$. The density matrix would thus be correctly reconstructed as

$$\rho = \begin{bmatrix} 0.5 & 0.5i \\ -0.5i & 0.5 \end{bmatrix} \tag{1.49}$$

where $a = 0.5$, $b = 0$ and $c = 0.5$ in Eq. 1.6. It can be further noted that the overcomplete set of measurements include projections onto the remaining basis states in each MUB, which leads to the following relations:

$$P_{|1\rangle} = 1 - a = 1 - P_{|0\rangle} \tag{1.50}$$

$$P_{\frac{1}{\sqrt{2}}(|0\rangle-|1\rangle)} = \frac{1}{2} - b = 1 - P_{\frac{1}{\sqrt{2}}(|0\rangle+|1\rangle)} \tag{1.51}$$

$$P_{\frac{1}{\sqrt{2}}(|0\rangle+i|1\rangle)} = \frac{1}{2} - c = 1 - P_{\frac{1}{\sqrt{2}}(|0\rangle-i|1\rangle)}. \tag{1.52}$$

Several problems here can now be noted due to natural variations in the measurement signals from sources such as error, noise and other uncertainties. Realistically, it is not possible to obtain perfect measurements and this can lead to two conflicting outcomes. Firstly, measurements in the complementary basis states might vary and thus violate the relations in Eq. 1.52. This would then lead to the question of which outcome to use. Secondly, variations in the actual measurement values could lead to a density matrix that does not represent a physical state. For instance, realistic measurement outcomes may instead be $P_{|0\rangle} = 0.54$, $P_{\frac{1}{\sqrt{2}}(|0\rangle+|1\rangle)} = 0.48$ and $P_{\frac{1}{\sqrt{2}}(|0\rangle-i|1\rangle)} = 1.02$. This results in a reconstructed density matrix,

$$\rho_R = \begin{bmatrix} 0.54 & 0.02 + 0.52i \\ 0.02 - 0.52i & 0.46 \end{bmatrix}, \tag{1.53}$$

that has eigenvalues of -0.022 and 1.022 and thus cannot represent a physical state due to the negative value. It follows then that the measurements need to be treated with a certain amount of uncertainty that allows a physical density matrix to always be constructed. Additionally, a way to incorporate or resolve variations in overcomplete measurement sets should be considered for a more accurate outcome. The answer to this lies in using minimisation procedures which is covered in the following section.

1.5.2 Maximum likelihood estimation

Two popular methods, maximum likelihood [114, 146, 147] and Bayesian mean [148–150] estimation, have been derived in order to obtain the most realistic density matrix that retains the physical nature and allows uncertainties in complimentary or overlapping projective measurements such as illustrated in Eq. 1.52 to, not only be resolved, but also provide a more accurate estimation. In this work, we employed the maximum likelihood technique and as such will covering it here, while noting the Bayesian method is also a viable alternative.

The premise of this estimation technique lies in guessing a density matrix and iteratively altering the parameters to adjust the matrix, while maintaining the required restraints e.g. non-negative eigenvalues. The projective outcomes of the guessed matrix are then compared to that of the related measurements that have been taken. When the difference between the projective outcomes and actual measured probabilities have been minimised, it can thus be assumed that the related guessed matrix is the most realistic and probable state of the system being measured. This procedure thus allows a range of measurements to be compared and used in order to find the most accurate outcome. As a result, the additional (overcomplete) measurements serve to improve the quality of the guessed matrix.

To do so, the aforementioned guessed density matrix must be of a form that restricts it to the conditions discussed in Section 1.1.2. This is achieved by using [147]

$$\rho_G = \frac{G^\dagger G}{Tr(G^\dagger G)}, \tag{1.54}$$

to construct it. Accordingly, ρ_G is has a unit trace, is Hermitian and positive semi-definite [114]. For convenience, G may be chosen to be a lower triangular matrix [114, 147] and so have the form of

$$G = \begin{bmatrix} a_1 & 0 \\ a_2 + ia_3 & a_4 \end{bmatrix}, \tag{1.55}$$

where $d = 2$ is used as an example and the diagonal entries are real. With this there are a sufficient number of parameters (d^2) to accurately estimate the density matrix of a system. In the case of Eq. 1.55, the set $\{a_1, a_2, a_3, a_4\}$ comprise the parameters that are adjusted iteratively. Equation 1.55 may be extended to accommodate the size of the density matrix one wishes to determine, provided sufficient measurements are made to span the system space.

As the triangular matrix being adjusted is substituted in Eq. 1.54, it follows that the guessed matrix always remains physical and adjusting the parameters then allows one to find the correct values for proper estimation of the system. With iterative adjustment of the parameters, projections ($\{|\psi_j\rangle\}$) are made on the guessed form with outcomes,

$$C_j^P = \mathcal{N} \langle \psi_j | \rho_G | \psi_j \rangle, \tag{1.56}$$

where $\mathcal{N}$ is a constant that converts the probabilities into signal values. It is then compared to the measured signal, C_j^E, for the corresponding experimental projection, $|\psi_j\rangle$, by using a likelihood function such as [119, 151],

$$\mathcal{L} = \sum_j \frac{(C_j^E - C_j^P)^2}{C_j^P}. \tag{1.57}$$

A smaller $\mathcal{L}$ value indicates greater similarity between the guessed and measured projections. When this function then converges to a minimum value, the related guessed matrix is then the density matrix of the system corresponding to the measurements that were taken.

1.5.3 Sampling dimensionality and purity

As explored in the previous sections, the task of determining a quantum system may be done through quantum tomographic methods, but these have various shortcomings with the scaling and complexity increases as higher dimensions are considered. This is more so when the number of particles increase such as in bipartite entangled systems. It follows that this becomes a notable drawback if a teleportation system which uses bipartite entanglement requires characterisation for the teleportation of high-dimensional states like quantum images. Alternatively, one may consider probing and sampling such an entangled system such that the dimensionality and purity characteristics can be determined. A recent method, developed by Nape *et al.* [131], allows one to do such a characterisation for entangled bipartite systems, but with a favourable linear scaling as higher dimensions are interrogated. Here, by probing the quantum system through projections onto superpositions of states with increasing sparsity, one is able to determine the dimensionality and purity at a plausible number of measurements. In the following section, a brief overview is provided with the technique being well described with greater detail in the publication [131].

This is done by considering the bipartite quantum system to be an isotropic state [67],

$$\rho = p\,|\psi\rangle\langle\psi| + \frac{1}{d^2}(1-p)\mathbb{I}, \tag{1.58}$$

where the density matrix is expanded into a pure state, $|\psi\rangle$ and a mixed state as determined by the d^2-dimensional identity operator $\mathbb{I}$. Accordingly, p is indicative of the purity ($\mathrm{Tr}(\rho^2)$) as it weights the pure part of the system and can be approximated as such in high-dimensions. More specifically, $\frac{1}{d+1} < p \leq 1$ instead of $\frac{1}{d} < \mathrm{Tr}(\rho^2) \leq 1$. For high dimensional states, one may approximate $\frac{1}{d+1} \sim \frac{1}{d}$, thus rendering p the purity. Measurement of the dimensionality comes into play as the pure part can be decomposed into a Schmidt basis as described in Section 1.1.5 with $\rho = |\psi\rangle\langle\psi| = \sum_j b_j\,|j\rangle\,|j\rangle$.

It follows that if the number of Schmidt states (K) and p is known, the density matrix can be estimated and constructed by using Eq. 1.58, for a given form of the Schmidt basis. How these values may be obtained is the basis of this method. Here, it involves looking at the visibilities

$$V_n = \frac{|P_n - P_n^{\perp}|}{|P_n + P_n^{\perp}|}, \tag{1.59}$$

for different superposition states of the Schmidt basis, as indexed by $n = 1, 3, ..., 2N-1$ and so forms an analyser with N being the number analysers in the set one wishes to measure. It can be noted that the higher N is, the larger the range of dimensions one is scanning over. The relative phase of each analyser is then changed with respect to the two entangled photons such that the probability signal (P) obtained between them reflects projections that are directly in (P_n) and out ($P_n^{\perp}$) of phase for a particular analyser (n). Consequently, no signal is expected for an out of phase projection and a peak signal expected for an in phase projection if the system is pure and the superpositions being probed are entangled in the system. Both probing outside the dimensions of the system and noise contributing to the second term raises $P_n^{\perp}$ and thus lowers the visibility. Accordingly, such a visibility measurement is not unique to a specific system described by a particular K and p, but rather is a monotonically increasing function with a set range of (K,p) combinations. The set of

visibilities $\{V_n\}$ arising from the increasingly sparse superpositions as n increases, however, does provide a unique solution and as such converges to a specific outcome as long as enough variations of the sparseness is probed.

The question may now be asked: What are the optimal superpositions to form these analysers in order to probe an entangled system? Nape et al. showed that this is given by

$$|M,\alpha\rangle_n = \mathcal{N}\sum_{j=0}^{d-1} c^n_{w_j,M}(\alpha)\,|j\rangle \tag{1.60}$$

where $\mathcal{N}$ is a normalisation factor, $M = \frac{n}{2}$, $|j\rangle$ are the basis states where $j \in \{0,1,...,d-1\}$, $w_j = j - \frac{d-1}{2}$ and

$$c^n_{w_j,M}(\alpha) = \begin{cases} e^{i\pi w_j(n-1)/n}\frac{-ie^{iw_j\alpha}}{\pi(M-w_j)} & \text{if } \mathrm{mod}(w_j,n) = 0 \\ 0 & \text{otherwise,} \end{cases} \tag{1.61}$$

which is the coefficient that tunes the comprising state amplitude and phases within each analyser, with α being a relative phase.

The optimal (K,p) for the system is then obtained in a similar method to maximum likelihood estimation in that the predicted visibilities for each analyser, $V^{\text{Th.}}_{2k-1}(K,p)$, given by the iterated purity and dimensionality parameters are compared to the measured values, $V^{\text{Ex.}}_{2k-1}$ by minimising the difference as given by the function

$$\mathcal{L}(K,p) = \sum \left| V^{\text{Th.}}_{2k-1}(K,p) - V^{\text{Ex.}}_{2k-1} \right|^2 \tag{1.62}$$

over all the N measured visibilities where $n = 2k-1$. The minimised value here results in the most likely dimension in which the system is entangled and the associated purity.

Similar to Section 1.5.1, we can visualise the analysers by considering application to the LG basis. Here, they can be reduced to the form

$$U_n(\phi,\theta) = \mathcal{M}\sum_{k=0}^{n-1} \exp\left(i\Phi_M\left(\phi;\beta_k \oplus \theta\right)\right), \tag{1.63}$$

with normalisation constant, $\mathcal{M}$, which turns out to be superpositions of fractional OAM modes [152, 153],

$$\exp\left(i\Phi_M(\phi;\alpha)\right) = \begin{cases} e^{iM(2\pi+\phi-\alpha)} & 0 \le \phi < \alpha \\ e^{iM(\phi-\alpha)} & \alpha \le \phi < 2\pi \end{cases}, \tag{1.64}$$

having the same charge, $M = n/2$, but rotated by an angle $\beta_k \oplus \alpha = \mathrm{mod}\{\beta_k + \alpha, 2\pi\}$ for $\beta_k = \frac{2\pi}{n}k$.

Chapter 2

Bringing in Non-linear Optics

A large component of being able to extend the dimensionality and versatility of the teleportation protocol lies in the use of a non-linear process in lieu of the linear optical component. Non-linear optics has gained traction since the invention of the laser [154], and is being actively developed to form a toolbox of interest that spans the creation, manipulation and detection of structured light [155, 156]. For instance, the optical building block of many quantum optical experiments relies on such elements in order to readily produce entangled photons [157, 158]. Furthermore, it allows the frequency of structured light to be altered for easier manipulation and detection in both the quantum [159–162] and classical regimes [163–172]. By introducing controlled structuring of light driving such processes, unique manipulations of the outputs are attained, ranging from tailoring the entanglement spectrum [173–175] to imprinting holographic control in another frequency [176–178]. In this chapter, we accordingly explore and test this component with application to implementing teleportation in mind. More specifically, we focus on the structured light phenomena resulting from the use of particular second-order non-linear processes.

After introducing the concepts of second-order non-linear optics, we look at the generation of entanglement in more detail with emphasis on widely-used OAM modes. With this, we experimentally consider the implications of phase-only approaches in the detected and generated modal purities of these modes at both a classical and quantum level. We then introduce mitigating measures to compensate for it and corrective measures are demonstrated which emphasise the effects of including amplitude control to maintain the naturally preserved structures that are eigenmodes of the wave-equation.

Secondly, we focus on sum-frequency generation where this is considered in the context of the manipulation of light for detection. Here we experimentally show, on the classical scale, that by structuring one input, modal detection is possible in another wavelength; this, by tailoring light to work with a nonlinear crystal as a modal projector. We then consider a quantum description of this process in the context of a fixed detection mode and time-reversal symmetries between spontaneous parametric down-conversion and sum-frequency generation; this, with the aim of using it as a projector for quantum teleportation.

2.1 Second-order nonlinear optics

In nonlinear optical processes, light is made to interact with a material which results in phenomena as a direct result of the material's optical properties being altered by the presence of the light [179]. Here the response of the material can be characterised by how the polarisation (dipole per unit volume) of the material, $\mathbf{P}$, responds to the strength of the optical electric field. $\mathbf{E}$, applied to it in time, t. This is shown generally

in Eq. 2.1

$$\mathbf{P}(t) = \epsilon_0[\chi^{(1)}\mathbf{E}(t) + \chi^{(2)}\mathbf{E}^2(t) + \chi^{(3)}\mathbf{E}^3(t) + ...], \tag{2.1}$$

where ϵ_0 is the permittivity of free space and χ is a tensor known as the optical susceptibility of the order expressed in the brackets. Here this response is obtained by expressing the linear material response $\mathbf{P}(t) = \epsilon_0\chi^{(1)}\mathbf{E}(t)$ as a power series of the applied electric field strength. From this, different responses or phenomenon are seen based on the term in the expansion. For instance, the second term ($\epsilon_0\chi^{(2)}\mathbf{E}^2(t)$) refers to a second-order non-linear response which gives rise to phenomena such as second harmonic generation (SHG), sum-frequency generation (SFG) and difference-frequency generation (DFG). The third term ($\epsilon_0\chi^{(3)}\mathbf{E}^3(t)$) is then a third-order non-linear response which gives rise to phenomenon such as third-harmonic generation, self-focusing and four-wave mixing among others. By making the non-linear susceptibility of a material for a specific order high, while diminishing that of the other orders, the specific non-linear process is promoted along with the phenomenon associated with it. Some additional criteria are then also needed in order to promote a specific phenomenon in a particular nonlinear order of a material. This will be covered in more detail later on.

As all the non-linear processes explored in this thesis relies on materials that have a high second-order non-linear response, our interest is restricted to the second term in Eq. 2.1 and the processes associated with it. More details about this and the other non-linear optical phenomenon can be found in Ref. [179], while details related to this work will only be covered here. More specifically, this lowest order nonlinear process requires non-centrosymmetric crystals where inversion symmetry is broken. Examples of such crystals include beta-barium borate (BBO), lithium niobate (LN), potassium dihydrogen phosphate (KDP) and potassium titanyl phosphate (KTP). It should be noted that while these crystals have a high second order nonlinear susceptibility, the processes still have a limited efficiency associated with the conversion of the input light field to the output phenomenon of the desired process. Each type of crystal also has a different efficiency as a result of its intrinsic properties.

When using such non-linear crystals, the inputs dictate the type of second-order process one wishes to excite. For instance, one may illuminate the crystal with light of two different wavelengths or frequencies, resulting a mixing of the frequency components that then forms a third frequency component. This process is known as three-wave mixing. When the two input frequencies cause the polarisation to oscillate at the sum of the two frequencies, SFG occurs and an output of frequency equal to the sum of the inputs are produced. If the frequencies of the two inputs are identical, the process is termed SHG as the frequency generated is the second harmonic of the inputs. Additionally, if instead, the two input frequencies cause the induced polarisation to oscillate at the frequency equal to the difference of the input energies, DFG results where an output of frequency equal to that difference is generated.

Going one step further, such a crystal can also be used to generate spontaneous parametric down conversion (SPDC) which is an intrinsically quantum process. Here the input field is instead a source of one high-energy frequency component which then decays into a pair of lower energy photons that together conserve the energy of the input. A single input thus produces two output fields in reverse of the classical processes mentioned above. Here, an additional feature due to the quantum nature of the process is that the pair of lower energy photons may be produced spontaneously without an input as the process is stimulated by quantum vacuum

fluctuations such that any coupled field may result in radiation [180, 181]. More details on the exact processes of SPDC and SFG as well as the outputs generated are explored in the sections that follow.

2.2 Spontaneous parametric down-conversion

As the photon pairs in SPDC are stimulated by vacuum fluctuations, several properties of this type of light source result. Here the pairs produced are only restricted by the conditions imposed by the nonlinear crystal and pump field used, meaning they can be generated by any energy and momentum combinations falling within the input conditions [182–184]. Each produced pair is thus also time-independent of the next, making it a process governed by Poissonian statistics. From the parametric nature of the process, the quantum state of the crystal remains unchanged in SPDC which allows the rules of conservation to dictate the allowed states of the generated photon pairs. This required conservation holds much significance in the field on quantum optics as it results in the produced pair sharing properties such as time, energy and momentum. Here the discussed ambiguities due to the way they are produced may then result in entanglement of these properties which is a well-used resource in the field.

2.2.1 Phase-matching

Figure 2.1 (a) shows a cartoon description of the SPDC process where a pump beam of angular frequency, ω_p interacting with a $\chi^{(2)}$ non-linear crystal results in the generation of two daughter photons of ω_s and ω_i, respectively. The constituents are commonly denoted *signal* and *idler* in order to distinguish them with historical context behind the specific names.

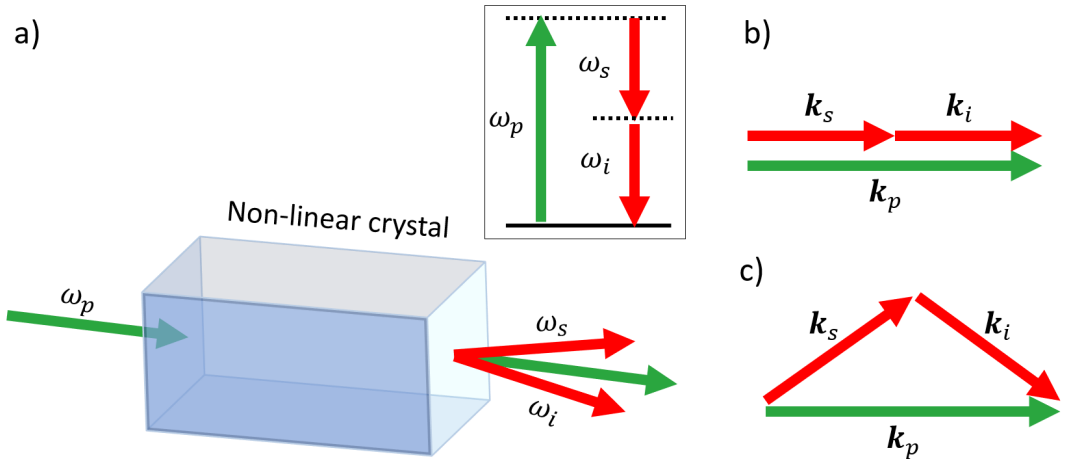


FIGURE 2.1: **Spontaneous parametric downconversion.** Diagrams of (a) the interaction geometry for spontaneous parametric downconversion with a $\chi^{(2)}$ non-linear crystal and interaction geometries for (b) collinear as well as (c) non-collinear phase matching scenarios. Inset shows the energy level diagram for such a process.

Due to the aforementioned conservation of energy, the angular frequencies of said signal and idler are governed by the relation that they should add to that of the

pump producing them, namely

$$\omega_p = \omega_s + \omega_i. \tag{2.2}$$

This relation is shown in the energy level diagram at the top right inset of Fig. 2.1 (a). Furthermore, the linear momentum of the produced photons should add to that of the pump, resulting in

$$\mathbf{k}_p = \mathbf{k}_s + \mathbf{k}_i, \tag{2.3}$$

which is expressed using the wavevectors, $\mathbf{k}$, of the respective pump, signal and idler photons. Here the efficiency of emission for the photons is greatest when these two relations (Eq. 2.2 and Eq. 2.3) are obeyed and the properties are conserved. This is known as the *phase matching condition* and the limitations imposed by meeting this holds for the entire length of the crystal. More specifically, it is only the fields that are in phase with the pump for the length of the crystal that will be built up and thus produce a reasonably observable output field. As different frequencies propagate at different velocities in a medium (chromatic dispersion), a phase mismatch results as the length of the crystal is traversed. Alternatively, the dispersion can be mitigated or rectified through use of the crystal's birefringence. This then causes the process to be sensitive to both polarisation and crystal geometry. With this, there are two types of phase-matching geometry that can be identified based on the matching of linear momentum. This is illustrated in Fig. 2.1 (b) and (c). In Fig. 2.1 (b) the output field wavevectors both propagate in the same direction as the pump field which is known as collinear SPDC. Conversely, in Fig. 2.1 (c) the output field propagates off-axis with respect to the pump, but with equal and opposite trajectories on either side. The second geometry is what is shown for the diagram in Fig. 2.1 (a) and is known as non-collinear SPDC.

Due to the polarisation sensitivity and phase-matching conditions, there are different phase-matching regimes which may be engineered. This results in different polarisation pairings which are detailed in Table 2.1. Here the distinction between

Regime	Pump polarisation	Signal polarisation	Idler polarisation
Type 0	o	o	o
Type I	e	o	o
Type II	e	o	e

TABLE 2.1: **Phase matching types.** Summary of various phase-matching regimes for second order non-liner interactions which differ for input and output field polarisation with respect to parallel orientation to the crystal ordinary (o) or extraordinary (e) axes.

the types are the relative polarisations with respect to the crystal ordinary and extraordinary axes. For instance, in Type-0 phase-matching, the input field should be parallel to the ordinary axis which then results in the generated fields also having polarisations only parallel to that axis. In Type-I, the opposite is true with the pump field polarisation needing to be parallel to the extraordinary axis which generates output fields parallel to the ordinary axis. For all the experiments in this thesis, the crystal types used are restricted to these first two described here.

Additionally, we make use of periodically poled KTP (PPKTP) crystals which employ an additional method to mitigate a mismatch in the wavevectors which is illustrated in Fig 2.2. Here, a wavevector mismatch, Δk, as shown in (b) is corrected by alternating the poling within each domain (Λ) such that the mismatch in the adjoining domain has the opposite sign, $-\Delta k$. Here the poling orientation in the crystal is indicated by the arrows in (a). In using this approach, the alternation allows the

mismatch to roughly cancel across each domain and, having done so, achieve quasi-phase matching (QPM). This effect is described by a phase-matching function [185]. For example, a collinear, non-degenerate configuration is approximated by a sinc function, [186–188]

$$\Phi(\mathbf{q}_s, \mathbf{q}_i) \propto \mathrm{sinc}(\tfrac{L\Delta k_z}{2}), \tag{2.4}$$

with the mismatch in the z-components of the wave vectors is

$$\Delta k_z = -\frac{\lambda_p}{4\pi n_p}|\mathbf{q}_s + \mathbf{q}_i|^2 + \frac{\lambda_s}{4\pi n_s}|\mathbf{q}_s|^2 + \frac{\lambda_i}{4\pi n_i}|\mathbf{q}_i|^2. \tag{2.5}$$

Here $\mathbf{q}_s$ ($\mathbf{q}_i$) is the two-dimensional transverse wave vector (i.e. the transverse momentum) of the signal (idler) photons of the downconverted wavelength, $\lambda_{s,i}$ from that of the pump of wavelength, λ_p. Here, perfect phase matching is seen when the parameters result in the sinc function equating to 1.

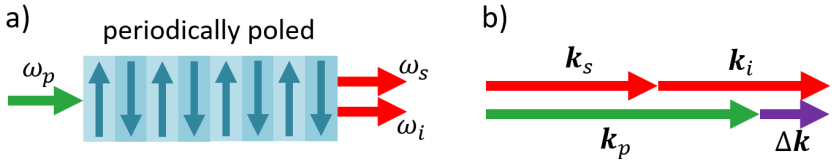


FIGURE 2.2: **Quasi-phase matching with periodic poling.** Example of (a) periodic poling in a non-linear crystal comprising alternating domains to compensate for the (b) wavevector mismatch.

2.2.2 Wavefunction and efficiencies

It is useful to derive the general expression of the SPDC state in terms of wavefunctions for the generated photons in the linear momentum basis. One such method evolves the quantum state using the non-linear phenomenological Hamiltonian [73, 189–191]. The complete state produced by SPDC can then be represented by

$$|\psi_{\mathrm{SPDC}}\rangle \approx |\mathrm{vac}\rangle + |\psi_{s,i}\rangle\, L\sigma + O\{\sigma^2\}, \tag{2.6}$$

where $|vac\rangle$ is the vacuum state, O refers to higher-order terms, L is the propagation length of the crystal and $\sigma \ll 1$ is the nonlinear coefficient. Here, $|\psi_{s,i}\rangle$ forms the generated two-photon contribution and when the frequencies ω_s and ω_i are assumed to be fixed, it is given by

$$|\psi_{s,i}\rangle = \int f(\mathbf{q}_s, \mathbf{q}_i)\hat{a}_s^\dagger(\mathbf{q}_s)\hat{a}_i^\dagger(\mathbf{q}_i)\,|\mathrm{vac}\rangle\; d^2q_s\, d^2q_i, \tag{2.7}$$

under the assumptions of sufficient interaction time, negligible frequency spread, constant terms with respect to wavevectors and that the transverse crystal dimensions are larger than the pump beam. Here $\hat{a}_s^\dagger(\mathbf{q}_s)$ ($\hat{a}_i^\dagger(\mathbf{q}_i)$) is the creation operator of photons with two-dimensional transverse wave vector $\mathbf{q}_s$ ($\mathbf{q}_i$) and $f(\mathbf{q}_s, \mathbf{q}_i)$ is the two-photon wave function of the pair of photons, s and i. This wavefunction is determined by the angular spectrum of the pump beam ($U(\mathbf{q}_p)$) and quasi phase-matching condition of the crystal (Eq. 2.4) [188, 192],

$$f(\mathbf{q}_s, \mathbf{q}_i) = \mathcal{N}U(\mathbf{q}_p)\mathrm{sinc}(\tfrac{L\Delta k_z}{2}). \tag{2.8}$$

As the quasi-phase matching condition is implemented by periodic poling of the nonlinear medium, a slight reduction in efficiency by a factor $2/\pi$ occurs, which is absorbed into the normalisation constant, $\mathcal{N}$. If pumping the crystal with a Gaussian mode, which is the generic case [193],

$$U(\mathbf{q}_p) = w_p\sqrt{2\pi}e^{-(\pi w_p|\mathbf{q}_p|)^2}. \tag{2.9}$$

It should now be noted that SPDC yields the two-photon entangled state when one neglects the higher-order terms (O) as well as the initial vacuum state in Eq. 2.6. A first-order approximation, resulting in the SPDC state being given by Eq. 2.7 is justified through an assumption that the majority pump photons do not produce the emission of photon pairs and thus the interaction is sufficiently weak. This is seen by the low values found for the non-linear coefficient, σ, which refers to the efficiency of this spontaneous process and is determined by

$$\sigma = \chi^{(2)}\sqrt{\frac{\hbar\omega_p\omega_s\omega_i}{8\epsilon_0 c^3 n_p n_s n_i}\frac{F_0}{A_p}}. \tag{2.10}$$

Here, F_0/A_p is the number of pump photons per second per area (photons/s/m^2), n refers to the respective refractive indices, c is the speed of light and the remaining terms retain their definitions.

2.2.3 Spatial entanglement in SPDC

When generating SPDC, the allowed properties of the generated photons must abide by the conservation of energy and momentum dictated by the crystal properties paired with the input field. With this, there are definite correlations between the output fields that must hold. Additionally, however, each individual photon may have some ambiguity across several degrees of freedom from the very nature of the generation which results in them being entangled [182–184]. As a result, SPDC is one of the most widely used resources in quantum optics for generating entangled pairs of photons with a variety of such degrees of freedom with which to choose such as energy-time [194, 195], path [196] and spatial modes [91, 111, 197–200]. A good review covering this is in Ref. [158].

For the purposes of this work we are interested in *discrete* spatial modes as an encoding basis and thus the entanglement generated therein. Here, this is well documented in SPDC and shown across several bases including the OAM [201, 202], HG [203–206] and pixels [91, 111] which was introduced in Section 1.4. The first task in order to teleport such images is to be able to implement high-dimensional teleportation with any of these spatial bases. In this sense and for convenience, we look at the OAM degree of freedom in more detail. Here, entanglement in the OAM spatial degree of freedom takes on the form

$$|\psi\rangle = \sum_{\ell} C_\ell\,|\ell\rangle_s\,|-\ell\rangle_i\,, \tag{2.11}$$

where $|C_\ell|^2$ gives the probability of finding the signal (idler) photon with $\ell\hbar$ ($-\ell\hbar$) OAM. Intuitively, one may see the conservation of orbital angular momentum as the principle governing these entanglement correlations [201, 202]. For instance, the pump beam is commonly a Gaussian state, implying the pump photon has an OAM of $\ell = 0$. The states of the entangled photons must then add to that of the pump, making them equal in magnitude, but opposite in sign.

2.2.4 Dimensional extent of OAM in SPDC

It is theoretically possible to have entanglement across infinitely many such OAM modes in line with the span of the actual basis, however, in practice there are parameters and efficiencies that confine this to a smaller number of modes. Despite such practical restrictions, entanglement with OAM has been shown up to very high dimensions [207–209] and extension to over $\ell = 10,000$ possible [210], making it a good basis in which to explore high-dimensional teleportation.

The limiting parameters affecting the extent of our spatial entanglement here may be reduced to two factors on the generation side: the pump size and crystal length. This may be seen by decomposing the SPDC wavefunction (Eq. 2.7) into the LG basis where

$$\psi_{0,\ell}(r,\phi;w_p) \propto (\beta r)^{|\ell|} e^{\left(-\frac{\beta^2 r^2}{2}\right)} e^{(-i\ell\phi)}, \tag{2.12}$$

is the basis mode function for $p = 0$ and the waist size is scaled with respect to that of the crystal and pump, $\beta = w_p \sqrt[4]{\frac{L}{2z_R}}$ in order to determine the coefficients, C_ℓ in Eq. 2.11. It may be noted that further decomposition into the radial terms, p, of the LG modes are possible [206, 211], but this is not covered here. Subsequent decomposition, yields the analytical expression [206],

$$C_\ell = \frac{4\alpha}{(1+\alpha)^2}\left|\frac{\alpha-1}{\alpha+1}\right|^{|\ell|}, \tag{2.13}$$

with $\alpha = w_p\sqrt{\frac{L}{k_p}}$ for pump wavenumber, k_p. The probability ($|C_\ell|^2$) of having the SPDC biphotons in the state $|\ell\rangle_s |-\ell\rangle_i$ can then be calculated for the pump size and crystal length to give a generational bandwidth. An example of this is shown in Fig. 2.3 (a) for $L = 5$ mm, $\lambda = 532$ nm and $w_p = 280\mu$m . Using the Schmidt number [193, 212], $K = \frac{[\sum_\ell C_\ell]^2}{\sum_\ell C_\ell^2}$, the number of modes present and thus the dimensionality can be indicated. It is worth noting that the Schmidt number yields the effective dimension of the state and does not necessarily corresponds to the dimensionality of the entanglement, for which the Schmidt rank can be used [95]. Here, this value is marked on the bandwidth plot where $K = 13$. Assuming a symmetric spectrum about $\ell = 0$, one may thus convert K to the range of OAM available (-$\ell_{\max}$ to $\ell_{\max}$) by $|\ell|_{\max} = \frac{K-1}{2}$. It follows that the effect of the pump size and crystal length on the generated dimensions (dictated by K) in the biphotons can be seen. Figure 2.3 (b) shows how this varies for the ranges $L = [0.5 : 10]$ mm and $w_p = [50 : 1000]\mu$m. It follows here that a shorter crystal length and larger pump beam size generates a larger number of modes in the SPDC being produced.

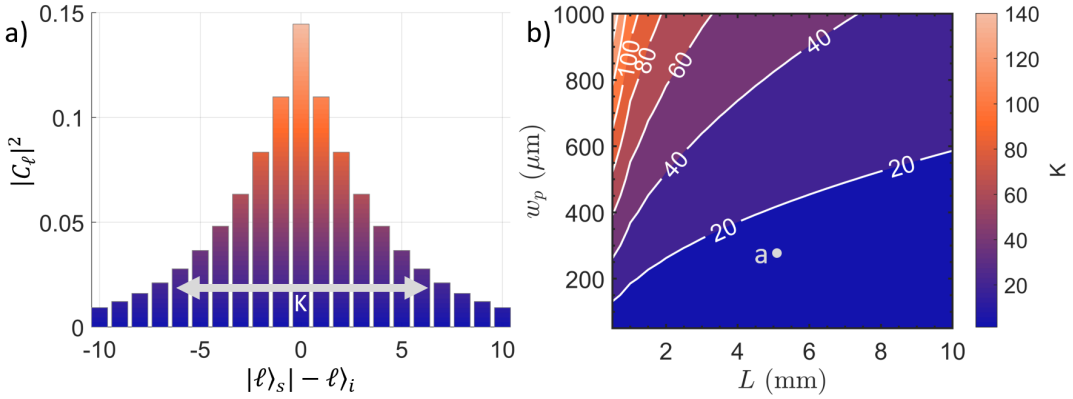


FIGURE 2.3: **SPDC generational OAM bandwidth.** Example of an (a) SPDC OAM bandwidth marked in the (b) pump beam waist size w_p and the non-linear crystal length L parameter space determining the OAM Schmidt number.

How these modes are distinguished, however, also affects what modes are seen and thus plays an inexorable role that must additionally be accounted for. Although OAM modes can be quantitatively detected by conformal mapping in mode sorters [213], a more standard approach exploits the reciprocity of light with phase flattening [214, 215] in order to distinguish the different spatial states by transforming them into a Gaussian-like state. This works on the principle of applying the reverse 'twist' on the mode of interest which results in the generation of a flat phase, akin to that of a Gaussian state. Common approaches to achieving this extend both to creation and detection and use azimuthal phase elements that harness either dynamic phase on spatial light modulators [216, 217], geometric phase with liquid crystals [105–107] or with metasurfaces [218] and have been pioneered to harness the radial degree of freedom by merging these approaches in a single element [219, 220]. Detection of the modal content then resorts to distinguishing the phase-flattened Gaussian state. For quantum mechanical experiments, this is usually achieved by coupling the light into a single mode fibre (SMF) which only propagates the Gaussian state and is then detected by instruments such as avalanche photodiodes (APDs) or single photon counting modules (SPCMs). More explicit experimental details are demonstrated in the next section. While this works as a highly sensitive single photon detection system, the nature of the SMF results an additional modal modulation with the Gaussian distribution describing the coupling of the flattened light into the fiber [221, 222]. As a result the measured bandwidth needs to account for the SPDC state and the overlap thereof with both of the chosen detection modes for either photon.

One may understand the interplay between the generation and detection parameters by considering the geometric picture as outlined in Ref. [222] where the overlaps in the near and far-field regimes are accounted for. From this, an upper bound on the generated bandwidth is derived,

$$K = 1 + 2\sqrt{\frac{\pi^2 w_p^2}{L\lambda}}, \tag{2.14}$$

given the pump waist, wavelength and crystal length. To incorporate the detection

beam waists, further derivation results in a convolution of near and far-field bandwidths where

$$K = \left(\sqrt{\left(1+4\gamma^2\right)^{-2} + \left(1+\frac{\pi^2 w_p^2}{\gamma^2 L\lambda}\right)^{-2}} \right)^{-1}, \tag{2.15}$$

which allows one to predict the dimensionality of the modes that one may detect, given a choice of the detection waist size $w_{s,i}$ backprojected to the crystal plane in the ratio $\gamma_{s,i} = \frac{w_p}{w_{s,i}}$.

In Fig 2.4 (a) we illustrate the effect on chosen detection size by showing the variation of K with $w_{s,i}$ and w_p as shown for the example used in Fig 2.3 (a).

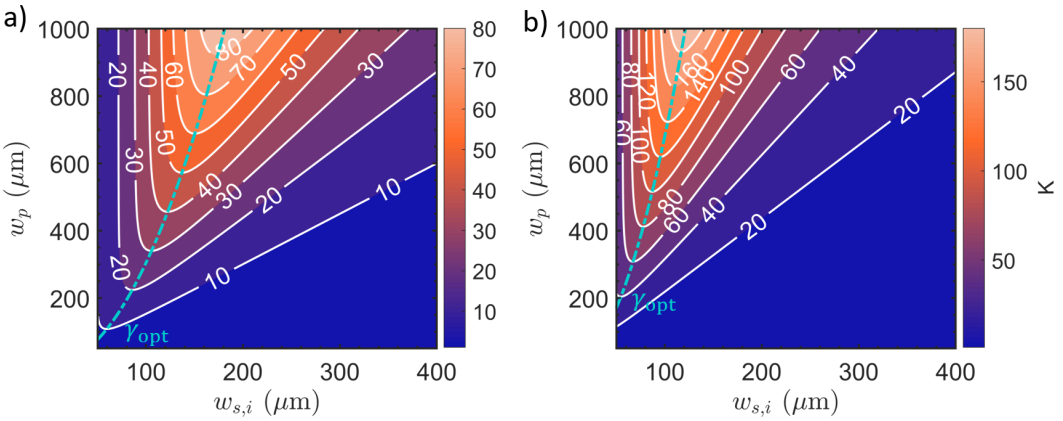


FIGURE 2.4: **SPDC measurable OAM bandwidth.** Example of measurable bandwidth as a function of the pump and detection beamsizes for a (a) $L = 5$ mm crystal and (b) $L = 1$ mm crystal. Dotted line indicates the optimal ratio for maximum bandwidth between detection and signal beam waists.

It follows that an optimal ratio exists as highlighted by a dotted line in the contour map. Furthermore, such an optimal value changes with the crystal length as shown by the shift of the maximal positions of K in Fig 2.4 (b) where $L = 1$ mm instead. The ratio thus depends on L as well as the pump waist. Here this can be seen in [222]

$$\gamma_{opt} \approx \sqrt[4]{\frac{\pi^2 w_p^2}{\lambda L}}, \tag{2.16}$$

which yields the optimal ratio for detection given the pump waist and crystal length.

2.3 Taking care: the modal purity of orbital angular momentum photons

This section is based on the paper:
Isaac Nape, Bereneice Sephton, Yao-Wei Huang, Adam Vallés, Cheng-Wei Qiu, Antonio Ambrosio, Federico Capasso, and Andrew Forbes , "Enhancing the modal purity of orbital angular momentum photons", APL Photonics 5, 070802 (2020)
B. Sephton contributed equally with I. Nape to experiments performed, data analysis and participated in the manuscript writing.

A factor bearing consideration, in many structured light photonic experiments, regards the actual transverse spatial distribution for the SPDC generated photons that carry the OAM and how this may affect the way we generate and detect this. In the previous section, we considered the SPDC distribution in terms of LG modes where two indices are required to describe the function, ℓ and p, respectively referring to the OAM and radial modes as highlighted in Section 1.4. It follows that both of these parameters in actuality require control, whether creating or detecting such modes. We are still only interested in the OAM distribution, but now look into how the radial degree of freedom is impacting the "purity" of these modes: this is to say where maximal signal is retained in the $p = 0$ order.

Many of the physical modulation methods noted in Section 2.2.4, do not consider modification of the amplitude and as such change the azimuthal phase alone. A consequence of ignoring the radial mode content results in hypergeometric modes [110] with the desired $p = 0$ OAM mode having its power distributed across many radial states [109]. This causes deleterious effects for the radial mode purity which negatively extends to the efficiency for subsequent creation and detection. While creation using such phase-only methods can be resolved by intra-cavity use, yielding pure modes [223, 224], such an approach is not possible for detection nor application to quantum states. Here we stress that reference to purity throughout this section refers to the radial mode purity, i.e., how much power is in, or detected in, the $p = 0$ OAM mode.

While such deleterious effects are minimal for low OAM charges, it becomes increasingly prominent as higher values, such as the highlighted high-dimensional SPDC from Section 2.2.4, are reached. Furthermore, large values of $\ell = 100$ and beyond are readily achieved using devices such as liquid crystal q-plates [225], spiral phase plate mirrors [210] and anisotropic diffractive waveplates [226] in the phase-only regime. Here applications such as working towards testing quantum foundations [209, 210] and creating sensitive photonic polarisation gears [225] require higher OAM modes. This results in the consequential radial purity no longer being negligible.

As a result, we consider the impact of phase-only modulation on the radial purity and experimentally show its relevance in both the classical and quantum case as well as its appearance in generation and detection schemes alike. Here, we pay attention to complex amplitude detection of these modes where measurements are considered for both the amplitude and phase distributions. With this we show that by adjusting the scale in the detection step can be used for enhanced detection efficiencies. Advantages are shown both classically and quantum mechanically. Reciprocally, we also demonstrate the creation of high purity OAM modes with complete azimuthal phase and radial mode control, thus creating a comprehensive approach to working with phase-only generation devices.

Furthermore, to make clear that the solution is not device specific, we employ two fundamentally different phase-only devices. More specifically, we used a metasurface enhanced with holographically programmed dynamic (or propagation) phase to produce ultra-high purity classical OAM modes and an SLM-only solution in the quantum realm. The metasurface comprises nano-structured rods patterned for complete control of the OAM state of light, vector and scalar, while the hologram written to a spatial light modulator uses dynamic phase to introduce complex amplitude modulation, thus engineering all degrees of freedom of the field. Moreover, the scheme is extendable to any OAM encoding device, not limited to SLMs or metasurfaces. Our results will be of particular benefit to both classical and quantum communication where a large alphabet with good signal-to-noise ratio is essential.

2.3.1 Concept

Here we first illustrate the concept by enhancing the creation and detection of high purity OAM modes. The objective is to reduce the contribution of unwanted radial modes and to concentrate all the energy into the zero order radial mode, both at the creation and detection steps. One may now ask, how can this be achieved in a generic manner?

To demonstrate this, we consider the creation of high purity OAM modes in the Laguerre-Gaussian basis (natural OAM basis) as given in Eq. 1.41. A pure OAM mode (the mode we desire) in this basis would have no radial modes ($p = 0$) and is described by Eq. 2.12 where $\beta r \to r$ as there is no pump scaling i.e.

$$\psi_{0,\ell}(r,\phi;w_0) \propto \left(\frac{r\sqrt{2}}{w_0}\right)^{|\ell|} \exp\left(-\frac{r^2}{w_0^2}\right) \exp(-i\ell\phi). \tag{2.17}$$

As ℓ appears in both the amplitude and phase terms, both amplitude and phase modulation are required to produce the genuine mode. It is the amplitude term, $(...)^{|\ell|}$, that actually results in the intensity null often associated with these modes. As mentioned before, however, a common approach to producing them is to approximate this by phase-only azimuthal modulation of a Gaussian beam. This is shown in Fig. 2.5 (a), and results in

$$\tilde{\psi}_\ell(r,\phi;w_0) \approx \exp\left(-\frac{r^2}{w_0^2}\right) \exp(-i\ell\phi). \tag{2.18}$$

This vortex beam results in the generation of many radial modes, shown in Fig. 2.5 (b), with low power content in the desired $p = 0$ mode. In fact, the modal powers for all p and a given ℓ can be expressed as

$$|c_{p\ell}|^2 = \frac{(p+|\ell|)!}{p!} \left| \frac{\Gamma(p+\frac{|\ell|}{2})\Gamma(\frac{|\ell|}{2}+1)}{\Gamma(\frac{|\ell|}{2})\Gamma(p+|\ell|+1)} \right|^2, \tag{2.19}$$

where $\Gamma(\cdot)$ is the gamma function. Here we propose how to overcome this in two approaches, one for creation and the other for detection.

For detection, we observe that the OAM mode scales with the embedded Gaussian beam size (w_0). It has been traditional to use this scale in the detection since, by reciprocity, this is the scale at which the vortex beam was initially created. However, ideal ($p = 0$) OAM modes would have a second moment radius of $w_\ell = w_0\sqrt{|\ell|+1}$ that corresponds to an intensity ring of radius $w_0\sqrt{\ell/2}$. This highlights that while the scale of the final OAM mode will certainly *depend* on w_0, it will not be equal to it. We select an optimal scale for the detection in order to maximize modal power in the desired $p = 0$ mode when the initial mode is *not* amplitude modulated (Eq. (2.18) and depicted in Fig. 2.5 (a)). In the case where a mode generated without amplitude modulation is detected with a system that assumes a scale of w_0, the measured power in the desired $p = 0$ mode approaches zero as the azimuthal index increases (see Appendix A). This case would represent the usual method of detection, particularly in quantum experiments with OAM. For example, an input vortex mode of ℓ = 1 at this scale has only about 80% of its energy in the $\psi_{0,1}$ mode, with the rest spread across higher radial modes. Furthermore, an input vortex mode of ℓ = 10 has less than 1% of its energy in the $\psi_{0,10}$ mode. This places severe limits on the available alphabet using OAM as a basis. We ask: what should the ℓ dependent scale parameter

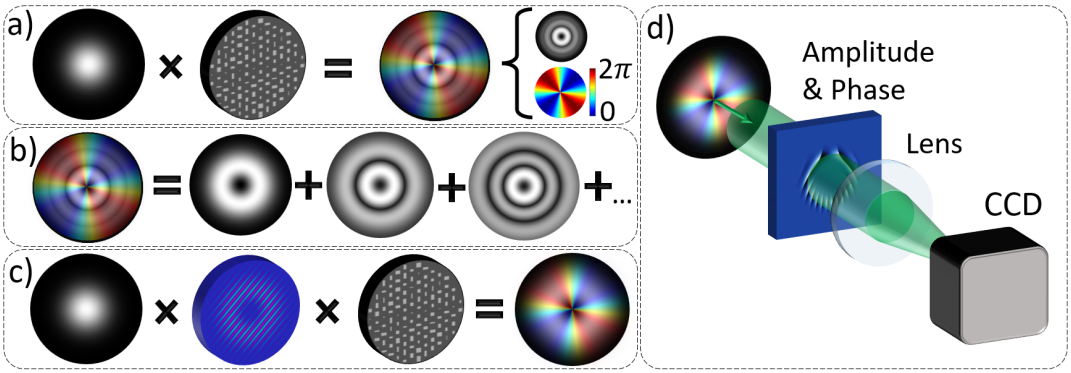


FIGURE 2.5: (a) A Gaussian beam modulated by an azimuthal phase, shown here as a metasurface, results in an OAM mode with many radial orders, shown in (b) as the sum of beams with several intensity rings. By combining dynamic and geometric phase control using holograms and metasurfaces, high purity OAM modes can be produced, as seen in (c). For detection of the modal composition of a beam, conjugate modulation of the mode being evaluated is applied and the Fourier plane on-axis intensity measured, as shown in (d).

be such that the expansion has the minimum power in the unwanted radial modes, $p \neq 0$? The salient point is that higher modal power is physically available but the detection system needs to be optimized to recover it. Accordingly, we exploit the fact that changing the scale in size-dependent bases can alter the detected modal content [227]. Here, the correct scale to achieve this can be expressed analytically as

$$w_{\text{opt}} = \frac{w_0}{\sqrt{|\ell|+1}}, \tag{2.20}$$

leading to an optimised modal power content in the $p = 0$ mode given by

$$|c_\ell(\alpha_{\text{opt}})|^2 = \left| \frac{2^{\frac{|\ell|}{2}} |\ell| \alpha \, \Gamma\left(\frac{|\ell|}{2}\right)}{(1+\alpha^2)^{\left(\frac{|\ell|}{2}+1\right)} \sqrt{\Gamma\left(|\ell|+1\right)}} \right|^2 \tag{2.21}$$

when

$$\alpha_{\text{opt}} = \frac{1}{\sqrt{|\ell|+1}}, \tag{2.22}$$

The implication of this is best visualized in a quantum experiment where the experimenter has full control over the detection steps but often little control over the creation steps. Rather than detecting for an incoming mode size of w_0, the detection system should be adjusted to a scale of w_{opt}. The prediction is a signal enhancement for a larger available alphabet of OAM modes.

While detection is enhanced by optimizing the available signal with w_{opt}, one cannot recover it to 100% as the vortex beam in Eq. (2.18) is not the desired mode. Amplitude modulation is needed. To illustrate this, we use metasurfaces to create OAM modes of very high order, and then circumvent the spread of power into higher order radial modes by employing holographically encoded complex amplitude modulation to correct for the missing amplitude term. By combining a metasurface for azimuthal phase control with high fidelity (since the vortex can be very well defined at the nano-scale) with holographic complex amplitude modulation, we are able to demonstrate ultra-high purity OAM states, even at very high OAM, as given by Eq. (2.17), with all the power in the $p = 0$ mode, illustrated in Fig. 2.5

(c). Here, the creation step is summarized which, when reversed, allows a detection route for enhanced signal over conventional approaches as illustrated in Fig. 2.5 (d).

Finally, in the quantum case the situation is a little different. There is no "initial" beam but only what one detects, which is related to a pseudo initial beam in the form of the pump mode at the crystal. Assuming the pump is Gaussian and the detection includes single mode fibers (the ubiquitous case), we derive the modal powers to be given by

$$|c_\ell(\alpha_{\text{opt}})|^2 = \left| \frac{2^{\frac{|\ell|+3}{2}} \sqrt{\frac{1}{|\ell|!}}\, \Gamma\left(\frac{|\ell|}{2}+1\right) \left(\frac{1}{\alpha^2}+\frac{1}{\eta^2}+2\right)^{-\left(\frac{|\ell|}{2}+1\right)}}{\pi^{3/2}\, w_0^2\, \eta\, \alpha^{|\ell|+1}} \right|^2, \tag{2.23}$$

with

$$\alpha_{\text{opt}} = \frac{\eta}{\sqrt{(2\eta^2+1)\,(|\ell|+1)}}, \tag{2.24}$$

where $\eta = \frac{w_p}{w_0}$ is the pump field and fiber mode size ratio in the plane of the crystal. This equation can easily be generalised to other pump geometries and detection modalities.

2.3.2 Experimental implementation

Dielectric metasurface

The metasurface device used for the creation of the classical OAM modes was a dielectric metasurface made of amorphous TiO_2 nano-posts with rectangular section (inset of Fig. 2.6 (a)) on a quartz substrate. Each post has a height of 600 nm while width and length (w_x, w_y) change in order to impart a different phase delay to the propagating visible light at 532 nm. More specifically, each nano-post imparts an overall phase delay δ to the propagating light and a phase delay difference $\Delta\chi$ between the field x and y components. This last term only depends upon the shape of the post and is called *form birefringence*: symmetric sections like squares or circles do not show form birefringence. Note that the amorphous TiO_2 used for this nano-structures is not optically birefringent at this wavelength. Our metasurface combines both propagation phase and Pancharatnam–Berry (PB) phase to convert any two orthogonal polarization states of the incident light into the conjugate helical modes with any arbitrary value of orbital angular momentum m and n, not just opposite values. This is possible by controlling the PB-phase, the overall phase and the form birefringence of each element. These spin to orbital angular momentum converters were denoted J-plates since the device controls the total angular momentum of the beam [218]. Figure 2.6 (a) shows the schematic image of the central part of a representative J-plate that converts two orthogonal linear polarization states (with field oriented along x and y respectively) into helical modes with the same polarization state and orbital angular momentum (m, n) = (10, 100). Fig. 2.6 (b) shows an optical microscope image of a J-plate producing helical modes with orbital angular momentum 10 and 100 for x- and y-linearly polarized incident light. Figs. 2.6 (c) and (d) show the Scanning electron micrographs (SEMs) of the realized device. Note that the nano-posts have different shape and orientation to implement the necessary phase gradient by combining propagation phase and PB-phase as described above. The J-plate is fabricated using electron-beam lithography followed by atomic layer deposition and etching. Note that the implemented azimuthal phase gradient

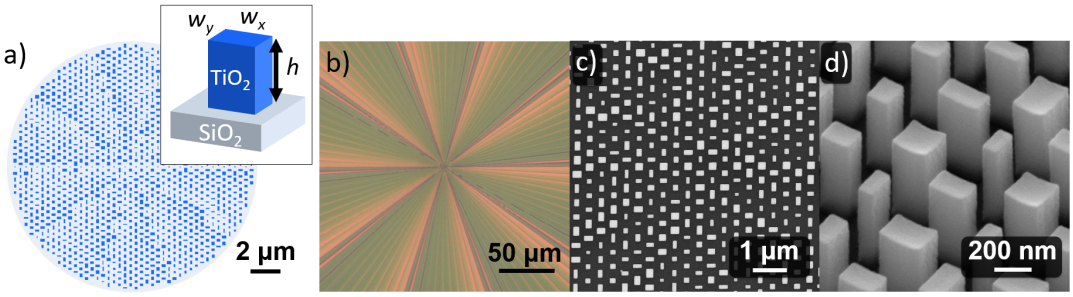


FIGURE 2.6: (a) Schematic of a J-plate design. The J-plate imprints two kinds of helical phase profiles for x- and y-incident polarization, resulting in output beams with orbital angular momentum $m\hbar$ and $n\hbar$, where m and n can be any independent integers. The metasurface elements are rectangular nano-posts made of amorphous TiO_2 with a fixed height $h = 600$ nm. By changing the width along x- and y-direction (w_x and w_y), the nano-posts impart phase delays given by δ_x and δ_y. (b-d) Optical micrographs (b) and Scanning electron micrographs (SEMs) (c and d) of a representative J-plate with OAM number $(m, n) = (10, 100)$. The SEMs show a top view (c) and angled view (d) of the device center.

is visible in the optical image of the device as color variation. In fact, nano-posts with different shapes have different scattering resonance frequencies, resulting in a colorful optical image. For instance, in Fig. 2.6 (b), it is easy to distinguish 10 sectors, each made of 10 inner sectors. This means that for the helical mode resulting from incident y-polarized light, in order to generate a beam with orbital angular momentum 100, a 2π azimuthal phase variation must be accumulated in an angle of just $2\pi/100$ (3.6°).

It is worth noting that the high azimuthal gradient necessary to impart a topological charge 100 to a propagating beam can be realized by means of SLMs. However, the typical pitch of such device is about 8 μm. In our metasurfaces, the unit cell dimension is 420 nm that represents an 20 times increase in resolution with respect to an SLM, crucial for high quality vortices. Moreover, an SLM does not affect the light polarization and cannot be used alone to encode spin-to-orbital angular momentum devices. Thus we elect to use this metasurface approach because the azimuthal phase is well defined down to nano-meter scales, for high quality azimuthal OAM modes. This allows us to emphasise the point that while the creation element is as ideal as can be, the purity of the resulting modes is nevertheless very low. It follows that while this work could be implemented with any phase-only device such as spiral phase plates or only an SLM (which is the case in the quantum experiment), we elect to employ the meta-surface in the classical case. The issue here is in the physics of the situation and not its implementation.

Enhanced generation scheme

To test the concept of enhanced purity in the creation as well as enhanced signal in the detection, we used the experimental set-ups shown in Fig. 2.7 (a) and (b) for classical and quantum light, respectively. In the classical experiment, a 532 nm wavelength horizontally polarized laser beam was generated through phase and amplitude modulation on a Holoeye Pluto spatial light modulator (SLM), allowing one to obtain any desired beam size and phase. The resulting mode traversed the metasurface (MS), which was further relayed with a 4-f system (F_1 and F_2 with focal lengths of 200 mm) onto another SLM for analysis. The measurement was performed by

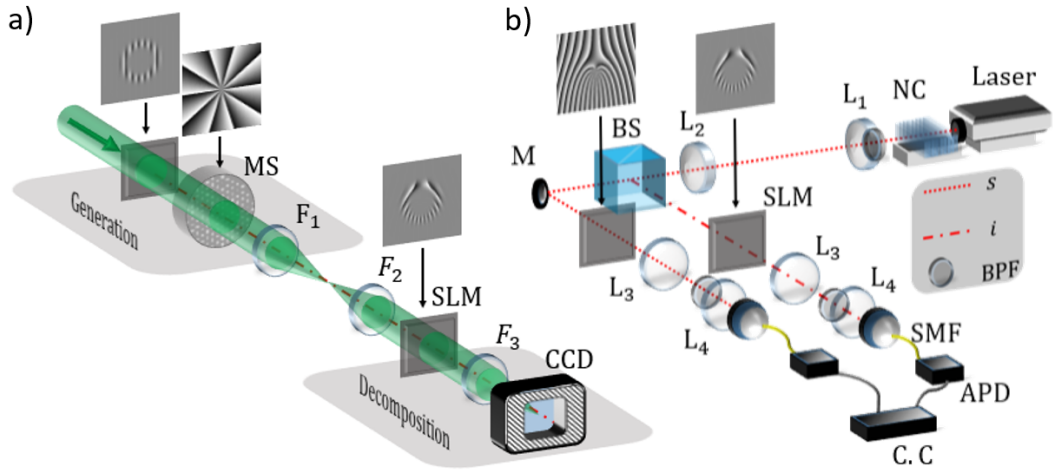


FIGURE 2.7: Illustrations of the (a) classical and (b) quantum experimental setups. SLM: spatial light modulator functioning in reflective mode but drawn here as transmissive; F,L: lens; CCD: charge-coupled device; NC: nonlinear crystal; BS: beam splitter; M: mirror; SMF: single mode fibre; APD: avalanche photodiode; BPF: band-pass filter; s: signal; i: idler; C.C.: coincidence counter. Overhead insets show representative phase maps for the respective beam manipulations carried out at each point.

detecting the on-axis intensity in the Fourier plane of the second SLM (F_3 with focal length of 300 mm), yielding the modal spectrum (see modal decomposition in Appendix A). Phase plots above the optical elements in Fig. 2.7 (a) exemplify the phase transformations imparted to the beam for amplitude correction of the MS and subsequent analysis thereof.

Enhanced two photon detection scheme

The set-up used for measurements on the entangled photons is illustrated in Fig. 2.7 (b). Our type I PPKTP crystals produced collinearly propagating photon pairs entangled in the OAM degree of freedom at 810 nm. The photon pairs were separated, in path, using a 50:50 beam splitter (BS). From the crystal plane, each pair was imaged onto an SLM with a 4f system (L_1 and L_2 having focal lengths of 100 mm and 500 mm each) and subsequently imaged (L_3 and L_4 having focal lengths of 750 mm and 2 mm each) into single mode fibres (SMF) for detection with APDs. The photons from each arm where correlated in time using a coincidence counter (C.C) with a 25 ns coincidence window. All measurements were obtained by recording the photons with an integration time of 5 seconds. A fixed ratio between the mode fibre radius (w_0) of the SMF and the pump photon was $\eta = 1.5$ was used during the experiment.

2.3.3 Results

Enhanced generation of OAM modes

In Figs. 2.8 (a) and (b) we compute the predicted radial modal power weighting ($|c_p|^2$) for $\ell = 10$ and $\ell = 1$ beams, respectively, as a function of ratio, $\alpha = w_\ell / w_0$. Each of which was generated by a metasurface. Accordingly, in each case, the beam waist size is varied on the projection hologram for the detection of each radial mode ranging from $p = 0$ to $p = 10$. Our aim is to engineer the mode by the metasurface and holographic control to produce $|c_0|^2 \to 1$, i.e., 100% of the power in the desired OAM mode in order to emphasise the effect of amplitude control in the generation

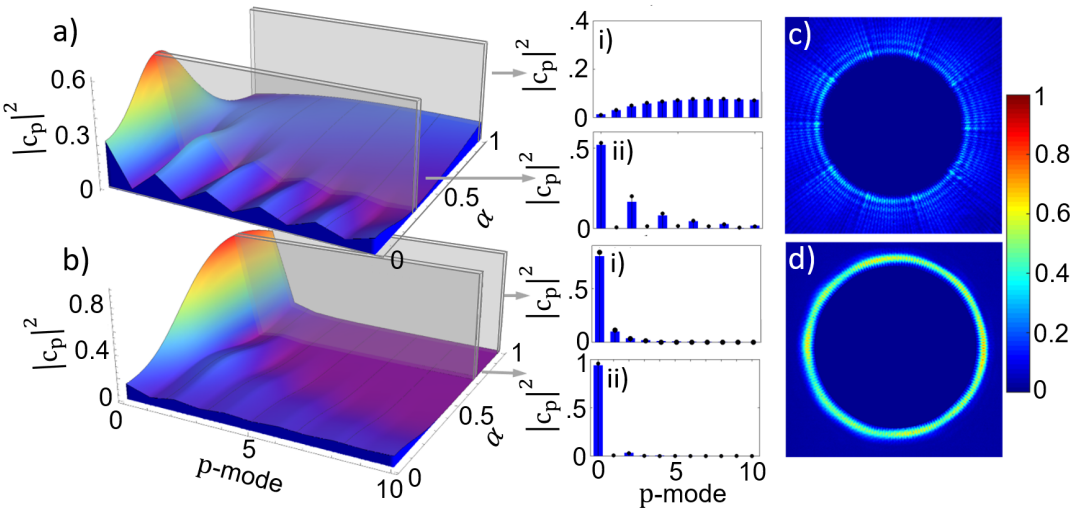


FIGURE 2.8: Normalised detection probabilities with variation in the p-mode index and $\alpha = w_\ell / w_0$ for (a) $\ell = 10$ and (b) $\ell = 1$. Measured p-mode spectra (blue bars) are given for detection with (i) the unadjusted mode size ($w_\ell = w_0$) and (ii) the optimal encoded mode size ($w_\ell = w_{\text{opt}}$) shown with the theoretical predictions (black bars). The normalisation was performed with respect to the p-mode distribution. False colour map images of an $\ell = 100$ generated beam with (c) phase-only modulation and (d) amplitude corrected phase modulation are shown.

process. We observe that if no initial amplitude control of the mode is performed and the traditional scale is used ($w_\ell = w_0$) in the detection, then the $|c_0|^2 \approx 0.8$ ($\ell = 1$) and $|c_0|^2 \approx 10^{-3}$ ($\ell = 10$). This is confirmed by experiment: the panels shown in (i) for both $\ell = 1$ and $\ell = 10$ modes show that the measured power in the radial modes is as predicted by theory. The bars represent the experimental data and the black dots the theory. For example, the cross-section highlighted by the gray panel at $w_\ell = w_0$ in the theory plot of Fig. 2.8 (a) is shown again in associated panel (i) as black dots (theory) with experimental data as blue bars. The measured power is spread across many unwanted radial modes, as predicted. There is second cross-section highlighted by the gray panel at w_{opt}, corresponding to the peak in the theory plot of Fig. 2.8 (a). The associated panel is in part (ii), again shown as black dots (theory) with experimental data as blue bars. Now the power in the $p = 0$ mode has substantially increased from <1% to about 50%. This confirms that optimizing the scale at the detection results in significant signal-to-noise enhancements, crucial for optical communication with OAM modes. The same trend is seen in (b) with its associated panels (i) and (ii), again with excellent agreement between theory and experiment. A decrease in the ratio α also results in an oscillation in the modal power as a function of radial index, with no power in the odd p modes. This truncated radial mode expansion becomes more evident as the scale outdistances w_0, due to the p parameter restriction ($p/2 \in \mathbb{N}$) when describing the resulting mode in the LG basis, as theoretically predicted [228].

So far only the detection step has been optimised. Next, we wish to apply full amplitude and phase control with our holographically enhanced metasurfaces. To do so we structure the amplitude only and pass the modified profile through the metasurface to impart the phase profile, akin to the method used by Ref. [229] and in similar concept the considerations of Refs. [230, 231]. The results for the two beams are discussed here and shown in Fig. 2.9(a) for $\ell = 10$ and Fig. 2.9(b) for

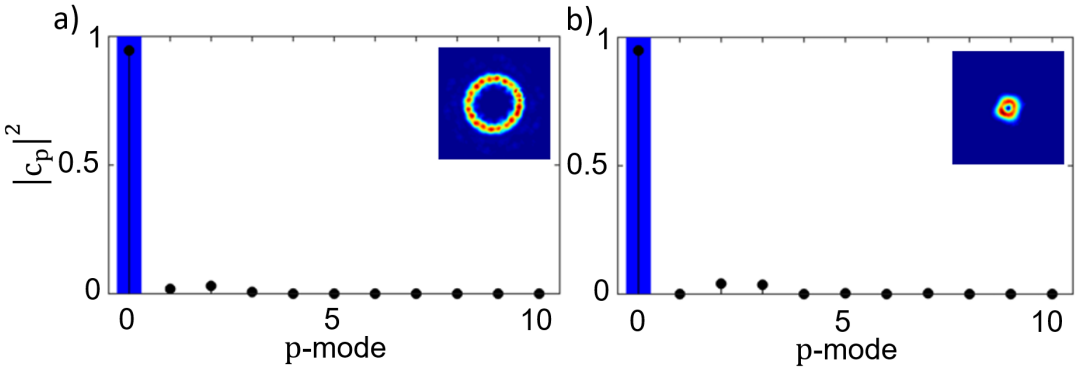


FIGURE 2.9: The p-mode spectrum when full amplitude and phase control is applied for (a) $\ell = 10$ and (b) $\ell = 1$. The bars represent the theory while the points represent the experiment. Insets show the processed transverse spatial distributions. The small intensity oscillations are due to the discrete nature of the metasurface nano-posts.

$\ell = 1$. The modal purity is as close to 100% as we can determine within experimental uncertainty: all the power is now in the desired ℓ with $p = 0$ mode, quantitatively characterised by $|c_0|^2$. Using $\ell = 10$ as an example, the initial modal power following traditional schemes was $|c_0|^2 \approx 4 \times 10^{-3}$, becoming $|c_0|^2 = 0.5$ after detection optimisation, and $|c_0|^2 \approx 1$ after full mode control. This represents about a $125\times$ and $250\times$ signal enhancement. The impact of our approach becomes more enhanced as one increases in ℓ. To illustrate this we perform these experiments with a metasurface to produce $\ell = 100$ modes (the highest reported to date by metasurface and metamaterials): Fig. 2.8 (c) shows such a beam created by only modulating the phase, while (d) shows the same beam but produced by our metasurface together with complex amplitude modulation. Even visually one can see the numerous rings in (c), which "collapse" into a single ring in (d): a high-purity OAM mode with an astonishing power enhancement in the desired mode. It is pertinent to point out that *all* phase-only approaches that only modulate a Gaussian beam by an azimuthal phase will produce the rings seen in (c) and is not a factor of the device efficiency. In most reports the rings are removed by optical filtering prior to recording and hence resulting in unwanted losses.

Enhanced quantum detection of OAM modes

The aforementioned tests modulated and detected classical light fields. To complement the classical results we also perform a quantum experiment, as shown in Fig. 2.7 (b). It may be noted that while the modes (ℓ, p) are discrete, surface plots were used as a guide so that the trend is easily seen (similar to the lines in Fig 2.10 (f)) and thus the discrete values are interpolated to yield the graphs. Here entangled photons were created using a PPKTP crystal via spontaneous parametric down-conversion (SPDC). Each of the entangled bi-photons were relay imaged to projective optics, with one set projecting onto a vortex state by an azimuthal phase profile and the other performing full ℓ control of both the amplitude and phase. This is the quantum equivalent of the classical prepare and measure experiment already reported in the previous section. However, as is customary in such quantum experiments, the detection system includes a single mode fibre so that only the $p = 0$ mode can be filtered out. Figure 2.10 (a) shows the experimental results for measuring the OAM spiral bandwidth as a function of the scale in the detection ($\alpha = w_\ell / w_0$), with

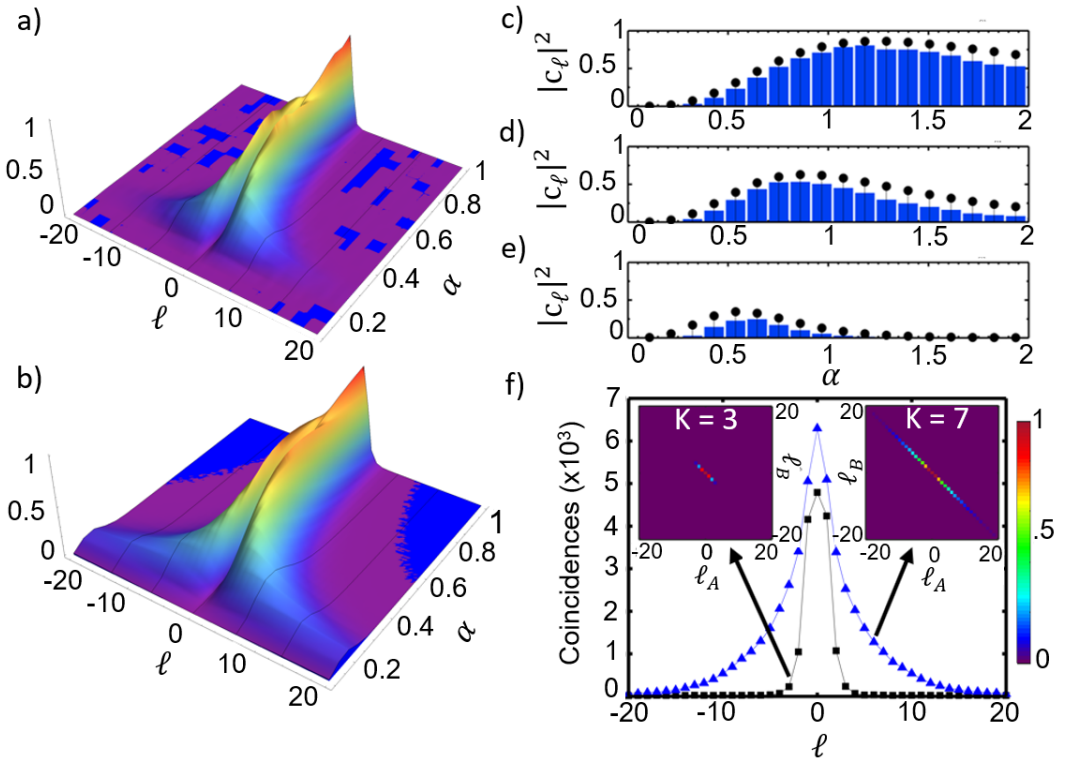


FIGURE 2.10: (a) Experimental and (b) simulated coincidence measurements based on the detection probabilities of OAM photons measured with the encoded holograms. (c) The normalized coincidences as a function of $\alpha = w_\ell/w_0$ for (c) $\ell = 1$ (d) $\ell = 2$ (e) $\ell = 5$. The bars represent the experimental data while the points represent the simulation. (f) Spiral-bandwidth plots obtained from the diagonal of the inset mode projections for (left) w_0 and (right) w_{opt}. Insets are density plots representing measured coincidences for OAM projections on the SLMs when the encoded LG beam size is w_0 (black squares) and the optimal mode sizes (w_{opt}) (blue triangles). Each data point was measured over a 5 seconds time interval.

the corresponding theoretical plot shown in (b). Clearly they are in excellent agreement. Cross-sections of the power in a specific ℓ mode, quantified by $|c_\ell|^2$, as a function of changing the scale α, is shown in (c)-(e) for ℓ = 1, 2 and 5, respectively. The theory (black dots) is in good agreement with the experimental data (blue bars). This confirms that the concept we have outlined is equally impactful with quantum light. We predict and observe that the coincidence rate can be dramatically increased by our approach, resulting in a visible spiral bandwidth beyond that possible without scale adjustment: the Schmidt number more than doubles from $K = 3$ to $K = 7$ as shown in Fig. 2.10 (f), demonstrating more than a doubling of the quantum dimensionality. This represents a significant increase in the available dimensions in our OAM Hilbert space and is a consequence of transferring power into the desired mode, thus lifting it from the noise. This experiment also serves to illustrate that it is not the *manner* of implementing the azimuthal phase pattern that matters - here only SLMs were used due to the unsuitability of the metasurface for the quantum photon wavelengths. For completeness we point out that we have not tested the quantum correlations in the new subspaces, and so make no statements on the entanglement. But since the SPDC process produces pure states [96, 202, 207, 208, 232], the full quantum toolkit can be applied to the new subspaces revealed from the noise, including testing for entanglement in high-dimensions [119].

2.3.4 Discussion and Conclusion

In many applications, the detection of OAM modes implicitly assumes a projection onto a Gaussian-like mode ($p \approx 0$), either by coupling into single mode fibres, by OAM mode sorting or by the match filters used in MUX/DEMUX optical communication systems. In such cases the detection approach we outlined here will yield an improved signal-to-noise ratio and thus a larger available alphabet, as we have demonstrated with both classical and quantum states. For completeness we point out that if the application and/or detection simply integrates out the radial modes, e.g., accumulates all power from a particular azimuthal mode (such as with phase-only azimuthal holograms [216]), then there will be neither a gain nor a loss from our approach.

We employed the meta-surface in the classical experiment as an example of a phase-only device which we note could have been replaced with any equivalent element to illustrate our concept. For example, a second SLM could have achieved the same outcome and this, in fact, was demonstrated with the quantum experiment. Here, a contrast in features between these two devices explicitly emphasises the generality of the effect and thus universality of how our optimisation may be of benefit. The choice of the meta-surface allowed us to simply demonstrate a high OAM charge ($\ell = 100$) with a good purity (see [224] for more analysis) which was easily achievable with the greater resolution. Additionally, due to the asymmetrical nature of the coupling in the device paired with the amplitude and phase control, that were achieved in separate steps, it would be possible to extended this to easily produce arbitrary high purity vector modes in line with Ref [229]. It may also be interesting to consider the combination of both techniques into a single integrated device in future studies, similar to that achieved by Refs [219, 220] or potentially employing phase corrections approaches [233, 234] for enhanced purity in all degrees of freedom.

In conclusion, we have outlined a simple approach for increasing the detection efficiency of classical and quantum experiments with OAM modes by a simple adjustment of the scale at which the measurements are made. In the quantum case this is all that is needed, since there is no "initial" mode: the state is determined by the measurement and has no reality prior to that. In the classical case, to truly maximise the signal requires very high-purity initial modes. We used novel metasurfaces that are holographically enhanced to control both the azimuthal and radial profile of OAM modes to create high-purity OAM beams up to $\ell = 100$. This applied research paper will be important to applications that seek to exploit OAM as a basis in classical and quantum experiments, particularly those pertaining to communication.

2.4 Sum-frequency generation

With sum frequency generation, the ability to generate a new optical field that shares the characteristics of the two input fields holds a variety of potential and applications in the manipulation of light. This has recently gained more interest as technological advances increase the efficiencies achievable [155]. This applies to both the classical and quantum aspects of light-based technology, ranging from communication [235, 236] to imaging [237–239] as well as from the creation step [164–172, 240, 241] to the detection step [43, 159, 163, 242, 243]. Furthermore, potential is held in optical processing and corrective measures [244–246].

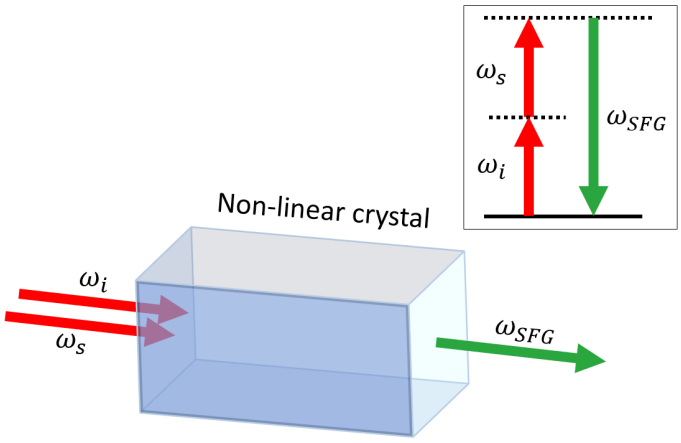


FIGURE 2.11: **Sum-frequency generation.** Diagram of the interaction geometry for sum-frequency generation with a $\chi^{(2)}$ non-linear crystal. Top right inset shows the energy level diagram.

Accordingly, we will briefly review the mechanism and modes generated in this technique and then classically explore this for mode detection with an idea of extending this to teleportation. A quantum description of such a mode detection case is then considered where a time-reversal argument between SPDC and SFG is invoked.

2.4.1 Phase-matching and efficiencies

In particular, for SFG, the generated frequency is equal to the sum of two input frequencies. The complex amplitudes of this frequency component can be derived from inserting each of the input electric fields i.e., $E_A e^{-i\omega_A t} + c.c.$ and $E_B e^{-i\omega_B t} + c.c.$ of defined angular frequencies, ω_A and ω_B, into Eq. 2.1 to get the associated non-linear polarisation [179]:

$$P(\omega_A + \omega_B) = 2\epsilon_0 \chi^{(2)} E_A E_B e^{-i(\omega_A+\omega_B)t}. \tag{2.25}$$

Here $c.c.$ refers to the complex conjugate of the expression and E_A (E_B) is the electric field amplitude of the input beam A (B). This process is illustrated in Fig 2.11 for a collinear geometry with the relation between the energy levels shown in the top right inset. Here, the parametric nature of this process results in the conservation of energy such that the input must equal that of the output:

$$\omega_A + \omega_B = \omega_{SFG}, \tag{2.26}$$
$$\mathbf{k}_A + \mathbf{k}_B = \mathbf{k}_{SFG}. \tag{2.27}$$

It can be seen here that Eq. 2.27 is actually the inverse of Eq. 2.2 and the geometry of the interaction as depicted in Fig. 2.11 as well. Such implications for the linear and angular momentum additionally can be seen to apply as overall conservation rules must still be obeyed. In fact, SFG can be considered as the time-reversal equivalent process of parametric down-conversion in that two lower energy photons combine to form a higher energy one and vice versa [247]. Here the efficiency of the process can be seen to be governed by the electric field amplitude, mediated by the strength of the second order non-linear susceptibility. This is in contrast to the SPDC where the conversion efficiency is constant or linear with intensity [247, 248].

When using SFG as a detection scheme, determining the efficiencies of the process is of importance in the physical implementation. For upconverting a single photon source, as in [242], this can be achieved as a function of the secondary higher power input and becomes relevant when using it as a projection system where entangled photons are involved. Here, the efficiency (η) for a single photon input (λ_B) to an output (λ_C) using a high pump power (λ_A) is given by [242]

$$\eta_{SFG} = \sin^2\left(\frac{\pi}{2}\sqrt{\frac{P_A}{P_{max}}}\right). \tag{2.28}$$

P_A is the input pump power and

$$P_{max} = \frac{c\epsilon_0 n_B n_A \lambda_B \lambda_A \lambda_C}{128(d_{eff})^2 L h_m}, \tag{2.29}$$

is the subsequent power (of λ_A) required to achieve 100% up-conversion of the input single photons. d_{eff} is the effective nonlinear coefficient, L is the length of the crystal and h_m is a reduction factor for focused Gaussian beams [249], which depends mainly on a focusing parameter L/b, determined by the confocal parameter $b = 2z_R$ (two times the Raleigh range). The respective refractive indices in the nonlinear crystal, n_j can be calculated from Sellmeier equations when the coefficients have been experimentally determined. A KTP crystal which will be used, for instance, has been reported [250, 251] to be accurately determined by using the two-pole Sellmeier equation

$$n(\lambda)^2 = A + \frac{B}{1-\frac{C}{\lambda^2}} + \frac{D}{1-\frac{E}{\lambda^2}} - F\lambda^2, \tag{2.30}$$

and $A - F$ are the experimentally determined coefficients which depend on the centred wavelength, e.g. $\lambda < 1$ μm [250] or above it [251].

It follows that one is able to use this relation to ascertain how the efficiency of the system (and thus detected counts) scales with a crystal length, pump power, nonlinear efficiencies and modal size. This will be relevant when considering the ability to use a non-linear crystal for Bell projections in teleportation. For the actual projection of the modes however, one should consider the interaction of different modes. This forms the basis of the next section where such interactions are explored classically and applied as a modal detection tool.

2.4.2 Classical demonstration of upconversion for spatial mode detection

This section is based on the paper:
Bereneice Sephton, Adam Vallés, Fabian Steinlechner, Thomas Konrad, Juan P. Torres, Filippus S. Roux, and Andrew Forbes, "Spatial mode detection by frequency upconversion," Opt. Lett. 44, 586-589 (2019)
B. Sephton performed the experiment and data analysis.

As was previously discussed, a common method for the detection of spatial modes results from running the generation process in reverse and exploiting the reciprocity of light [214, 215, 252, 253]. This relies on employing optical components which range from diffractive to refractive elements as was listed in Section 2.2.4 and used in Section 2.3. It can additionally be mentioned that other detection approaches also exist, where specific optical transformations facilitate the sorting and thus detection of mode sets such as Laguerre-Gaussian [213, 254], Bessel-Gaussian [255] and

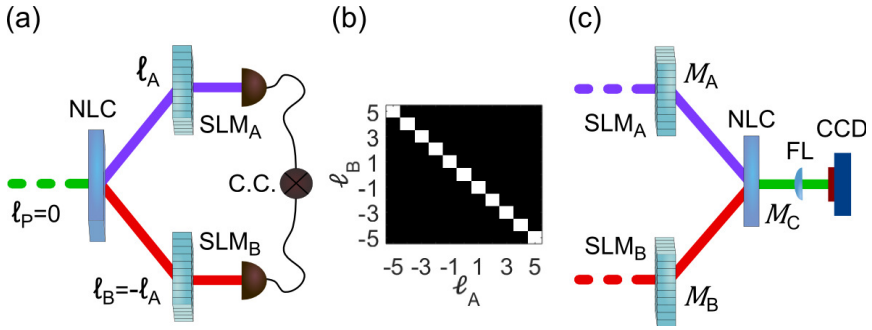


FIGURE 2.12: (a) In a traditional quantum experiment, a Gaussian mode pumps a nonlinear crystal (NLC) mediating the generation of two entangled photons with OAM values of ℓ and $-\ell$. (b) Example of flat and anti-correlated modal spiral spectrum of the paired down-converted photons. (c) In the frequency up-conversion process, two incoming signals are engineered to be in specific states. The up-converted signal is detected in the far field, so that there is a non-zero signal only when the phases are conjugate.

Hermite-Gaussian (HG) [256] modes. A common thread here is that all of these techniques use linear optics, which also extends to the creation step as well. As mode creation, however, has been considerably demonstrated with nonlinear optics [164–172], we also consider if this may not also be applied to the detection of modes as well.

Concept

To do so, it is instructive to first review how SPDC generates correlated modes, which we do here for a Gaussian pump and OAM modes [257]. For instance, when a Gaussian beam pumps the SPDC process, we know that it mediates the OAM generation of the signal (A) and idler (B) photons such that they satisfy $\ell_A = -\ell_B$, as depicted in Fig. 2.12 (a). When measuring the spatial state of the entangled photons, with methods such as explained earlier, e.g. SLMs, an anti-correlated spiral spectrum in OAM is obtained [232]. This is simulated in Fig. 2.12 (b). If SLM A is set to detect the $\ell = 2$ mode by phase-flattening and coupling into a SMF, the detector in arm B the only "clicks" in coincidence with A when SLM B similarly projects onto $\ell = -2$.

For detection of these spatial modes, we can consider exploiting the dual process, or SFG, as is depicted in Fig. 2.12(c). Signals A and B are then rather up-converted to signal C, whose on-axis intensity is observed and detected for in the far field. If A and B are OAM modes, a non-zero SFG signal is obtained only when $\ell_A + \ell_B = 0$ as addition of charges would otherwise yield a ring (when $\ell_A + \ell_B \neq 0$). The spatial modes of the light in A and B are controlled by SLMs, so the mode in A can be determined precisely by a measurement on the up-converted signal in conjunction with a known spatial projection on B. It follows that the nonlinear crystal plays the role of detector here rather than the generator. In this section, this concept is demonstrated experimentally with both OAM and HG modes, before illustrating that it may be extended to arbitrary mode structures.

We consider two input optical beams with spatial modes $M_A(\mathbf{x})$ and $M_B(\mathbf{x})$, that overlap at the nonlinear crystal to produce an up-converted beam with spatial mode $M_C(\mathbf{x})$. In a paraxial thin-crystal approximation where we can neglect diffraction in the SFG process, the up-converted field can be calculated from the differential

equation for SFG and expressed as

$$M_C(\mathbf{x}) = gM_A(\mathbf{x})M_B(\mathbf{x}), \tag{2.31}$$

where g is a constant that represents the strength of the process. It can thus be seen that the spatial characteristics of the produced field shares that of the inputs, modulated by the strength of the interaction. This can now exploited to implement a mode selector and as such detect them. By installing a $2f$-system behind the SFG crystal, the Fourier transform of the output field is produced in the back focal plane $\mathcal{M}_C(\mathbf{u}) = \mathcal{F}\{M_C\}$. In the center of the back focal plane, one obtains

$$\mathcal{M}_C(\mathbf{u} = 0) \propto \int M_A(\mathbf{x})M_B(\mathbf{x})d^2x, \tag{2.32}$$

which has the form of an inner product. If one input beam is an unknown linear combination of orthogonal modes, i.e. $M_A(\mathbf{x}) = \sum_n C_n\Phi_n(\mathbf{x})$, preparation of the other input beam as the complex conjugate of one particular mode in the crystal plane $M_B(\mathbf{x}) = \Phi_m^*(\mathbf{x})$, allows one to determine the modal content of the unknown beam. This is shown by

$$\mathcal{M}_C(\mathbf{u} = 0) \propto \sum_n C_n \int \Phi_n(\mathbf{x})\Phi_m^*(\mathbf{x})d^2x = C_m. \tag{2.33}$$

Measurement of the intensity in the centre of the back focal plane would then give $|C_m|^2$, similar to detection with modal decomposition. It can be noted that this approach can be further extended to implement a full state tomography of the unknown optical field [132].

Experiment

Using the outlined concept, we now proceed to the experiment shown schematically in Fig. 2.13. A 5-mm-long nonlinear periodically-poled potassium titanyl phosphate (PPKTP) crystal was pumped with two lasers (A and B) at wavelengths of 1565 nm and 806 nm, respectively, so as to obtain up-converted light at a wavelength of 532 nm via SFG. The crystal length was chosen to be 50× shorter than the Rayleigh length of the overlapping beams so that the thin crystal approximation is valid. We used a non-degenerate SFG type-0 process, which required vertically polarised inputs of different wavelengths, and gave us the highest nonlinear coefficient (quadratically proportional to the up-conversion efficiency). A 806 nm wavelength narrow band diode laser (Roithner) was used to generate one of the intense laser beams directed through the crystal, obtaining 50 mW of optical power after being spatially filtered with a 50-μm-diameter pinhole (PH) to form a collimated Gaussian mode. The spatially cleaned and horizontally polarised laser beam was then directed onto a liquid crystal SLM (Holoeye), allowing modulation of the spatial distribution and phase characteristics of the first diffracted order, creating our mode, M_B. After selection with an aperture, the first order was directed through the PPKTP crystal. A half-wave plate (HWP) changed the polarisation to vertical for the SFG process to occur.

A pigtailed laser diode, tuned to a wavelength of $\lambda = 1565$ nm through temperature control, was collimated to produce a Gaussian mode of 50 mW optical power. The laser light was then modulated with a second SLM to create our mode M_A, the corresponding mode was similarly selected with an aperture and vertically polarized with a HWP. The two modulated laser beams were then combined with a

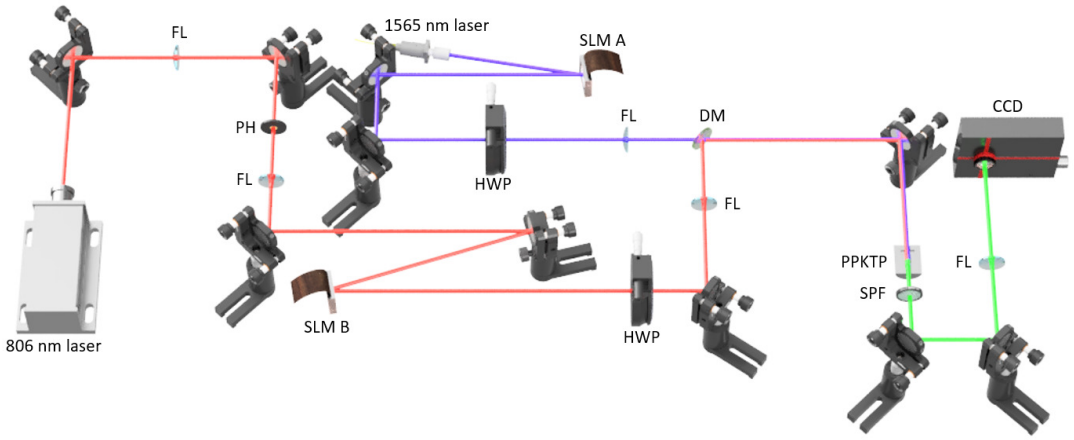


FIGURE 2.13: Schematic of the experimental up-conversion spatial mode detection setup. 806nm laser: high-power single frequency diode laser (Roithner); 1565 nm laser: single mode fiber pigtailed laser diode (Thorlabs); FL: Fourier lens; PH: pin hole; SLM: spatial light modulator (Holoeye); HWP: half-wave plate; DM: dichroic mirror; PPKTP: 5-mm-long nonlinear periodically-poled potassium titanyl phosphate crystal (Raicol); SPF: short-pass filter; CCD: CCD camera (Spiricon).

dichroic mirror, allowing collinear SFG in the nonlinear crystal. A short-pass filter (SPF) separated the up-converted signal from the detectable pump wavelengths. The generated mode was detected on a CCD with the on-axis intensity being measure. Alternatively, however, the generated mode could also have been coupled into a SMF.

Two versions of the experimental setup were constructed: the first with the crystal in the Fourier plane of the SLMs and the second, to perform a high resolution up-conversion test, relaying the SLM plane into the crystal plane by using the proper imaging system. To work in the Fourier plane for the first setup configuration, a $f = 750$ mm lens was placed f-away from the SLM and the crystal. The resulting signal was measured in the far-field by placing a $f = 250$ mm lens after the crystal. Figure 2.13 depicts the first version of the setup used to obtain the mode detection results. In the second version, an $f = 100$ mm lens was then incorporated into a $4f$-system before the crystal, relaying the SLMs plane into the crystal, allowing one to work with amplitude modulation generated images. A $4f$-system was also constructed to image the crystal plane onto the CCD by adding a second $f = 300$ mm lens.

Results

Using OAM and HG modes as examples, we show the outcomes in Figs. 2.14 and 2.15, respectively, where they confirm the concept of spatial mode detection by up-conversion. To quantify the quality of this spatial mode detection technique, a cross-talk matrix measurement was performed [258] to determine how well the desired input modes can be distinguished from the rest of the orthogonal modes. In Fig. 2.14, it can be seen that the orthogonality relations are obeyed with little cross-talk between neighbouring spatial modes. Accordingly, the concept that a known projection in arm B (on SLM B) together with a non-zero SFG "signal" results in a pattern sensitive detector for the mode in arm A is validated. For instance, we see that when M_A has OAM of $\ell_A = 1$, then a non-zero signal is found only when $\ell_B = -1$. Each column in Fig. 2.14 has been normalized with all its terms adding to unity, prior

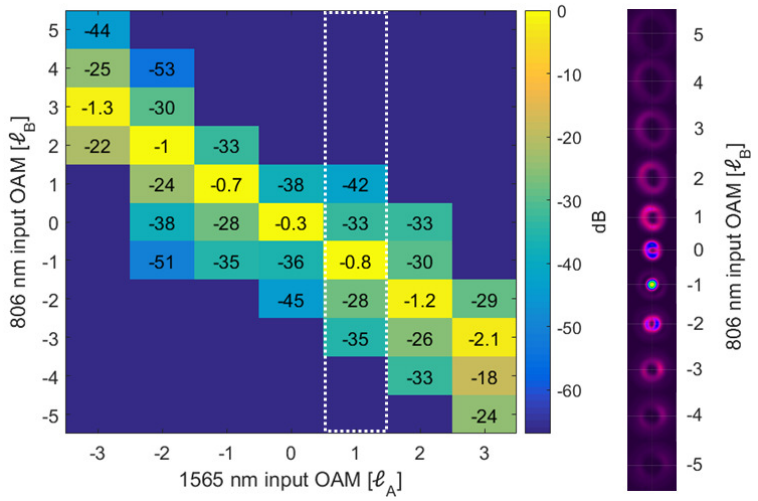


FIGURE 2.14: Cross-talk expressed in dB relative to the power in an input OAM mode with a particular helical charge for the 1565 nm ($\ell_A = [-3, 3]$) and performing a modal decomposition by varying the helical charge of the input OAM mode for the 806 nm ($\ell_B = [-5, 5]$). We have obviated the cross-talk values below -60 dB. The inset rightmost column shows the captured intensities for the OAM input mode $\ell_A = 1$, marked with a dotted white rectangle, to indicate where the central pixels are extracted.

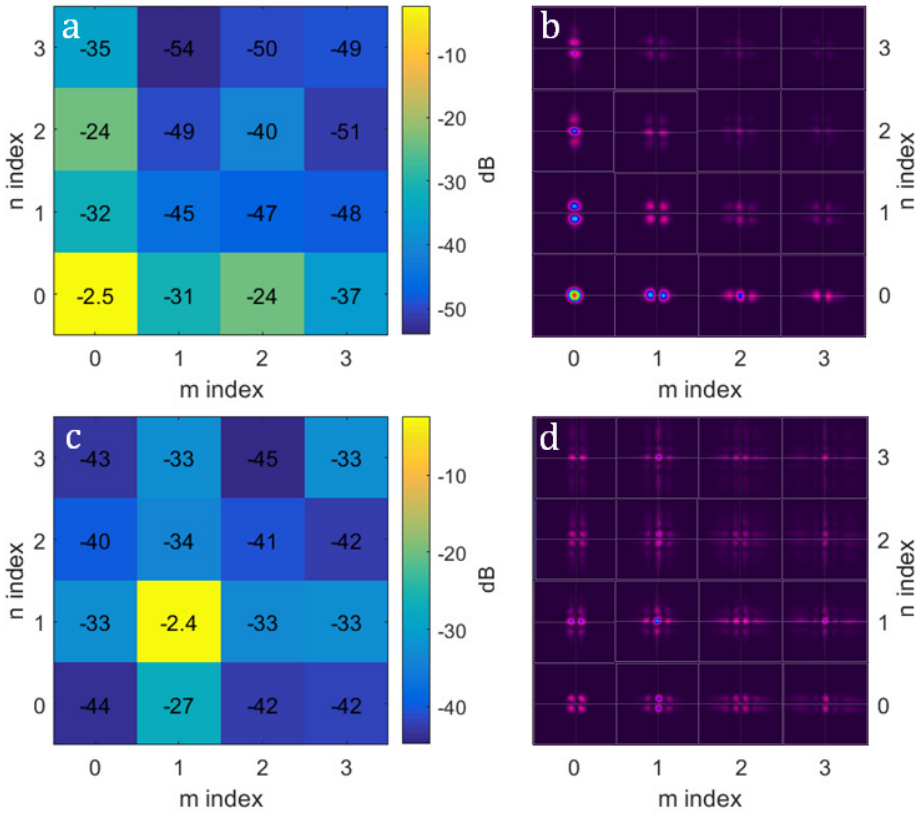


FIGURE 2.15: HG modal cross-talk given in dB for two different input $HG_{m,n}$ modes. The 1565 nm laser beam is encoded with (a) $HG_{0,0}$ and (c) $HG_{1,1}$, performing a modal decomposition with the 806 nm input laser beam such as $HG_{n,m}$, with the m, n indexes ranging within [0,3]. We show the captures obtained in the right indicating the weightings of the detected modes in the left, by extracting the center pixel value in the intensity plots for (b) $HG_{0,0}$ and (d) $HG_{1,1}$. Dotted cross-hairs indicate the central coordinate.

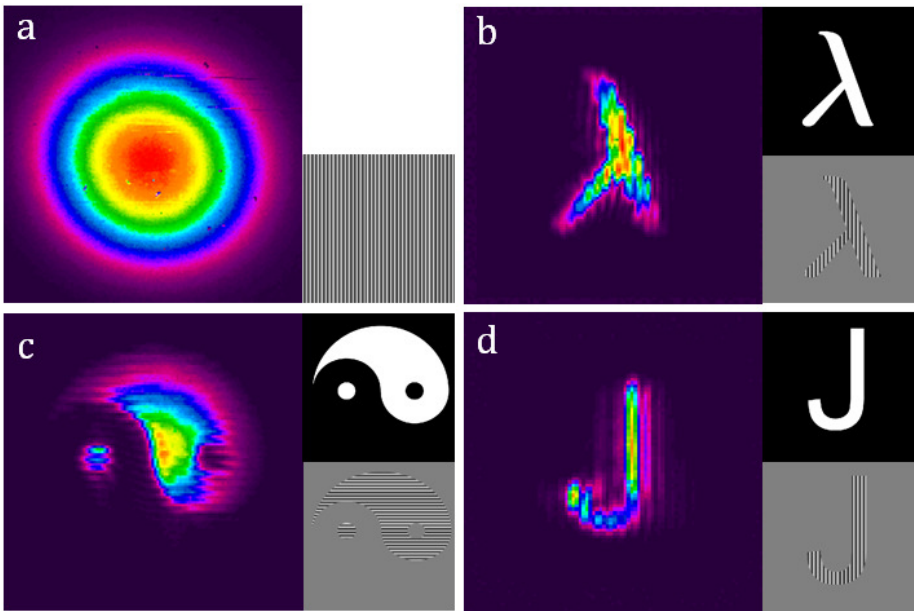


FIGURE 2.16: Up-converted images measured as M_C with M_A (1565 nm) as a Gaussian, shown in (a), and M_B (806 nm) set to be (b) lambda, (c) yin yang and (d) jay symbols. The insets show the applied amplitude modulated mask and the corresponding hologram to imprint the image onto mode M_B. The emerging fringes are the Moiré pattern due to the finite resolution of the SLM screen.

to expressing the cross-talk between the detected neighboring spatial modes in dB. The cross-talk measured values were found to be of -30 dB on average, having in the worst case scenario a value of -18 dB, being able also to easily isolate the correct input mode. The rightmost inset in Fig. 2.14 shows actual camera images, with a bright central spot only for the detected mode, with all other signals having practically no on-axis intensity. Slight asymmetry of the modes were due to aberrations in the generation system. Note that we do not measure the radial properties of our OAM basis. Hence, we neglect the increase of radial modes when considering the up-conversion process of counter-rotating vortices [167], as it plays no role in the OAM mode detection. While our OAM measurement was phase-only, phase and amplitude modes may be detected, which we demonstrate with HG modes in Fig. 2.15.

Figures 2.15(a) and (c) show the measurement outcome when a modal decomposition was performed on a 1565 nm laser beam with a particular encoded $\mathrm{HG}_{m,n}$ input mode, with indexes (a) $m = n = 0$ and (c) $m = n = 1$. The laser beam centered at 806 nm was used to perform a tomographic scan by varying the m and n indexes within the range [0,3], while measuring the resulting signal after the up-conversion process. Each cross-talk modal decomposition plot in Figs. 2.15(a) and (c) has been normalized with all its terms adding to unity, prior to being expressed in dB. A maximum on-axis intensity is obtained only when the 806 nm intense beam is encoded with the modes $\mathrm{HG}_{0,0}$ and $\mathrm{HG}_{1,1}$, as can be seen in Figs. 2.15(b) and (d), respectively. Here, since $M_A = \mathrm{HG}_{0,0}$ (or $\mathrm{HG}_{1,1}$), all on-axis intensities for M_B are zero except for the case when $M_A = M_B^* = \mathrm{HG}_{0,0}$ (or $\mathrm{HG}_{1,1}$). The average efficiency of the process was $\approx 10^{-4}$, and further study is needed considering whether the efficiency is mode dependent.

The extrapolation to more complex mode structures is limited only by the transverse resolution that can be obtained from the up-conversion process [237, 259, 260].

In order to demonstrate the complexity of possible modes, we encoded various complex images in arm B, while keeping the other laser beam in arm A as a Gaussian mode. Note that even if swapping the modes in A and B, the resulting outcome would be the same. In Fig. 2.16 we show the resulting images after the up-conversion transfer, confirming the dynamic range of the technique, i.e., the technique works even with high resolution spatial modes, being able to transfer also the emerging Moiré pattern due to the finite resolution of the SLM screen. To test whether we were measuring only the up-converted 532 nm signal in all our results and not the residual 806 nm input (also detectable by the CCD camera), we changed the polarisation of the 1565 nm beam to horizontal, checking that the up-converted signal disappeared completely. This confirms a previously predicted result [237].

Conclusion

In conclusion, a simple concept has been outlined for spatial mode detection by up-conversion and demonstrated it experimentally, using a variety of spatial mode structures. This experimental configuration paves the way for spatial mode detection of infrared band signals, but measuring them in the visible with cheaper and faster silicon based detector technology. The detection approach outlined here is based on mode projections and therefore not as efficient as mode sorters [213], but nevertheless shows excellent modal discrimination. Even though we have demonstrated the technique with high intensity signals, the results are immediately applicable to single photon states too by employing single photon counting detectors [261].

2.4.3 A wavefunction description for a non-linear mode projector

In the previous section, we demonstrated the ability to use SFG for spatial mode detection and by choosing to detect on the Gaussian state, correlations between the two input states are actually established. This is akin to what is seen for the quantum entangled states generated in SPDC, as mentioned. It follows that we may perhaps ask the question as to if this can be used as a projector onto a specific Bell state in order to obtain the same degree of freedom in the range of spatial modes that was seen. While the full formalism is undertaken in the following chapter, we close this section by exploring a quantum description of such a correlation-enforced detection.

This may be done by considering SFG as the reverse process of SPDC [262] which was covered in Section 2.2.2. Here, in congruence with Section 2.4.2, we consider the case where photons A and B (with wave vectors $\mathbf{q}_A$ and $\mathbf{q}_B$, respectively) are up-converted to an 'anti-pump' photon C. It then follows that the process can be represented by the bra-vector

$$\left\langle \psi^{\mathrm{SFG}}_{A,B} \right| = \int \langle \mathrm{vac} |\, \hat{a}_A(\mathbf{q}_A)\hat{a}_B(\mathbf{q}_B) f^*_{\mathrm{SFG}}(\mathbf{q}_A, \mathbf{q}_B)\, d^2q_A\, d^2q_B, \tag{2.34}$$

in analogy to Eq. (2.6). As we are interested in the case where we are projecting the two inputs onto a Gaussian (e.g. detection with a SMF), the associated two-photon wave function is also given by

$$f^*_{\mathrm{SFG}}(\mathbf{q}_A, \mathbf{q}_B) = \mathcal{N} e^{-(\frac{1}{2} w_C |\mathbf{q}_C|)^2} \mathrm{sinc}(\tfrac{1}{2} L \Delta k_z), \tag{2.35}$$

with w_C being the anti-pump beam waist (replacing w_p), and L the nonlinear crystal length. The wave vector mismatch Δk_z differs from in Eq. 2.5 only in the replacement of $\mathbf{q}_s$ and $\mathbf{q}_i$ by $\mathbf{q}_A$ and $\mathbf{q}_B$, respectively, along with the associated values for λ. As can be seen, the first term in the two-photon wavefunction refers to the Gaussian angular spectrum which was the pump in the SPDC case with associated normalisation factors now absorbed into $\mathcal{N}$. It may be noted that if we were considering detection with a different mode such as $\psi_{\ell\neq 0}$, this would instead become the angular spectrum (or Fourier transform) of that modal function. For simplicity, as will be seen later, we keep the projection to that of Eq. 2.35.

Chapter 3

Stimulated high-dimensional spatial teleportation

This chapter is based on the paper:
Bereneice Sephton, Adam Vallés, Isaac Nape, Mitchell A. Cox, Fabian Steinlechner, Thomas Konrad, Juan P. Torres, Filippus S. Roux, and Andrew Forbes, "Stimulated teleportation of high-dimensional information with a nonlinear spatial mode detector," under review at Nature Photonics (2022)
B. Sephton performed the experiment as well as contributed to data analysis and writing of the manuscript.

As was indicated, quantum teleportation since its inception in 1993 [3] has made a large impact in quantum related research and technologies. Physical realisation thus forms a significant component in further developing and establishing, both on the fundamental level as a different form of communicating, to facilitating quantum-related technologies. Here, a notable component of various schemes, however, rely on the ability to teleport states that have high dimensions, offering many practical advantages [62, 67, 263]. Photonics offers a particularly promising approach when considering physical media for the basic scheme with large networks already established on the use of such entities [264–267] and many developed toolboxes [155, 268, 269] despite room for further development as well as a large degree of control readily possible on light's properties by the available technology [269–271]. Experimental progress on increasing the dimensions in teleportation, however, has been slow due to the significant experimental hurdle of requiring ancillary photons in linear detection schemes [272], where d dimensions requires $d-1$ photons. The implication of this can be seen in the state-of-the-art for entanglement preparation and detection, achieving only four coincidences per hour for a ten-photon state [273], making high-dimensional teleportation practically infeasible and extension to objectives such as the teleportation of many pixel quantum images formidable.

As a result, to date quantum teleportation has been demonstrated with continuous [28, 31, 32, 34] and discrete [14, 26] variables as two-dimensional qubits only, including with a complete Bell measurement using nonlinear optics for polarisation qubits [43]. Orbital angular momentum (OAM), a topical basis for high-dimensional encoding, has seen many advances in quantum protocols [99, 100, 199, 201, 274] but here too only qubit teleportation has been demonstrated using OAM [76, 275] and hybrid spin-OAM states [53].

We have seen in Chapter 2, however, that non-linear optics has provided another tool-set which affords many new approaches from modal detection in another wavelength to optical processing [244, 245]. Additionally, it is already a ready and commonplace source of on-demand entanglement. The question one may now ask is can we harness this as a resource to obtain practically feasible high-dimensional

teleportation by incorporating it into the Bell projection? Here, although theoretical schemes have been proposed to teleport d-dimensional qudits using nonlinear approaches [72–74], none have yet been demonstrated experimentally. In particular, the state-of-the-art remains with linear approaches where it reaches only three-dimensional teleportation by path entanglement [68, 69], due to the penalty of ancillary photons, and further has the concomitant hurdle that the experiment must be custom built for the dimension to be teleported.

In this chapter, we consider the experimental implementation of a non-linear scheme, using OAM as the initial basis of choice with mind to extend it to pixels for the teleportation of quantum images. Here all aspects are covered, beginning with a full theoretical treatment to numerically simulating, experimentally implementing and characterising the scheme. In order to increase the nonlinear optical efficiency, we use a coherent state as the input for what we call a *stimulated* teleportation process, cognisant that any technological advance that facilitates single photon input states can be implemented with no change to the present experimental configuration. With this, we experimentally demonstrate a versatile and scalable nonlinear spatial teleportation channel for arbitrary dimensions. Using photons as carriers and the spatial modes of light as our encoding basis, we teleport information expressed across different eigenmode spatial bases, from qubit OAM modes to nine dimensional Hermite-Gaussian modes, all with high similarity and all using the same one entangled pair as a quantum resource.

3.1 Theoretical and numerical framework

In Chapter 2, we introduced the quantum wavefunctions, allowing us to describe the states produced from SPDC and, the time-reversal operation, SFG. Here we take these descriptions and develop the formalism, showing first that teleportation is possible, before establishing a teleportation channel operator by invoking state-channel duality which allows us to analytically incorporate restrictions that would affect the physical implementation of this scheme. Furthermore, we use OAM as a test basis and numerically simulate the outcome of altering the various parameters in the scheme in order to later experimentally confirm and characterise the operation of our system, pushing the bounds of high-dimenstional teleportation.

3.1.1 Teleportation with SFG

We formulate the general scheme for quantum teleportation that we will use here, developed akin to Refs. [72, 276]. The state that is teleported, however, is a high-dimensional single-photon state where the spatial mode is selected from a high-dimensional basis. Subsequently, the quantum state we wish to teleport is represented as

$$|\psi_A\rangle = \int \alpha(\mathbf{q}_A)\hat{a}_A^\dagger(\mathbf{q}_A)\,|\text{vac}\rangle\; d^2q_A, \tag{3.1}$$

where $\alpha(\mathbf{q}_A)$ is the angular spectrum associated with the chosen spatial mode, $\hat{a}_A^\dagger(\mathbf{q}_A)$ is the creation operator of photons with two-dimensional transverse wave vector $\mathbf{q}_A$ and $|\text{vac}\rangle$ is the vacuum state. The frequency ω_A is assumed to be fixed in this case.

Using SPDC, a single pair of entangled photons ($|\psi_{BC}\rangle$) is prepared with a state as described in Eq. 2.7 to form the channel between Alice and Bob. Here we consider the photons with transverse wave vectors $\mathbf{q}_B$ and $\mathbf{q}_C$ instead of $\mathbf{q}_s$ and $\mathbf{q}_i$,

respectively. It follows that state of the combined system is then

$$\begin{aligned}|\psi_{ABC}\rangle &= |\psi_A\rangle \otimes |\psi_{BC}\rangle \\ &= \int \alpha(\mathbf{q}_A) f(\mathbf{q}_B, \mathbf{q}_C) \hat{a}_A^\dagger(\mathbf{q}_A) \hat{a}_B^\dagger(\mathbf{q}_B) \hat{a}_C^\dagger(\mathbf{q}_C) \, |\text{vac}\rangle \; d^2q_A \, d^2q_B \, d^2q_C. \end{aligned} \tag{3.2}$$

By applying SFG to the state in Eq. 3.2, an up-converted photon D from a pair of photons A and C is produced. Photon B is thus the photon sent to Bob for teleportation of the desired state. With this, the resulting quantum state of the system becomes

$$\begin{aligned}|\psi_{BD}\rangle = \int & g(\mathbf{q}_A, \mathbf{q}_C, \mathbf{q}_D) f(\mathbf{q}_B, \mathbf{q}_C) \alpha(\mathbf{q}_A) \hat{a}_B^\dagger(\mathbf{q}_B) \\ & \times \hat{a}_D^\dagger(\mathbf{q}_D) \, |\text{vac}\rangle \; d^2q_A \, d^2q_B \, d^2q_C \, d^2q_D, \end{aligned} \tag{3.3}$$

where $g(\mathbf{q}_A, \mathbf{q}_C, \mathbf{q}_D)$ is the kernel for the SFG process.

If we apply the critical phase-matching condition as described in Eq. 2.27, $\mathbf{q}_A + \mathbf{q}_C = \mathbf{q}_D$ and the expression becomes

$$\begin{aligned}|\psi_{BD}\rangle = \int & g(\mathbf{q}_A, \mathbf{q}_D - \mathbf{q}_A, \mathbf{q}_D) f(\mathbf{q}_B, \mathbf{q}_D - \mathbf{q}_A) \alpha(\mathbf{q}_A) \\ & \times \hat{a}_B^\dagger(\mathbf{q}_B) \hat{a}_D^\dagger(\mathbf{q}_D) \, |\text{vac}\rangle \; d^2q_A \, d^2q_B \, d^2q_D, \end{aligned} \tag{3.4}$$

where $\mathbf{q}_C$ is eliminated in terms of $\mathbf{q}_A$ and $\mathbf{q}_D$. From this, it can be seen that the wave vector of photon A is now related to that of the teleportation photon B, based on the arguments of f.

Similar to the operation described in Section 2.4.3, performing a projective measurement of the SFG photon D in terms of a mode $U(\mathbf{q}_D)$, allows the teleported state to be heralded. This is analogous to projecting into one of the Bell states as seen in Section 1.3 and results in the state of Bob's photon B to be given by

$$|\psi_B\rangle = \int \beta(\mathbf{q}_B) \hat{a}_B^\dagger(\mathbf{q}_B) \, |\text{vac}\rangle \; d^2q_B, \tag{3.5}$$

where

$$\beta(\mathbf{q}_B) = \int U^*(\mathbf{q}_D) g(\mathbf{q}_A, \mathbf{q}_C, \mathbf{q}_D) f(\mathbf{q}_B, \mathbf{q}_C) \alpha(\mathbf{q}_A) \; d^2q_A \, d^2q_C \, d^2q_D. \tag{3.6}$$

A successful teleportation process would imply that $\beta(\mathbf{q}) = \alpha(\mathbf{q})$. It requires that

$$\int U^*(\mathbf{q}_D) g(\mathbf{q}_A, \mathbf{q}_C, \mathbf{q}_D) f(\mathbf{q}_B, \mathbf{q}_C) \; d^2q_C \, d^2q_D \approx \delta(\mathbf{q}_B - \mathbf{q}_A). \tag{3.7}$$

One may now ask, under what circumstances are we able to satisfy this condition? Firstly, we may assume that the mode $U(\mathbf{q})$ for the measurement of the SFG photon D (the *anti-pump*) is the same as the mode of the pump beam. Using the same argument as Section 2.4.3 where the SFG process can then be regarded as the conjugate of the SPDC process, the more general SFG expression can be reduced to

$$\int U^*(\mathbf{q}_D) g(\mathbf{q}_A, \mathbf{q}_C, \mathbf{q}_D) \; d^2q_D \sim f^*(\mathbf{q}_A, \mathbf{q}_C). \tag{3.8}$$

The two-photon wave function is consequently a product of the pump mode and the phase-matching function, which, akin to Eq. 2.35, is in the form of a sinc-function:

$$f(\mathbf{q}_B, \mathbf{q}_C) \sim U(\mathbf{q}_B + \mathbf{q}_C)\text{sinc}\left(\eta|\mathbf{q}_B - \mathbf{q}_C|^2\right), \tag{3.9}$$

where η represents the dimension parameter and subsequently determines the width of the function. Under suitable experimental conditions (see Appendix B.1), the sinc-function only contributes when its argument is close to zero so that the sinc-function can be replaced by 1. Furthermore, if the modes for the pump and the anti-pump are made wide enough, they can be regarded as plane waves, which are represented as Dirac δ functions in the Fourier domain. It would then follow that

$$f(\mathbf{q}_B, \mathbf{q}_C) \approx \delta(\mathbf{q}_B + \mathbf{q}_C), \tag{3.10}$$

and

$$\int U^*(\mathbf{q}_D)g(\mathbf{q}_A, \mathbf{q}_C, \mathbf{q}_D)\, d^2q_D \approx \delta(\mathbf{q}_A + \mathbf{q}_C), \tag{3.11}$$

which together produces the required result in Eq. 3.7 to yield successful teleportation, after integration over $\mathbf{q}_C$ has been evaluated.

Subsequently, by detecting the up-converted photon D, the state of photon B being held by Bob is heralded to be

$$|\psi_B\rangle = \int \alpha(\mathbf{q})\hat{a}_B^\dagger(\mathbf{q})\,|\text{vac}\rangle\; d\mathbf{q}. \tag{3.12}$$

As a result, the teleportation process can be performed successfully with SFG, provided that the applied approximations are valid under the experimental conditions being used.

3.1.2 The teleportation channel: physical limitations

In order to simulate the teleportation process, it can be viewed as a communication channel with imperfections such as loss and a limited bandwidth. As such, an operation that represents the teleportation channel may be obtained by overlapping a photon from the SPDC state with one of the inputs for the SFG process. Here, we use the SPDC state, $|\psi_{\text{SPDC}}\rangle = \left|\psi_{B,C}^{(\text{SPDC})}\right\rangle$ as was defined in Eq. 2.7 and rewrite the generalised two-photon wave function, symbolically provided in Eq. 3.9, to have the representation described in Section 2.2.2 for a Gaussian pump and $\mathbf{q}_p = \mathbf{q}_B + \mathbf{q}_C$ such that

$$f_{\text{SPDC}}(\mathbf{q}_B, \mathbf{q}_C) = \mathcal{N}e^{-\left(\frac{1}{2}w_p|\mathbf{q}_B+\mathbf{q}_C|\right)^2}\text{sinc}(\tfrac{1}{2}L_p\Delta k_z). \tag{3.13}$$

$\mathcal{N}$ is then the normalisation constant, w_p is the pump beam radius and L_p is the nonlinear crystal length. The mismatch in the wave vectors z-components (Δk_z) for non-degenerate collinear quasi-phase matching is accordingly given by Eq. 2.4 where indicies B and C replace s and i.

The associated SFG process, $\left\langle\psi_{C,A}^{(\text{SFG})}\right|$, is described by Eq. 2.34 for photons C and A so that index $B \to C$. The two-photon wave function is then given by

$$f_{\text{SFG}}^*(\mathbf{q}_C, \mathbf{q}_A) = \mathcal{N}e^{-\left(\frac{1}{2}w_D|\mathbf{q}_C+\mathbf{q}_A|\right)^2}\text{sinc}(\tfrac{1}{2}L_D\Delta k_z), \tag{3.14}$$

with w_D being the anti-pump beam waist, L_D being the nonlinear crystal length used for SFG and the wave vector mismatch Δk_z differs as described.

A *teleportation channel operator* can now be defined as the partial overlap between $\left|\psi^{(\mathrm{SPDC})}_{B,C}\right\rangle$ and $\left\langle\psi^{(\mathrm{SFG})}_{C,A}\right|$, where only the photons associated with C are contracted. The resulting operator is then given by

$$\begin{aligned}\hat{T} &= \left\langle \psi^{(\mathrm{SFG})}_{C,A}|\psi^{(\mathrm{SPDC})}_{B,C}\right|\left|\psi^{(\mathrm{SFG})}_{C,A}|\psi^{(\mathrm{SPDC})}_{B,C}\right\rangle \\ &= \int |\mathbf{q}_B\rangle\, T(\mathbf{q}_B,\mathbf{q}_A)\, \langle \mathbf{q}_A|\; d^2q_A\, d^2q_B,\end{aligned} \tag{3.15}$$

where $|\mathbf{q}_B\rangle = \hat{a}^\dagger_B(\mathbf{q}_B)\,|\mathrm{vac}\rangle$, $\langle \mathbf{q}_A| = \langle \mathrm{vac}|\,\hat{a}_A(\mathbf{q}_A)$ and the kernel for the channel is

$$T(\mathbf{q}_B,\mathbf{q}_A) = \int f^*_{\mathrm{SFG}}(\mathbf{q}_C,\mathbf{q}_A) f_{\mathrm{SPDC}}(\mathbf{q}_B,\mathbf{q}_C)\, d^2q_C. \tag{3.16}$$

It follows that this then describes how spatial information is transferred by the teleportation process when implemented with SFG.

The teleportation process can be simplified by using the thin-crystal approximation, as was discussed in Appendix B.1. Here the Rayleigh ranges of the pump beam and anti-pump beam are made much larger than their respective crystal lengths. As a result, $L/z_R \to 0$, for both the pump and the anti-pump which allows the phase-matching sinc functions in Eqs. 3.13 and 3.14 to be approximated as Gaussian functions [96]

$$\mathrm{sinc}(\tfrac{1}{2}L\Delta k_z) \to e^{(-L\Delta k_z)}. \tag{3.17}$$

This results in the associated wave functions becoming

$$f_{\mathrm{SPDC}}(\mathbf{q}_B,\mathbf{q}_C) = \mathcal{N} e^{-\left(\frac{1}{2}w_p|\mathbf{q}_B+\mathbf{q}_C|\right)^2} e^{\left(-L_p\Delta k_z(\mathbf{q}_B,\mathbf{q}_C)\right)}, \tag{3.18}$$

and

$$f^*_{\mathrm{SFG}}(\mathbf{q}_C,\mathbf{q}_A) = \mathcal{N} e^{-\left(\frac{1}{2}w_D|\mathbf{q}_C+\mathbf{q}_A|\right)^2} e^{(-L_D\Delta k_z(\mathbf{q}_C,\mathbf{q}_A))}. \tag{3.19}$$

Substituting Eq. 3.18 and 3.19 into Eq. 3.16 then yields

$$\begin{aligned}T(\mathbf{q}_B,\mathbf{q}_A) =& \mathcal{N}^2 \int \exp\left[-\tfrac{1}{4}w_p^2|\mathbf{q}_B+\mathbf{q}_C|^2 - \tfrac{1}{4}w_D^2|\mathbf{q}_C+\mathbf{q}_A|^2\right. \\ &\left. - L_p\Delta k_z(\mathbf{q}_B,\mathbf{q}_C) - L_D\Delta k_z(\mathbf{q}_C,\mathbf{q}_A)\right]\; d^2q_C.\end{aligned} \tag{3.20}$$

By setting $L_p = L_D = 0$ and evaluating the integral, the thin-crystal limit expression

$$\begin{aligned}T(\mathbf{q}_B,\mathbf{q}_A) =& \frac{\mathcal{N}^2}{\pi(w_D^2+w_p^2)} \exp\left[-\frac{w_D^2w_p^2}{4(w_D^2+w_p^2)}|\mathbf{q}_B-\mathbf{q}_A|^2\right] \\ =& T'(\mathbf{q}_B-\mathbf{q}_A),\end{aligned} \tag{3.21}$$

is obtained.

According to the Choi-Jamoilkowski (state-channel) duality [277–279], we can treat the channel operation in Eq. 3.20 as an entangled state. As a result, it may be used to calculate a Schmidt number as in Section 2.2.4. This may subsequently be interpreted as the effective number of modes that the channel can transfer and thus

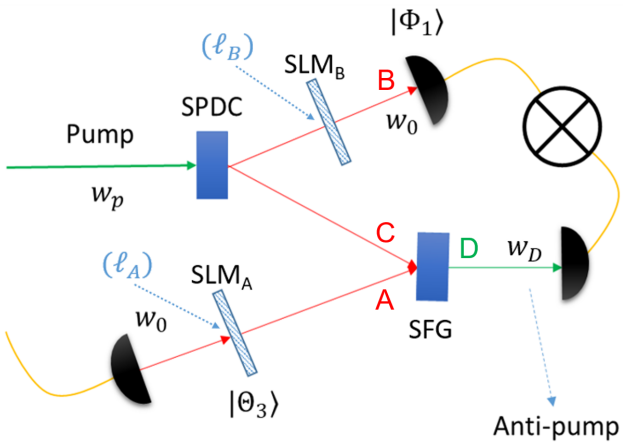


FIGURE 3.1: **Teleportation channel scheme with optimisation parameters.** A pump photon with a waist size of w_p impinges on a nonlinear crystal, generating two photons, photon B and photon C. Photon C is transmitted to a second crystal for SFG where it is absorbed with another independent photon encoded with the mode $|\Theta_A\rangle$, corresponding to a mode field with a waist size of w_0. We will call this independent photon, photon A. To recover the spatial information of photon A, we scan the spatial mode of photon B with spatial projections mapping onto the state $|\Phi_B\rangle$ with a corresponding mode field that also has a waist size of w_D. ℓ_A and ℓ_B refer to the encoded and projected vortex states displayed on the spatial light modulators (SLMs).

a dimensional capacity. Consequently, the modal capacity can be calculated as

$$K = \frac{\left[\int T^2(\mathbf{q}_A, \mathbf{q}_B) \mathrm{d}^2\mathbf{q}_A \mathrm{d}^2\mathbf{q}_B\right]^2}{\int \left[\int T(\mathbf{q}_A, \mathbf{q}_C) T(\mathbf{q}_C, \mathbf{q}_B) \mathrm{d}^2\mathbf{q}_C\right]^2 \mathrm{d}^2\mathbf{q}_A \mathrm{d}^2\mathbf{q}_B}. \tag{3.22}$$

This can then be further simplified, where we set $L_p = L_D = L$ and arrive at the result

$$K = \frac{n_A n_B w_D^2 w_p^2}{(w_D^2 + w_p^2)(n_A \lambda_B + n_B \lambda_A) L}. \tag{3.23}$$

It may be noted that although the Schmidt number provides an indication of the number of modes that can be transferred by the teleportation process, it does not tell us what the modes are that can be transferred. To determine this, the system can be numerically simulated, which is done for OAM in the next section.

3.1.3 Numerically simulating teleportation for OAM

In order to test the teleportation system, we consider OAM spatial modes as the information basis for reasons outlined in Sections 2.2.3 and 2.2.4. Here we use the frameworks detailed in the previous sections to numerically simulate the bandwidth that can be teleported as the physical parameters are altered. With Eq. 3.21, the conditional probabilities for encoding and detecting spatial modes using photons A and C can be simulated, respectively. A summary of the scheme with the derived parameters affecting the performance of the system is given in Fig. 3.1.

We can now consider how to emulate the different states from the generation of the entangled photons and desired teleportation states to the detection parameters. Here, the up-conversion beam waist (w_D) is set by the mode field diameter (MFD) of the SMF used to project the upconverted photons onto the Gaussian mode. The

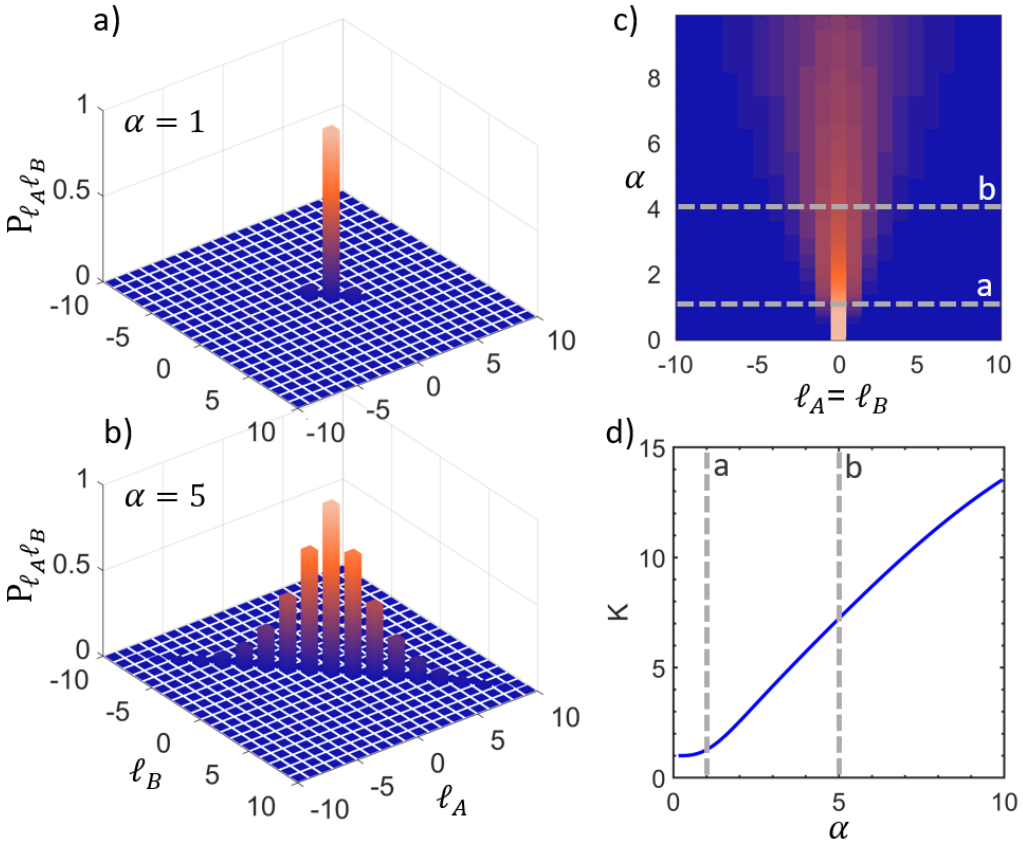


FIGURE 3.2: **Simulated spiral bandwidths and dimensionalities from measurements of photon B relating to encoded states of photon A.** Example renormalised teleported spiral bandwidths for vortex modes when (a) $\alpha = w_p/w_0 = 1$ and (b) $\alpha = 5$, using a fixed $\beta = w_p/w_D = 1$. These are marked as dashed lines in a wider (c) density plot of the spiral spectrum diagonal ($\ell_A = \ell_B$) as a function of α and (d) the calculated dimensionality (K), measured from the Schmidt number as a function of α.

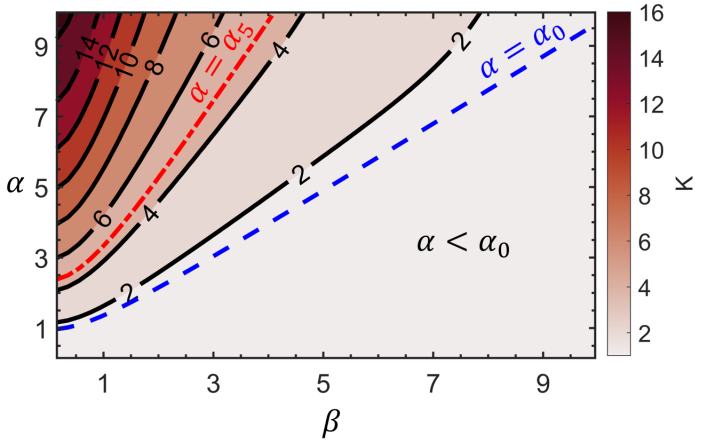


FIGURE 3.3: **Generalised OAM teleportation channel capacity analysis.** Contour plot of the dimensionality (K) as a function of β and α. For higher dimensionality we need a small $\beta < 1$ and large α. The blue single dash line corresponds to the minimum $\alpha = \alpha_0$ for teleporting a spatial mode through the setup. The red double dashed line corresponds to the minimum $\alpha = \alpha_5$ for teleporting OAM modes with $\ell = [-2, 2]$ giving access to no more than $K = 5$ dimensions.

spatial information we wish to teleport from photon A to photon B can be expressed as the following respective spatial modes

$$|\Phi_B\rangle = \int \phi(\mathbf{q}_B)\,|\mathbf{q}_B\rangle\; d^2q_B, \tag{3.24}$$

and

$$|\Theta_A\rangle = \int \theta(\mathbf{q}_A)\,|\mathbf{q}_A\rangle\; d^2q_A, \tag{3.25}$$

where $\phi(\cdot)$ and $\theta(\cdot)$ are the transverse field amplitudes. Taking the teleportation operator in Eq. 3.15, we can then obtain the overlap probability amplitude with these states with

$$\langle\Phi_B|\,\hat{T}\,|\Theta_A\rangle = \int \phi^\dagger(\mathbf{q}_B)\theta(\mathbf{q}_A)T'(\mathbf{q}_B-\mathbf{q}_A)\,d^2q_B\,d^2q_A. \tag{3.26}$$

Due to the weighting function of the channel matrix depending only on the relative momenta, the integral can be simplified to

$$\langle\Phi_B|\,\hat{T}\,|\Theta_A\rangle = \int \phi^\dagger(\mathbf{q}_B)\theta'(\mathbf{q}_B)\,d^2q_B, \tag{3.27}$$

where $\theta'(\mathbf{q}) = \theta * T$ represents a simple convolution.

As we are interested in simulating the system in the OAM basis, the general spatial modes in Eq. 3.24 and 3.25 will be specified as $|\Phi_B\rangle, |\Theta_A\rangle \in \{|\ell\rangle, \ell \in \mathcal{Z}\}$. Additionally, we shall consider the phase-only modes as described in Section 2.3 in order to conserve modulation efficiency, as will be discussed later. Photon A may thus be described by the phase-only vortex mode,

$$|\ell\rangle = \int G(\mathbf{q};w_0)\exp(i\ell\phi_q)\;\;|\mathbf{q}\rangle\,d^2q, \tag{3.28}$$

where ℓ is the corresponding OAM of the mode, ϕ is the azimuth coordinate and $G(\mathbf{q};w_0)$ is a Gaussian mode with a transverse waist of w_0 at the crystal plane. Photon B is then also projected onto these vortex modes. As we have seen in Chapter 2, the projection and generation beam sizes of phase-only OAM modes affects the accessible bandwidth and detection efficiencies. By defining the parameters $\alpha = w_p/w_0$ and $\beta = w_p/w_D$, we then simplify these variables into ratios with respect to the SPDC pump size. Using this, the optimal experimental settings for measuring a large spectrum of these modes through the channel can be investigated by looking at the conditional probability of detecting the mode ℓ_B when sending ℓ_A into the teleportation system. This can then be determined from the overlap of these states with the teleportation channel operator,

$$P(\alpha)_{\ell_B,\ell_A} = |\,\langle\ell_B|\,\hat{T}\,|\ell_A\rangle\,|^2. \tag{3.29}$$

Figure 3.2 shows how this varies for various values of α when keeping the anti-pump and SPDC pump modes are the same size i.e. fixing $\beta = 1$ ($w_D = w_p$). Initially, we show examples of two spiral bandwidths in (a) and (b) where $\alpha = 1$ and $\alpha = 5$, respectively. Clear diagonals with non-zeros probabilities for $\ell_A = \ell_B$ and zeros elsewhere indicate a successful scheme with the simulation showing that the measured modes reflect what is sent into the system. When considering the effect of increasing α, a wider spectrum with more non-zero diagonal modes is seen. It follows that the size of the light beam carrying the state to be teleported and detected

mode sizes must be significantly smaller than the SPDC mode to see a wider spectrum. This trend can be seen more clearly in (c) where larger values of α widen the modal spectrum where only the diagonals are extracted.

We then quantify the dimensionality of the channel and thus supported OAM modes in the system by employing the Schmidt number,

$$K(\alpha) = \frac{1}{\sum_\ell P_\ell^2(\alpha)}, \tag{3.30}$$

where $P_\ell(\alpha) = |\langle \ell | \hat{T} | \ell \rangle|^2$. The subsequent dimensionality K is given in Fig. 3.2 (d) as a function of α. It can be seen that an increase in the dimensionality of the modes requires a large α i.e. $w_p > w_0$.

We may now consider the effect of changing β with α by varying both parameters and looking at the subsequent Schmidt number. Figure 3.3 shows the corresponding numerically simulated outcome in a contour plot. Here, a larger value for β yields a larger accessible dimensionality. Consequently, for detection of a dimensionality larger than two,

$$\alpha > \alpha_0 = \frac{n_A}{n_B}\sqrt{\beta + 1}. \tag{3.31}$$

The blue dashed line in Fig. 3.3 corresponds to α_0 for different β values. Indeed the dimensionality below this region is less than $K = 2$. This is due to w_0 corresponding to the Gaussian argument of the vortex modes and not the optimal mode size of the generated or detected vortex mode.

To detect higher dimensional states, the scaling of higher order modes must be taken into account. Therefore, by noting that OAM basis modes increase in size by a factor of $M_\ell = \sqrt{|\ell| + 1}$ the relation $\alpha > \alpha_\ell$ where $\alpha_\ell = \sqrt{\beta + 1} M_\ell$ should be satisfied. This observation is illustrated for α_5 as the red dashed line in Fig. 3.3. Below this line, only states with less than $K = 5$ dimensions are accessible. Accordingly, α_ℓ sets a restriction on the upper limit of the dimensions accessible with the teleportation system.

3.2 Experimental implementation

Having derived the theoretical framework and evaluated the effects of the experimental parameters for the OAM basis, we now move on to experimentally realising the teleportation setup. To do so, the experimental implementation is covered in two sections. Firstly, we cover the experimental concept to establish an intuitive basis for the protocol, before confirming and characterising our scheme by testing the bandwidths generated for a chosen range of parameters. Here we confirm experimentally up to 15 dimensions, while exceeding the classical limit. Following this, we look at the final experimental implementation with the full range of elements described in more detail.

After testing the system behaves as numerically predicted by our formalism, we progress further to evaluating an optimal configuration which pushes the bounds of the dimensionality with the available resources and subsequently evaluating the resulting dimensionality and fidelities associated with the subsystems. With photons acting as carriers of spatially encoded information, we then demonstrate the system where the information is teleported across many spatial bases, from qubit OAM modes to MUBS and nine dimensional Hermite-Gaussian modes, forming a step towards teleporting images. The experimental challenges and errors are also considered in detail, following this. We then discuss the efficiencies of employing

SFG in such a system and the use of a coherent state as the input for what we call a *stimulated* teleportation process and map a transition from stimulated to quantum teleportation. Accordingly, in this section, we implement a proof-of-principle experiment which is supported by a full theoretical treatment and offers an exciting new route to teleportation of information between quantum systems that will benefit from technological advances in the future.

3.2.1 Working principle

A general schematic of our experiment, similar to Fig. 3.1, is shown in Figure 3.4 (a) for reference as we cover the full experimental concept. Here, two entangled photons, B and C, are produced from a nonlinear crystal (NLC_1) which is configured for collinear non-degenerate spontaneous parametric downconversion (SPDC). Photon C is sent to interact with the state to be teleported (carried by photon A), which is prepared by Alice using a spatial light modulator (SLM_A). Bob then measures the teleported photon B, also with a spatial light modulator (SLM_B). In most schemes where qubits are being teleported, the interaction of photons A and C takes the form of a Bell state analyser with linear optical elements. This is often a combination of beam splitters and polarising beam splitters. Conversely, this results in the teleportation being a probabilistic process. When looking at implementations beyond qubits, these linear optical solutions result in mixed states [275] unless additional photons (ancillary photons) are added [68, 69], as has been highlighted.

As was outlined in Section 3.1.1, we instead overlap photons A and C in a second nonlinear crystal (NLC_2), and detect the frequency upconverted photon D, generated by means of SFG. The success of teleportation is then rather conditioned on the measurement of the single photon D, where the projective state here takes the place of the Bell projections from Section 1.3. A coherent state is used for the input because the larger average number of photons in the coherent state enhances the probability for up-conversion. All the photons in the coherent state, however, carry the same modal information which we want to teleport. One such photon then takes part in the up-conversion process to produce the photon that is detected to signal the teleportation of the modal information to Bob's photon. The coherent input state and the output single photon state in this case can be considered as *carriers* of the quantum information to be teleported, i.e., coherent superpositions of photonic spatial modes.

Noticeably, a linear optical Bell state analyser for qubits, which form a 2×2 quantum gate, would ordinarily require two detectors, one for each of the photons A and C (often from the two output arms of the beam splitter). This allows one of the Bell states to be distinguished. When adding more dimensions, so too are photons such that the d-fold detection is needed [280]. In the nonlinear version here, there is only one upconverted photon and thus only one detector is needed to equivalently distinguish one of the Bell states; this, regardless of the dimension.

In order to understand the teleportation process better, we use the orbital angular momentum modes as simulated in Section 3.1.3 for an instructive example. Consequently, we pumped the SPDC crystal with a Gaussian mode ($\ell_p = 0$ and $p_p = 0$). The intuitive argument then follows where, from OAM conservation in SPDC (Section 2.2.3), $\ell_p = 0 = \ell_B + \ell_C$ and from the correlations established when detecting $\ell_D = 0$ with a SMF (Section 2.4.2 and 2.4.3), $\ell_D = 0 = \ell_A + \ell_C$, we find $\ell_A = \ell_B = -\ell_C$. That is to say, a coincidence is only detected when both A and B are conjugate to C, and thus the prepared state (A) matches the teleported state (B). In

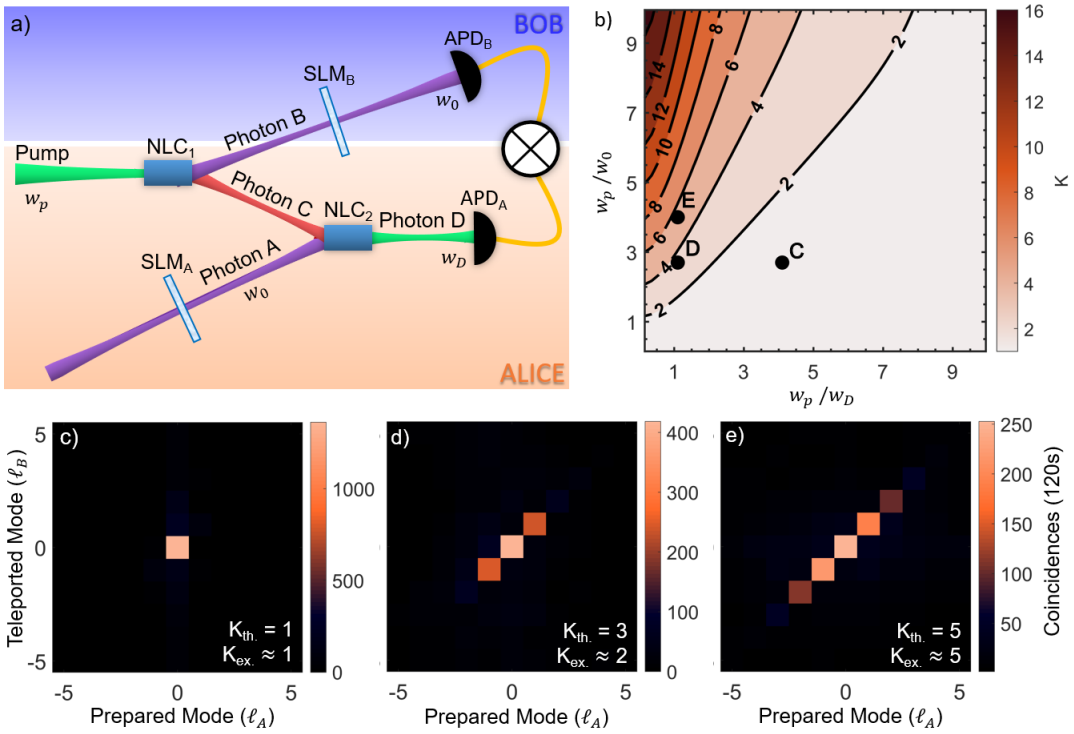


FIGURE 3.4: **Realising a teleportation channel based on nonlinear optical detection.** (a) A pump photon ($\lambda_p = 532$ nm) undergoes spontaneous parametric downconversion (SPDC) in a nonlinear crystal (NLC$_1$), producing a pair of entangled photons (signal B and idler C), at wavelengths of $\lambda_B = 1565$ nm and $\lambda_C = 808$ nm, respectively. Photon B is directed to a spatial mode detector comprising a spatial light modulator (SLM$_B$) and a single mode fibre coupled avalanche photo-diode detector (APD). The state to be teleported is prepared as photon A using SLM$_A$ ($\lambda_A = 1565$ nm), and is overlapped in a second nonlinear crystal (NLC$_2$) with photon C, resulting in an upconverted photon D which is sent to a single mode fibre coupled APD. Photons B and D are measured in coincidence to find the joint probability of the prepared and measured states using the two SLMs. (b) The teleportation channel's theoretical modal bandwidth (K) as a function of the pump (w_p) and detected photons' (w_0 and w_D) radii, with experimental confirmation shown in (c) through (e) corresponding to parameter positions C, D and E in (b). K_{th} and K_{ex} are the theoretical and experimental teleportation channel capacities, respectively. The cross-talk plots are shown as orbital angular momentum (OAM) modes prepared and teleported. The raw data is reported with no noise suppression or background subtraction, and considering the same pump power conditions in all three configurations.

the more general case, it can be seen that if the projective detection of photon D (anti-pump) is configured to be into the same mode as the initial SPDC pump, the up-conversion process acts as the conjugate of the SPDC process, and the state of photon A is teleported to photon B without any unitary corrections necessary from Bob. This, of course, takes place under pertinent experimental conditions, namely, perfect anti-correlations between the signal and idler photons from the SPDC process in the chosen basis, and an up-conversion crystal with length and phase-matching to ensure for anti-correlations between photons A and C as detailed in Appendix B.1.

To determine a bound on the modal capacity of the teleportation channel, we follow the approach established in Sections 3.1.2 and 3.1.3 where we treat the teleportation process as a communication channel with an associated channel operator. Invoking the Choi-Jamoilkowski state-channel duality [279], we calculate the Schmidt number (K) as given in Eq. 3.22 and compare. This is then interpreted as the effective number of modes the channel can transfer (its modal capacity). Following on from Section 3.1.3, the controllable parameters remain the beam radii of the pump (w_p), and the spatially filtered photons D (w_D) and B (w_0). Using the simulated channel capacity for OAM modes, we vary these parameters in the experimental setup and compare them as indicated on Figure 3.4 (b). Furthermore, we show three experimental examples of this trade-off in Figures 3.4 (c), (d) and (e), where the parameters for each is summarised in Table 3.1 which corresponds to the mars on the contour plot in Figure 3.4 (b).

Fig. 1	$\beta = w_p/w_0$	$\alpha = w_p/w_D$
c	4.1	2.7
d	1.1	2.7
e	1.1	4.1

TABLE 3.1: **Experimentally tested parameters.** Parameters values used experimentally to test the numerically simulated dimensionality trends.

As a result, we confirm that a large pump mode relative to the detected teleported modes is optimal for capacity. It may be noted that a large pump mode with respect to the crystal length also increases the channel capacity, consistent with Section 2.2.4. However, this comes at the expense of coincidence events, the probability of detecting the desired OAM mode, which must be balanced with the noise threshold in the system. Good agreement between theoretical (K_{th}) and experimentally measured (K_{ex}) capacities validates the theory.

3.2.2 Experimental details

In this section, we explore the experimental setup in more detail, which is found in Fig. 3.5. Here a 1.5 W linearly polarised continuous wave (CW) Coherent Verdi laser centred at a wavelength of $\lambda_p = 532$ nm was focused down using a $f_1 = 750$ mm lens to produce a pump spot size of $2w_p \approx 600$ µm in a periodically-poled potassium titanyl phosphate (PPKTP) crystal (NLC_1), yielding signal and idler photons at wavelengths $\lambda = 1565$ nm and 806 nm. A HWP placed before the crystal facilitated polarisation matching. A 750 nm long-pass filter (LPF) placed directly after the crystal blocked the unconverted pump beam, while a long-pass dichroic mirror (DM_1) centred at $\lambda = 950$ nm transmitted the $\lambda_B = 1565$ nm down-converted photon through to the receiver party (labelled 'Bob') and reflected the $\lambda_C = 806$ nm down-converted photons. The reflected photon was relayed onto the second PPKTP

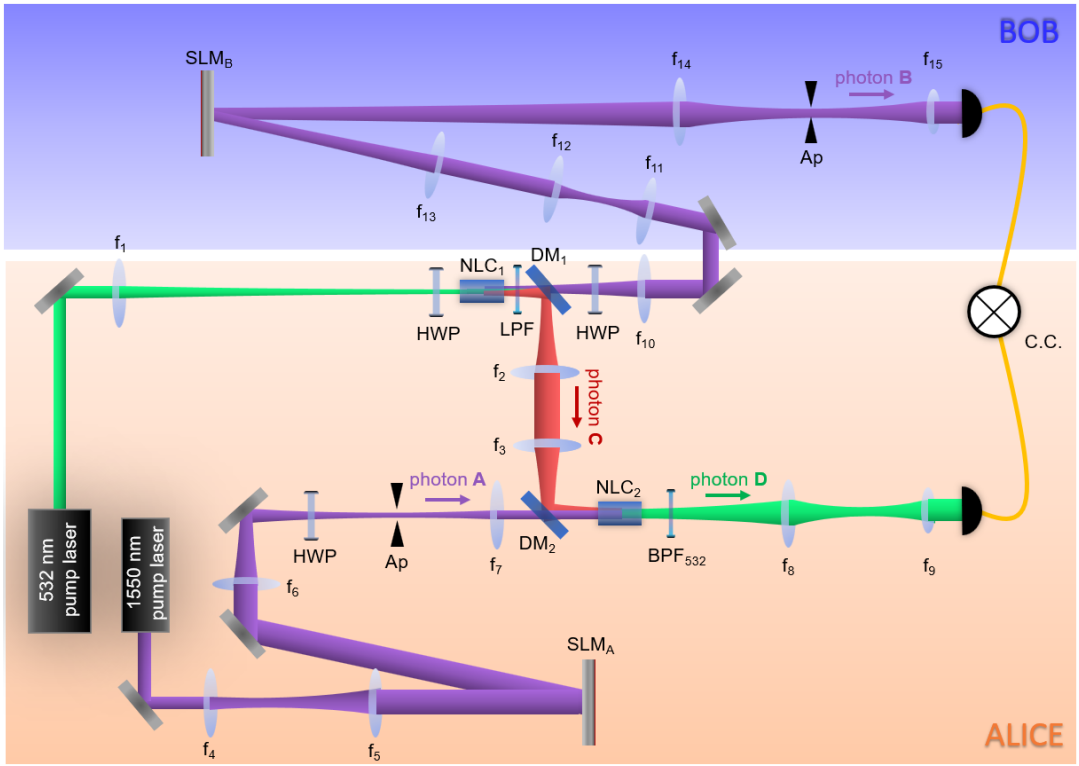


FIGURE 3.5: Detailed experimental setup description for high-dimensional spatial teleportation without ancillary photons. Ap: Aperture; BPF: Bandpass filter; DM: Dichroic mirror; f: Lens focal length; LPF: Lowpass filter; HWP: Half-waveplate; NLC: $\chi^{(2)}$ Non-linear crystal; SLM: Spatial light modulator (phase-only).

crystal (NLC$_2$), with a 1:1 imaging $4f$-system (focal lengths of $f_2 = f_3 = 175$ mm), for sum-frequency generation (SFG).

Both crystals used for up- and down-conversion were 1 x 2 x 5 mm PPKTP crystal with poling period 9.675 µm for type-0 phase matching. They were spatially orientated so that frequency conversion occurred for vertically polarised pump (and seed) light, producing vertically polarised photons. Phase matching for collinear generation of 1565 nm and 806 nm SPDC as well as up-conversion of 806 nm photons with the 1565 nm structured pump was achieved through control of the crystal temperatures.

The intense state to be teleported was created by a phase-only modulation by a spatial light modulator (SLM) of a 3.5 W horizontally polarised EDFA amplified 1565 nm laser that was expanded onto SLM$_A$ with a 1:3 imaging $4f$-system of $f_4 =$ 50 mm and $f_5 = 150$ mm. The polarisation of the modulated light was rotated to vertical using a second HWP to meet the phase-matching condition for SFG. A second 10:1 imaging $4f$-system (focal lengths $f_6 = 750$ mm and $f_7 = 75$ mm) with an aperture (Ap) in the Fourier plane resized and isolated the 1st diffraction order of the modulated beam from the SLM$_A$. The prepared state then formed a 200 μm spot size in the second PPKTP crystal and was overlapped with the 806 nm photons by means of another long-pass dichroic mirror centered at 950 nm (DM$_2$) to generate up-converted photons of 532 nm. A 532$\pm$3 nm band-pass filter (BPF$_{532}$) after the crystal blocked the residual down-converted photons and two-photon absorption noise from the 1565 nm pump laser, allowing the up-converted photons to be coupled into a single-mode fiber (SMF) with a $f_8 = 750$ mm and $f_9 = 4.51$ mm imaging $4f$-system. The photons were detected with a Perkin-Elmer VIS avalanche

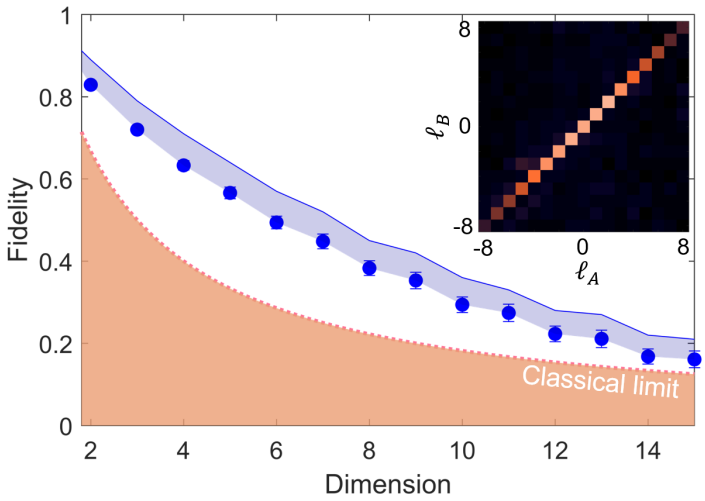


FIGURE 3.6: **Quality of the teleportation process.** Experimental fidelities (points) for teleportation channel dimensions up to the maximum achievable channel capacity of $K = 15 \pm 1$, all well above the classical limit (dashed line). The solid line forms a maximum fidelity for the measured teleported state. The inset shows the measured OAM modal spectrum of the optimised teleportation channel with maximum coincidences of 320 per second for a 5 minute integration time. The raw data is reported with no noise suppression or background subtraction. Error bars are produced from error propagation of Poissonian statistics and uncertainties the analysis method.

photodiode (APD) and in coincidence with the photon sent to 'Bob'.

The transmitted $\lambda = 1565$ nm down-converted photons sent to 'Bob' were expanded and imaged onto a second SLM with two $4f$-systems (focal lengths of f_{10} = 100 mm, f_{11} = 200 mm, f_{12} = 150 mm and f_{13} = 750 mm) for spatial tomographic projections of the teleported state. Here the spatially modulated photons were then filtered with an aperture and resized ($4f$-system with focal lengths f_{14} = 750 mm and f_{15} = 2.0 mm) for coupling into an SMF, which was detected by an IDQuantique ID220 InGaAs free-running APD. A PicoQuant Hydraharp 400 event timer allowed the projected SFG and SPDC photons to be measured in coincidence (C.C.).

3.2.3 Probing the limits

We now test the limits of our system by using the confirmed theory to adjust the experimental parameters and optimise the teleportation channel capacity. With this, we reached a maximum of $K \approx 15$ for OAM modes, as shown in the inset of Figure 3.6. It should be noted that this limit is not fundamental and is set only by our experimental resources of which we detail the challenges in Section 3.2.7. The balance of channel capacity with noise is shown in Fig. 3.6. Here, we are able to experimentally establish a teleportation setup where the channel supports at least 15 OAM modes, exceeding the currently demonstrated limit of three modes with linear optics.

In order to quantitatively characterise this channel, we employ the method [131] described in Section 1.5.3 and probe the purity and dimension. Here, we used the OAM analysers described in Eq. 1.63, with the teleportation channel substituted for the state: $\rho = \sum_\ell \lambda_\ell |\ell\rangle_A |\ell\rangle_B \rightarrow \hat{T} = \sum_\ell \lambda_\ell |\ell\rangle_A \langle\ell|_B$. As such, the input photon was then encoded with the state of one analyser and the teleported photon interrogated with the second analyser in order to measure the visibility fringes and reconstruct the state from the bounds. The fidelity for the channel, F_{Ch}, was then computed by

overlapping the truncated subspaces of dimensions d' from the reconstructed density matrix, with a channel state having perfect correlations. From this we compute the teleportation fidelity,

$$\mathcal{F} = \frac{F_{Ch}d' + 1}{d' + 1}. \tag{3.32}$$

which is detailed further in Appendix B.2.

With this, we estimate a channel fidelity which decreases with channel dimension, but is always well above the upper bound of the achievable fidelity for classical teleportation, given by $F_{\text{classical}} \leq \frac{2}{d+1}$ for d dimensions and shown as the classical limit (dashed line) in Figure 3.6. Blue points show the teleportation fidelity, measured from Eq. 3.32, using the channel fidelity F_{Ch}. Here, the channel fidelity measures the quality of the correlations that can be established between Alice and Bob over the two particle d^2 subspace while the teleportation fidelity, $\mathcal{F}$ measures how well Bob can measure states transmitted over the channel by Alice, requiring measurements over a single particle d dimensional space. Since $F_{Ch} \leq \mathcal{F} = \frac{F_{Ch}d+1}{d+1}$ [281], it follows that $\mathcal{F}$, shown as the solid line above the shaded region in Fig. 3.6, sets the upper-bound for the teleportation fidelity and is therefore the highest achievable fidelity for our system.

3.2.4 Rotating states, reconstructing the channel and breaking the state of the art

Having characterised our teleportation channel, we move forward to demonstrating the use of it and, in doing so, demonstrate the teleportation and detection of a variety of states. This extends from showing detection visibilities by rotating our states to reconstructing the channel state with at the state-of-the-art dimensionality, before moving forwards to breaking this limit by teleporting a variety of four-dimensional states. These results are shown in Fig. 3.7.

More specifically, in Fig. 3.7 (a) we show results for the teleportation channel in two, three and four dimensional spaces. We confirm teleportation beyond just the computational basis by introducing a modal phase angle, θ, on Bob's arm relative to Alice ($\theta = 0$) for the two-dimensional state $|\Psi\rangle = |\ell\rangle + \exp(i\theta)\,|-\ell\rangle$ (we omit the normalization throughout the text for simplicity). We vary the phase angle while measuring the resulting coincidences for three example OAM subspaces, $\ell = \pm 1$, ± 2 and ± 3. The raw coincidences, without any noise subtraction, are plotted as a function of the phase angle in Figure 3.7 (a), confirming the teleportation across all bases. The resulting raw visibilities vary from 85% to 79%, with background subtracted visibilities (see Appendix B.4) all above 96%. Example results for the qutrit state $|\Psi\rangle = |-1\rangle + |0\rangle + |1\rangle$ are shown in Figure 3.7 (b) as the real and imaginary parts of the density matrix, reconstructed by quantum state tomography, obtaining a teleported qutrit with an average channel fidelity of 0.82 ± 0.016 (see Appendix B.7 for all detailed measurements with the raw coincidences from the projections in all orthogonal and mutually unbiased basis). We further note that the measured fidelity is higher than that shown in Fig. 3.6 due to the effect of Procrustean filtering and size flattening (see Appendices B.3 and B.8). Further analysis of judiciously chosen teleported states themselves lead to even higher values (see Appendix B.5 and B.8).

Having replicated the present state-of-the-art, we proceed to break it and illustrate the potential of the teleportation channel by sending four-dimensional states of the form $|\Psi\rangle = |-3\rangle + \exp(i\theta_1)\,|-1\rangle + \exp(i\theta_2)\,|1\rangle + \exp(i\theta_3)\,|3\rangle$, with intermodal phases of $\{\theta_1, \theta_2, \theta_3\} = \{-\pi/2, -\pi, -\pi/2\}, \{-\pi/2, 0, \pi/2\}, \{\pi/2, \pi, \pi/2\}$

and $\{\pi/2, 0, -\pi/2\}$. All possible outcomes from these mutually unbiased basis

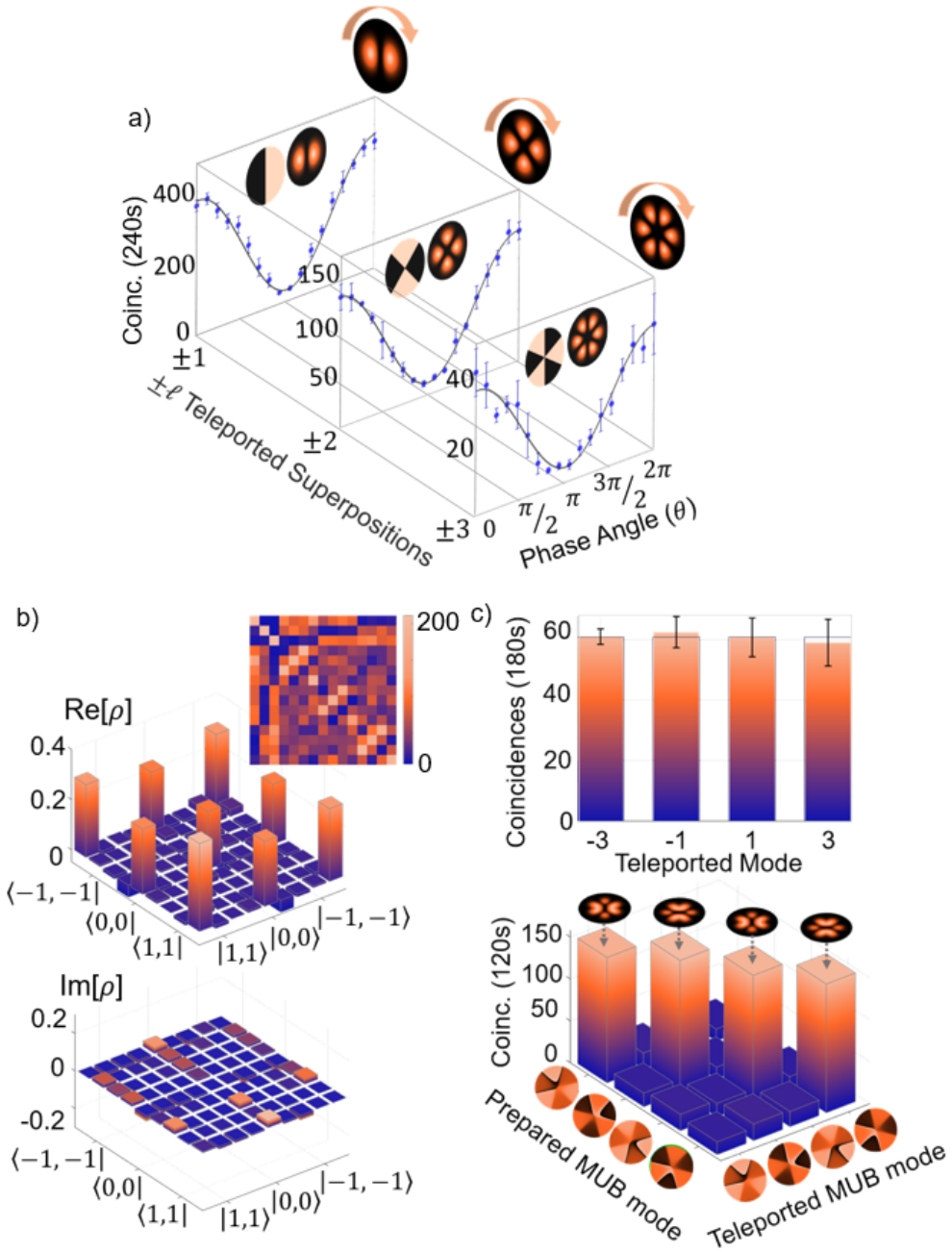


FIGURE 3.7: **Visibilities and quantum state tomography.** (a) Measured coincidences (points) and fitted curve (solid) as a function of the phase angle (θ) of the corresponding detection analyser for the state $|\phi\rangle = |\ell\rangle + \exp\{(i\theta)\}\,|-\ell\rangle$, for three OAM subspaces of $\ell = \pm 1$, ± 2, and ± 3 (further details in Appendix B.4). (b) The real (Re[ρ]) and imaginary (Im[ρ]) parts of the density matrix (ρ) for the qutrit state $|\Psi\rangle = |-1\rangle + |0\rangle + |1\rangle$ as reconstructed by quantum state tomography. The inset shows the raw coincidences with maximum coincidences of 220 detected per second from the tomographic projections (full details in the Appendix B.3 and B.7). (c) Measurements for the teleportation of a 4-dimensional state, constructed from the states $\ell = \{\pm 1, \pm 3\}$, with the inset graph showing the detection (solid bars) of all the prepared (transparent bars) OAM states comprising one of the MUB states. The raw data is reported with no noise suppression or background subtraction and error bars produced from multiple measurements.

(MUBs) are shown in Fig. 3.7 (c). We encoded each superposition (one at a time) in SLM_A and projected photon B in each of the four states. The strong diagonal with little cross-talk confirms teleportation across all states. The inset shows an example state: the teleported state (solid bars) with the prepared state (transparent bars) for a similarity of $S = 0.98 \pm 0.047$ (see Section 3.2.6). Furthermore, we have also teleported various unbalanced superpositions of OAM states (see Appendix B.6), being able to assign different weightings. The encoded states are the following: $|\Psi\rangle = 2|-1\rangle + 3|0\rangle + |1\rangle$, $|\Psi\rangle = 2|-2\rangle + 3|0\rangle + |2\rangle$, $|\Psi\rangle = |-2\rangle + 2|0\rangle + |2\rangle$, and $|\Psi\rangle = 2|-3\rangle + |-1\rangle + |1\rangle + 2|4\rangle$. The result in Figure 3.7 (c) also confirms that the channel is not basis dependent, since this superposition of OAM states is not itself an OAM eigenmode. Here, the teleported state (solid bars) is in very good agreement with the prepared state (transparent bars).

3.2.5 Changing the basis symmetry - a step towards pixel states

Reinforcing the basis-independence of our teleportation system, we proceed to teleport $d = 3$ and $d = 9$ states in the Hermite-Gaussian ($HG_{n,m}$) basis with indices n and m as was introduced in Section 1.4.2. Here, we may note the symmetry of the basis being used has changed from polar to Cartesian coordinates. It follows that this is a step further towards teleportation in the pixel basis, and thus the direct teleportation of complex images, with similar additional considerations in modal size mismatch resulting in the presentation of cross-talk. These are shown in Figure 3.8 and, similarly, demonstrate a very good agreement between the prepared and teleported states. More variation from that of the encoded states may be noted in Fig. 3.8 (b) due to a greater complexity of the phase structure as a result of the high number of modes being simultaneously teleported.

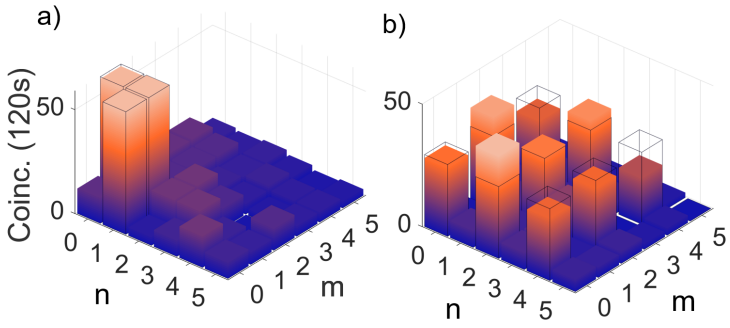


FIGURE 3.8: **Teleportation in the Hermite-Gaussian basis**. Coincidence measurements for teleportation of a (a) 3-dimensional and (b) 9-dimensional $HG_{n,m}$ state, constructed from the states $(n,m) = \{(0,1),(1,0),(1,1)\}$ and $(n,m) = \{(0,0),(2,0),(0,2),(2,2),(2,4),(4,2),(4,4)\}$, respectively. The teleported state (solid bars) is in good agreement with the prepared state (transparent bars). The raw data is reported with no noise suppression or background subtraction.

3.2.6 Bringing it all together: A similarity comparison

A final summary of example teleported states is shown in Figure 3.9. Here we use a normalised distance measure to quantify the quality of the states being teleported, which we denoted the *Similarity*,

$$S = 1 - \frac{\sum_j |(|C_j^{Ex.}|^2 - |C_j^{Th.}|^2)|}{\sum_j |C_j^{Ex.}|^2 + \sum_j |C_j^{Th.}|^2}. \tag{3.33}$$

Here we take the normalised intensity coefficients, $|C_j^{Th.}|^2$, encoded onto SLM_A for the *jth* basis mode comprising the state being teleported (i.e. $|\Phi\rangle = \sum_j C_j |j\rangle$) and compare it with the corresponding *jth* coefficient $|C_j^{Ex.}|^2$ detected after traversing the teleportation channel (made with *jth*-mode projections on SLM_B). A small difference in values between encoded and detected state results in a small 'distance' between the prepared and received value. As such, the second term in Eq. 3.33 diminishes with increasing likeness of the states, causing the Similarity measure to tend to 1 for unperturbed teleportation of the state.

Consequently, we cover a variety of dimensions ranging from two through nine, and across the various bases exploited. The prepared (transparent bars) and teleported (solid bars) states are in good agreement, confirming the quality of the channel.

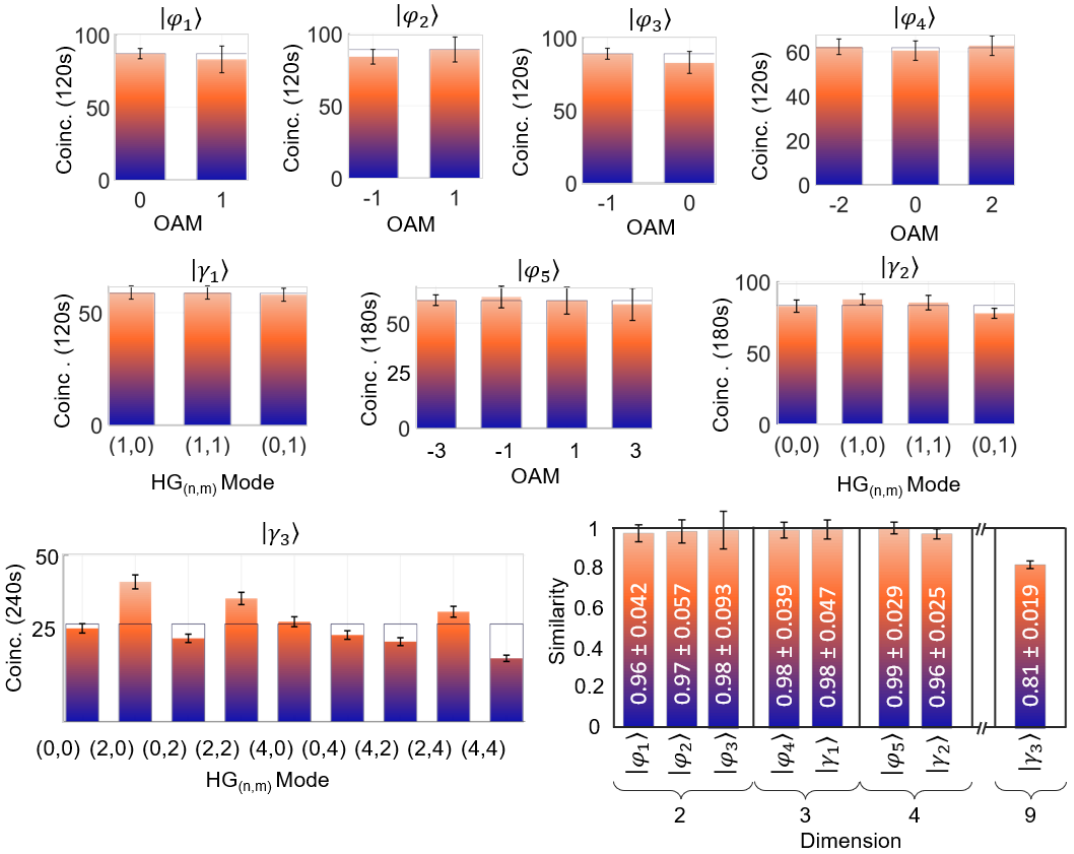


FIGURE 3.9: **Summary of teleported states**. Similarities for teleportation of a 2,3,4 and 9-dimensional superposition states in the OAM (represented as $|\varphi\rangle$) and HG (represented as $|\gamma\rangle$) bases shown and labelled to the left. Raw data are reported without noise suppression or background subtraction Teleported states are $|\varphi_1\rangle = |0\rangle + |1\rangle$, $|\varphi_2\rangle = |-1\rangle + |1\rangle$, $|\varphi_3\rangle = |0\rangle + |-1\rangle$, $|\varphi_4\rangle = |-2\rangle + |0\rangle + |2\rangle$, $|\gamma_1\rangle = |HG_{1,0}\rangle + |HG_{1,1}\rangle + |HG_{0,1}\rangle$, $|\varphi_5\rangle = |-3\rangle - i|-1\rangle + |1\rangle + i|3\rangle$, $|\gamma_2\rangle = |HG_{0,0}\rangle + |HG_{1,0}\rangle + |HG_{1,1}\rangle + |HG_{0,1}\rangle$ and $|\gamma_3\rangle = |HG_{0,0}\rangle + |HG_{2,0}\rangle + |HG_{0,2}\rangle + |HG_{2,2}\rangle + |HG_{4,0}\rangle + |HG_{0,4}\rangle + |HG_{4,2}\rangle + |HG_{2,4}\rangle + |HG_{4,4}\rangle$. Error bars given are from multiple measurements

3.2.7 Challenges and errors

A feature of this demonstration involved optimisation of the experimental parameters to allow for accessing higher dimensions, while maintaining enough signal for

detection and minimising noise contributions. Accordingly, the experimental constraints in the system can be categorised into sources of noise, sources of experimental error and limitations imposed by the experimental parameters.

Limitations imposed by experimental parameters. As eluded to with the numerical simulation of parameters in Section 3.1.3, an interplay between the detection and pump waists changes the dimensionality accessible in our system. A byproduct of altering these sizes for higher dimensionality is the reduction in the efficiency at which the lower-order modes are detected. This factor is illustrated in Fig. 3.10. Here, the relative detection efficiency of the lowest order mode ($\ell = 0$) is shown for the parameter space that was used to optimise the dimensionality. It follows that an increase in dimensionality, as indicated by the demonstrated parameter points (c)-(e) from Fig. 3.4, results in a notable decrease in the simulated efficiency is seen. This is then further reflected experimentally in the spiral bandwidths where the coincidences dropped significantly with the dimensionality increase.

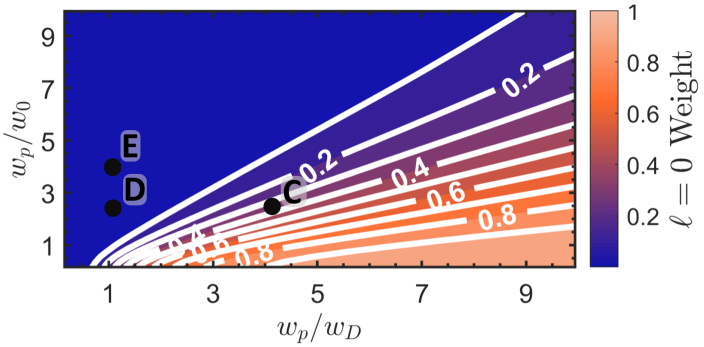


FIGURE 3.10: **Modal detection efficiencies with experimental parameters.** Numerical simulation of the change in detection efficiency for $\ell = 0$ as the experimental parameters are optimised for higher dimensionality. Points C-E indicated correspond to experimental parameters tested in Fig. 3.4.

This inverse relation between accessing larger dimensions at the expense of lower order mode detection efficiency can be understood as the result of mismatching the lower order spatial mode sizes in favour of the higher-order spatial mode sizes. This occurring both in the up-conversion crystal between the SPDC (photon C) and structured pump (photon A) as well as the relative detection sizes of the single mode fibres in either arm (detection of photons B and D). This interplay between accessible dimensionality and detection sizes is reminiscent of the factors covered in Sections 2.2.4 and 2.3 when considering similar detection of the direct SPDC modes generated in quantum entanglement sources such as ours and, as such, readily extends to this system.

Sources of noise. A notable source of noise in the production of entangled photon pairs by pumping a crystal is the generation of additional pairs within the same coincidence window [282–284]. This results in impurity in the detected coincidences as they form a statistical mixture rather than a pure source in which to utilise [285]. As a result, the event of generating multiple bi-photons serves to reduce the fidelity of the entanglement resource and thus the teleported states. Several works have been published in an active effort to solve this [286–288], however this involves generally complex configurations. The straightforward approach to mitigating the additional bi-photon generation events is reduction in the intensity at which the crystal is pumped. While this reduces the efficiency at which the desired single bi-photons are produced, a much larger reduction in the multiple bi-photon probabilities serves

to increase the fidelity. It follows that the experiment was carried out at the lowest possible SPDC pump powers (∼1.2 W) in order to mitigate this while maintaining enough signal for detection in arm D, given the maximum SFG pump power allowed by the damage threshold in SLM_A.

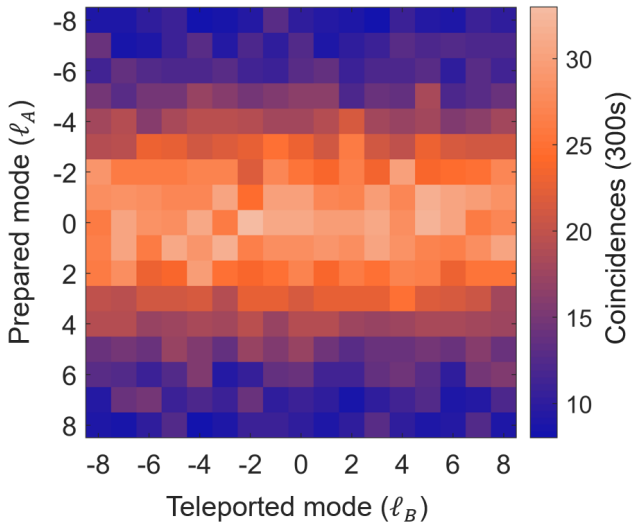


FIGURE 3.11: **Mode dependent detected noise.** Spiral bandwidth plot spanning $\ell = [-8, 8]$ showing the measured background noise indicating higher noise for lower order modes.

Here, the detected background counts in the up-conversion arm becomes notable so as to maintain higher purities so that higher fidelity teleportation may be achieved. For instance, the signal to noise ratio for the $\ell = 0$ teleported mode in the high-dimensional optimised setup was $\sim$ 500 cps upconverted single photons (signal) to $\sim$ 360 cps noise (upconversion was blocked). The sources of background counts were due to the dark counts from the detector itself as well as unavoidable stray pump light propagating towards the detector. As a result, this signal to noise ratio has a notable impact on the detected results due to increased accidentals [67, 289].

A large mismatch in counts between the two detectors is also a direct result of the low up-conversion efficiency currently associated with non-linear processes. As such, a large number of SPDC photons is detected by Bob whereas a much lower number of SPDC photons are up-converted and consequently detected by Alice. This mismatch means the probability of detecting accidental coincidence counts is higher than if the signals were similar (as in a linear scheme). Here accidentals refer to the event of erroneously detecting a coincidence due to two uncorrelated photons arriving at both detectors at the same time. The number of accidentals (C_{Acc}) expected may be calculated using $C_{Acc} = S_A S_B W$ where S_A (S_B) are the counts detected in Alice's (Bob's) arm and W is the time window in which coincidences are collected. The number of accidentals thus increases directly with the mismatch in counts as the number of possible coincidences is limited by the lowest signal detected. Subsequently, this varies with the detection efficiency (discussed above) and has an inverse relationship with the dimensionality of the system. For instance, a mismatch of $\sim$ 500 counts per second (cps) in the up-conversion arm compared to $\sim$ 650 000 cps in Bob's arm yields a 1300 times increase in the predicted number of accidentals when our system is optimised for high dimensions as opposed to unitary up-conversion efficiency. This was mitigated by narrowing the coincidence detection window (W).

Another factor for consideration is the use of a strong laser pump in the up-conversion process. It has been well documented that additional processes occur with the use of a strong pump due to the high number of input photons [161, 290, 291]. While choice of a long-wavelength pump relative to the signal wavelength helps suppress the spontaneous Raman scattering contributing to this [291–293], factors still remain for consideration. Here the third harmonic of 1565 nm lies around 522 nm and the additional up-conversion of SPDC flourescence as well as the secondary lobes in the SPDC sinc relation with the bandwidth generated would all result in the detection of noise photons that decrease the fidelity of the teleported state. Here we employ the use of a narrow-band band-pass filter centred at 532 nm with an acceptance range of ± 3 nm at full width at half maximum (FWHM) before the up-conversion detector, in order to mitigate this effect.

Consequently, it may be noted that due to the presence of mode-dependent detection efficiency, a mode-dependence in the noise detected is present for the teleported states. This is shown in Fig. 3.11 where background noise detected outside of the coincidence window (as shown in Appendix B.3) is shown for a typical spiral bandwidth. The teleported modes ranged from $\ell = -8$ to 8 and were scanned for in the same range. A larger noise contribution is shown here for the lower order teleported modes which then falls off as the modal order increases.

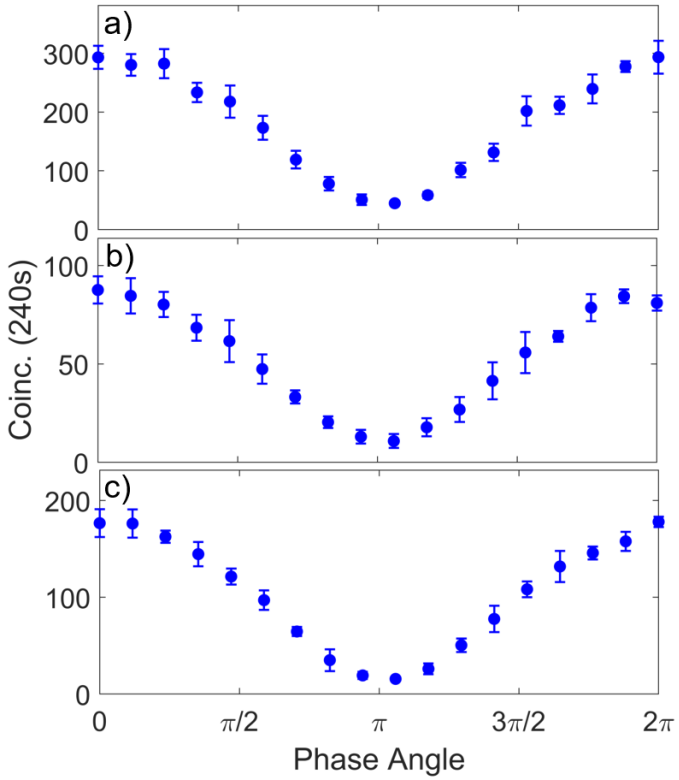


FIGURE 3.12: **Visibilities with detection parameters.** Experimental visibility curves obtained by rotating $\theta = [0, 2\pi]$ in the detection mode $(|-1\rangle + e^{i\theta}|1\rangle)$ for teleported state $|\psi\rangle = |-1\rangle + |1\rangle$ for (a) 1 μs deadtime and 1.5 ns coincidence window, (b) 5 μs deadtime and 1.5 ns coincidence window as well as (c) 1 μs deadtime and 0.5 ns coincidence window. Error bars given are from multiple measurements.

Furthermore, due to the properties of InGaAs-based SPAD detectors used in the detection of 1565 nm light, a lower efficiency, longer deadtime and more afterpulsing compared to Si-based SPADs for visible photon detection contributes to the noise seen. Here, deadtime refers to the amount of time where no photons can be detected

after a previous detection event. The lower limit enabled by the detector is 1 µs compared to 22 ns for the visible detector. Afterpulsing refers to additional artificial detections when measuring counts and is an intrinsic property of the device due to trapped electron-hole pairs which causes new avalanches after an actual detection event [294, 295]. For our detector, an estimated afterpulsing probability of 5.2 % at 1 μs deadtime and 20% efficiency results in the detection of additional erroneous signal which relies on the amount of signal being seen. For intance 650000 counts results in close to 40000 incorrect counts. Increasing the deadtime of the detector decreases the afterpulsing probability and thus the noise, but then results in a lower rate of detection which can be seen as a decrease in the time-averaged overall detection efficiency with respect to the visible detector. Futhermore, inherent dark counts of the detector occurs due to electrons being set free from vibrational conditions induced by heat and thus generates an undesired avalanche (detection event), despite a temperature of -50 °C. This dark count induced noise is independent of the detection rate and sets a lower signal floor of approx. 2000 counts. The tradeoff between deadtime, number of detected coincidences with the InGaAs detector (IDQ220 free-running) and the effect of narrowing the coincidences detection window was analysed using the visibility curves, shown in Fig. 3.12 and Table 3.2, for the teleported $\ell = \pm 1$ state.

Fig 3.12	Coinc. Window	Deadtime	Visibility	Max. Coinc.
(a)	1.5 ns	1 μs	0.74 $\pm$0.10	293 $\pm$27.9
(b)	1.5 ns	5 μs	0.78 $\pm$0.10	87.6 $\pm$6.9
(c)	0.5 ns	1 μs	0.84 $\pm$0.10	178 $\pm$5.4

TABLE 3.2: **Visibilities for different parameters.** Comparison of the visibility and maximum detected coincidences with different detector deadtimes and coincidence windows for results obtained by rotating $\theta = [0, 2\pi]$ in the detection mode $(|-1\rangle + e^{i\theta}|1\rangle)$ for teleported state $|\psi\rangle = |-1\rangle + |1\rangle$. Uncertainties are calculated from multiple measurements

An increase in the deadtime from 1 µs to 5 µs, shown in the comparison between Fig 3.12 (a) and (b), increased the visibility by 4% as a lower noise contribution was occurring from the InGaAs detector. This, however, also resulted in only a third of the coincidences being retained in the adjustment as a result of a reduction in the efficiency rate. Conversely, when reducing the coincidence detection window from 1.5 ns to 0.5 ns, a much larger increase of 10% in the visibility was seen with more of the signal being retained (2/3 of the signal in (a)). Such an increase in the visibility can be readily explained as the 'lost' coincidences were the result of reducing the acceptance of additional pairs, spectral spread correlations in time and the probability of measuring accidentals. As such, the photons reducing the fidelity of the teleported state were excluded as opposed to simply reducing the efficiency in order to reduce the number of erroneous detection event due to properties of the detector. Accordingly, the increased signal offset the small loss in visibility for the deadtime, making the 1 μs the optimal parameter, while the reduction in signal for increased visibility with the lower coincidence window resulted in the 0.5 ns being the optimal measurement setting.

Sources of experimental error. Aberrations due to imaging the beam tightly into the crystal, propagating the beam through several imaging systems and crystal inhomogeneity serve to induce errors in the purity of the modes being teleported. Here, higher order modes are also subject to aperture effects in the optical system and due faster expansion upon propagation, 'see' a greater area of the optical components. As such, they encounter more aberrations as propagated throughout the

system. Temperature fluctuations due to external temperature variations also cause variations in the alignment, while an air-conditioner is used to try mitigate the effects. The experiment spans a 2 × 1 m optical table and as such air fluctuations from the air-conditioner cause beam wander and thus increases fluctuations in the measured coincidences. Isolation of the experiment with a curtain was used to mitigate this along with longer integration times combined with averaging over several measurements.

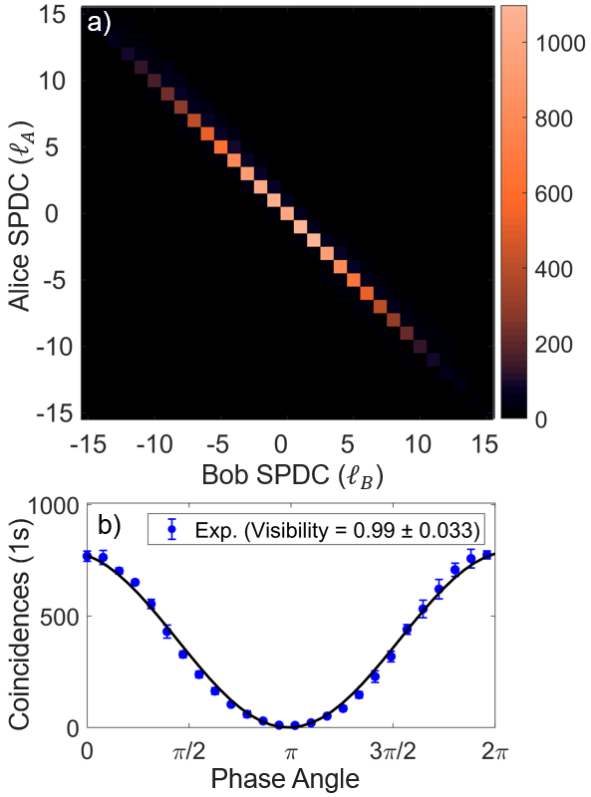


FIGURE 3.13: **Channel SPDC characterisation.** Experimental (a) spiral bandwidth of the channel SPDC and (b) visibility curve obtained by rotating phase angle, $\theta = [0, 2\pi]$, in the detection mode ($|-1\rangle + e^{i\theta}|1\rangle$) in Bob's arm for the state $|\psi\rangle = |-1\rangle + |1\rangle$ in the arm used for teleportation. No noise subtraction or error correction was performed on the data. Error bars given are from multiple measurements

Quality of the entanglement channel. The channel SPDC was also briefly measured and analysed for the optimised channel which yielded a teleportation of capacity of $K \approx 15$. This was done in terms of an initial spiral bandwidth and then a comparative visibility curve for the qubit state $|\psi\rangle = |-1\rangle + |1\rangle$ projected onto in the teleportation arm. Fig. 3.13 shows the experimental results with the bandwidth in (a) giving a Schmidt number of $K_{SPDC} = 17.9$ and visibility curve in (b) giving a visibility of 0.99 ± 0.033. It follows that we find the SPDC channel capacity larger than the teleported capacity ($K_{SPDC} \approx 18$ compared to $K_{Tele} \approx 15$), but within a similar range. This may be attributed to the inefficiency of the teleportation process where lower weightings for the larger order modes caused these to fall below the efficiency required for up-conversion. The Gaussian fall-off of the weightings for the higher-order modes seen here are also reflected in the bandwidth taken for the teleportation channel. Furthermore, the SPDC visibility for the $|-1\rangle + |1\rangle$ state shows a very high visibility of 0.99 ± 0.033, indicating a high fidelity. In comparison to the curve measured in Fig. 3.7, we find the visibility comparable to that of the

background subtracted value (0.96 ± 0.044), showing the measured noise in the system (as described previously) a significant contributor to the loss in fidelity of the teleported states.

As a large contribution of the noise factors are due to the use of strong pumps and mismatch in detected counts, it follows that the values shown for the system form a lower bound in the potential performance. Here, improvement in the up-conversion efficiency would serve to decrease the mismatch in counts, increase the signal which results in a lowering of the input coherent state power as well as the SPDC pump power and decrease the barrier for up-conversion of more higher order modes.

3.2.8 Looking forward: From stimulated to quantum teleportation

We may estimate the upconversion efficiency in our system by considering Eq. 2.28 in Section 2.4 for $\lambda > 1\mu$m. Here the parameter indices remain similar with a strong pump (A), single photon input (B), leading to the upconverted photon where D replaces C. In our case, we expect the reduction factor to be small ($h_m \approx 0.06$), due to the poor ratio between the crystal length and confocal parameter. This, additionally, considering the mode mismatch between the SFG pump beam waist ($w_A \sim 100$ μm for the $\ell = 0$ case) and the input photon C (with a similar beam waist as the Gaussian beam pumping the SPDC process: $w_p \sim 300$ μm). For a type-0 periodically poled KTP crystal, $d_{eff} = \frac{2}{\pi} d_{33} \approx 10$ pm/V [296] (the $2/\pi$ factor is required when considering quasi phase-matching). Hence, we can up-convert the photon C into photon D with an efficiency of $\eta_{SFG} = 0.3\%$, considering that we pump with $P_A =$ 3.5 W of optical power, the two input modes are Gaussian modes and we do not consider the losses in the system.

It follows that a bright coherent state produced by a laser is required in order to enhance the up-conversion efficiency of the nonlinear crystal and make the teleportation practical. The outcomes, however, are conditioned on biphoton coincidences. An intrinsic characteristic of the state transfer process with a bright coherent state is that the sender does not need to know the quantum state to be teleported, a feature that differentiates quantum teleportation from remote state preparation [297]. In this sense, the input coherent state and the output single photon state can be considered as *carriers* of spatial information, which is the resource being teleported. That is to say, the approach we present is a technical solution to a technological limitation, and despite encoding the quantum state in many copies, our scheme requires the same ingredients of the quantum teleportation protocols to teleport such spatial information. For this reason we propose this approach as a *stimulated* teleportation process whereby the additional photons from the coherent state simply serve to stimulate the upconversion process.

The experimental setup was designed so we could use the commercial crystal with the highest nonlinear coefficient, considering also a big enough aperture to enlarge the teleportation channel capacity, i.e., PPKTP crystal for a type-0 three wave mixing processes. Furthermore, lasers working in the CW regime facilitates the concentration of all quantum information in the desired spectral range, while distributing the coincidence events along the whole temporal span being able to reduce the multi-photon accidental events (noise). Despite these advantages, we still need to encode the teleportee spatial state in $\sim 10^{10}$ photons (3.5 W at 1565 nm) to achieve an up-conversion efficiency of 0.3 % for the optimum $\ell = 0$ case. However, we expect that this experimental challenge will stimulate further improvements in the

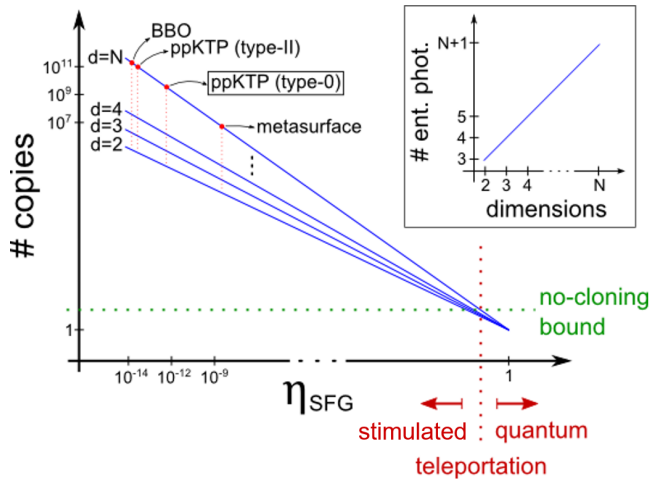


FIGURE 3.14: **Nonlinear efficiency vs quantumness of the teleportation**. Conceptual plot showing the convergence of the number of copies carrying the d-dimensional teleportee state as the SFG is increased. Red dots help to identify the different examples of commercial nonlinear crystals (ppKTP type-0 being our case), and the *all-dielectric* metasurface of Ref. [298] with a notably increased nonlinear coefficient. The plot in the inset shows an example of the amount of extra ancillary photons required to teleport the same d-dimensional teleportee state using linear optics.

field of nonlinear optics rather than placing an upper limit on efficiency in similar future schemes.

Figure 3.14 presents an intuitive road map towards the perfect quantum teleportation using nonlinear detection systems, taking into account the inevitable improvement of the up-conversion efficiencies in the short future. Recent advances in metasurfaces and metamaterials with nonlinear response [298], for example, could see physical crystals replaced with these *all-dielectric* meta-optical solutions for even greater efficiency gains (more than 3 orders of magnitude higher than commercial nonlinear crystals). Here we refer to the number of copies as the number of photons per coincidence window, carrying the information of the teleportee quantum state which is required to obtain a teleportation fidelity above the classical limit. In the case of raw up-conversion efficiencies, without any losses in the transmission and detection sections, the no-cloning bound (green dashed horizontal line) will depend on the system's overall noise. This will dictate what will be the nonlinear efficiency for which we can ensure that the sender cannot keep a better copy than the teleported one and define the conceptual separation between stimulated and quantum teleportation (red dashed vertical line). It is important to note that the number of copies needed to successfully teleport any arbitrarily high-dimensional quantum state, converges to 1 when the nonlinear efficiency is improved in our scheme. This is not the case when utilising linear optics detection systems, as conceptually plotted in the inset of Fig. 3.14, where the number of ancillary photons needed grows linearly with the number of dimensions to be teleported.

It is thus sufficed to say that 9 orders of magnitude improvement over current metasurface technologies is necessary in order to reach the no-cloning bound, making it a significant challenge for the present. This is not to say, however, that this is not without possibility, with already three orders of magnitude having been recently achieved.

3.3 Discussion and conclusion

Both linear and our nonlinear teleportation schemes require an entangled photon pair as a quantum resource, but linear optical approaches for qudit teleportation require ancillary photons in a manner that the experimental configuration is hard-coded for a particular channel's dimensionality, e.g., the present state-of-the-art ($d = 3$) is custom designed by a computer simulation [299]. These ancillary photons allow distinguishability for higher-dimensional Bell states with linear optical components to make the necessary Bell projections. The nonlinear approach we demonstrate uses the same experimental configuration, and only one entangled pair, for teleportation across multiple dimensions and across many spatial bases. In our stimulated teleportation process we exploit a bright coherent state produced by a laser as the input source in order to enhance the up-conversion efficiency of the nonlinear crystal, but with the outcomes still conditioned on biphoton coincidences. The low efficiency of the SFG process ($\eta_{\mathrm{SFG}} \approx 0.3\%$ for the $\ell = 0$ projection) is in part due to the large beam sizes for a good channel capacity and our continuous wave laser regime, which facilitates the concentration of all quantum information in the desired spectral range, while distributing the coincidence events along the whole temporal span being able to reduce the multiphoton accidental events. The teleportation efficiency is further decreased by the probability for a Bell projection, which is $1/d^2$, to an overall teleportation efficiency of $\eta_t = \eta_{\mathrm{SFG}}/d^2$, the fraction of Bob's photons that can be found to carry the teleported spatial mode.

However, both limiting factors might be increased. There is experimental indication that η_{SFG} can be improved by orders of magnitude by using artificial nonlinear media such as metasurfaces and metamaterials [298], and can in principle reach unity. The limiting factor $1/d^2$ is due to the probabilistic projection into one of the Bell states, but our scheme has the potential to be made deterministic by using mode sorters [300] rather than filters in the up-conversion detection arm. Alternatively, a complete Bell measurement can be designed that distinguishes the upconverted Bell states by employing a mode sorter along with a consecutive transformation of the remaining Bell states not upconverted because of destructive interference; this by relative phase shifts onto the former ones and detecting them. Both possibilities to eliminate the limiting factor $1/d^2$ are promising, but would need further investigation, which is beyond the scope of this paper. Comparatively, deterministic linear Bell schemes have been proposed [301–306], which mostly relies on the use of auxiliary degrees of freedom through hyper-entanglement to distinguish the Bell states. So far, only two-dimensional experiments [302, 303] have been realised with the extension to arbitrary higher-dimensions being a recent theoretical endeavour [305, 306]. As the auxiliary resource lies in the degree of freedom, the scaling occurs in the optics rather than photons. For instance, a recent proposal suggests the use of quantum fourier transform [307], which, requires $\sim d\log_2(d)$ beamsplitters scaling for OAM [307], making this quite impractical. In contrast, the use of a mode sorter would be only one optical element that, in principal, need not change with the dimension.

So, while the need for *ancillary* photons is fundamental to linear optical solutions in teleportation, the need for *additional* photons in the nonlinear case is a technological need because of present low efficiency, and is surely to improve in the future. The efficiency can in theory reach unity, bringing d-dimensional teleportation to an efficiency dictated by the creation of the required entangled pair, $\gamma \approx 10^{-10}$ for SPDC. In contrast, the existing linear optical teleportation roadmap has the intrinsic efficiency limit that scales exponentially with dimension, e.g. $\gamma^{(d-1)/2}$ if SPDC is used

to create the required photons, hence a much higher penalty for source inefficiency.

Alternatively, one may consider the performance of our system relative to other related nonlinear analysers. Here, a complete bell state analyser was achieved for polarisation states [43] with an efficiency of 0.1%-1% for a similar input of $\sim 10^{10}$ photons. This scheme and demonstration, however, was confined to the two dimensions given by the polarisation degree of freedom. Another, alternate scheme in [308], the proposed a nonlinear interaction for entanglement swapping with time-bin encoding. Here, the experiment was proof of principle considering only the efficiencies of upconversion. Here they measured a value of 1.16×10^{-6}%, considering photon-level inputs and a non-linear waveguide for upconversion, which was just shy of the required 1.4×10^{-6}% to achieve the success probability of 3×10^{-10}% for four-fold coincidence detection with 90% fidelity necessary. Other potential nonlinear waveguides were suggested to improve this, however, indicating it could be possible to achieve the swapping in the near future.

The original formulation of quantum teleportation considered the teleportation of the polarization state between two single-photon quantum systems. However, in a general teleportation scheme the input and output states might be different systems. What is teleported is the relevant information of a quantum state, encoded into another quantum state, but not the whole of characteristics that define the quantum states. This is the case, for instance, for the teleportation between quantum states of light and matter, where a quantum state encoded in a light pulse can be teleported onto a macroscopic object, i.e., an atomic ensemble containing 10^{12} caesium atoms [15]. What constitutes the core of teleportation is the capacity to teleport *unknown* information of a quantum system to another system, assisted by entanglement and classical communication. The fact that the teleportation protocol should work for *arbitrary states*, differentiating it teleportation from remote state preparation.

The merits of using this protocol may additionally be noted over that of straightforwardly sending the information between the parties as there exists multiple copies at present. Converse to the latter idea, here entangled photons are shared before the information is transmitted and are quantum in nature. This, in principle, results in two-fold consequences. Firstly, this opens the possibility of realising a secure channel over which the information can be sent i.e. provided the sender is trusted, eavesdropping outside of the sender could be prevented. Secondly, it may be possible to use this pre-sharing to correct for errors due to the environmental effects in the path traversed between the communicating parties before or as the information is teleported [309]. Lastly, one may consider the fact that the many copies on this classical carrier of the information one wishes to transmit is then, in addition sent to another location, becomes the state of a quantum carrier and thus facilitates a change in the nature of the entity being used to contain the information.

In conclusion, we have demonstrated the teleportation of spatial information in a channel with a tuneable dimensionality and encoding basis. Our results validate the non-classical nature of the channel without any noise suppression or background subtraction. Importantly, our comprehensive theoretical treatment outlines the tuneable parameters that determine the modal capacity of the teleportation channel, such as modal sizes at the SPDC crystal and detectors, requiring only minor experimental adjustments (for example, the focal length of the lenses). The 15-dimensional channel for the OAM and HG modes highlights the exciting prospect this approach holds for the teleportation of unknown high-dimensional spatial states. The modal capacity of our channel was limited only by experimental resources, while future research could target an increase of the number of teleported modes by optimising

the choice of the relevant parameters, improving nonlinear processes, and flattening the Schmidt spectrum of the entangled two-photon state. Our proof-of-principle experiment sets a new state-of-the-art and offers a new roadmap towards versatile teleportation solutions based on nonlinear optics.

Chapter 4

Application, future work and conclusions

Having established and characterised our high-dimensional teleportation system, we consider potential applications and extensions of the system in this Chapter. More specifically, the application of our teleportation system to that of complex images is explored in more detail and a method developed to measure the success based on single-pixel ghost imaging. Afterwards, we briefly outline potential avenues forward in this projects from improving the system to extending it towards additional degrees of freedom. Finally, we conclude on this work and the potential impact.

4.1 Towards teleporting phase objects

In this section, we look towards applying the teleportation system to applications such as teleporting the states of complex objects. This has the potential to hold interest as it may be used to convey object-related information such as a measured fingerprint or biological samples directly, instead of encoding it in another less convenient basis such as OAM. Additionally, in the current scheme, it allows one to duly transfer the information of such a classically probed object to a quantum carrier (photon), thus directly imprinting classically obtained information which could then be taken advantage of for quantum-based information processing in the future [310–312], where the cost preparing quantum images from classical data is a necessary consideration [312–315]. This is in addition to having it conveyed to another desired location. Similar to the discussion on the current merits of stimulated teleportation, while the nature of the carrier is classical and thus not necessarily secure at that point of the protocol, the nature of the entanglement link is quantum mechanical and thus has the potential for security against an eavesdropper between the communication parties. Looking to the future, in the event SFG efficiencies are increased through technological advancement, it would then also make it possible to directly transfer the information relating to samples being imaged quantum mechanically. As such, in addition to being able to use less-destructive illumination levels [316, 317], one is able to also convey this more securely. In order to consider such an application, we first look at taking the teleportation setup where it was used for teleporting different modes derived from the paraxial wave equation and now consider using it for the teleportation of pixel quantum images. In this sense, we want to teleport and detect images made from discretised position states that have both phase and amplitude information. In order to do so, we numerically simulate the system capacity in a similar fashion to what was done for the OAM states. Experimentally however, this approach results in decreased efficiency as a result of decreased power

in the input beam as well as decreased detection signal which scales unfavourably with increasing resolution. Furthermore, this does not directly allow for the detection of encoded phase values. We then borrow from the ghost imaging approach, developed for single-pixel imaging with photons, and develop a technique which allows the phase information to be retrieved. By exploiting two-dimensional spatial scanning masks here, there is an intrinsic preservation of signal in the detection step which scales more favourably with increasing resolution [318].

4.1.1 Numerical simulation

First, we consider the generation of single-pixel states which takes the same form used in Refs [111, 131, 319] and as described in Section 1.4.3. Accordingly, the SPDC distribution is divided into discrete regions of space with each region forming a basis state or pixel. This forms an entangled basis as the generated position correlations [320] between the entangled photons form position correlations. The states here are modelled by

$$|j\rangle = \int G(\mathbf{q}; w) M_j^{d^2}(w) \, |\mathbf{q}\rangle \, dq^2; \tag{4.1}$$

where $G(\mathbf{q}; w)$ retains its Gaussian definition, representing either the distribution from the generation beam or detection SMF. $M_j^{d^2}(w)$ represents the j^{th} pixel in the basis where d^2 is the chosen dimension and thus image resolution and is similarly scaled with the Gaussian parameter. Here, we consider the simplest case where the pixels are given by a $d \times d$ grid of square 'macro-pixels', although different distributions are possible [91]. It then follows that the spatial modes representing the pump photon A and SPDC photon B in Eq. 3.25 and 3.24, respectively, will now be specified as $|\Phi_B\rangle, |\Theta_A\rangle \in \{|j\rangle, j \in \mathbb{N}\}$. Similarly, the conditional probabilities of detecting mode $|j\rangle_B$ when sending $|j\rangle_A$ into the teleportation system is determined from the overlap of these pixel states with the teleportation channel operator,

$$P(\alpha)_{j_B, j_A} = |\langle j_B| \hat{T} |j_A\rangle|^2, \tag{4.2}$$

where $\alpha = w_p / w_0$ remains the scaling parameter for the pump and detection sizes.

Figure 4.1 shows the numerically obtained results for a fixed $\beta = 1$ and variations in the α parameter for $d = 5$, corresponding to 25-dimensional basis. Two conditional detection pixel spectra are shown in (a) and (b) for $\alpha = 1$ and $\alpha = 10$, respectively. A clear diagonal ($j_A = j_B$) with null non-diagonal entries indicates teleportation and detection of the correct states, similar to the modal cases in Chapter 3. Converse to Fig. **??**, the spectra shown here does not fall-off from the centre. This is due to the raster scanning approach used where the pixels progress from the top-right most pixel and follows a row-by-row scan until the end of the grid is reached as shown in the top right inset of (a). From the Gaussian distributions of the generation or detection distributions, larger coefficients are found at periodicities that relate to positions near the central regions of the grid. An asymmetry in the periodic distribution may additionally be noted due to an artefact of the numerical simulation where pixels resizing resulted in slight shifting of the pixel distributions. Changing α to a larger value in this case results in a larger number of non-zero diagonal values, which is indicative of a higher dimensional capacity. This can also be seen in (c) where the diagonal is plotted against α and increasing α beyond 1, yields more non-zero entries in the spectrum. Interestingly, values of $\alpha < 1$ also gives a larger dimensionality, which was not seen for OAM.

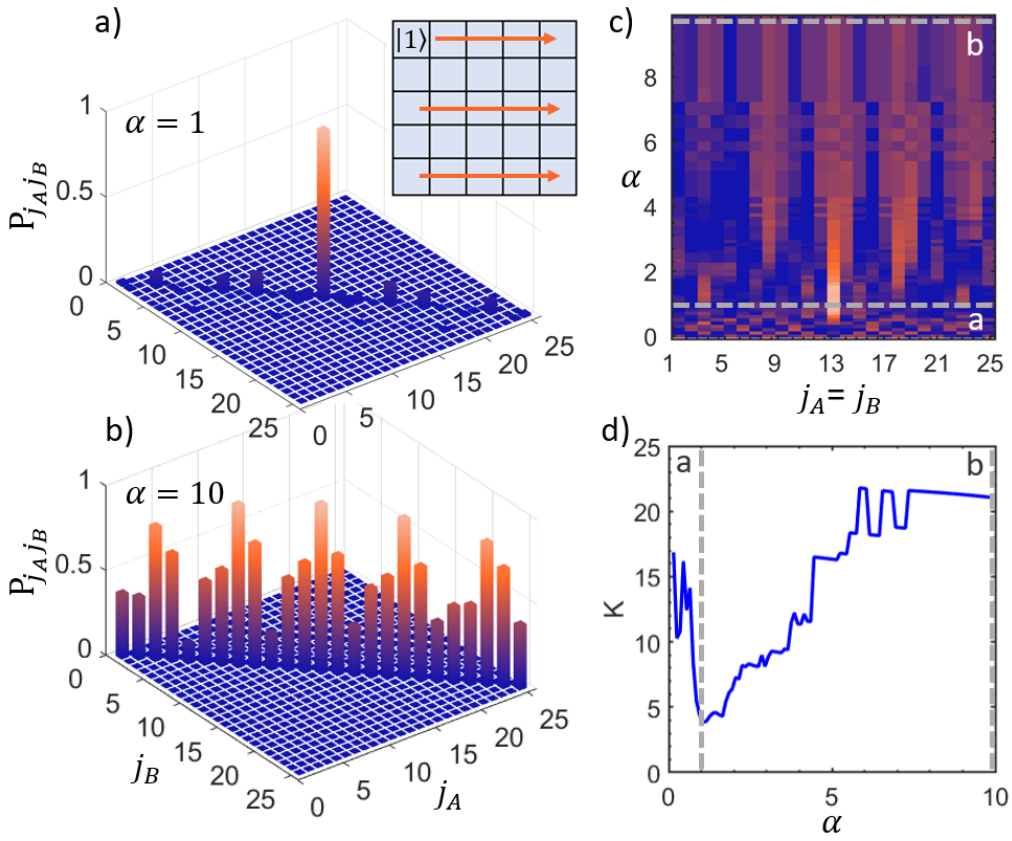


FIGURE 4.1: **Simulated pixel bandwidths and dimensionalities from measurements of photon B relating to encoded states of photon A.** Example renormalised teleported pixel bandwidths for a 5×5 discretised position space when (a) $\alpha = w_p/w_0 = 1$ and (b) $\alpha = 10$, using a fixed $\beta = w_p/w_D = 1$. These are marked as dashed lines in a wider (c) density plot of the spiral spectrum diagonal ($j_A = j_B$) as a function of α and (d) the calculated dimensionality (K), measured from the Schmidt number as a function of α. The pixel order in the space is indicated in the top-right inset of (a).

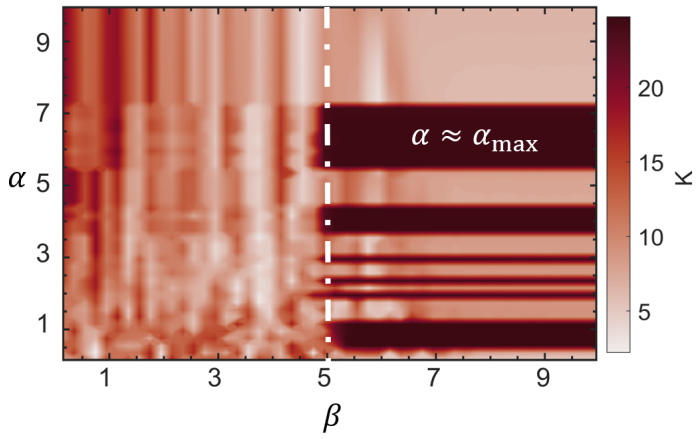


FIGURE 4.2: **Generalised pixel teleportation channel capacity analysis.** Contour plot of the dimensionality (K) as a function of β and α. For higher dimensionality we need a larger $\beta > 5$ and large α. The white dash line corresponds to the general value of $\beta = 5$, which indicates parameter values in which close to maximal dimensionality ($K = 25$) is achievable.

Additionally, we use the Schmidt number measure,

$$K(\alpha) = \frac{1}{\sum_j P_j^2(\alpha)}, \tag{4.3}$$

to indicate the measurable teleportation capacity and thus dimensionality of our system for pixel states. The numerical simulated outcomes for this is given in Fig. 4.1 (d) with the minimum observed for $\alpha = 1$ appearing in the analysis. It can also be seen that while the dimensionality increases for $\alpha < 1$, it does not reach as high a capacity as obtained with larger α.

The effect of varying β and α may now be explored. In this case, a deviation from the OAM case is evident. Here, maximal dimensionality also requires a large β where > 5 allows one to achieve the maximal teleportation capacity of $K = 25$ for the chosen 5×5 pixel grid. In this case, particular ranges for α here that does not necessarily require high values e.g. $5 < \alpha < 7$. For $\beta < 5$, greater dimensionality is achievable mostly when both β is made very small and α very large, similar to what was found for OAM. Here, however, the maximum dimensionality for the chosen pixel grid is not achievable with $K \approx 22$.

It follows that adjustments of the detection sizes where a smaller value is used for the upconverted beam size may result in optimal tuning in the pixel basis. A particular issue to consider in the use of single pixels is that the unit basis state divides the input power by as many times as there are states in the system, contrary to that of the modal states used in Chapter 3. As a result, the upconversion efficiency is also divided, which would make it more difficult to obtain sufficient signal-to-noise levels. The more states being sent, however, the larger the upconversion efficiency as a whole here. Another approach is to consider the teleportation of complex objects as a whole and how one may confirm their teleportation by detection. Single pixel scanning, used in this numerical simulation, results in a significant drop in detection signal. This renders the current approach increasingly difficult as resolution is increased, making the pixel size smaller. Additionally, there is limited effectiveness in discriminating the phase of the object being interrogated, discerning 0 to π steps only [321]. As a result, we instead develop an easily integrate-able technique that borrows from the single-pixel ghost imaging toolbox in order to address these two

issues in the next section.

4.1.2 Retrieving phase images

This section is based on the paper:
Bereneice Sephton, Isaac Nape, Chané Moodley, Jason Francis and Andrew Forbes, "Revealing the embedded phase in single pixel quantum ghost imaging," Optica, 10, 286-291 (2023)
B. Sephton performed the experiment as well as contributed to data analysis and writing of the manuscript.

Much of the imaging capacity is lost if only amplitude images can be teleported. In fact, when we mention quantum images here, we borrow from the general term to mean the information of the images being obtained contain both phase and amplitude information. Currently the following techniques allow single pixel detection of amplitude. To do so, we borrow from quantum ghost imaging. In quantum ghost imaging, one photon from an entangled pair interacts with the object and is bucket-detected (no spatial resolution) while the other non-interacting photon is directed to a spatially resolved imaging detector [322, 323]. While neither photon alone has information of the object, an image can be formed by measuring the mutual correlations through coincidences. Initially ascribed to the quantum entanglement of photons [324, 325], it has since been shown that ghost imaging is possible using classical correlations too [326, 327]. Ghost imaging has seen significant growth in the past two decades [316, 328–330], with the promise of enhanced resolution [331, 332], and expanding their application to the imaging of photosensitive objects by lower photon fluxes [333, 334], as well as extending into the x-ray [335, 336] and electron wavelength spectrum [337, 338]. Imaging quality has steadily improved while acquisition times have steadily decreased, fueled by advances in computational [339, 340], compressive sensing [341, 342] and deep learning based methods [318, 343–347]. Quantum imaging offers the advantage of low photon levels, typical to quantum experiments, that permit imaging of light-sensitive structures thereby avoiding photo-damage [316]. Additionally, a distinct embodiment of quantum ghost imaging offers special performance where it is possible to produce non-degenerate signal and idler photons. The object is probed or illuminated with one wavelength while the spatial information is recorded at another wavelength where the imaging detector is less noisy, more sensitive or cost effective [333].

Quantum ghost imaging has traditionally been used to image amplitude objects, first with two-dimensional spatial projective masks such as Hadamard [348] and random [339], and more recently with advanced camera systems. Despite these advances, optical phase imaging has progressed much slower, and is a non-trivial experimental task with limited advances to date. Applications, however, range from biological [334, 349] to materials [350, 351] and extend into communications with quantum images [352]. Such phase imaging to date has been achieved with enhanced phase contrast [353], interferometric approaches [354, 355], more recently using quantum-correlation enabled Fourier ptychography [356] and polarisation enabled holography [357] all using modern cameras. While these techniques can produce a range of desired results, they have some shortcomings: the phase contrast imaging techniques return partial information and so only work well for objects with binary phases, the ptychography and interferometric approaches are alignment intensive, prone to instability, and are costly since single photon cameras are required.

A distinct consequence of the physical correlations produced in the single-pixel environment, however, has been overlooked. We develop, for the first time, a full theoretical treatment of the correlation measurements and projections in the two-dimensional spatial scanning technique. As a result, we reveal compelling physics, showing the traditional construction approaches using two-dimensional masks such as the Hadamard yields a natural projection that produces phase information for free. By intelligently altering this construction, we develop a novel method, showing that the full complex amplitude image can be reconstructed where only one additional measurement per scanning mask is required. Moreover, we demonstrate that this physical principle need not be confined to one basis set of these two-dimensional masks, illustrating the same for random masks as well. In doing so, we bypass the need for physical interferometry which is notoriously unstable and complex to align, replacing this with digital masks that can instead be encoded on inexpensive spatial light modulators. Advantageously, this is easy to align in quantum experiments and readily available in most optical labs, making our approach convenient and simple. Subsequently, we both further develop the understanding of such scanning techniques and exploit it to obtain unambiguous full-phase and amplitude information. As a result, we show that conventional single-pixel ghost imaging setups are already able to see detailed phase objects without any physical adjustments and rather only an additional spatial mask projection which we readily derive from the masks already used. Incorporation into the vanilla single-pixel setups is thus trivial. The advantages of single-pixel imaging is also gained here where high resolution at low flux rates is possible and inexpensive non-resolvable detectors facilitating a large range of wavelengths extend this to scenarios not viable for the sensitive, high-resolution cameras. Furthermore it is important to note that the use of entangled photons paves the way for imaging biological samples as the lower photon levels, characteristic of quantum imaging, avoids photo-damage to light sensitive structures present in biological matter.

Method

To illustrate this, we implemented an all-digital ghost imaging setup with spatial masks generated on spatial light modulators (SLMs) as shown schematically in Fig. 4.3 (a). Light from a diode laser (wavelength λ = 405 nm and radius, w_p = 2 mm) was then used to pump a 2 mm long temperature controlled type I PPKTP non-linear crystal (NLC). From the SPDC parameters, we estimate the resolution of the system to have an upper bound of $\sim$ 487 pixels [331]. The temperature was set to optimally obtain collinear SPDC of entangled bi-photons at a wavelength of 810 nm. Any unconverted pump photons were then filtered out with a bandpass filter placed after the NLC. Next, the entangled photons were separated into two paths with a 50:50 beam splitter (BS) with the digital object encoded on an SLM in path A (object arm), projective digital masks for imaging, also written to a SLM, in path B (image arm) with a blazed grating on each SLM. The object and image photons were coupled into single mode fibres connected to avalanche photo-diodes (APDs) for detection in coincidence (C.C.). The SLMs and fibres were all positioned in the image plane of the crystal as indicated by dashed lines in the figure. We note that the pair rate of the quantum source is small and additional components such as SLMs and detectors in the single photon path reduces the overall number of photons to the detectors. Parameters such as extending the integration time until an adequate number of single photons are detected [358] and strong assumptions on the detector noise such

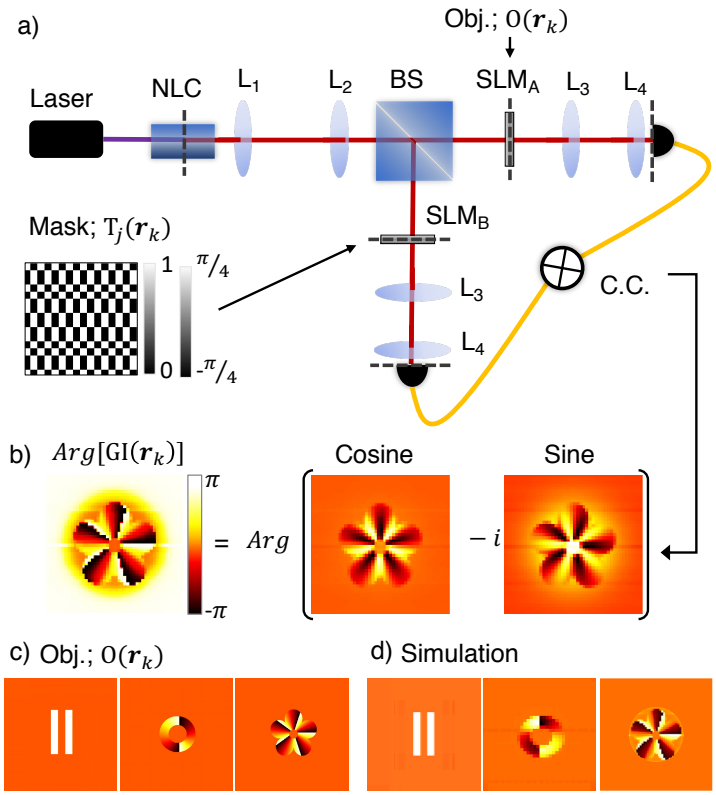


FIGURE 4.3: A schematic diagram of the implemented quantum ghost imaging setup. (a) Entangled bi-photons are produced via spontaneous parametric down-conversion (SPDC) at the NLC. The entangled photons are spatially separated and each imaged onto a SLM. Required holograms are displayed on each SLM. Coincidence measurements are done between both paths and the coincidences are used to reconstruct an image of the object. For each object two measurements are taken, as numerically simulated in (b). These two images are then combined such that the argument reveals the total phase. (c) Shows the digital phase-only objects used in the experiment, while the simulated image reconstructions are shown in (d) showing how the digital objects are expected to perform. L_1 = 50 mm, L_2 = 750 mm, L_3 = 750 mm, L_4 = 2 mm.

as background count subtraction [91] may be altered to mitigate this loss. An intensity flattening technique, as described in Ref. [91], may ensure precise projective measurements when measuring in the Fourier plane.

Here we elucidated the "hidden" phase features of the objects from correlation measurements between the photons in each arm. In the discrete position basis, $\{|\mathbf{r}_j\rangle\}$, the (entangled) bi-photon state have correlations described by the state

$$|\Phi\rangle = \frac{1}{N}\sum_{j=0}^{N-1} |\mathbf{r}_j\rangle_A |\mathbf{r}_j\rangle_B , \tag{4.4}$$

where N indicates the number of discrete position basis states that are correlated in the x or y coordinate. For most ghost imaging experiments, an object is decomposed using a complete set of projection states $|M_j\rangle$ or equivalently $\mathbf{M}_j$ in matrix form. We can thus describe the object in this basis following the decomposition

$$|O\rangle = \sum_{j=0}^{N-1} \sqrt{p_j} e^{i\alpha_j} |M_j\rangle . \tag{4.5}$$

Here p_j is the probability of projecting onto the basis state $|M_j\rangle$ and α_j are the corresponding phases. Furthermore, the spatial profile of the object is given by, $\langle \mathbf{r}_j|O\rangle = O(\mathbf{r}_j)$ corresponding to the complex matrix $\mathbf{O}$.

As an example, we will consider the basis modes constructed from the Walsh-Hadamard transform [359] with column vectors h_n. In matrix form, the projection states are $\mathbf{M}_{j\to(nm)} = h_n \otimes h_m$ which comprises arrays of ± 1 pixels (in and out of phase). After renormalisation following, $|T_j\rangle = 1/\sqrt{2}\left(|M_0\rangle + |M_j\rangle\right)$, where $\langle \mathbf{r}_j|M_0\rangle = 1/\sqrt{N}$, the final projection states correspond to matrices, $\mathbf{T}_j^{\cos}$, that have entries that are 0s and 1s.

Traditionally the ghost image is reconstructed from the second order correlation function [360]

$$\mathbf{GI}_{\cos} = \frac{1}{N}\sum_{j=0}^{N-1}\left[|c_j|^2 - \langle |c_j|^2_N\rangle\right]\mathbf{M}_j. \tag{4.6}$$

The ensemble averages are computed as $\langle A_j\rangle_N = \sum_{j=0}^{N-1} A_j/N$. While it is common to use projection masks, $\mathbf{T}_j^{\cos}$, in Eq. 4.6 in the reconstruction procedure, it suffices to use the Hadamard masks, $\mathbf{M}_j$, instead because $\mathbf{GI}_{\cos}$ is independent of the reference mode, M_0 (see Appendix C). To reveal the spatial phase information in the object, we first compute $\langle |c_j|^2_N\rangle = p_0/2 + \langle p_j\rangle_N/2 + \langle\sqrt{p_o p_j}\cos(\Delta\alpha_j)\rangle_N$. After substitution into Eq. Eq. 4.6 and further simplification (see Appendix C), the measured ghost image is

$$\mathbf{GI}_{\cos} = \frac{1}{N}\left(\sqrt{p_0}\mathrm{Re}\left(\mathbf{O}\right) + \frac{1}{2}\mathbf{H}_d\mathbf{P}\mathbf{H}_d^\dagger - g_{\cos}\mathbf{R}_0\right), \tag{4.7}$$

where the first term is the real part of the object, $\mathrm{Re}\left[\mathbf{O}\right] = |\mathbf{O}|\cos\left(\arg\left(\mathbf{O}-\alpha_0\right)\right)$. The second term is the Hadamard transform of matrix, $\mathbf{P} = |\mathbf{H}_d\mathbf{O}\mathbf{H}_d^\dagger|^2$ where $|\cdot|^2$ is the element wise absolute value squared. Each "pixel" entry in $\mathbf{P}$ maps onto a probability p_j. The last term removes the DC component, by subtracting the first pixel $\mathbf{R}_0 \to \delta_{j0}|r_j\rangle$ weighted by the factor $g_{\cos}$. Moreover, the weighting, $g_{\cos}$, is a constant that depends on the ensemble average of the probabilities, p_j, and cosines of the phases (see Appendix C). It can be shown that in some cases the second term does not overlap spatially with the desired first term, and therefore can be removed from the constructed image by simply cropping it out (see Appendix C).

Following the same arguments, the sine of the phase, corresponding to the "imaginary part" of the ghost image can be computed by applying the same analysis but with an adjustment to the projection masks, i.e., the new projections are $\mathbf{T}_j^{\sin} = \frac{1}{\sqrt{2}}(\mathbf{M}_j + i\mathbf{M}_0)$, having a relative phase of $\pi/2$. The resulting detection probabilities are then $|c_j|^2 = p_0/2 + p_j + \sqrt{p_o p_j}\sin(\Delta\alpha_j)$. Accordingly, the detected ghost image becomes

$$\mathbf{GI}_{\sin} = \frac{1}{N}\left(\sqrt{p_0}\mathrm{Im}\left(\mathbf{O}\right) + \frac{1}{2}\mathbf{H}_d\mathbf{P}\mathbf{H}_d^\dagger - g_{\sin}\mathbf{R}_0\right), \tag{4.8}$$

having an embedded imaginary part of the object profile where $\mathrm{Im}\left(\mathbf{O}\right) = |\mathbf{O}|\sin\left(\arg\left(\mathbf{O}\right) - \alpha_0\right)$. The constant $g_{\sin}$ weights the DC component to be subtracted and depends on the ensemble average of the probabilities, p_j, as well as the sine of the phases (see Appendix C). Realisation of imaginary image reconstruction is then achieved using Eq. 4.6 where the projected sine probabilities c_j are paired with the corresponding Hadamard masks $\mathbf{M}_j$ such that a real image is formed with the required sine phase information.

Accordingly, two image reconstructions (cosine and sine) are required to fully reconstruct a phase object, as illustrated in Fig. 4.3 (b). Applying this to three phase objects, shown in Fig. 4.3 (c), results in the simulated outcomes shown in Fig. 4.3 (d). Experimentally, the cosine projection was obtained by displaying masks on the SLM_B in which the blazed grating was turned off (amplitude of 0) in certain pixels and on (amplitude of 1) in others. The location of the on or off pixels was determined by the specific mask in the basis set (for full details of the scanning technique see Refs. [318, 347]). The sine projection was then obtained by displaying the same masks with an identical pixel arrangement, however, the "on" and "off" pixel states were instead replaced with $1 + i$ and $1 - i$ phase states, respectively. Furthermore, we emphasise that both reconstructed images contain the amplitude of the object, i.e. $|\mathbf{O}|$, in addition to the phase dependent components, enabling for the extension of our technique to complex amplitude objects using quantum ghost imaging.

Results

Initially, we show the experimental reconstruction of two amplitude-only objects in Fig. 4.4, namely two vertical slits (a) and an annular ring (b) with 64×64 scanned super-pixels (yielding a scanning resolution of 128 μm). These were achieved by modulating only the amplitude of the photons with SLM_A (leaving a flat phase) and using the cosine projection masks on SLM_B to detect and thus reconstruct the amplitude object according to the algorithm in Eq. 4.6. Insets in the corners of the figure show the transmission masks used. A good correlation between the object and detected distribution can thus be seen.

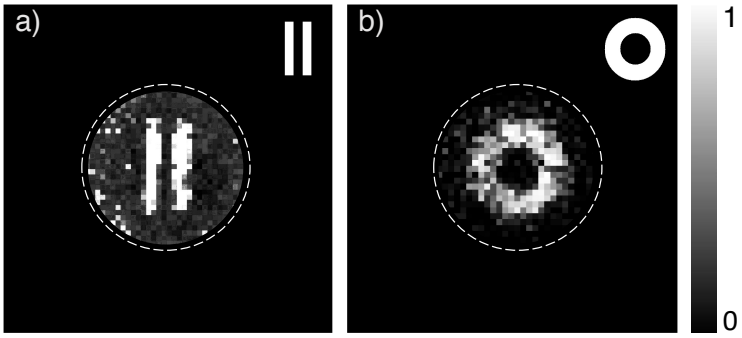


FIGURE 4.4: Reconstructed amplitude-only images using the Walsh-Hadamard masks for (a) an intensity slit, and (b) an intensity ring. The outer area of the dashed white circle indicates the region in which noise was suppressed due to lack of SPDC signal. The amplitude-only objects are shown as insets.

By converting the amplitude objects in Fig. 4.4 to pure phase objects shown in Fig 4.5, we show that phase information is also embedded in the ghost imaging technique and retrieved by an additional sine projection. Here, we illustratively compare the numerical simulation (Sim) with the experimentally (Exp) reconstructed phase-only π-phase slit and the azimuthal phase ring. Insets at the bottom show both the experimentally reconstructed cosine and sine projections. While, previously, we focused on the Walsh-Hadadmard basis, here we also show that this phase retrieval can be extended to the pseudo-complete random basis. As can be seen, the total phase of the object is recovered for both the Walsh-Hadamard in (a) and random masks in (b), showing not only phase steps for the π-phase slit, but also contrast in the phase gradient by the spiral features with the azimuthal phase ring. Apart from

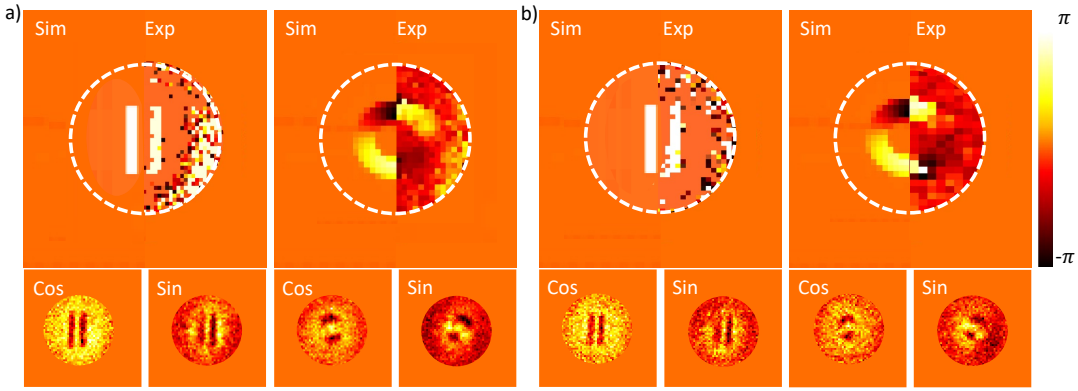


FIGURE 4.5: Numerical simulations (Sim) showing excellent agreement with the Experimental reconstructions (Exp) for the *pi*-phase slit and the azimuthal gradient ring using (a) Walsh-Hadamard and (b) random masks. Experimental images were denoised with image processing tools and contrast adjustment after reconstruction. The outer area of the dashed white circle indicates the region in which noise was suppressed due to lack of SPDC signal. Insets show the corresponding cosine and sine components of the experimental reconstructions.

noise distortion, we show good visual agreement between the numerical simulation and the reconstructed experimental images. In these acquisitions, single photon counts ranging between 40k to 100k, yielding coincidences between 500 to 2000 were obtained in these measurements. It may also be noted that a flat circular phase background persists within the detected region on the SLMs that was illuminated with the SPDC photons. Past this region, a larger variation of noise persists due to lack of signal. We have therefore suppressed the noise in the region where there is no signal, illustrated by a dashed white circle.

To assess the degree of agreement between the numerical simulations and experimental phase reconstructions in Fig. 4.5, we show cross-section plots in Fig. 4.6. The phase values per pixel of the slits are shown in (a) for a representative horizontal cross-section. Random fluctuations in the phase values near the edges of the profile may be noted due to low signal as a result of being near the end of the detection region. We show good agreement between the numerical simulation (gray dotted line) and the experimental images for both the Walsh-Hadamard (blue diamonds) and random (red circles) basis reconstructions. Similarly, in Fig. 4.6 (b), the phase values per pixel are given in the azimuth direction for a set radius within the annular ring. Again, we show excellent agreement between the numerical simulation and experimental reconstructions for both scanning methods.

Lastly, in Fig. 4.7 (a) we show the experimental reconstruction for the detailed spiral phase flower, which was numerically demonstrated in Fig. 4.3 (b). Here, both the cosine and sine projections (middle and right) are given which were used to reconstruct the full phase profile (left). Using Walsh-Hadamard masks, we imaged at a higher resolution of 128 $\times$ 128 superpixels (60 μm scanning resolution), with counts ranging between 100k to 350k and coincidences between 1500 to 3000 across the projections. Importantly, we see that the use of 2D spatial projective masks reveals the entire phase structure including all phase steps and phase gradients, albeit with the presence of noise. Furthermore, in Fig. 4.7 (b) we apply an additional amplitude modulation such that the flat phase components instead have an amplitude of 0 with 1 elsewhere, as illustrated in the intensity of the left image (Complex Obj.). Using the same mask projections as in (a), the spatial structures of both the amplitude ($A = |\mathrm{GI}_{(cos)} + i\mathrm{GI}_{(sin)}|$) and phase of this object were reconstructed with the

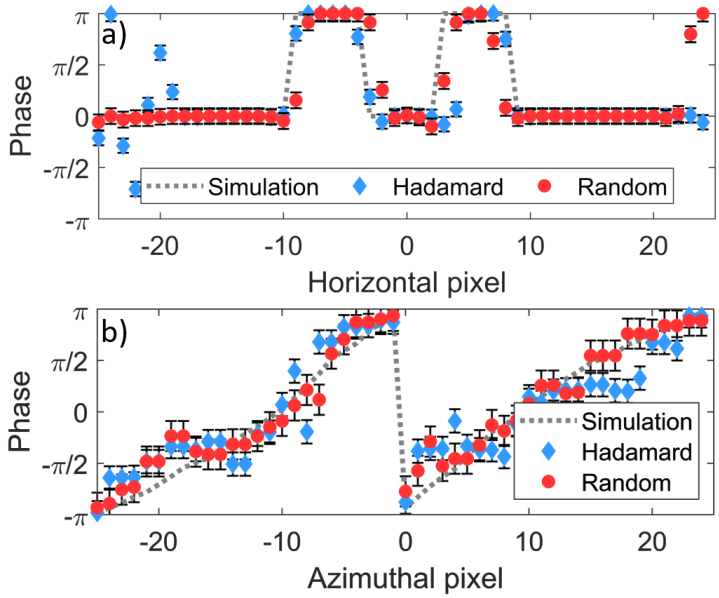


FIGURE 4.6: Phase image cross-sections showing the phase value per pixel for the numerically simulated reconstruction given by the grey dotted line and experimental reconstructions for both the Walsh-Hadamard (blue diamonds) and random masks (red dots) for (a) the π-phase slit in the horizontal direction, and (b) phase ring in the azimuth direction for a radius set inside the ring. Error bars shown are from error propagation of Poissonian statistics.

numerically simulated outcomes in the upper-right corners and raw reconstructed structures rendered in three-dimensions below. Thresholding the amplitude in Fig. 4.7 (b, right) shows a good the comparative structure of the retrieved intensity with respect to the numerically simulated result. We note fluctuations in the intensity were seen due to notable sensitivity of the amplitude reconstruction to noise and additional experimental imperfections, making this approach non-trivial in accurately determining this compenent of the distribution. Nonetheless, an excellent reconstruction of the phase is possible and definite similarity between the encoded, simulated and experimental data is present for the amplitude, showing it is possible to retrieve the information of a complex object using our approach.

In contrast to other approaches, we have reduced the number of necessary measured variables to two (cosine and sine), we require n^2 measurements for each variable, where $n \times n$ pixels is the image resolution. We showed that the required interference naturally arises from the correlation measurements without interferometry. While calculated projective measurements in pursuit of phase have found development in classical single-pixel demonstrations [361, 362], in such approaches 4-step phase shifting is still needed, requiring multiple measurements to reconstruct the desired phase information. In our approach, we reveal that the traditional second order quantum correlations allows the phase information to be available for free and acquired with a single adjustment in each digital mask. Our work makes two advancements; (i) reveals the previously overlooked phase response of observables in single pixel quantum ghost imaging and (ii) offers an intelligible means to extracting the desired phase with controlled projective measurements. We have, therefore, developed and implemented a stable, cost-effective quantum ghost imaging technique to reconstruct the full phase profile of a phase object by measuring a fewer number of variables while retrieving phase steps and phase gradients with the use of single pixel detectors and no need for computationally intense iterative algorithms to

extract the phase.

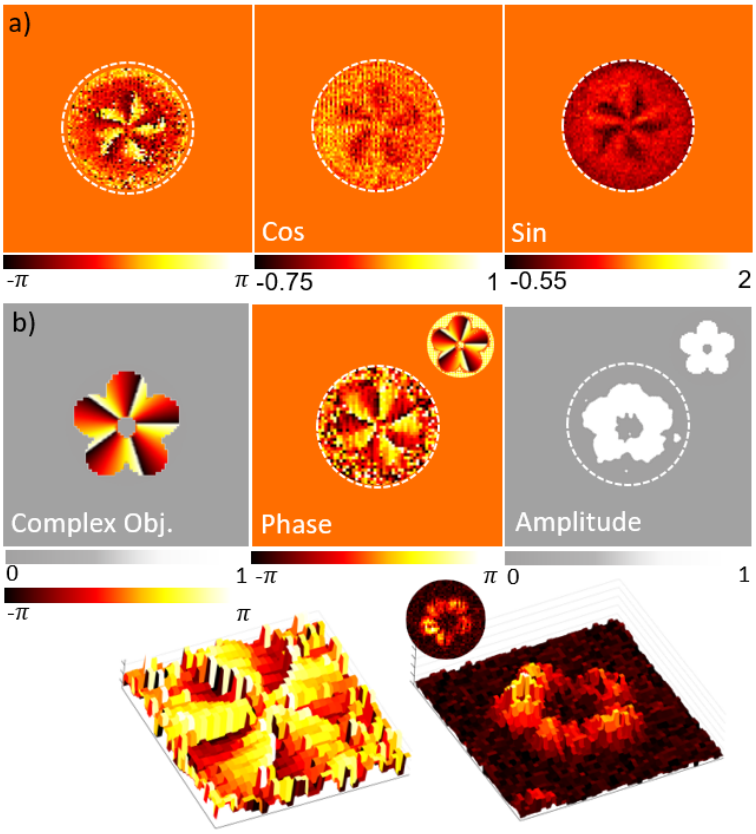


FIGURE 4.7: Experimental ghost image of a (a) pure phase and (b) complex amplitude gradient spiral flower using Walsh-Hadamard masks. The full phase profile was denoised after reconstruction by image processing tools and contrast adjustment. The cosine (middle) and sine (right) components are shown for completeness in (a). The complex aplitude object (left) was reconstructed to give phase (middle) and threshold amplitude (right) in (b). Three-dimensional renders of the raw reconstruction data are shown below.

Conclusion

In conclusion, we have shown that with our new approach, the 2D spatial masks used in traditional ghost imaging hold sufficient information to not only fully reconstruct and reveal complex phase structures, but the full complex amplitude as well. Here we demonstrated clear phase steps and azimuthal phase gradients in the image reconstructions. Our cosine and sine projective masks reconstructed both counterparts of the image, which when combined, revealed the entire phase profile of our encoded phase-only objects. By comparing the simulated and experimental phase values per pixel, we have shown good agreement, albeit with noise distortions present. Furthermore, we show the intrinsic nature of our technique and the versatility thereof by imaging with both the Walsh-Hadamard and random spatial bases. We speculate that this naturally present interference, arising from our 2D spatial mask correlation measurements, has been overlooked due to the swift transition to sophisticated cameras. Nevertheless, this all-digital set-up allows full amplitude and phase retrieval without complicated interferometric or computational techniques, and can be enhanced further by a judicious choice of mask type and image processing tools. A larger sensitivity in the amplitude reconstruction is noted,

however, requiring additional care. While we demonstrated this technique on digital complex amplitude objects it is well suited to achieve simple and stable quantum imaging of complex objects where the low photon numbers, typical in quantum experiments, are useful for applications in both the physical and biomedical domains. Additionally, the technique can be extended into the non-degenerate regime where biological samples can be probed with one wavelength (i.e. infrared), while the spatial information of the twin photon is recorded at another wavelength (which can be either visible or near-infrared). We thus consider it an ideal candidate for characterisation of any teleported images of complex objects such as biological samples in our system.

4.1.3 Outlook and considerations

It thus follows that our teleportation system can be applied towards other real-world applications where, for instance, direct images of biological samples can be sent to another position without needing to process the data or have the channel contain the data. In order to facilitate this, the parameters of our system could be optimised for capacity in a similar manner to what was achieved in the OAM basis. Here we consider discretised pixel states as an encoding basis in addition to the modal approach. Ways forward include tailoring the basis pixels, to get optimal pixel detection with minimal overlap of the discrete states as in Ref. [91]. This tends towards intelligent entanglement concentration where detection of the individual states are a priority. It should be noted that, in this approach, the arbitrary nature of the input is reduced as this involves altering the input mode to mitigate the effects of the channel. Alternatively, the overall detection of an arbitrary spatial distribution can be achieved with the single-pixel phase scheme developed in Section 4.1.2. Here, the nature of the way the information is detected means it need not be confined to projections for each of the single states in the basis, but can rather be projected onto the alternate scanning basis that preserves the signal and allows the overall value such as a complex image of a cell or a fingerprint to be easily reconstructed after teleportation. Additional challenges remain here, as the result of the nature of the pixel state. Here, when considering the upconversion of a single state (i.e. pixel), it becomes increasingly challenging with dimension as the power is divided and thus the efficiency is decreased. This in contrast to the modal states such as OAM and HG where a decrease in efficiency occurs in the higher modal states, but this is at a lower rate and is due to coupling mismatch as the mode size changes with respect to the optics and detection fiber as well as the spatial complexity. This leads to an inverse relation where a larger array of encoded states would result in better teleportation performance up to a point as more power is present where, in contrast, the distribution sensitivity and complexity is increased in the modal approach for more encoded states which then results in a decrease in the teleportation performance.

4.2 Future Work

Extensions of our system and its potential capacities is considered here for future direction and additional applications of this work.

4.2.1 Deterministic teleportation

A large motivator for using a non-linear approach in the detection step, has been motivated by its potential to discern all the outcomes when interacting photons. For

instance, Ref. [308] proposed an entanglement swapping operation performed with spontaneous parametric downconversion and theoretically showed it can be made faithful without postselection using SFG. Ref. [43] showed the ability to distinguish all the two-dimensional Bell states, also using SFG.

In linear optics, for example, post-selection on dual coincidences from beamsplitter ports allows for one of the two-dimensional Bell states to be distinguished [363] and highly complex additions of interferometers or entanglement needed to attempt all [302, 364]. This renders the realistic outcome a probabilistic success as teleportation can only be successful for cases where the interaction resulted in that particular Bell state, allowing the associated correction to be applied. Alternatively, if all such states were both discernible and identifiable for every detected photon resulting in the teleportation, the scheme would then become deterministic. As such, our approach holds promise for being able to achieve feasible high-dimensional deterministic teleportation. Additional adaptations may need to be made to the SFG process for some of the high dimensional Bell states due to destructive interference in the SFG process [365], but these may take the form of simply including an optic that induces an extra phase shift based on the OAM. Here a dove prism may thus be included in the setup before the SFG crystal.

Advantages to achieving such a system, consequently results in a more efficient process with more of the entangled resource being used and exploited, leading the way to a more practical and faster implementation of this protocol.

4.2.2 Hybrid entanglement state teleportation: Expanding degrees of freedom

The current teleportation scheme considers using an SPDC source that contains entanglement in a single degree of freedom only. However, when one considers a different crystal type, such as type II [192] or dual-configurations [366], additional degrees of freedom are also readily correlated. For example, non-separability can exist between both the polarisation and spatial degrees of freedom of the generated photons, such that

$$|\psi\rangle_{A,B} = \frac{1}{\sqrt{2}} \sum_{\ell=-\infty}^{\infty} c_\ell \left(|H,\ell\rangle_A |H,-\ell\rangle_B + |V,\ell\rangle_A |V,-\ell\rangle_B \right) \tag{4.9}$$

where H (V) refers to horizontal (vertical) polarisation and c_ℓ is the complex weighting coefficient. Such simultaneous entanglement between multiple degrees of freedom is termed *hybrid entanglement* [366] and is of further interest as it poses additional avenues for quantum information processing such as hyper-parallel quantum computation [367] and high-capacity quantum key distribution [368].

Other teleportation schemes have additionally extended their implementations to include additional degrees of freedom such as in a polarisaion and OAM in photon [53] or atomic momenta states [369]. These schemes, however, hold the same dimensional limitations for reasons discussed in this thesis.

Intuitively, the capacity of a teleportation system relies on that of the channel. For instance, teleportation for a set number of modes, must first exist in the capacity of the entangled resource, this being SPDC in our case. Similarly, the degrees of freedom one wishes to teleport with must also already be entangled in the channel used. As such, to enable simultaneous teleportation of different degrees of freedom, such as polarisation and OAM, the correlations or entanglement between them should exist in the channel resource. In the case of polarisation and OAM, the resource should

be such as given in Eq. 4.9. It follows that by introducing a hyperentangled SPDC source and taking care to have a similar projection system in the upconversion step, high dimensional teleportation over more than one degree of freedom is possible, opening the way to increased capacities, typologies [370] and overall versatility.

4.2.3 Tailoring the source for optimal teleportation

As eluded to in the previous section, the properties of the entanglement channel in teleportation affects the outcome of what may, or may not be teleported. This naturally extends to the quality of the entanglement source which was shown in Appendix B.8 to affect the achievable fidelities for our system.

Forms of correcting for the non-maximal entanglement between different higher order modes include, among others, Procrustean filtering (as described in Appendix B.3), altering properties of the basis in which information is being transmitted as in [91] or sifting with interference filters [371]. An overall deleterious outcome of these approaches, however, is that the improved outcome is at the cost of resources or signal [372]. For instance, the spacing and sizing of the pixel states in Ref. [91] reduces the number of modes that could be encoded in the same dimensions and in Procrustean filtering the signal from higher-order modes is sacrificed.

Another approach to consider is instead addressing the issue at the source, where the properties of the pump is altered. The concept of shaping the pump for SPDC distribution is in no means new, with works showing shifts in the entanglement spectrum [373, 374] or more elaborate tailoring [175]. In fact, by changing the size of our SPDC pump, we were, to a minor degree, changing the pump to alter the properties or form of our SPDC entanglement spectrum so that the system capacity and higher-dimensional spectra quality could be improved. Here, one could look at improving the efficacy of the teleportation system by using such techniques to tailor the SPDC source, while conserving efficiency. One could also look at how the pump could be shaped to support other spatial modes outside of OAM, such as in the pixel basis in order to maintain the versatility of this scheme.

4.3 Conclusion

Quantum teleportation, since the inception in 1993, has seen many advances from a large variety of implementations using many different types of physical systems to increasing the fidelities achievable and extending the distances it can cover. Despite these advances, increasing the dimensionality of these systems has been a challenging undertaking with a maximum remaining at three. The key restriction of this results from using linear optics in the interaction step between the information carrier and entanglement resource. In this thesis, we worked towards overcoming this challenge by changing the fundamental interaction mechanism and looking towards conveying the information with spatial states of light. Such spatial states have already found incorporation into other quantum protocols for their high dimensional properties, extending from communications to imaging. To do so, this thesis looked at establishing background, investigations and techniques to form a pivotal step in bridging the incorporation of quantum teleportation with high-dimensional spatial states. This, in an effort towards providing practically feasible high-dimensional quantum teleportation.

In investigations towards establishing such a system, the properties of orbital angular momentum states generated in spontaneous parametric down-conversion

(SPDC) were investigated in detail. Here, we established that a fundamental consequence of neglecting amplitude modulation leads to the spread of modal content into higher-order radial modes which increases with charge and results in deleterious modal purities. We further showed size-dependence in the detection step occurs and provide a simple approach to achieve optimal mitigation of this effect. Subsequently, maximal power in the fundamental radial order can be retained, increasing detection efficiencies. The fundamental nature of this type of phase-only generation was illustrated by extending tests from quantum to classical systems and using different generational mechanisms. With appropriate amplitude modulation, the deleterious spread in modal power was eliminated, albeit at the cost of generational efficiencies. It followed that, in the quantum demonstration, detection sizes were established as a prerequisite for achieving power in higher-order modes and resulted in contributing to the detection of higher dimensions.

In a different experiment, we exploited the reverse SPDC non-linear process and used sum-frequency generation as a detection mechanism. Here, we successfully showed SFG as a modal detector, using a variety of spatial structures. Furthermore, by exploiting non-degeneracy, it forms a solution towards spatial mode detection in the infra-red wavelength band, such that cheaper and more technologically advanced devices in the visible band could be used for detection. This mechanism is immediately applicable to single photon states as well, which we later exploited for teleportation.

Incorporating the upconversion projection technique and size-dependence of OAM detection, a conceptually and physically simple teleportation system was then successfully implemented, surpassing the dimensional limitations of quantum teleportation systems. This was achieved in a scalable and on-demand manner across different bases and exhibiting a dimensional capacity of five times the state of the art with 15 dimensions. This, without the need for additional resources such as auxiliary photons required for linear schemes and having the ability to tailor the properties by simply altering detection and modal sizes. As such, the first practically feasible and physically implementable high-dimensional teleportation system was presented. A consequence of low non-linear upconversion efficiencies resulted in the need to encode such states in a classical coherent carrier which allowed the process to be stimulated by virtue of many copies being present. In lieu of this technological solution, we called the implementation *stimulated* teleportation. This protocol, however, applies on the photon level, making it applicable to quantum carriers of the information upon improvement in up-conversion efficiencies. While, it cannot presently be used with carriers that are quantum in nature, and thus forgos features such as entanglement swapping, we establish a potential pivotal step towards a teleportation system that could allow for such development in the future. It thus allows for a new way forward in thinking about and developing this line of technology, with both an immediate and future impact in the field.

While addressing the technological challenge is beyond the scope of this thesis, we looked towards further applications, where it could be used to directly transfer images of complex objects. This, as an extension of quantum images in the broader sense, as described by superpositions of basis states with amplitude and phase information. To do so, a characterisation technique was developed for detecting phase images, while conserving signal, by borrowing from traditional single-pixel ghost imaging techniques. Here, a thorough theoretical framework was provided, showing phase characteristics can be seen in traditional amplitude 2D single-pixel scanning. This was then extended such that only one additional projection is required per measurement to fully and unambiguously reconstruct complex phase

structures without the need for highly sensitive cameras or unstable interferometric approaches. As such, we provided an easily implementable and versatile technique that allows for simple detection of complex images, such as that of biological samples.

Accordingly, throughout this thesis, we have established different detection techniques for spatial modes and phase images. A simple way was shown to optimise detection efficiencies in quantum and classical systems where phase-only OAM is used. Notably, a stimulated teleportation system was built that has exceeded the teleportation capacity of quantum teleportation systems in an effort towards teleporting quantum images and the images of complex objects in a more literal sense.

Appendix A

Supplementary information for modal purity of OAM photons

A.1 OAM in the Laguerre-Gaussian basis

Consider the generation of an OAM mode in the Laguerre-Gaussian (LG) basis, as shown in Fig. 2.5. Such transverse modes of radial order p and azimuthal order ℓ are solutions to the wave equation in quadratic index media, including free-space and graded index fibre, and may be expressed at the $z = 0$ (waist plane) as

$$\psi_{p,\ell}(r,\phi;w_0) \propto \left(\frac{r\sqrt{2}}{w_0}\right)^{|\ell|} L_p^{\ell}\left(\frac{2r^2}{w_0^2}\right) \times \exp\left(-\frac{r^2}{w_0^2}\right)\exp(-i\ell\phi). \tag{A.1}$$

Here L_p^{ℓ} is the Laguerre polynomial and w_0 is a scale parameter within the basis, sometimes referred to as the embedded Gaussian. The OAM content of the beam is associated with the azimuthal phase, $\exp(i\ell\phi)$. A pure OAM mode in this basis, the mode we desire, would have no radial modes ($p = 0$) and described by

$$\psi_{0,\ell}(r,\phi;w_0) \propto \left(\frac{r\sqrt{2}}{w_0}\right)^{|\ell|} \exp\left(-\frac{r^2}{w_0^2}\right)\exp(-i\ell\phi). \tag{A.2}$$

Such OAM modes are traditionally created by ignoring the ℓ dependent amplitude term, the first term in the aforementioned equation, instead modulating a Gaussian beam by the desired phase, namely

$$\tilde{\psi}_{\ell}(r,\phi;w_0) \approx \exp\left(-\frac{r^2}{w_0^2}\right)\exp(-i\ell\phi). \tag{A.3}$$

Ideal vortex beams would have no radial modes, with all or most of the energy in the $p = 0$ mode for a given ℓ and a given scale, w_0. Indeed, many applications exploit the detection of vortex beams through a filter that passes only the $p = 0$ mode, for example, in quantum experiments with OAM modes where the detector allows only a Gaussian of size w_0 to couple into a single mode fibre. While it is known that modes of the type given by Eq. 2.18 are better referred to as Hypergeometric, it remains generally unappreciated that it is the ℓ dependent radial amplitude term (the first term) in Eq. 2.17, and not the azimuthal phase term itself ($\ell\phi$), which is responsible for the characteristic intensity null associated with vortex beams. The observation of a null in vortex beams without this amplitude term is instead due

to high spatial frequencies induced by the helicity of the phase together with their attenuation due to the finite apertures in the optical system. In fact, contrary to the intention, a consequence of the azimuthal phase implementation approach is the generation of many radial modes. To see this we may expand the vortex mode back into the LG basis

$$\exp\left(\frac{-r^2}{w_0^2}\right)\exp(-i\ell\phi) = \sum_{p,\ell} c_{p\ell}\psi_{p,\ell}(r,\phi;w_0), \tag{A.4}$$

to find the weighting coefficients as

$$c_{p\ell} = \sqrt{\frac{(p+|\ell|)!}{p!}}\frac{\Gamma(p+\frac{|\ell|}{2})\Gamma(\frac{|\ell|}{2}+1)}{\Gamma(\frac{|\ell|}{2})\Gamma(p+|\ell|+1)}, \tag{A.5}$$

where $\Gamma(\cdot)$ is the gamma function and $|c_{p\ell}|^2$ is the power in the mode of indices p and ℓ. The implication is that the power in the desired $p = 0$ mode approaches zero as the azimuthal index increases.

If the expansion of Eq. A.4 was changed to a new scale, then the modal power weightings would likewise change, from $c_{p\ell} \to \hat{c}_{p\ell}$ when $w_0 \to w_\ell$.

With brevity, we illustrate this analytically by maximizing the overlap integral between the normalized LG (p=0) mode and the vortex mode given by

$$c_{\ell;\alpha} = \mathcal{N}_\ell(\alpha, w_0)\iint \psi_\ell^*(r,\phi,\alpha w_0)\tilde{\psi}_\ell(r,\phi;w_0)d^2r, \tag{A.6}$$

where $\mathcal{N}_\ell(\alpha, w_0)$ is the product of normalization factors for the LG, vortex mode and α scales the size of the LG mode. The overlap has the analytic solution given as

$$c_{\ell;\alpha} = \frac{2^{\frac{|\ell|}{2}}|\ell|\alpha\,\Gamma\left(\frac{|\ell|}{2}\right)}{(1+\alpha^2)^{\left(\frac{|\ell|}{2}+1\right)}\sqrt{\Gamma\left(|\ell|+1\right)}} \tag{A.7}$$

Subsequently, the probability $|c_{\ell;\alpha}|^2$ integral is maximised for each ℓ when

$$\alpha = \frac{1}{\sqrt{|\ell|+1}}. \tag{A.8}$$

Further, in the quantum case, one has to include the pump profile and Gaussian profiles of the detection fiber modes. As such, the overlap integral now takes the form

$$\begin{aligned} c_{\ell;\alpha} =& \tilde{\mathcal{N}}_\ell(\alpha, w_0, w_p)\iint \psi_\ell^*(r,\phi,\alpha w_0)\tilde{\psi}_\ell(r,\phi;w_0) \\ &\times \exp\left(\frac{r^2}{w_p^2}\right)\exp\left(\frac{2r^2}{w_0^2}\right)d^2r. \end{aligned} \tag{A.9}$$

Here $\mathcal{N}_\ell(\cdot)$ absorbs the normalization factors for the mode functions and w_p is the mode size of the pump photon at the crystal plane.

$$c_{\ell;\alpha} = \frac{2^{\frac{|\ell|+3}{2}}\sqrt{\frac{1}{|\ell|!}}\,\Gamma\left(\frac{|\ell|}{2}+1\right)\left(\frac{1}{\alpha^2}+\frac{1}{\eta^2}+2\right)^{-\left(\frac{|\ell|}{2}+1\right)}}{\pi^{3/2}\,w_0^2\,\eta\,\alpha^{|\ell|+1}} \tag{A.10}$$

Accordingly, $c_{\ell;\alpha}$ is again maximized by a weighting factor of

$$\alpha = \frac{\eta}{\sqrt{(2\eta^2+1)\,(|\ell|+1)}}, \tag{A.11}$$

where $\eta = \frac{w_p}{w_0}$ is the pump field and fiber mode size ratio which we assume is fixed in the experiment.

A.2 Modal decomposition

An important technique, essential for analyzing the generated beams in terms of established modes, is modal decomposition. This technique is often used for characterizing beams, whereby any optical field may be expressed as a linear combination of basis modes:

$$U(r) = \sum_j c_j M_j(r). \tag{A.12}$$

Here $r = (x, y)$ is the spatial coordinate in the transverse plane and $M_j(r)$ represents the basis mode. The complex correlation coefficient, $c_j = \rho_j \exp\left(i\delta\varphi_j\right)$ weights the contribution of each of the basis modes where ρ_j is the corresponding mode amplitude and $\delta\varphi_j$ the intermodal phase difference between the jth mode and a selected reference mode. Accordingly, any arbitrary input field, U(r), may be described by a weighted superposition of these modes. Orthonormality of M_j can be exploited to ascertain the weighting coefficients (c_j) by taking an inner product between the input field and desired mode:

$$c_j = \langle U(r)|M_j\rangle = \iint U(r)M_j^*(r)d^2r, \tag{A.13}$$

where integration is over all space and M_j^* is the complex conjugate of M_j. The complex conjugate of a basis mode is often referred to as a match filter. Determination of the coefficient in terms of the field product ($U(r)M_j^*$) is possible by taking the Fourier transform of Eq. A.13 to yield:

$$U_j(k_x, k_y) = \iint U(x,y)M_j^*(x,y)\exp\left(-i(k_x x + k_y y)\right)dxdy, \tag{A.14}$$

where k_x, k_y are wave vectors. The on-axis point $(k_x, k_y) = (0, 0)$, produces an expression equivalent to Eq. A.13:

$$U_j(0,0) = \iint U(r)M_j^*(r)d^2r = c_j. \tag{A.15}$$

It follows that the intensity at the field center, $I(0,0)$, will then yield the power weighting (i.e. square of the weighting coefficient)

$$I_j^{\rho}(0,0) = |U_j(0,0)|^2 = |c_j|^2. \tag{A.16}$$

A.3 Holograms

Implementing a chosen field modulation, for either generating a desired structure or exploiting the reciprocity of light for modal decomposition, one may use a spatial light modulator (SLM) to spatially alter the phase (Φ) and amplitude (U) of the incoming beam, i.e. $E_{in}(x,y) = U_{in}(x,y)\exp\{(i\Phi_{in}(x,y))\}$, into a desired output field,

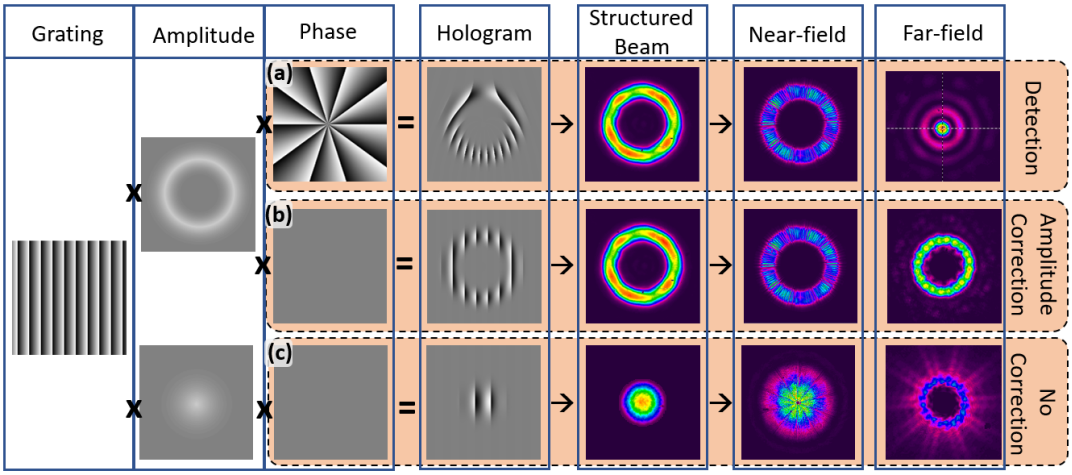


FIGURE A.1: Diagram of the holograms and field structure for holographic analysis of the meta-surface generated modes. Grating, amplitude and phase components are combined to form the holograms shown for the 3 cases evaluated in this paper. (a) Detection of the modes in the azimuthal and radial bases with varying encoded beam waists. (b) Correction of the modal amplitude to generate OAM modes with pure radial profiles. We believe that the residual rings observed in the farfield are due to pixelation from the nano-posts and possibly due to no aperturing before the CCD. (c) Traditional phase-only OAM generation with Gaussian input onto the meta-surface. Far-field images shown in (b) and (c) were post-processed to remove a central intensity spot, resulting from the presence of the unmodulated Gaussian remaining after the meta-surface. This was achieved by setting the central values to 0 and thus allows one to see only the amplitude correction and modulation effects of the meta-surface as well as demonstrating what one would see in detection for a 100% efficient device.

$E_{out}(x,y) = U_{out}(x,y)\exp\{(i\Phi_{out}(x,y))\}$, along the transverse plane (x,y) in which the SLM is placed. The phase required to engineer this alteration between input and output fields is then the hologram, $H(x,y)$. Implementation of the hologram with the incoming and reflected (output) beam field may be described as:

$$E_{in}(x,y)e^{i\mathbf{k_{in}}\cdot\hat{\mathbf{r}}} \times e^{iH(x,y)} = E_{out}(x,y)e^{i\mathbf{k_{out}}\cdot\hat{\mathbf{r}}}. \tag{A.17}$$

where $\hat{\boldsymbol{r}} = (\boldsymbol{x}, \hat{\boldsymbol{y}}, \boldsymbol{z})$ and $\mathbf{k}$ is the associated wave-vector. It follows then that the hologram to obtain the desired output field is determined from the input by

$$e^{iH(x,y)} = \frac{E_{out}}{E_{in}} e^{i(\mathbf{k_{out}}-\mathbf{k_{in}})\cdot\hat{\mathbf{r}}} \tag{A.18}$$

$$= \frac{U_{in}(x,y)}{U_{out}(x,y)} e^{i(\Phi_{out}(x,y)-\Phi_{in}(x,y))} e^{i(\mathbf{k_{out}}-\mathbf{kin})\cdot\hat{\mathbf{r}}}. \tag{A.19}$$

Here $\Phi \in [-\pi,\pi]$, $U \in [0,1]$ and if the angle between $\mathbf{k_{out}}$ and $\mathbf{k_{in}}$ is small, the modulated light may be separated into the first order with the application of a phase grating. For example, $\Phi_{grating}(x,y) = \text{Mod}[(2\pi x)/\Lambda, 2\pi]$ with $\Lambda = (2\pi)/(\mathbf{k_{out}} - \mathbf{k_{in}})$ yielding the grating period. The desired phase profile is then generated by using the relative phase offset with a grating:

$$\Phi_H = \Phi_{out}(x,y) - \Phi_{in}(x,y) + \Phi_{grating}. \tag{A.20}$$

Structuring the amplitude is obtained by varying the grating depth to reduce the

diffraction efficiency of the light directed to the first order (desired output beam). This allows light to be diverted away and the desired amplitude profile, $U_{des}(x,y) = U_{out}/U_{in}$ to be 'cookie cut' out of the input beam amplitude. Choice selection of a function $f(U_{des}(x,y))$ to modulate the depth of the hologram phase profile, thus produces the desired amplitude structure in the output beam. Accordingly, the hologram may be analytically generated with the form:

$$H(x,y) = f(U_{des}(x,y))\Phi_H(x,y). \tag{A.21}$$

When overfilling the SLM with a collimated beam, a flat phase front ($\Phi_{in} = 0$) and uniform intensity distribution ($U_{in} = 1$) can be assumed, simplifying the analytical solution to include that of only the desired amplitude and phase. A 256-level gray scale phase map is then generated and displayed on the SLM. Here the display alters the phase and efficiency of the light retained of the field at each pixel (x,y), according to the encoded gray level.

Generation of such a phase map has several methods of variable accuracy according to the amplitude modulation function used. Accordingly, using Eq. A.1, such a phase map was produced for the generation of LG beams for decomposition, allowing the characteristics of the J-plate generated modes to be evaluated. Images of the hologram along with the generated beam is given in Fig. A.1 (a) for the $\ell = 10$ case. Here the near-field image of a $\ell = -10$ generated beam is seen incident on the J-plate, yielding the resulting far-field structure with on-axis intensity. This is an example of experimental OAM detection in 'reverse' modal decomposition.

Figure A.1 (b) shows the hologram generated for structuring only the amplitude of the incident beam for holographic enhancement of the meta-surface generated mode. For generation of such a hologram, the phase term was removed in Eq. A.1 ($\phi = 0$) so that the amplitude was adjusted, but the phase front remained uniform. Accordingly, modulation of the amplitude (SLM) and phase (J-plate) then yielded a pure $LG_{0,10}$ mode as shown by defined annular ring in the far-field. Conversely, without structuring the amplitude of the beam incident onto the meta-surface, the radial purity of the mode is compromised as shown in (c). Here, a Gaussian mode was generated and directed through the meta-surface for traditional OAM generation, yielding a noticeable radial spread in power as additional p-modes are excited during propagation.

Appendix B

Suplementary information for stimulated high-dimensional spatial teleportation

B.1 Suitable experimental conditions for teleportation with SFG

With SPDC being a suitable source of entanglement for our protocol, we consider in more detail what the experimental conditions need to be to achieve successful teleportation with the aid of SFG. For this purpose, we consider a collinear SPDC system with some simplifying assumptions. Even though details may be different from a more exact solution, the physics is expected to be the same.

As shown in the previous section, the success of the process requires that $\mathbf{q}_B = -\mathbf{q}_C$, provided that the pump beam is a Gaussian mode, which implies perfect anti-correlation of the wave vectors between the signal (photon B) and idler (photon C). It is achieved when (a) the argument of the sinc-function can be set to zero, which is valid under the *thin-crystal approximation*, and (b) the beam waist of the pump beam w_p is relatively large, leading to the *plane-wave approximation*.

The scale of the sinc-function is inversely proportional to $\sqrt{\lambda_p L}$ where λ_p is the wavelength of pump (or anti-pump) and L is the length of the nonlinear crystal (L = 5 mm in our case). To enforce the requirement that its argument is evaluated close to zero, we require that the integral only contains significant contributions in this region. Therefore, the angular spectrum of the pump mode with which it is multiplied, must be much narrower than the sinc-function. The width of the angular spectrum of the pump mode is inversely proportional to the beam waist w_p. Therefore, the condition requires that

$$\frac{1}{\lambda_p L} \gg \frac{1}{w_p^2} \quad \Rightarrow \quad 1 \gg \frac{\lambda_p L}{w_p^2} \propto \frac{L}{z_R}, \tag{B.1}$$

where z_R is the Rayleigh range of the pump beam. The relationship shows that the sinc-function can be replaced by 1 if the Rayleigh range of the pump beam is much larger than the length of the nonlinear crystal, leading to the thin-crystal approximation. We see that this condition is consistent with the requirement that w_p is relatively large, which is required for the plane-wave approximation.

Similar conditions are required for the second nonlinear crystal that performs SFG. In that case, two input photons with angular frequencies ω_A and ω_C, respectively, are annihilated to generate a photon with an angular frequency $\omega_D = \omega_A + \omega_C$, imposed by energy conservation. The size of the mode that is detected,

takes on the role of w_p and the length of the second nonlinear crystal replaces the length L of the first crystal. The wavelength after the sum-frequency generation process is the same as that of the pump for the SPDC λ_p. The equivalent conditions for the momentum conservation impose an anti-correlation $\mathbf{q}_A = -\mathbf{q}_C$, considering we only project the upconverted photon D onto the Gaussian mode (fundamental spatial mode), as implied in Eq. 3.11.

B.2 Fidelity of the teleportation channel

To quantify the quality of the teleportation process, we use *fidelity*. It is defined for pure states as the squared magnitude of the overlap between the initial state that was to be teleported $|\psi_A\rangle$ and the final teleported state that was received by Bob $|\psi_B\rangle$:

$$F = |\langle\psi_A|\psi_B\rangle|^2. \tag{B.2}$$

In the ideal case, where the teleported state is $|\psi_B\rangle = \int \alpha(\mathbf{q})\hat{a}_B^\dagger(\mathbf{q})|\text{vac}\rangle\, d\mathbf{q}$ (as detailed in Section 3.1.1), the fidelity is $F = 1$. However, in a practical experiment, the conditions for the ideal case cannot be met exactly. Therefore, the fidelity is given more generally by

$$\begin{aligned} F &= \int \alpha^*(\mathbf{q}_B)\beta(\mathbf{q}_B)\, d^2q_B \\ &= \int \alpha^*(\mathbf{q}_B)U^*(\mathbf{q}_D)g(\mathbf{q}_A, \mathbf{q}_D - \mathbf{q}_A, \mathbf{q}_D) \\ &\quad \times f(\mathbf{q}_B, \mathbf{q}_D - \mathbf{q}_A)\alpha(\mathbf{q}_A)\, d^2q_B\, d^2q_A\, d^2q_D. \end{aligned} \tag{B.3}$$

Here, $f(\mathbf{q}_B, \mathbf{q}_C)$ is the two photon wave-function of the SPDC state, while $g(\mathbf{q}_A, \mathbf{q}_C, \mathbf{q}_D)$ and $U^*(\mathbf{q}_D)$ are the SFG kernel and projection mode for photon D (the up-converted photon), respectively. It is possible to envisage a classical implementation of the state-transfer process. One would make a complete measurement of the initial state, send the information to Bob and he will then prepare the same state at his side. To ensure that the teleportation process can outperform this classical state-transfer process, the fidelity of the process must be better than the maximum fidelity that the classical teleportation process can obtain.

In order to determine the classical bound on the fidelity by which we measure the teleported state $|\psi\rangle$, we define the probability of measuring a value a by

$$P_\psi(a) = \langle\psi|\,\hat{E}_a\,|\psi\rangle\,, \tag{B.4}$$

where $\hat{E}_a$ is an element of the positive operator valued measure (POVM) for the measurement of the initial state. These elements obey the condition.

$$\sum_a \hat{E}_a = \mathbb{I}, \tag{B.5}$$

where $\mathbb{I}$ is the identity operator. The estimated state associated with such a measurement result is represented by $|\psi_a\rangle$.

For the classical bound, we consider the average fidelity that would be obtained for all possible initial states. This average fidelity is given by

$$\begin{aligned}\mathcal{F} &= \int \sum_a P_\psi(a) |\langle\psi|\psi_a\rangle|^2 \, d\psi, \\ &= \int \sum_a \langle\psi| \hat{E}_a |\psi\rangle \, |\langle\psi|\psi_a\rangle|^2 \, d\psi,\end{aligned} \tag{B.6}$$

where $d\psi$ represents an integration measure on the Hilbert space of all possible input state. We assume that this space is finite-dimensional but larger than just two-dimensional. Since all the states in this Hilbert space are normalized, the space is represented by a hypersphere. A convenient way to represent such an integral is with the aid of the Haar measure. For this purpose, we represent an arbitrary state in the Hilbert space as a unitary transformation from some fixed state in the Hilbert space $|\psi\rangle \to \hat{U}|\psi_0\rangle$, so that $d\psi \to dU$. The average fidelity then becomes the following

$$\begin{aligned}\mathcal{F} &= \int \sum_a \langle\psi_a| \hat{U} |\psi_0\rangle \langle\psi_0| \hat{U}^\dagger \hat{E}_a \hat{U} |\psi_0\rangle \langle\psi_0| \hat{U}^\dagger |\psi_a\rangle \, dU \\ &= \int \sum_a \mathrm{tr}\{\hat{\rho}_a \hat{U} \hat{\rho}_0 \hat{U}^\dagger \hat{E}_a \hat{U} \hat{\rho}_0 \hat{U}^\dagger\} \, dU.\end{aligned} \tag{B.7}$$

The general expression for the integral of the tensor product of four such unitary transformations, represented as matrices, is given by

$$\begin{aligned}\int U_{ij}(U^\dagger)_{kl} U_{mn}(U^\dagger)_{pq} \, dU =& \frac{1}{d^2-1}\left(\delta_{il}\delta_{jk}\delta_{mq}\delta_{np} + \delta_{iq}\delta_{jp}\delta_{ml}\delta_{nk}\right) \\ &- \frac{1}{(d^2-1)d}\left(\delta_{il}\delta_{jp}\delta_{mq}\delta_{nk} + \delta_{iq}\delta_{jk}\delta_{ml}\delta_{np}\right).\end{aligned} \tag{B.8}$$

Using this result in Eq. (B.7), we obtain

$$\mathcal{F} = \frac{1}{(d+1)d}\left(d + \sum_a \langle\psi_a| \hat{E}_a |\psi_a\rangle\right), \tag{B.9}$$

where d is the dimension of the Hilbert space and where we imposed $\mathrm{tr}\{\hat{\rho}_0\} = \mathrm{tr}\{\hat{\rho}_0^2\} = \mathrm{tr}\{\hat{\rho}_a\} = 1$. We see that $\mathcal{F}$ is maximal if E_a represents rank 1 projectors and $E_a|\psi_a\rangle = |\psi_a\rangle$, that is, $E_a = |\psi_a\rangle\langle\psi_a|$. Then $\sum_a \langle\psi_a| \hat{E}_a |\psi_a\rangle = d$. It follows that the upper bound of the fidelity achievable for the classical state-transfer process is given by [281]

$$\mathcal{F} \leq \frac{2}{d+1}. \tag{B.10}$$

The fidelity obtained in teleportation needs to be better than this bound to outperform the classical scheme.

Furthermore, we can consider the particular teleportation of a subspace smaller than the supported by the teleportation channel capacity (detailed in Section 3.1.2). The teleportation fidelity of the channel for each subspace d' within the d dimensional state, ρ, can be computed by truncating the density matrix and overlapping it with a channel state that has perfect correlations. The theoretical fidelity is given by the expression [281]

$$F_{Ch} = \frac{d'(p'-1) + d'^2}{d'^2}, \tag{B.11}$$

where p' and d' are the purity and dimensionality of truncated states. While this assumes that the channel has a random noisy component given by $\mathbb{I}_{d'^2}/d'^2$, the photon Bob receives only has a noise component given by $\mathbb{I}_{d'}/d'$ therefore the teleportation fidelity for each photon is given by,

$$\mathcal{F} = \frac{F_{Ch}d' + 1}{d' + 1}. \tag{B.12}$$

Here the separability criterion admits the classical bounds $\frac{1}{d'^2} \leq F_{Ch} \leq \frac{1}{d'}$ and $\frac{1}{d'} \leq \mathcal{F} \leq \frac{2}{d'+1}$ for the full channel and a single state received by Bob, respectively.

B.3 Procrustean filtering

Experimental factors required compensation when evaluating the teleported results in the OAM basis and required the application of correction to the detected coincidences. These were the result of a convolution of corrections resulting from a non-flat spiral bandwidth from the SPDC photons [96, 232], variation in the overlap of the down-converted 806 nm photons and the 1565 nm photons in the SFG process (as shown by the teleportation operator) and the fixed-size Gaussian filter resulting

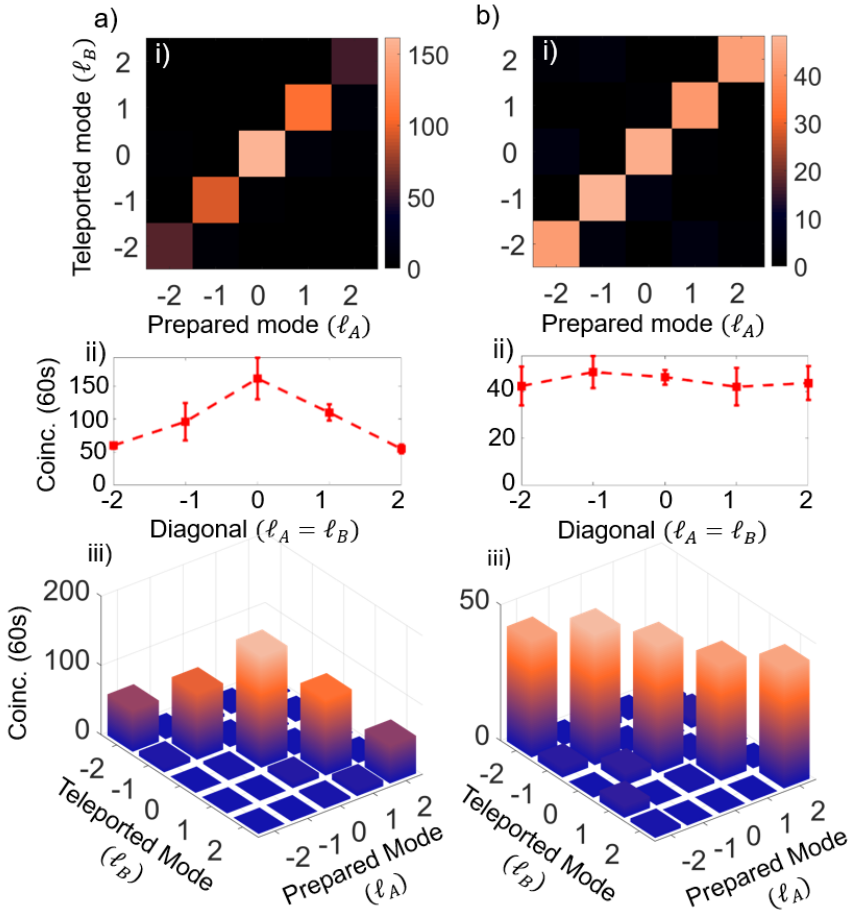


FIGURE B.1: **Procrustean filtering of the OAM modes.** (a) Unflattened and (b) flattened spiral bandwidths by decreasing the grating depth for lower ℓ-values. Here (i) gives the density plot, (ii) shows the diagonal of (i) and (iii) renders the data in 3D where the diagonal values are highlighted. Error bars are calculated from multiple measurements.

from detection with a SMF [221]. Figure B.1(a) shows the spiral bandwidth (at 2 minute integration time per point) resulting from these factors with a (i) density plot and the associated (ii) correlated modes diagonal as well as a (iii) 3D-representation, highlighting the non-flat spectrum.

As a flat spiral bandwidth is preferable for unbiased teleportation of states, the modal weights were equalised by a mode-specific decrease of the grating depth for the holograms, allowing one to implement Procrustean filtering [117, 375, 376] and thus sacrificing signal for the smaller $|\ell|$ values.

Figure B.1(b) shows the result of implementing an ℓ-dependent grating depth compensation. Here it can be seen that the detected weights across the 5 OAM modes were flattened to within the experimental uncertainties, with a small increase in the $\ell = -1$ mode due to laser fluctuation. This, however, does come at the cost of a smaller signal-to-noise ratio as is demonstrated in the density and 3D-plots given in (b)(i) and (b)(iii), respectively (maximum coincidences are less by about a third). Figures B.1 (ii) show the diagonals for clearer comparison of the modal weights and present noise.

B.4 Background subtraction

Due to the low efficiencies in the up-conversion process, a low signal-to-noise ratio was an experimental factor. The noise in our system is generated by various effects, e.g. the dark counts, originated in the avalanche photodiodes (APDs), also contributing to false (accidental) coincidence events. An additional mode-dependent noise was also observed as a result of two photon absorption occurring for lower ℓ-values as the 1565 nm pump power density is higher. See Supplementary Note 9 for a more detailed description of the different sources of error in our system. As a result, the visibilities and fidelities of the states are decreased. Here, reducing the temporal window for which the coincidences were detected aided to reduce the noise at the cost of some signal. Another method which was employed was to measure the detected 'coincidences' far away from the actual arrival window of the entangled photons. In other words, the easiest way to statistically quantify this noise is to count the coincidence events when the difference of the time of arrival between photons B and D is much larger than the coincidence window. That measurement

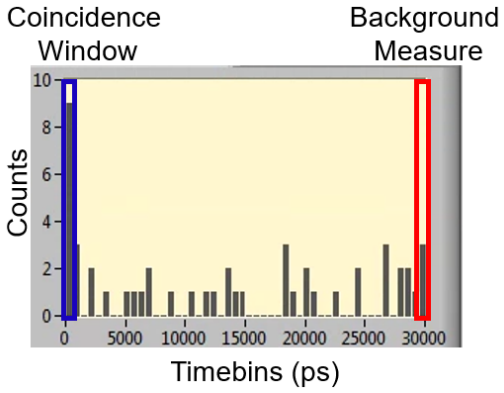


FIGURE B.2: **Illustration of background measurement.** Histogram showing the arm delays with the coincidence windows for a 3s integration time, demonstrating the measured background values for noise correction.

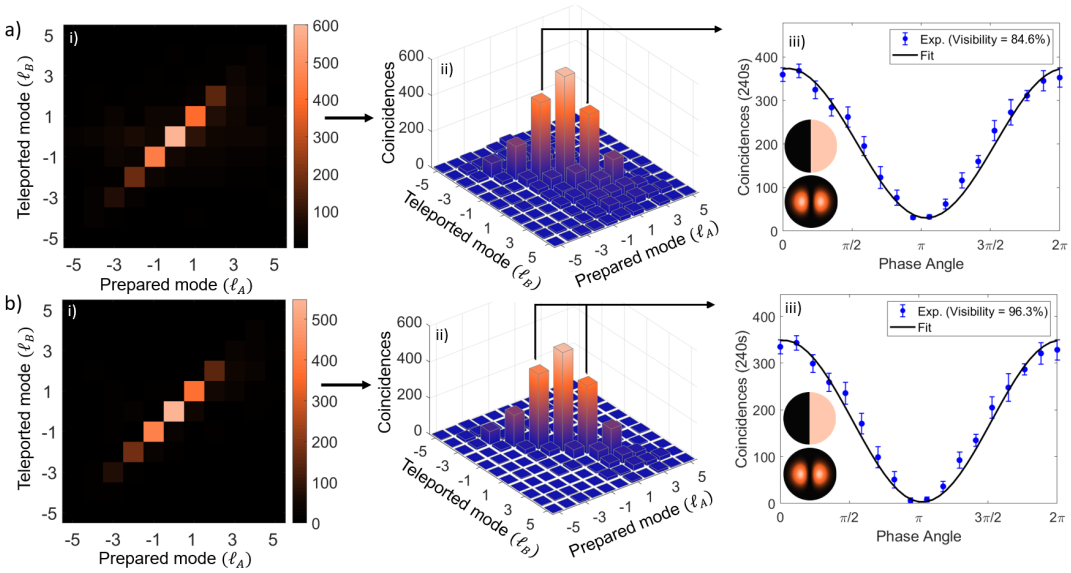


FIGURE B.3: **Effects of applying noise correction to the results.** Plots showing the (a) raw measured coincidences and (b) coincidences corrected by subtracting the background measured in an uncorrelated time-bin for the (i) spiral bandwidth with a (ii) 3D rendering and (iii) the visibility measurable for rotating the projected state for the $\ell = \pm 1$ teleported state. Error bars are calculated from multiple measurements.

was then taken as the background noise of the system and subtracted from the actual measured coincidences. This is illustrated in the histogram shown in Fig. B.2 of the measured coincidences vs. time delay for the signals received from Alice and Bob's arm. Here the blue rectangle highlights the coincidences being detected while the red highlights the values taken to be the background or noise signal.

These measured coincidence values were consequently in the same length time bin (coincidence window = 0.5 ns) with the time delay being 30 ns outside of the actual coincidence window (20 times away from the actual coincidence window). By subtracting the noise signal, the actual coincidences from the teleportation process could be determined. The results of this subtraction is then showcased in Fig. B.3 for the spiral bandwidth and visibility from a superposition OAM state of $\ell = \pm 1$. Here, Fig. B.3 (a) shows the raw measured results, while (b) illustrates the effects of subtracting the measured noise from the coincidences as described in Fig. B.2. The spiral bandwidth is shown in Fig. B.3 (i), ranging from $\ell = -5$ to $\ell = 5$ and with a 5 minute integration time per projection measurement. The 3D rendering of the measurements is shown in (ii), so that the noise can be easily identified. And the $\ell = \pm 1$ superposition state is shown in (iii), where the projection state was rotated by adjusting the inter-modal phase from $\theta = [0, 2\pi]$. In all cases a clear improvement in the measured states can be seen with particular attention to the increase in visibility of Fig. B.3 (b, iii) from (a,iii), reaching almost a perfect fidelity of the teleported state.

A summary of the difference in visibilities for rotations of the different projected modes shown in Fig. 3 (a) of the main text is further provided in Table B.1, along with the other results given throughout the paper.

B.5 Qutrit teleportation

To benchmark our protocol with respect to other reported high-dimensional teleportation protocols, a state tomography on each of the 12 MUB states for the current

OAM Superposition	**Raw Visibility**	**B. Sub. Visibility**
$\|1\rangle + \|-1\rangle$	0.85 $\pm$0.029	0.96 $\pm$0.044
$\|2\rangle + \|-2\rangle$	0.83 $\pm$0.10	0.96 $\pm$0.12
$\|3\rangle + \|-3\rangle$	0.79 $\pm$0.19	0.97 $\pm$0.23
$\|4\rangle + \|-4\rangle$	0.65 $\pm$0.24	0.94 $\pm$0.35
3D Tomography	**Raw Fidelity**	**B. Sub. Fidelity**
$\|-1\rangle + \|0\rangle + \|1\rangle$	0.82 $\pm$0.016	0.92 $\pm$0.017
2D OAM Superposition	**Raw Similarity**	**B. Sub. Similarity**
$\|\varphi_1\rangle$	0.96 $\pm$0.042	0.96 $\pm$0.051
$\|\varphi_2\rangle$	0.97 $\pm$0.057	0.97 $\pm$0.069
$\|\varphi_3\rangle$	0.98 $\pm$0.093	0.98 $\pm$0.10
3D OAM Superposition	**Raw Similarity**	**B. Sub. Similarity**
$\|\varphi_4\rangle$	0.98 $\pm$0.039	0.96 $\pm$0.06
4D OAM Superposition	**Raw Similarity**	**B. Sub. Similarity**
$\|\varphi_5\rangle$	0.98 $\pm$0.047	0.97 $\pm$0.065
3D HG Superposition	**Raw Similarity**	**B. Sub. Similarity**
$\|\gamma_1\rangle$	0.99 $\pm$0.029	0.99 $\pm$0.042
4D HG Superposition	**Raw Similarity**	**B. Sub. Similarity**
$\|\gamma_2\rangle$	0.96 $\pm$0.025	0.95 $\pm$0.037
9D HG Superposition	**Raw Similarity**	**B. Sub. Similarity**
$\|\gamma_3\rangle$	0.81$\pm$0.019	0.80 $\pm$0.025

TABLE B.1: **Results summary of background subtracted and raw data.** Experimental visibilities, fidelities and similarities calculated for the teleportation channel and teleported states comparing raw and background subtracted (B. Sub.) outcomes. Abbreviated states are: $|\varphi_1\rangle = |0\rangle + |-1\rangle$, $|\varphi_2\rangle = |-1\rangle + |1\rangle$, $|\varphi_3\rangle = |0\rangle - |1\rangle$, $|\varphi_4\rangle = |-2\rangle + |0\rangle + |2\rangle$, $|\gamma_1\rangle = |HG_{1,0}\rangle + |HG_{1,1}\rangle + |HG_{0,1}\rangle$, $|\varphi_5\rangle = |-3\rangle - i\,|-1\rangle + |1\rangle + i\,|3\rangle$, $|\gamma_2\rangle = |HG_{0,0}\rangle + |HG_{1,0}\rangle + |HG_{1,1}\rangle + |HG_{0,1}\rangle$ and $|\gamma_3\rangle = |HG_{0,0}\rangle + |HG_{2,0}\rangle + |HG_{0,2}\rangle + |HG_{2,2}\rangle + |HG_{4,0}\rangle + |HG_{0,4}\rangle + |HG_{4,2}\rangle + |HG_{2,4}\rangle + |HG_{4,4}\rangle$, as given in Section 3.9. Slightly better similarities may be noted in some cases for the raw values of the superposition on states as the Procrustean filtering applied was optimised for the raw data. Uncertainties are calculated from multiple measurements.

three-dimensional limit was performed. The resulting fidelities for each can be seen in Fig. B.4. Each of the MUB states are

$$|\psi_1\rangle = |a\rangle \tag{B.13}$$
$$|\psi_2\rangle = |b\rangle \tag{B.14}$$
$$|\psi_3\rangle = |c\rangle \tag{B.15}$$
$$|\psi_4\rangle = \frac{1}{\sqrt{3}}(|a\rangle + |b\rangle + |c\rangle) \tag{B.16}$$
$$|\psi_5\rangle = \frac{1}{\sqrt{3}}(|a\rangle + \omega\,|b\rangle + \omega^2\,|c\rangle) \tag{B.17}$$
$$|\psi_6\rangle = \frac{1}{\sqrt{3}}(|a\rangle + \omega^2\,|b\rangle + \omega\,|c\rangle) \tag{B.18}$$
$$|\psi_7\rangle = \frac{1}{\sqrt{3}}(\omega\,|a\rangle + |b\rangle + |c\rangle) \tag{B.19}$$
$$|\psi_8\rangle = \frac{1}{\sqrt{3}}(|a\rangle + \omega\,|b\rangle + |c\rangle) \tag{B.20}$$
$$|\psi_9\rangle = \frac{1}{\sqrt{3}}(|a\rangle + |b\rangle + \omega\,|c\rangle) \tag{B.21}$$
$$|\psi_{10}\rangle = \frac{1}{\sqrt{3}}(\omega^2\,|a\rangle + |b\rangle + |c\rangle) \tag{B.22}$$
$$|\psi_{11}\rangle = \frac{1}{\sqrt{3}}(|a\rangle + \omega^2\,|b\rangle + |c\rangle) \tag{B.23}$$
$$|\psi_{12}\rangle = \frac{1}{\sqrt{3}}(|a\rangle + |b\rangle + \omega^2\,|c\rangle), \tag{B.24}$$

and were prepared from the $\ell = \{-1, 0, 1\}$ OAM subspace in our case where $a = -1, b = 0, c = 1$ and $\omega = e^{i\frac{2\pi}{3}}$. Here, the phase profiles of each are shown as insets along the x-axis in the figure.

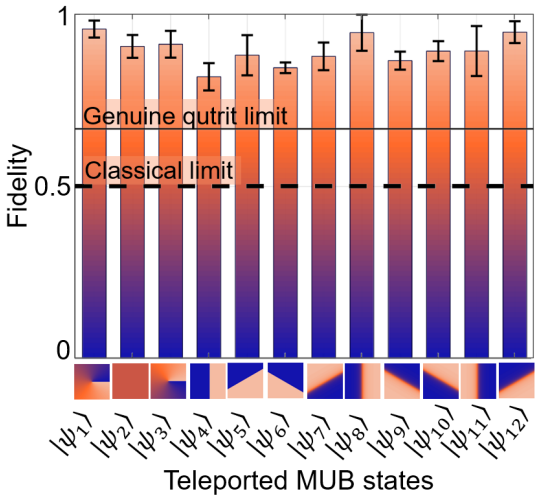


FIGURE B.4: **Teleported MUB states.** Experimental fidelities measured for state tomography performed on all 12 teleported MUB states for a $d = 3$ space comprised OAM modes ℓ = {-1,0,1}. Dashed (solid) lines indicate the classical (genuine qutrit) limit and phase insets along the x-axis show the MUB state phase profiles. The data is raw and not background subtracted. Error bars are calculated from multiple measurements.

Based on the MUB tomography projection measurements, the density matrix ρ_{Ex}, for each of the teleported MUB states was reconstructed using the maximum likelihood algorithm [114] as outlined in Section 1.5.2. The exact fidelities, calculated from $F = \mathrm{Tr}(\sqrt{\sqrt{\rho_{Th}}\rho_{Ex}\sqrt{\rho_{Th}}})^2$ where ρ_{Th} is the theoretical density matrix of the pure MUB state being detected, are then given in Table B.2. Corresponding results for the 12 MUB states reported in Refs. [68, 69] are shown in columns to the right for comparison and a final fidelity, averaged over all the states, given at the bottom. It follows, that our protocol compares well with those reported where $F_{ave} = 0.895 \pm 0.042$ in our scheme compares to $F_{ave} \approx 0.75 \pm 0.055$ [68] and $F_{ave} = 0.70 \pm 0.026$ [69]

State	This work	Ref [68] (app.)	Ref [69]
$\|\psi_1\rangle$	0.96 $\pm$0.025	0.76 $\pm$0.053	0.74 $\pm$0.029
$\|\psi_2\rangle$	0.91 $\pm$0.033	0.81 $\pm$0.067	0.69 $\pm$0.029
$\|\psi_3\rangle$	0.91 $\pm$0.039	0.78 $\pm$0.063	0.71 $\pm$0.031
$\|\psi_4\rangle$	0.82 $\pm$0.039	0.73 $\pm$0.065	0.63 $\pm$0.056
$\|\psi_5\rangle$	0.88 $\pm$0.058	0.73 $\pm$0.067	0.73 $\pm$0.049
$\|\psi_6\rangle$	0.84 $\pm$0.015	0.81 $\pm$0.055	0.69 $\pm$0.063
$\|\psi_7\rangle$	0.88 $\pm$0.041	0.80 $\pm$0.057	0.67 $\pm$0.049
$\|\psi_8\rangle$	0.95 $\pm$0.053	0.72 $\pm$0.059	0.66 $\pm$0.055
$\|\psi_9\rangle$	0.87 $\pm$0.026	0.61 $\pm$0.068	0.75 $\pm$0.056
$\|\psi_{10}\rangle$	0.89 $\pm$0.029	0.75 $\pm$0.058	0.67 $\pm$0.050
$\|\psi_{11}\rangle$	0.89 $\pm$0.073	0.77 $\pm$0.049	0.76 $\pm$0.047
$\|\psi_{12}\rangle$	0.85 $\pm$0.031	0.73 $\pm$0.065	0.65 $\pm$0.062
F_{ave}	0.90 $\pm$0.042	0.75 $\pm$0.055	0.70 $\pm$0.026

TABLE B.2: **Comparison of d = 3 teleported MUB states.** Comparison of the teleported fidelities calculated from raw (not background subtracted) data. for all 12 MUB states with those in reported in existing literature for high-dimensional teleportation. Values estimated from the graphs presented in the respective publications are labelled (app.).

B.6 Unbalanced teleportation

In the following section, four different states of unequal amplitude weightings were constructed and teleported as illustrated in Fig B.5. In keeping with Section , we omit normalisation in the states for simplicity. Here the states, $|\psi\rangle = 2|-1\rangle + 3|0\rangle + |1\rangle$, $|\psi\rangle = 2|-2\rangle + 3|0\rangle + |2\rangle$, (c) $|\psi\rangle = |-2\rangle + 2|0\rangle + |2\rangle$ and $|\psi\rangle = 2|-3\rangle + |-1\rangle + |1\rangle + 2|4\rangle$ were prepared and shown in Fig B.5 (a) to (d), respectively. The bar outlines indicate the prepared state weights. Filled-in areas then show the measured values after teleportation to Bob's arm. Subsequently, similarities of (a) 0.98 $\pm$0.078, (b) 0.99 $\pm$0.072, (c) 0.99 $\pm$0.061 and (d) 0.95 $\pm$0.04 were calculated, using Eq. 3.33 in Section 3.2.6. Good agreement between the prepared and measured values can thus be seen, indicating that general states with different amplitudes may be teleported using our scheme.

B.7 Raw experimental measurements with uncertainties

Additional plots are given in this section showing the uncertainties related to measurements in Section 3.2 where it was not possible to plot the error bars. Figure B.6 shows the tomography data that was taken in order to reconstruct the

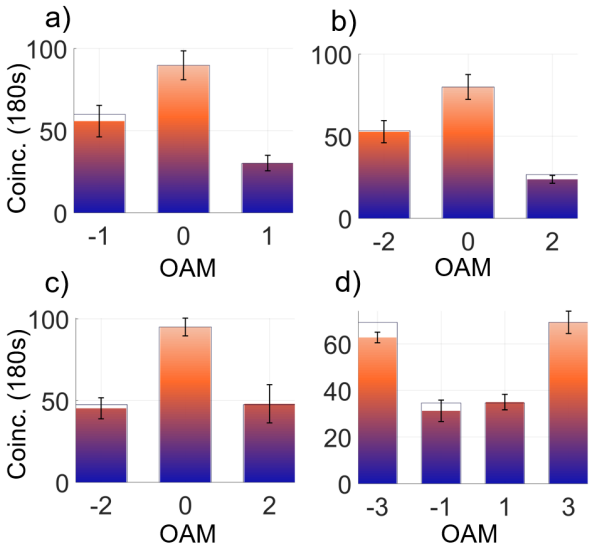


FIGURE B.5: **Teleportation of unevenly weighted states.** Experimental measurements (filled bars) of uneven encoded superposition states (bar outlines) for (a) $|\psi\rangle = 2|-1\rangle + 3|0\rangle + |1\rangle$, (b) $|\psi\rangle = 2|-2\rangle + 3|0\rangle + |2\rangle$, (c) $|\psi\rangle = |-2\rangle + 2|0\rangle + |2\rangle$ and (d) $|\psi\rangle = 2|-3\rangle + |-1\rangle + |1\rangle + 2|4\rangle$. Uncertainties are calculated from multiple measurements.

three-dimensional channel density matrix that was provided in Fig. 3.7. The two-dimensional superposition sub-spaces are indicated by the brackets with the general form of the superposition shown above. The set of values $[0, \frac{\pi}{2}, \pi, \frac{3\pi}{2}]$ gives the specific θ angle used to generate the state prepared and/or measured. The values printed in each of the measurement blocks show the experimental standard deviation.

Uncertainties associated with the detection matrix for the four-dimensional MUB constructed from $\ell = [-3, -1, 1, 3]$ in Fig. 3.7 is shown in Fig. B.7. Similarly to Fig. B.6, the false colormap indicates the coincidences measured with each of the respective errors printed in the measurement blocks.

Figure B.8 shows the raw averaged measurements taken for the three-dimensional state tomography across all 12 MUB states as was listed in Eq. B.14-B.24. Here the colormap indicates the coincidence counts measured over a 120s and the printed values in the measurement blocks indicates the standard deviation associated with each measurement. The phase profiles of each MUB state are shown as insets along the x- and y- axes in the figure. As can be seen, clear detection of the prepared MUB state is obtained which is given by the strong diagonal with close to null values in the off-diagonal terms in each basis. Based on these measurements, the density matrix ρ_{Ex}, for each of the teleported MUB states was reconstructed using the maximum likelihood algorithm [114, 119].

We give the standard deviations of the largest spiral bandwidth plot taken in Fig. B.9. This corresponds to the spiral bandwidth ranging from $\ell = [-8, 8]$ shown in the subplot of Fig. 3.6. The false colour shows the average coincidences detected over a 240s integration time with the numbers again giving the calculated standard deviation obtained from each measurement.

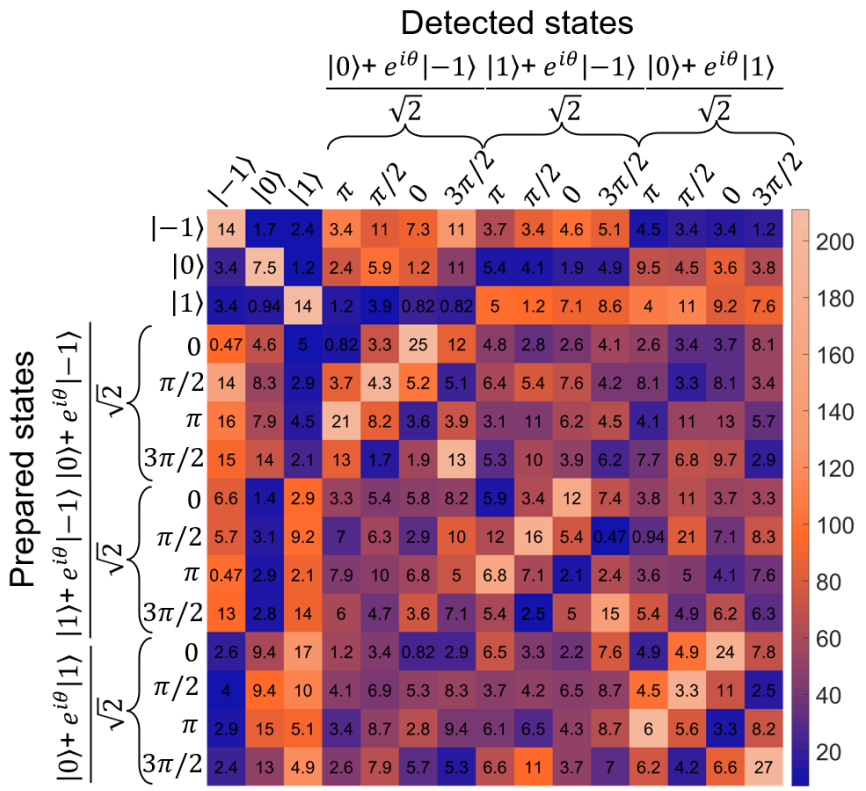


FIGURE B.6: **Channel tomography measurements with uncertainties.** Experimental measurement plot shown with the detected coincidences given by the false colormap and the associated uncertainties, calculated from multiple measurements, printed in each measurement block. $\theta = 0, \frac{\pi}{2}, \pi$ and $\frac{3\pi}{2}$ as indicated for each of the bracketed superposition subspaces.

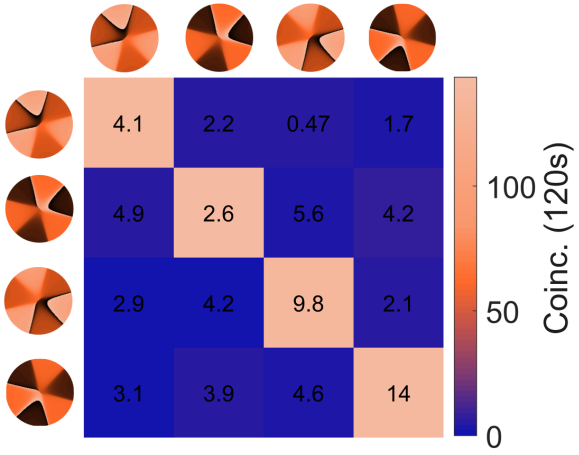


FIGURE B.7: **Four-dimensional MUB measurements with uncertainties.** Experimental measurement plot shown with the detected coincidences given by the false colormap and the associated uncertainties, calculated from multiple measurements, printed in each measurement block.

B.8 Teleportation fidelity results

In Fig. B.10 we show the fidelities measured from the dimensionality and purity test [131]. Our method extracts the fidelity of the channel F_{Ch} described in Section B.2. From this we can compute the expected fidelity for each photon that Bob receives

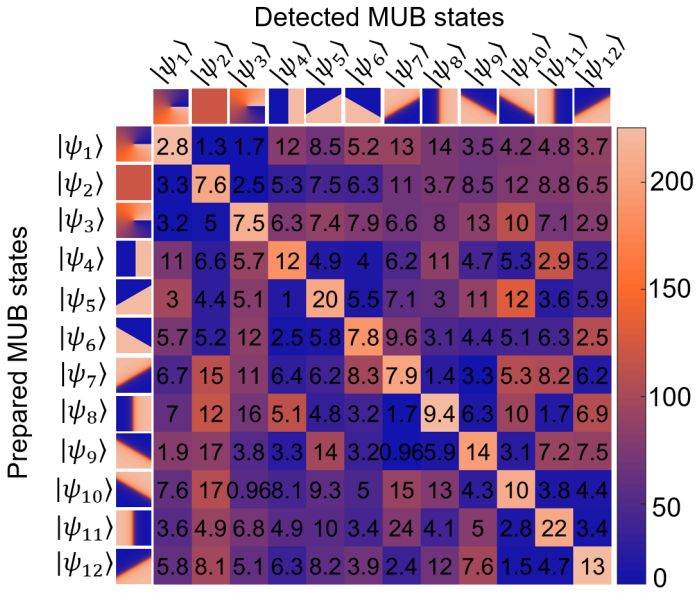


FIGURE B.8: **Teleported MUB states tomography.** Experimental state tomography measurements measured with an integration with of 120s performed on the 12 MUB states for a d = 3 space comprised OAM modes ℓ = {-1,0,1}. Numbers printed on the measurement blocks indicate the associated standard deviations measured from multiple measurements.

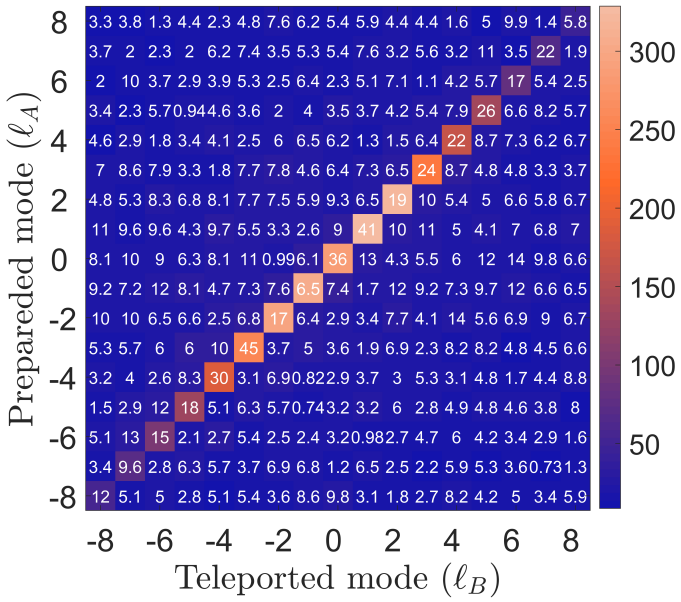


FIGURE B.9: **Spiral bandwidth measured for high dimensionally tuned setup.** Experimental measurements with standard deviations, calculated from multiple rounds, printed on the average coincidences shown by the false colormap for the spiral bandwidth of an optimally tuned system where $K \approx 15$.

as $\mathcal{F} = \frac{F_{Cl}d+1}{d+1}$ [281]. Since our spectrum was not uniform, i.e., resembling a system with perfect correlation, we also show the expected fidelity (F_{max}) for such a system. Nonetheless, our measurements are all above the classical teleportation bound while d = 2, 3 and 4 are above cloning bound.

One aspect to note is the Gaussian-like falloff of the experimentally measured correlations as the higher order modes are detected in both the SPDC entangled

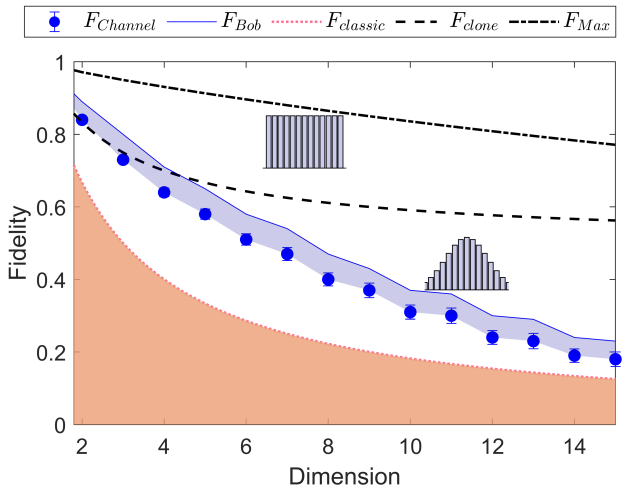


FIGURE B.10: **Teleportation Fidelities.** The measured teleportation fidelities for the channel ($F_{channel}$) for states that bob receives (F_{Bob}). The classical ($F_{classic}$) and cloning bounds (F_{clone}) are also shown. Our system shows the possibility of teleporting up to $d = 4$ dimensions. Moreover, since our spectrum for the OAM basis was not flat (maximal correlations), we show how a flat spectrum would improve the teleportation fidelities (F_{max}) under the same experimental conditions.

photons which were measured in Fig. 3.13 as well as the teleportation signal shown in figures such as Fig. B.3. This feature of such higher-order modes is well-known and studied due to the detection sizes as described in Section 2.3 and effect of the SPDC pump shape [221, 222]. In the process of optimising the teleportation channel bandwidth, however, the modal detection and up-conversion sizes were incidentally adjusted such that the first three modes (i.e. $|-1\rangle, |0\rangle$ and $|1\rangle$) were especially flat with respect to each other. This is shown in the example distribution given in Fig. B.11 as well as seen in the projective measurements shown in Fig. B.6. As such, for

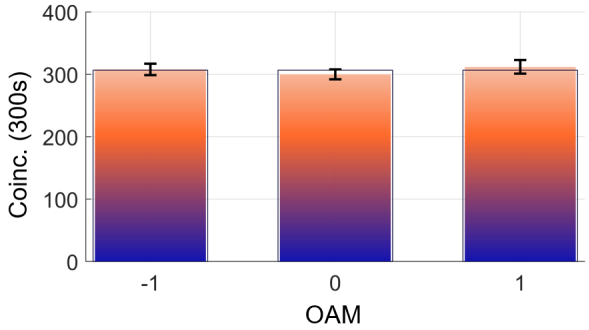


FIGURE B.11: **Size-matched flattened modes.** Example of the experimentally measured teleported spectrum diagonal for the lowest three modes used to comprise the twelve $d = 3$ MUB teleported states. Error bars are calculated from multiple measurements.

these lower order modes, the system correlations resembled the prefect correlations indicated by the F_{max} (dotted line) more closely than the Gaussian fall-off model used to extract the fidelities as given by the blue dots and lines. With this factor, the MUB states comprised of these modes gave higher than predicted fidelities shown in Fig. B.4 with values ranging between 0.82 and 0.96 (which is close to the F_{max} value for $d = 3$).

Appendix C

Supplementary information for detecting phase images

C.1 Revealing the embedded phase information

Suppose we have an object that can be represented using a discrete pixel location states $\{|\mathbf{r}_j\rangle\}$. Since the object can be represented as a matrix, $\mathbf{O}$, we can also use a matrix basis, $\{\mathbf{R}_j,\ j = 0, 1, ..N-1\}$ where, to map each pixel location in two-dimensional space. The matrices have d by d dimensions for corresponding x and y directions, respectively.

The quantity computed in the ghost imaging experiment can be written as [360]

$$\mathbf{GI} = 1/N \sum_{j=0}^{N-1} \Big[|c_j|^2 - \langle |c_j|^2 \rangle_N \Big] \mathbf{T}_j, \tag{C.1}$$

The coefficients c_j correspond to the overlap probability between the object and the mask $\mathbf{T}_j$ represented by a (d, d) matrix. The masks, $\mathbf{T}_j$, are computed from the Hadamard basis $\{\mathbf{M}_j \equiv |M_j\rangle\ ,\ j = 0, 1, ..N = d^2\}$

$$\mathbf{T}_j = \frac{1}{\sqrt{2}}(\mathbf{M}_j + \mathbf{M}_0). \tag{C.2}$$

Each mode, $\mathbf{M}_j$, is found by computing outer products of column vectors of the d dimensional Walsh-Hadamard transform matrix H_d, i.e., $\mathbf{M}_{j\to(m,n)} = h_n \otimes h_m$ and can be written as a superposition of the original pixel location basis, $\{\mathbf{R}_j,\ j = 1, 2, ..d^2\}$. Here $\mathbf{M}_0$ is a reference mode that rescales the pixels (equivalently matrix entries) from having values proportion to -1 and 1 to now having 0s and 1s.

Given Eq. C.2 and, we can express the overlap probabilities as

$$\mathbf{GI} = 1/N \sum_{j=0}^{N-1} \Big[|c_j|^2 - \langle |c_j|^2 \rangle_N \Big] \mathbf{M}_j, \tag{C.3}$$

showing that we only need the basis $\{\mathbf{M}_j\}$ in the reconstruction. Next, we expand the detection probabilities

$$\begin{aligned} |c_j|^2 &= |\langle T_j | O \rangle|^2, \\ &= p_0/2 + p_j/2 + \sqrt{p_o p_j} \cos(\Delta\alpha_j), \end{aligned} \tag{C.4}$$

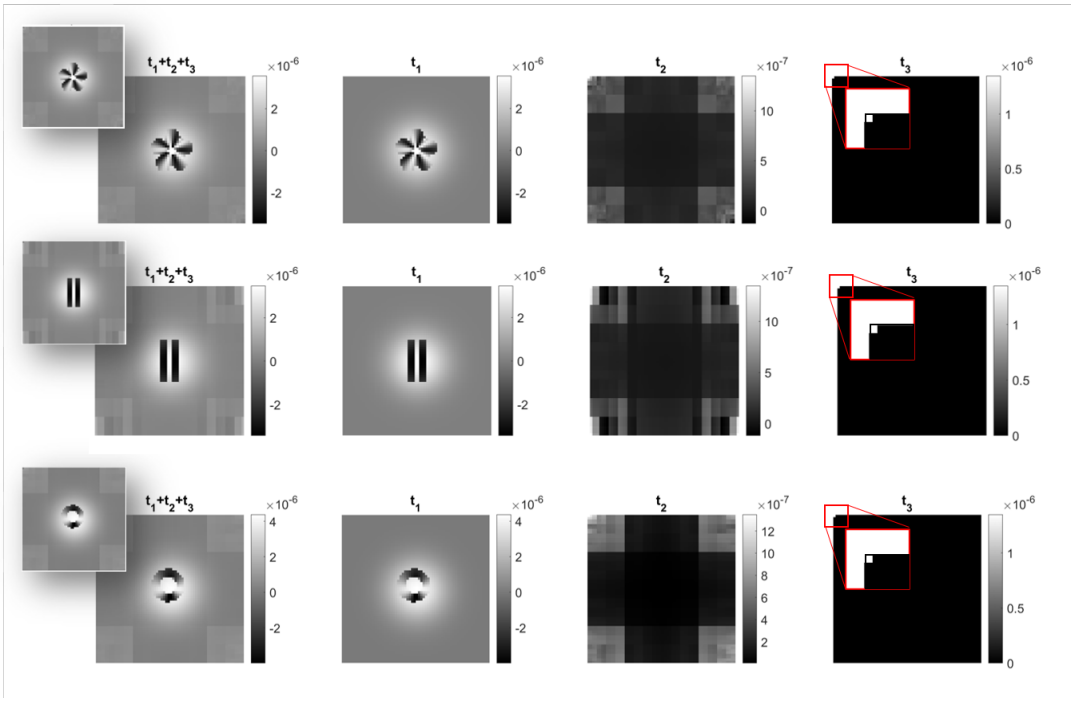


FIGURE C.1: Examples of the computed terms in the ghost imaging protocol. Here the labels $t_{1,2,3}$ correspond to the first, second and third term in $\mathbf{GI}_{\cos}$. The inset in the firs column corresponds to the ghost image obtained from the algorithm in Eq C.1. The insets in the fourth column show the DC component to be subtracted.

where $\Delta\alpha_j = \alpha_j + \alpha_0$. The resulting probabilities are proportional to the joint probability between the two photons when measured in coincidence. Here we have assumed that the object can be decomposed as in the Hadamard basis following

$$\mathbf{O} = \sum_{k}^{N} \sqrt{p_k} e^{i\alpha_k} \mathbf{M}_j, \tag{C.5}$$

or equivalently using braket notation

$$|O\rangle = \sum_{k} \sqrt{p_k} e^{i\alpha_k} \left|M_j\right\rangle, \tag{C.6}$$

with given probabilities $p_k = |\langle O, M_K | O, M_K \rangle|^2$ and phase α_k. Another important point to note is that the probabilities, p_k, can also be computed as a matrix,

$$\mathbf{P} = \left(\sum_{j=0}^{N-1} p_j \mathbf{R}_j \right), \tag{C.7}$$

which will be useful later for computing the final ghost image.

Next, we expand the coefficients in Eq. C.3 using Eq. C.4 and further simply it

$$\begin{aligned} \mathbf{GI}_{\cos} = & 1/N \sum_{j=0}^{N-1} \Big[\sqrt{p_0 p_j} \cos(\Delta\alpha_j) + \frac{p_j}{2} - \\ & \left(\langle p_j \rangle_N / 2 + \sqrt{p_0} \langle p_j \cos(\Delta\alpha_j) \rangle_N \right) \Big] \mathbf{M}_j. \end{aligned} \tag{C.8}$$

We see that the first term can be computed from the real part of Eq. C.5

$$\begin{aligned}\frac{\sqrt{p_0}}{N}\mathrm{Re}\left[\mathbf{O}\right] :=& \frac{1}{N}\sum_{j=0}^{N-1}\sqrt{p_0 p_j}\cos\left(\Delta\alpha_j\right)\mathbf{M}_j \\ =& \frac{\sqrt{p_0}}{N}|\mathbf{O}|\cos\left(\arg\left(\mathbf{O}\right)-\alpha_0\right).\end{aligned} \tag{C.9}$$

For the second term in Eq. C.8 we invoke Eq. C.7 and compute,

$$\begin{aligned}\sum_{j=0}^{N-1} p_j\mathbf{M}_j =& \frac{1}{2N}\sum_{j=0}^{N-1} p_j\mathbf{H}_d\mathbf{R}_j\mathbf{H}_d^\dagger \\ =& \frac{1}{2N}\mathbf{H}_d\left(\sum_{j=0}^{N-1} p_j\mathbf{R}_j\right)\mathbf{H}_d^\dagger \\ =& \frac{1}{2N}\mathbf{H}_d\mathbf{P}\mathbf{H}_d^\dagger,\end{aligned} \tag{C.10}$$

showing that it can be computed from a simple Hadamard transform of the probability matrix. Furthermore, the matrix $\mathbf{P}$ can also be computed via the Hadamard transform, as $P = |\mathbf{H}_d\mathbf{O}\mathbf{H}_d|^2$, where $|\cdot|^2$ is the element wise absolute value squared. This can be seen by substituting Eq. C.5 as follows,

$$\begin{aligned}\mathbf{P} = |\mathbf{H}_d\mathbf{O}\mathbf{H}_d|^2 =& |\mathbf{H}_d\sum_{k}^{N}\sqrt{p_k}e^{i\alpha_k}\mathbf{M}_k\mathbf{H}_d^\dagger|^2, \\ =& \sum_{k}^{N}|\sqrt{p_k}e^{i\alpha_k}|^2\mathbf{H}_d\mathbf{M}_k\mathbf{H}_d^\dagger, \\ =& \left(\sum_{k=0}^{N-1} p_k\mathbf{R}_k\right).\end{aligned} \tag{C.11}$$

Computing the matrix $\mathbf{P}$ using the transform is less computationally expensive than computing the coefficients p_k via the modal overlaps.

Finally, as for the last term in Eq. C.8, we can take the ensemble averages $g_{\cos} = \sqrt{N}/N(\langle p_j\rangle_N/2 + \sqrt{p_0}\langle p_j\cos\left(\Delta\alpha_j\right)\rangle_N)$ outside the summation and remain with $\sum_{j=0}^{N-1} 1/\sqrt{N}\mathbf{M}_j = \mathbf{R}_0$ which is the DC component.

Using Eq. C.9 and Eq. C.10 we can write Eq. C.8 as

$$\mathbf{GI}_{\cos} = \frac{1}{N}\left(\sqrt{p_0}\mathrm{Re}\left(\mathbf{O}\right) + \frac{1}{2}\mathbf{H}_d\mathbf{P}\mathbf{H}_d^\dagger - g_{\cos}\mathbf{R}_0\right). \tag{C.12}$$

We summarise the meaning of each term: (i) term 1 is the real part of the object profile up a global phase α_0, term 2 depends on the spectral density of the object, while the last term corresponds to the DC component.

Following the same arguments, the imaginary part of the ghost image can be computed by applying the same analysis but with $\mathbf{T}_j = \frac{1}{\sqrt{2}}(\mathbf{M}_j + i\mathbf{M}_0)$, resulting in the probabilities becoming

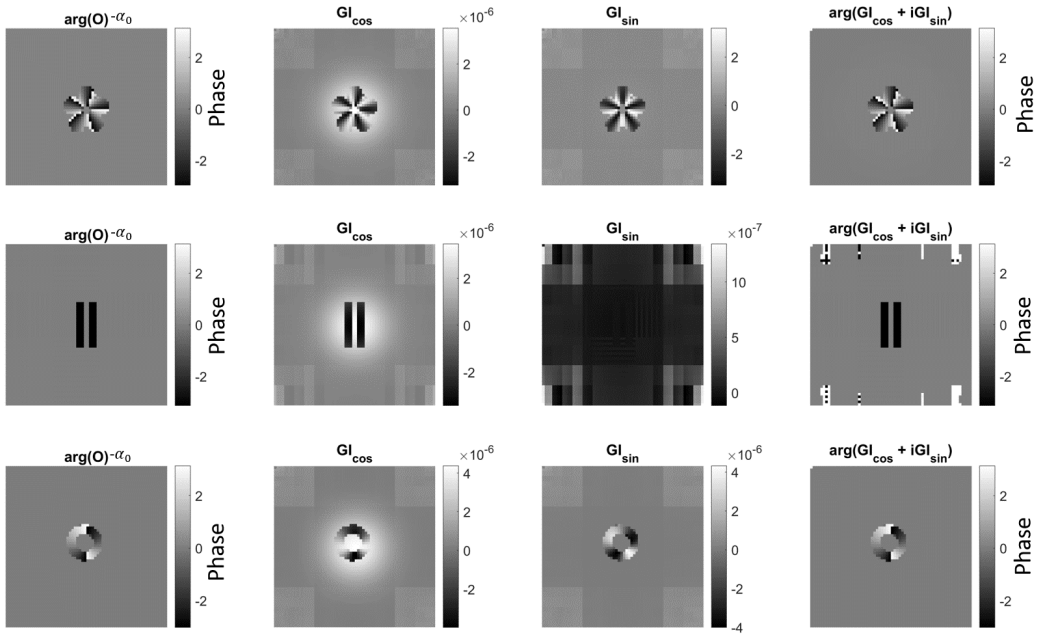


FIGURE C.2: Example theoretical phase reconstruction from the ghost images.

$|c_j|^2 = p_0/2 + p_j + \sqrt{p_0 p_j}\sin(\Delta\alpha_j)$. Accordingly, the ghost image becomes

$$\mathbf{GI}_{\sin} = \frac{1}{N}\left(\sqrt{p_0}\mathrm{Im}\left(\mathbf{O}\right) + \frac{1}{2}\mathbf{H}_d\mathbf{P}\mathbf{H}_d^{\dagger} - g_{\sin}\mathbf{R}_0\right), \tag{C.13}$$

having an embedded imaginary part of the object profile $\mathrm{Im}\left(\mathbf{O}\right) = |\mathbf{O}|\sin\left(\arg\left(\mathbf{O}\right) - \alpha_0\right)$ and $g_{\sin} = \sqrt{N}/N\left(\langle p_j\rangle_N/2 + \sqrt{p_0}\langle p_j\sin(\Delta\alpha_j)\rangle_N\right)$.

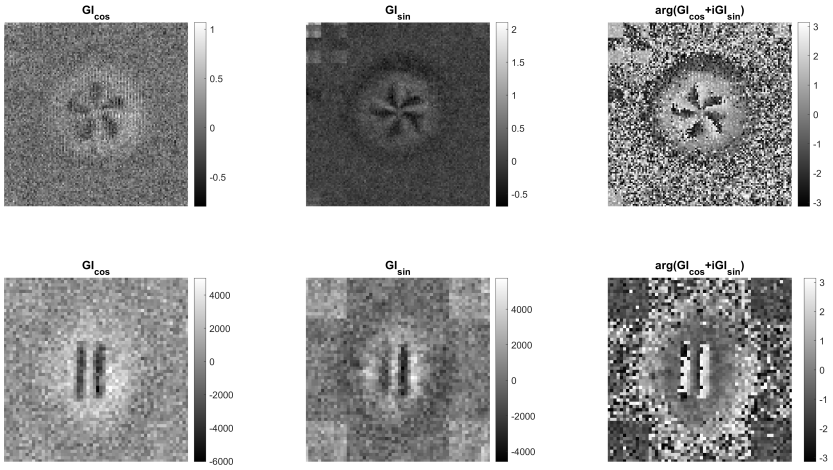


FIGURE C.3: Uncropped experimentally measured ghost images.

Bibliography

1. Fort, C. *The complete books of Charles Fort* (Courier Corporation, 1974).
2. Vaidman, L. *Teleportation: Dream or reality?* in *AIP Conference Proceedings* **461** (1999), 172–184.
3. Bennett, C. H. *et al.* Teleporting an unknown quantum state via dual classical and Einstein-Podolsky-Rosen channels. *Physical Review Letters* **70,** 1895 (1993).
4. Nielsen, M. A. & Chuang, I. *Quantum computation and quantum information* (Cambridge University Press, 2002).
5. Wilde, M. M. *Quantum information theory* (Cambridge University Press, 2013).
6. Weedbrook, C. *et al.* Gaussian quantum information. *Reviews of Modern Physics* **84,** 621 (2012).
7. Braunstein, S. L. & Van Loock, P. Quantum information with continuous variables. *Reviews of Modern Physics* **77,** 513 (2005).
8. Gisin, N., Ribordy, G., Tittel, W. & Zbinden, H. Quantum cryptography. *Reviews of Modern Physics* **74,** 145–195 (2002).
9. Briegel, H.-J., Dür, W., Cirac, J. I. & Zoller, P. Quantum repeaters: the role of imperfect local operations in quantum communication. *Physical Review Letters* **81,** 5932 (1998).
10. Raussendorf, R. & Briegel, H. J. A one-way quantum computer. *Physical Review Letters* **86,** 5188 (2001).
11. Gottesman, D. & Chuang, I. L. Demonstrating the viability of universal quantum computation using teleportation and single-qubit operations. *Nature* **402,** 390–393 (1999).
12. Kimble, H. J. The quantum internet. *Nature* **453,** 1023–1030 (2008).
13. Lloyd, S. *et al.* Closed timelike curves via postselection: theory and experimental test of consistency. *Physical Review Letters* **106,** 040403 (2011).
14. Nielsen, M. A., Knill, E. & Laflamme, R. Complete quantum teleportation using nuclear magnetic resonance. *Nature* **396,** 52–55 (1998).
15. Sherson, J. F. *et al.* Quantum teleportation between light and matter. *Nature* **443,** 557–560 (2006).
16. Krauter, H. *et al.* Deterministic quantum teleportation between distant atomic objects. *Nature Physics* **9,** 400–404 (2013).
17. Chen, Y.-A. *et al.* Memory-built-in quantum teleportation with photonic and atomic qubits. *Nature Physics* **4,** 103–107 (2008).
18. Bao, X.-H. *et al.* Quantum teleportation between remote atomic-ensemble quantum memories. *Proceedings of the National Academy of Sciences* **109,** 20347–20351 (2012).
19. Gao, W. *et al.* Quantum teleportation from a propagating photon to a solid-state spin qubit. *Nature Communications* **4,** 1–8 (2013).

20. Bussières, F. *et al.* Quantum teleportation from a telecom-wavelength photon to a solid-state quantum memory. *Nature Photonics* **8,** 775–778 (2014).
21. Steffen, L. *et al.* Deterministic quantum teleportation with feed-forward in a solid state system. *Nature* **500,** 319–322 (2013).
22. Pfaff, W. *et al.* Unconditional quantum teleportation between distant solid-state quantum bits. *Science* **345,** 532–535 (2014).
23. Barrett, M. *et al.* Deterministic quantum teleportation of atomic qubits. *Nature* **429,** 737–739 (2004).
24. Riebe, M. *et al.* Deterministic quantum teleportation with atoms. *Nature* **429,** 734–737 (2004).
25. Riebe, M. *et al.* Quantum teleportation with atoms: quantum process tomography. *New Journal of Physics* **9,** 211 (2007).
26. Olmschenk, S. *et al.* Quantum teleportation between distant matter qubits. *Science* **323,** 486–489 (2009).
27. Nölleke, C. *et al.* Efficient teleportation between remote single-atom quantum memories. *Physical Review Letters* **110,** 140403 (2013).
28. Furusawa, A. *et al.* Unconditional quantum teleportation. *science* **282,** 706–709 (1998).
29. Bowen, W. P. *et al.* Experimental investigation of continuous-variable quantum teleportation. *Physical Review A* **67,** 032302 (2003).
30. Zhang, T. C., Goh, K., Chou, C., Lodahl, P. & Kimble, H. J. Quantum teleportation of light beams. *Physical Review A* **67,** 033802 (2003).
31. Takei, N., Yonezawa, H., Aoki, T. & Furusawa, A. High-fidelity teleportation beyond the no-cloning limit and entanglement swapping for continuous variables. *Physical Review Letters* **94,** 220502 (2005).
32. Yonezawa, H., Braunstein, S. L. & Furusawa, A. Experimental demonstration of quantum teleportation of broadband squeezing. *Physical Review Letters* **99,** 110503 (2007).
33. Takei, N. *et al.* Experimental demonstration of quantum teleportation of a squeezed state. *Physical Review A* **72,** 042304 (2005).
34. Lee, N. *et al.* Teleportation of nonclassical wave packets of light. *Science* **332,** 330–333 (2011).
35. Yukawa, M., Benichi, H. & Furusawa, A. High-fidelity continuous-variable quantum teleportation toward multistep quantum operations. *Physical Review A* **77,** 022314 (2008).
36. Takeda, S., Mizuta, T., Fuwa, M., Van Loock, P. & Furusawa, A. Deterministic quantum teleportation of photonic quantum bits by a hybrid technique. *Nature* **500,** 315–318 (2013).
37. Braunstein, S. L. & Kimble, H. J. Teleportation of continuous quantum variables. *Physical Review Letters* **80,** 869 (1998).
38. Vaidman, L. Teleportation of quantum states. *Physical Review A* **49,** 1473 (1994).
39. Bouwmeester, D. *et al.* Experimental quantum teleportation. *Nature* **390,** 575–579 (1997).
40. Ursin, R. *et al.* Quantum teleportation across the Danube. *Nature* **430,** 849–849 (2004).

41. Boschi, D., Branca, S., De Martini, F., Hardy, L. & Popescu, S. Experimental realization of teleporting an unknown pure quantum state via dual classical and Einstein-Podolsky-Rosen channels. *Physical Review Letters* **80,** 1121 (1998).

42. Jin, X.-M. *et al.* Experimental free-space quantum teleportation. *Nature Photonics* **4,** 376–381 (2010).

43. Kim, Y.-H., Kulik, S. P. & Shih, Y. Quantum teleportation of a polarization state with a complete Bell state measurement. *Physical Review Letters* **86,** 1370 (2001).

44. Yin, J. *et al.* Quantum teleportation and entanglement distribution over 100-kilometre free-space channels. *Nature* **488,** 185–188 (2012).

45. Ma, X.-S. *et al.* Quantum teleportation over 143 kilometres using active feed-forward. *Nature* **489,** 269–273 (2012).

46. Marcikic, I., De Riedmatten, H., Tittel, W., Zbinden, H. & Gisin, N. Long-distance teleportation of qubits at telecommunication wavelengths. *Nature* **421,** 509–513 (2003).

47. De Riedmatten, H. *et al.* Long distance quantum teleportation in a quantum relay configuration. *Physical Review Letters* **92,** 047904 (2004).

48. Landry, O., van Houwelingen, J. A. W., Beveratos, A., Zbinden, H. & Gisin, N. Quantum teleportation over the Swisscom telecommunication network. *JOSA B* **24,** 398–403 (2007).

49. Lombardi, E., Sciarrino, F., Popescu, S. & De Martini, F. Teleportation of a vacuum–one-photon qubit. *Physical Review Letters* **88,** 070402 (2002).

50. Giacomini, S., Sciarrino, F., Lombardi, E. & De Martini, F. Active teleportation of a quantum bit. *Physical Review A* **66,** 030302 (2002).

51. Fattal, D., Diamanti, E., Inoue, K. & Yamamoto, Y. Quantum teleportation with a quantum dot single photon source. *Physical Review Letters* **92,** 037904 (2004).

52. Metcalf, B. J. *et al.* Quantum teleportation on a photonic chip. *Nature Photonics* **8,** 770–774 (2014).

53. Wang, X.-L. *et al.* Quantum teleportation of multiple degrees of freedom of a single photon. *Nature* **518,** 516–519 (2015).

54. Xia, X.-X., Sun, Q.-C., Zhang, Q. & Pan, J.-W. Long distance quantum teleportation. *Quantum Science and Technology* **3,** 014012 (2017).

55. Takesue, H. *et al.* Quantum teleportation over 100 km of fiber using highly efficient superconducting nanowire single-photon detectors. *Optica* **2,** 832–835 (2015).

56. Valivarthi, R. *et al.* Teleportation systems toward a quantum internet. *PRX Quantum* **1,** 020317 (2020).

57. Herbst, T. *et al.* Teleportation of entanglement over 143 km. *Proceedings of the National Academy of Sciences* **112,** 14202–14205 (2015).

58. Ren, J.-G. *et al.* Ground-to-satellite quantum teleportation. *Nature* **549,** 70–73 (2017).

59. Simon, C. Towards a global quantum network. *Nature Photonics* **11,** 678–680 (2017).

60. Wehner, S., Elkouss, D. & Hanson, R. Quantum internet: A vision for the road ahead. *Science* **362** (2018).

61. Gisin, N. & Massar, S. Optimal quantum cloning machines. *Physical Review Letters* **79,** 2153 (1997).
62. Bouchard, F., Fickler, R., Boyd, R. W. & Karimi, E. High-dimensional quantum cloning and applications to quantum hacking. *Science Advances* **3,** e1601915 (2017).
63. Bouchard, F. *et al.* Experimental investigation of high-dimensional quantum key distribution protocols with twisted photons. *Quantum* **2,** 111 (2018).
64. Bechmann-Pasquinucci, H. & Tittel, W. Quantum cryptography using larger alphabets. *Physical Review A* **61,** 062308 (2000).
65. Cerf, N. J., Bourennane, M., Karlsson, A. & Gisin, N. Security of quantum key distribution using d-level systems. *Physical Review Letters* **88,** 127902 (2002).
66. Ali-Khan, I., Broadbent, C. J. & Howell, J. C. Large-alphabet quantum key distribution using energy-time entangled bipartite states. *Physical Review Letters* **98,** 060503 (2007).
67. Ecker, S. *et al.* Overcoming noise in entanglement distribution. *Phys Rev X* **9,** 041042 (2019).
68. Luo, Y.-H. *et al.* Quantum teleportation in high dimensions. *Physical Review Letters* **123,** 070505 (2019).
69. Hu, X.-M. *et al.* Experimental high-dimensional quantum teleportation. *Physical Review Letters* **125,** 230501 (2020).
70. Son, W., Lee, J., Kim, M. & Park, Y.-J. Conclusive teleportation of a d-dimensional unknown state. *Physical Review A* **64,** 064304 (2001).
71. Werner, R. F. All teleportation and dense coding schemes. *Journal of Physics A: Mathematical and General* **34,** 7081 (2001).
72. Molotkov, S. Quantum teleportation of a single-photon wave packet. *Physics Letters A* **245,** 339–344 (1998).
73. Walborn, S. P., Monken, C., Pádua, S. & Ribeiro, P. S. Spatial correlations in parametric down-conversion. *Physics Reports* **495,** 87–139 (2010).
74. Humble, T. S. Spectral and spread-spectral teleportation. *Physical Review A* **81,** 062339 (2010).
75. Kumar, P. Quantum frequency conversion. *Optics Letters* **15,** 1476–1478 (1990).
76. Liu, S., Lou, Y. & Jing, J. Orbital angular momentum multiplexed deterministic all-optical quantum teleportation. *Nature Communications* **11,** 1–8 (2020).
77. Forbes, A., de Oliveira, M. & Dennis, M. R. Structured light. *Nature Photonics* **15,** 253–262 (2021).
78. Ndagano, B. & Forbes, A. Characterization and mitigation of information loss in a six-state quantum-key-distribution protocol with spatial modes of light through turbulence. *Physical Review A* **98,** 062330 (2018).
79. Mafu, M. *et al.* Higher-dimensional orbital-angular-momentum-based quantum key distribution with mutually unbiased bases. *Physical Review A* **88,** 032305 (2013).
80. Mirhosseini, M. *et al.* High-dimensional quantum cryptography with twisted light. *New Journal of Physics* **17,** 033033 (2015).
81. Hufnagel, F. *et al.* Underwater quantum communication over a 30-meter flume tank. *arXiv 2004.04821* (2020).

82. Wang, F.-X. *et al.* Characterizing High-Quality High-Dimensional Quantum Key Distribution by State Mapping Between Different Degrees of Freedom. *Physical Review Applied* **11,** 024070 (2019).

83. Sit, A. *et al.* High-dimensional intracity quantum cryptography with structured photons. *Optica* **4,** 1006 (2017).

84. Nape, I. *et al.* Self-healing high-dimensional quantum key distribution using hybrid spin-orbit Bessel states. *Optics Express* **26,** 26946–26960 (2018).

85. Cozzolino, D. *et al.* Orbital angular momentum states enabling fiber-based high-dimensional quantum communication. *Physical Review Applied* **11,** 064058 (2019).

86. Chen, Y. *et al.* Underwater transmission of high-dimensional twisted photons over 55 meters. *PhotoniX* **1,** 5 (2020).

87. Martin, A. *et al.* Quantifying photonic high-dimensional entanglement. *Physical Review Letters* **118,** 110501 (2017).

88. Kues, M. *et al.* On-chip generation of high-dimensional entangled quantum states and their coherent control. *Nature* **546,** 622–626 (2017).

89. Schaeff, C., Polster, R., Huber, M., Ramelow, S. & Zeilinger, A. Experimental access to higher-dimensional entangled quantum systems using integrated optics. *Optica* **2,** 523–529 (2015).

90. Hu, X.-M. *et al.* Efficient generation of high-dimensional entanglement through multipath down-conversion. *Physical Review Letters* **125,** 090503 (2020).

91. Valencia, N. H. *et al.* High-dimensional pixel entanglement: efficient generation and certification. *Quantum* **4,** 376 (2020).

92. Metcalf, H. J. & van der Straten, P. in *Laser Cooling and Trapping* 39–56 (Springer New York, New York, NY, 1999). ISBN: 978-1-4612-1470-0.

93. Einstein, A., Podolsky, B. & Rosen, N. Can quantum-mechanical description of physical reality be considered complete? *Physical Review* **47,** 777 (1935).

94. Bell, J. S. & Bell, J. S. *Speakable and unspeakable in quantum mechanics: Collected papers on quantum philosophy* (Cambridge university press, 2004).

95. Terhal, B. M. & Horodecki, P. Schmidt number for density matrices. *Physical Review A* **61,** 040301 (2000).

96. Law, C. & Eberly, J. Analysis and interpretation of high transverse entanglement in optical parametric down conversion. *Physical Review Letters* **92,** 127903 (2004).

97. Pors, J. *et al.* Shannon dimensionality of quantum channels and its application to photon entanglement. *Physical Review Letters* **101,** 120502 (2008).

98. Wootters, W. K. & Zurek, W. H. A single quantum cannot be cloned. *Nature* **299,** 802–803 (1982).

99. Forbes, A. & Nape, I. Quantum mechanics with patterns of light: progress in high dimensional and multidimensional entanglement with structured light. *AVS Quantum Science* **1,** 011701 (2019).

100. Erhard, M., Fickler, R., Krenn, M. & Zeilinger, A. Twisted photons: new quantum perspectives in high dimensions. *Light: Science & Applications* **7,** 17146–17146 (2018).

101. Griffiths, D. J. *Introduction to electrodynamics* (Pearson Education Inc., 2005).
102. Andrews, D. L. & Babiker, M. *The angular momentum of light* (Cambridge University Press, 2012).
103. Allen, L., Beijersbergen, M. W., Spreeuw, R. & Woerdman, J. Orbital angular momentum of light and the transformation of Laguerre-Gaussian laser modes. *Physical Review A* **45,** 8185 (1992).
104. Rosales-Guzmán, C. & Forbes, A. *How to shape light with spatial light modulators* 57. ISBN: 9781510613027 (SPIE Press, 2017).
105. Marrucci, L., Manzo, C. & Paparo, D. Optical spin-to-orbital angular momentum conversion in inhomogeneous anisotropic media. *Physical Review Letters* **96,** 163905 (2006).
106. Brasselet, E., Murazawa, N., Misawa, H. & Juodkazis, S. Optical vortices from liquid crystal droplets. *Physical Review Letters* **103,** 103903 (2009).
107. Kim, J. *et al.* Fabrication of ideal geometric-phase holograms with arbitrary wavefronts. *Optica* **2,** 958–964 (2015).
108. Devlin, R. C. *et al.* Spin-to-orbital angular momentum conversion in dielectric metasurfaces. *Optics Express* **25,** 377–393 (2017).
109. Sephton, B., Dudley, A. & Forbes, A. Revealing the radial modes in vortex beams. *Applied Optics* **55,** 7830–7835 (2016).
110. Karimi, E., Zito, G., Piccirillo, B., Marrucci, L. & Santamato, E. Hypergeometric-gaussian modes. *Optics Letters* **32,** 3053–3055 (2007).
111. O'Sullivan-Hale, M. N., Khan, I. A., Boyd, R. W. & Howell, J. C. Pixel entanglement: experimental realization of optically entangled d= 3 and d= 6 qudits. *Physical Review Letters* **94,** 220501 (2005).
112. Pauli, W. *Handbuch der Physik, Quantentheorie* 1933.
113. Wootters, W. K. & Fields, B. D. Optimal state-determination by mutually unbiased measurements. *Annals of Physics* **191,** 363–381 (1989).
114. James, D. F. V., Kwiat, P. G., Munro, W. J. & White, A. G. Measurement of qubits. *Phys. Rev. A* **64,** 052312 (5 2001).
115. Vaziri, A., Weihs, G. & Zeilinger, A. Experimental two-photon, three-dimensional entanglement for quantum communication. *Physical Review Letters* **89,** 240401 (2002).
116. Gröblacher, S., Jennewein, T., Vaziri, A., Weihs, G. & Zeilinger, A. Experimental quantum cryptography with qutrits. *New Journal of Physics* **8,** 75 (2006).
117. Dada, A. C., Leach, J., Buller, G. S., Padgett, M. J. & Andersson, E. Experimental high-dimensional two-photon entanglement and violations of generalized Bell inequalities. *Nature Physics* **7,** 677–680 (2011).
118. Renes, J. M., Blume-Kohout, R., Scott, A. J. & Caves, C. M. Symmetric informationally complete quantum measurements. *Journal of Mathematical Physics* **45,** 2171–2180 (2004).
119. Agnew, M., Leach, J., McLaren, M., Roux, F. S. & Boyd, R. W. Tomography of the quantum state of photons entangled in high dimensions. *Physical Review A* **84,** 062101 (2011).
120. Giovannini, D. *et al.* Characterization of high-dimensional entangled systems via mutually unbiased measurements. *Physical Review Letters* **110,** 143601 (2013).

121. Bavaresco, J. *et al.* Measurements in two bases are sufficient for certifying high-dimensional entanglement. *Nature Physics* **14,** 1032–1037 (2018).

122. Gross, D., Liu, Y.-K., Flammia, S. T., Becker, S. & Eisert, J. Quantum state tomography via compressed sensing. *Physical Review Letters* **105,** 150401 (2010).

123. Cramer, M. *et al.* Efficient quantum state tomography. *Nature Communications* **1,** 1–7 (2010).

124. Ahn, D. *et al.* Adaptive compressive tomography with no a priori information. *Physical Review Letters* **122,** 100404 (2019).

125. Salazar, R. & Delgado, A. Quantum tomography via unambiguous state discrimination. *Physical Review A* **86,** 012118 (2012).

126. Paiva-Sánchez, C., Burgos-Inostroza, E., Jiménez, O. & Delgado, A. Quantum tomography via equidistant states. *Physical Review A* **82,** 032115 (2010).

127. Martınez, D. *et al.* Experimental quantum tomography assisted by multiply symmetric states in higher dimensions. *Physical Review A* **99,** 012336 (2019).

128. Zambrano, L., Pereira, L., Niklitschek, S. & Delgado, A. Estimation of pure quantum states in high dimension at the limit of quantum accuracy through complex optimization and statistical inference. *Scientific Reports* **10,** 1–9 (2020).

129. Hou, Z. *et al.* Experimental realization of self-guided quantum process tomography. *Physical Review A* **101,** 022317 (2020).

130. Rambach, M. *et al.* Robust and efficient high-dimensional quantum state tomography. *Physical Review Letters* **126,** 100402 (2021).

131. Nape, I. *et al.* Measuring dimensionality and purity of high-dimensional entangled states. *Nature Communications* **12,** 1–8 (2021).

132. Altepeter, J. B., Jeffrey, E. R. & Kwiat, P. G. Photonic state tomography. *Advances in Atomic, Molecular, and Optical Physics* **52,** 105–159 (2005).

133. Toninelli, E. *et al.* Concepts in quantum state tomography and classical implementation with intense light: a tutorial. *Advances in Optics and Photonics* **11,** 67–134 (2019).

134. Altepeter, J. B., Jeffrey, E. R. & Kwiat, P. G. Phase-compensated ultra-bright source of entangled photons. *Optics Express* **13,** 8951–8959 (2005).

135. De Burgh, M. D., Langford, N. K., Doherty, A. C. & Gilchrist, A. Choice of measurement sets in qubit tomography. *Physical Review A* **78,** 052122 (2008).

136. Ivonovic, I. Geometrical description of quantal state determination. *Journal of Physics A: Mathematical and General* **14,** 3241 (1981).

137. Durt, T., Englert, B.-G., Bengtsson, I. & Życzkowski, K. On mutually unbiased bases. *International journal of quantum information* **8,** 535–640 (2010).

138. Klappenecker, A. & Rötteler, M. *Constructions of Mutually Unbiased Bases* in *Finite Fields and Applications* (eds Mullen, G. L., Poli, A. & Stichtenoth, H.) (Springer Berlin Heidelberg, Berlin, Heidelberg, 2004), 137–144. ISBN: 978-3-540-24633-6.

139. Bengtsson, I. *Three ways to look at mutually unbiased bases* in *AIP Conference Proceedings* **889** (2007), 40–51.

140. Butterley, P. & Hall, W. Numerical evidence for the maximum number of mutually unbiased bases in dimension six. *Physics Letters A* **369,** 5–8 (2007).

141. Brierley, S. & Weigert, S. Maximal sets of mutually unbiased quantum states in dimension 6. *Physical Review A* **78,** 042312 (2008).

142. Brierley, S. & Weigert, S. *Mutually unbiased bases and semi-definite programming* in *Journal of Physics: Conference Series* **254** (2010), 012008.

143. Brierley, S., Weigert, S. & Bengtsson, I. All mutually unbiased bases in dimensions two to five. *Quantum Information & Computation* **10,** 803–820 (2010).

144. Adamson, R. & Steinberg, A. M. Improving quantum state estimation with mutually unbiased bases. *Physical Review Letters* **105,** 030406 (2010).

145. Nagali, E., Sansoni, L., Marrucci, L., Santamato, E. & Sciarrino, F. Experimental generation and characterization of single-photon hybrid ququarts based on polarization and orbital angular momentum encoding. *Physical Review A* **81,** 052317 (2010).

146. Hradil, Z. Quantum-state estimation. *Physical Review A* **55,** R1561 (1997).

147. Banaszek, K., D'ariano, G., Paris, M. & Sacchi, M. Maximum-likelihood estimation of the density matrix. *Physical Review A* **61,** 010304 (1999).

148. Jones, K. Principles of quantum inference. *Annals of Physics* **207,** 140–170 (1991).

149. Blume-Kohout, R. Optimal, reliable estimation of quantum states. *New Journal of Physics* **12,** 043034 (2010).

150. Granade, C., Combes, J. & Cory, D. Practical bayesian tomography. *New Journal of Physics* **18,** 033024 (2016).

151. Jack, B. *et al.* Precise quantum tomography of photon pairs with entangled orbital angular momentum. *New Journal of Physics* **11,** 103024 (2009).

152. Götte, J. B., Franke-Arnold, S., Zambrini, R. & Barnett, S. M. Quantum formulation of fractional orbital angular momentum. *J Mod Opt* **54,** 1723–1738 (2007).

153. Oemrawsingh, S. *et al.* Experimental demonstration of fractional orbital angular momentum entanglement of two photons. *Phys Rev Lett* **95,** 240501 (2005).

154. Maiman, T. Stimulated optical radiation in ruby. *Nature* **187,** 493–494 (1960).

155. Buono, W. T. & Forbes, A. Nonlinear optics with structured light. *Opto-Electronic Advances* **5,** 210174–1 (2022).

156. Chang, D. E., Vuletić, V. & Lukin, M. D. Quantum nonlinear optics—photon by photon. *Nature Photonics* **8,** 685–694 (2014).

157. Lee, J.-C. & Kim, Y.-H. Spatial and spectral properties of entangled photons from spontaneous parametric down-conversion with a focused pump. *Optics Communications* **366,** 442–450 (2016).

158. Erhard, M., Krenn, M. & Zeilinger, A. Advances in high-dimensional quantum entanglement. *Nature Reviews Physics* **2,** 365–381 (2020).

159. Vandevender, A. P. & Kwiat, P. G. High efficiency single photon detection via frequency up-conversion. *Journal of Modern Optics* **51,** 1433–1445 (2004).

160. Lehmann, L. *et al.* Single photon MIR upconversion detector at room temperature with a PPLN ridge waveguide. *Optics Express* **27,** 19233–19241 (2019).

161. Yao, N. *et al.* Optimizing up-conversion single-photon detectors for quantum key distribution. *Optics Express* **28,** 25123–25133 (2020).

162. Hlaváček, A. *et al.* Bioconjugates of photon-upconversion nanoparticles for cancer biomarker detection and imaging. *Nature Protocols* **17,** 1028–1072 (2022).

163. Wen, X. *et al.* Ghost imaging second harmonic generation microscopy. *Applied Physics Letters* **116,** 191101 (2020).

164. Buono, W. *et al.* Polarization-controlled orbital angular momentum switching in nonlinear wave mixing. *Optics Letters* **43,** 1439–1442 (2018).

165. Alves, G., Barros, R., Tasca, D., Souza, C. & Khoury, A. Conditions for optical parametric oscillation with a structured light pump. *Physical Review A* **98,** 063825 (2018).

166. Rodrigues, R. *et al.* Orbital angular momentum symmetry in a driven optical parametric oscillator. *Optics Letters* **43,** 2486–2489 (2018).

167. Pereira, L. J., Buono, W. T., Tasca, D. S., Dechoum, K. & Khoury, A. Z. Orbital-angular-momentum mixing in type-II second-harmonic generation. *Physical Review A* **96,** 053856 (2017).

168. Buono, W., Moraes, L., Huguenin, J., Souza, C. & Khoury, A. Arbitrary orbital angular momentum addition in second harmonic generation. *New Journal of Physics* **16,** 093041 (2014).

169. Zhdanova, A. A., Shutova, M., Bahari, A., Zhi, M. & Sokolov, A. V. Topological charge algebra of optical vortices in nonlinear interactions. *Optics Express* **23,** 34109–34117 (2015).

170. Trajtenebrg-Mills, S. & Arie, A. Shaping light beams in nonlinear processes using structured light and patterned crystals. *Optical Materials Express* **7,** 2928–2942 (2017).

171. Li, Y., Zhou, Z.-Y., Ding, D.-S. & Shi, B.-S. Dynamic mode evolution and phase transition of twisted light in nonlinear process. *Journal of Modern Optics* **63,** 2271–2278 (2016).

172. Karnieli, A. & Arie, A. Fully controllable adiabatic geometric phase in nonlinear optics. *Optics Express* **26,** 4920–4932 (2018).

173. Valencia, A., Ceré, A., Shi, X., Molina-Terriza, G. & Torres, J. P. Shaping the waveform of entangled photons. *Physical Review Letters* **99,** 243601 (2007).

174. Boucher, P., Defienne, H. & Gigan, S. Engineering spatial correlations of entangled photon pairs by pump beam shaping. *Optics Letters* **46,** 4200–4203 (2021).

175. Bornman, N., Tavares Buono, W., Lovemore, M. & Forbes, A. Optimal Pump Shaping for Entanglement Control in Any Countable Basis. *Advanced Quantum Technologies* **4,** 2100066 (2021).

176. Yariv, A. Four wave nonlinear optical mixing as real time holography. *Optics Communications* **25,** 23–25 (1978).

177. Liu, H. *et al.* Dynamic computer-generated nonlinear-optical holograms. *Physical Review A* **96,** 023801 (2017).

178. Liu, H., Zhao, X., Li, H., Zheng, Y. & Chen, X. Dynamic computer-generated nonlinear optical holograms in a non-collinear second-harmonic generation process. *Optics Letters* **43,** 3236–3239 (2018).

179. Boyd, R. W. *Nonlinear optics* ISBN: 9780123694706 (Elsevier Inc., 2008).

180. Ou, Z.-Y. J. *Multi-photon quantum interference* (Springer, 2007).

181. Riek, C. *et al.* Direct sampling of electric-field vacuum fluctuations. *Science* **350,** 420–423 (2015).

182. Migdall, A., Polyakov, S. V., Fan, J. & Bienfang, J. C. *Single-photon generation and detection: physics and applications* (Academic Press, 2013).

183. Baek, S.-Y. & Kim, Y.-H. Spectral properties of entangled photon pairs generated via frequency-degenerate type-I spontaneous parametric down-conversion. *Physical Review A* **77,** 043807 (2008).

184. Vamivakas, A. N., Saleh, B. E., Sergienko, A. V. & Teich, M. C. Theory of spontaneous parametric down-conversion from photonic crystals. *Physical Review A* **70,** 043810 (2004).

185. Grice, W. P. & Walmsley, I. A. Spectral information and distinguishability in type-II down-conversion with a broadband pump. *Physical Review A* **56,** 1627 (1997).

186. Dosseva, A., Cincio, Ł. & Brańczyk, A. M. Shaping the joint spectrum of down-converted photons through optimized custom poling. *Physical Review A* **93,** 013801 (2016).

187. Laudenbach, F. *et al.* Numerical Investigation of Photon-Pair Generation in Periodically Poled M TiO X O 4 (M= K, Rb, Cs; X= P, As). *Physical Review Applied* **8,** 024035 (2017).

188. Saleh, B. E., Abouraddy, A. F., Sergienko, A. V. & Teich, M. C. Duality between partial coherence and partial entanglement. *Physical Review A* **62,** 043816 (2000).

189. Mandel, L. & Wolf, E. *Optical coherence and quantum optics* (Cambridge university press, 1995).

190. Steinlechner, F. *Sources of photonic entanglement for applications in space* (2015).

191. Torres, J. P., Banaszek, K. & Walmsley, I. in *Progress in Optics* 227–331 (Elsevier, 2011).

192. Anwar, A., Perumangatt, C., Steinlechner, F., Jennewein, T. & Ling, A. Entangled photon-pair sources based on three-wave mixing in bulk crystals. *Review of Scientific Instruments* **92,** 041101 (2021).

193. Zhang, Y., Roux, F. S., McLaren, M. & Forbes, A. Radial modal dependence of the azimuthal spectrum after parametric down-conversion. *Physical Review A* **89,** 043820 (2014).

194. De Riedmatten, H., Marcikic, I., Zbinden, H. & Gisin, N. Creating high dimensional entanglement using mode-locked lasers. *Quantum Information & Computation* **2,** 425–433 (2002).

195. Thew, R. T., Acin, A., Zbinden, H. & Gisin, N. Bell-type test of energy-time entangled qutrits. *Physical Review Letters* **93,** 010503 (2004).

196. Rossi, A., Vallone, G., Chiuri, A., De Martini, F. & Mataloni, P. Multipath entanglement of two photons. *Physical Review Letters* **102,** 153902 (2009).

197. Neves, L. *et al.* Generation of entangled states of qudits using twin photons. *Physical Review Letters* **94,** 100501 (2005).

198. Leach, J. *et al.* Quantum correlations in optical angle–orbital angular momentum variables. *Science* **329,** 662–665 (2010).

199. Molina-Terriza, G., Torres, J. P. & Torner, L. Twisted photons. *Nature Physics* **3,** 305–310 (2007).

200. Yarnall, T., Abouraddy, A. F., Saleh, B. E. & Teich, M. C. Experimental violation of Bell's inequality in spatial-parity space. *Physical Review Letters* **99,** 170408 (2007).

201. Mair, A., Vaziri, A., Weihs, G. & Zeilinger, A. Entanglement of the orbital angular momentum states of photons. *Nature* **412,** 313–316 (2001).

202. Franke-Arnold, S., Barnett, S. M., Padgett, M. J. & Allen, L. Two-photon entanglement of orbital angular momentum states. *Physical Review A* **65,** 033823 (2002).

203. Walborn, S., Pádua, S. & Monken, C. Conservation and entanglement of Hermite-Gaussian modes in parametric down-conversion. *Physical Review A* **71,** 053812 (2005).

204. Ren, X.-F., Guo, G.-P., Li, J. & Guo, G.-C. Entanglement of the Hermite–Gaussian modes states of photons. *Physics Letters A* **341,** 81–86 (2005).

205. Straupe, S., Ivanov, D., Kalinkin, A., Bobrov, I. & Kulik, S. Angular Schmidt modes in spontaneous parametric down-conversion. *Physical Review A* **83,** 060302 (2011).

206. Miatto, F. M., Brougham, T. & Yao, A. M. Cartesian and polar Schmidt bases for down-converted photons. *The European Physical Journal D* **66,** 1–8 (2012).

207. Svozilık, J., Peřina Jr, J. & Torres, J. P. High spatial entanglement via chirped quasi-phase-matched optical parametric down-conversion. *Physical Review A* **86,** 052318 (2012).

208. Krenn, M. *et al.* Generation and confirmation of a (100$\times$ 100)-dimensional entangled quantum system. *Proceedings of the National Academy of Sciences* **111,** 6243–6247 (2014).

209. Fickler, R. *et al.* Quantum entanglement of high angular momenta. *Science* **338,** 640–643 (2012).

210. Fickler, R., Campbell, G., Buchler, B., Lam, P. K. & Zeilinger, A. Quantum entanglement of angular momentum states with quantum numbers up to 10,010. *Proceedings of the National Academy of Sciences* **113,** 13642–13647 (2016).

211. Miatto, F. M., Yao, A. M. & Barnett, S. M. Full characterization of the quantum spiral bandwidth of entangled biphotons. *Physical Review A* **83,** 033816 (2011).

212. Grobe, R., Rzazewski, K. & Eberly, J. Measure of electron-electron correlation in atomic physics. *Journal of Physics B: Atomic, Molecular and Optical Physics* **27,** L503 (1994).

213. Berkhout, G. C. G., Lavery, M. P. J., Courtial, J., Beijersbergen, M. W. & Padgett, M. J. Efficient Sorting of Orbital Angular Momentum States of Light. *Physical Review Letters* **105,** 153601 (2010).

214. Bouchard, F. *et al.* Measuring azimuthal and radial modes of photons. *Optics Express* **26,** 31925–31941 (2018).

215. Forbes, A., Dudley, A. & McLaren, M. Creation and detection of optical modes with spatial light modulators. *Advances in Optics and Photonics* **8,** 200–227 (2016).

216. Carpentier, A. V., Michinel, H., Salgueiro, J. R. & Olivieri, D. Making optical vortices with computer-generated holograms. *American Journal of Physics* **76,** 916–921 (2008).

217. Bolduc, E., Bent, N., Santamato, E., Karimi, E. & Boyd, R. W. Exact solution to simultaneous intensity and phase encryption with a single phase-only hologram. *Optics Letters* **38,** 3546–3549 (2013).

218. Devlin, R. C., Ambrosio, A., Rubin, N. A., Mueller, J. B. & Capasso, F. Arbitrary spin-to–orbital angular momentum conversion of light. *Science* **358,** 896–901 (2017).

219. Rafayelyan, M. & Brasselet, E. Laguerre–Gaussian modal q-plates. *Optics Letters* **42,** 1966–1969 (2017).

220. Rafayelyan, M., Gertus, T. & Brasselet, E. Laguerre-Gaussian quasi-modal q-plates from nanostructured glasses. *Applied Physics Letters* **110,** 261108 (2017).

221. Roux, F. S. & Zhang, Y. Projective measurements in quantum and classical optical systems. *Physical Review A* **90,** 033835 (2014).

222. Miatto, F. *et al.* Bounds and optimisation of orbital angular momentum bandwidths within parametric down-conversion systems. *The European Physical Journal D* **66,** 1–6 (2012).

223. Naidoo, D. *et al.* Controlled generation of higher-order Poincaré sphere beams from a laser. *Nature Photonics* **10,** 327–332 (2016).

224. Sroor, H. *et al.* High-purity orbital angular momentum states from a visible metasurface laser. *Nature Photonics* **14,** 498–503 (2020).

225. D'ambrosio, V. *et al.* Photonic polarization gears for ultra-sensitive angular measurements. *Nature Communications* **4,** 1–8 (2013).

226. Nersisyan, S. R., Tabiryan, N. V., Steeves, D. M. & Kimball, B. R. The promise of diffractive waveplates. *Optics and Photonics News* **21,** 40–45 (2010).

227. Qassim, H. *et al.* Limitations to the determination of a Laguerre–Gauss spectrum via projective, phase-flattening measurement. *JOSA B* **31,** A20–A23 (2014).

228. Vallone, G. Role of beam waist in Laguerre–Gauss expansion of vortex beams. *Optics Letters* **42,** 1097–1100 (2017).

229. Sang, B. *et al.* Generation of pure Laguerre-Gaussian vector beams on the higher-order Poincaré sphere by hollow Gaussian beams through dielectric metasurfaces. *Optics Communications* **439,** 27–33 (2019).

230. Matsumoto, N. *et al.* Generation of high-quality higher-order Laguerre-Gaussian beams using liquid-crystal-on-silicon spatial light modulators. *JOSA A* **25,** 1642–1651 (2008).

231. Ando, T., Ohtake, Y., Matsumoto, N., Inoue, T. & Fukuchi, N. Mode purities of Laguerre–Gaussian beams generated via complex-amplitude modulation using phase-only spatial light modulators. *Optics Letters* **34,** 34–36 (2009).

232. Torres, J., Alexandrescu, A. & Torner, L. Quantum spiral bandwidth of entangled two-photon states. *Physical Review A* **68,** 050301 (2003).

233. Jesacher, A., Maurer, C., Schwaighofer, A., Bernet, S. & Ritsch-Marte, M. Near-perfect hologram reconstruction with a spatial light modulator. *Optics Express* **16,** 2597–2603 (2008).

234. Choudhary, S. *et al.* Measurement of the radial mode spectrum of photons through a phase-retrieval method. *Optics Letters* **43,** 6101–6104 (2018).

235. Radnaev, A. *et al.* A quantum memory with telecom-wavelength conversion. *Nature Physics* **6,** 894–899 (2010).

236. Jain, N. & Kanter, G. S. Upconversion-based receivers for quantum hacking-resistant quantum key distribution. *Quantum Information Processing* **15,** 2863–2879 (2016).

237. Vasilyev, M. & Kumar, P. Frequency up-conversion of quantum images. *Optics Express* **20,** 6644–6656 (2012).

238. Huang, K., Fang, J., Yan, M., Wu, E. & Zeng, H. Wide-field mid-infrared single-photon upconversion imaging. *Nature Communications* **13,** 1–9 (2022).

239. Barh, A., Rodrigo, P. J., Meng, L., Pedersen, C. & Tidemand-Lichtenberg, P. Parametric upconversion imaging and its applications. *Advances in Optics and Photonics* **11,** 952–1019 (2019).

240. Steinlechner, F., Hermosa, N., Pruneri, V. & Torres, J. P. Frequency conversion of structured light. *Scientific Reports* **6,** 1–8 (2016).

241. Liu, S. *et al.* High-dimensional quantum frequency converter. *Physical Review A* **101,** 012339 (2020).

242. Albota, M. A. & Wong, F. N. Efficient single-photon counting at 1.55 μm by means of frequency upconversion. *Optics Letters* **29,** 1449–1451 (2004).

243. Kumar, S. *et al.* Spatiotemporal mode-selective quantum frequency converter. *Physical Review A* **104,** 023506 (2021).

244. Qiu, X., Li, F., Zhang, W., Zhu, Z. & Chen, L. Spiral phase contrast imaging in nonlinear optics: seeing phase objects using invisible illumination. *Optica* **5,** 208–212 (2018).

245. Rocha, J. *et al.* Speckle filtering through nonlinear wave mixing. *Optics Letters* **46,** 3905–3908 (2021).

246. Zhang, H., Kumar, S. & Huang, Y.-P. Mode selective up-conversion detection with turbulence. *Scientific Reports* **9,** 1–9 (2019).

247. Couteau, C. Spontaneous parametric down-conversion. *Contemporary Physics* **59,** 291–304 (2018).

248. Süzer, Ö. & Goodson III, T. G. Does pump beam intensity affect the efficiency of spontaneous parametric down conversion? *Optics Express* **16,** 20166–20175 (2008).

249. Boyd, G. & Kleinman, D. Parametric interaction of focused Gaussian light beams. *Journal of Applied Physics* **39,** 3597–3639 (1968).

250. Fan, T. Y. *et al.* Second harmonic generation and accurate index of refraction measurements in flux-grown KTiOPO 4. *Applied optics* **26,** 2390–2394 (1987).

251. Fradkin, K., Arie, A., Skliar, A. & Rosenman, G. Tunable midinfrared source by difference frequency generation in bulk periodically poled KTiOPO 4. *Applied Physics Letters* **74,** 914–916 (1999).

252. Flamm, D., Naidoo, D., Schulze, C., Forbes, A. & Duparré, M. Mode analysis with a spatial light modulator as a correlation filter. *Opt. Lett.* **37,** 2478–2480 (2012).

253. Flamm, D. *et al.* All-digital holographic tool for mode excitation and analysis in optical fibers. *Journal of Lightwave Technology* **31,** 1023–1032 (2013).

254. Fontaine, N. K. *et al.* Laguerre-Gaussian mode sorter. *Nature Communications* **10,** 1–7 (2019).

255. Dudley, A. *et al.* Efficient sorting of Bessel beams. *Opt. Express* **21,** 165–171 (2013).

256. Zhou, Y. *et al.* Hermite–Gaussian mode sorter. *Optics Letters* **43,** 5263–5266 (2018).

257. Padgett, M. J. Orbital angular momentum 25 years on. *Optics Express* **25,** 11265–11274 (2017).

258. Li, G., Bai, N., Zhao, N. & Xia, C. Space-division multiplexing: the next frontier in optical communication. *Advances in Optics and Photonics* **6,** 413–487 (2014).

259. Midwinter, J. Image conversion from 1.6 μ to the visible in lithium niobate. *Applied Physics Letters* **12,** 68–70 (1968).

260. Boyd, R. W. & Townes, C. An infrared upconverter for astronomical imaging. *Applied Physics Letters* **31,** 440–442 (1977).

261. Dayan, B., Pe'er, A., Friesem, A. A. & Silberberg, Y. Nonlinear interactions with an ultrahigh flux of broadband entangled photons. *Physical Review Letters* **94,** 043602 (2005).

262. Merkouche, S., Thiel, V. & Smith, B. J. Positive operator-valued measure for two-photon detection via sum-frequency generation. *Physical Review A* **103,** 043711 (2021).

263. Barreiro, J. T., Wei, T.-C. & Kwiat, P. G. Beating the channel capacity limit for linear photonic superdense coding. *Nature Physics* **4,** 282–286 (2008).

264. Peev, M. *et al.* The SECOQC quantum key distribution network in Vienna. *New Journal of Physics* **11,** 075001 (2009).

265. Stucki, D. *et al.* Long-term performance of the SwissQuantum quantum key distribution network in a field environment. *New Journal of Physics* **13,** 123001 (2011).

266. Fröhlich, B. *et al.* A quantum access network. *Nature* **501,** 69–72 (2013).

267. Chen, Y.-A. *et al.* An integrated space-to-ground quantum communication network over 4,600 kilometres. *Nature* **589,** 214–219 (2021).

268. Roux, F. S. Toolbox for non-classical state calculations. *Journal of Optics* **23,** 125201 (2021).

269. He, C., Shen, Y. & Forbes, A. Towards higher-dimensional structured light. *Light: Science & Applications* **11,** 1–17 (2022).

270. Dorrah, A. H. & Capasso, F. Tunable structured light with flat optics. *Science* **376,** eabi6860 (2022).

271. Karpiński, M., Davis, A. O., Sośnicki, F., Thiel, V. & Smith, B. J. Control and measurement of quantum light pulses for quantum information science and technology. *Advanced Quantum Technologies* **4,** 2000150 (2021).

272. Calsamiglia, J. Generalized measurements by linear elements. *Physical Review A* **65,** 030301 (2002).

273. Wang, X.-L. *et al.* Experimental ten-photon entanglement. *Physical Review Letters* **117,** 210502 (2016).

274. Cozzolino, D., Da Lio, B., Bacco, D. & Oxenløwe, L. K. High-dimensional quantum communication: benefits, progress, and future challenges. *Advanced Quantum Technologies* **2,** 1900038 (2019).

275. Zhang, Y. *et al.* Simultaneous entanglement swapping of multiple orbital angular momentum states of light. *Nature Communications* **8,** 1–7 (2017).

276. Molotkov, S. Experimental scheme for quantum teleportation of a single-photon packet. *arXiv preprint quant-ph/9807013* (1998).

277. Jamiołkowski, A. Linear transformations which preserve trace and positive semidefiniteness of operators. *Reports on Mathematical Physics* **3,** 275–278 (1972).

278. Choi, M.-D. Completely positive linear maps on complex matrices. *Linear Algebra and its Applications* **10,** 285–290 (1975).

279. Jiang, M., Luo, S. & Fu, S. Channel-state duality. *Physical Review A* **87,** 022310 (2013).

280. Goyal, S. K., Boukama-Dzoussi, P. E., Ghosh, S., Roux, F. S. & Konrad, T. Qudit-teleportation for photons with linear optics. *Sci Rep* **4,** 4543 (2014).

281. Horodecki, M., Horodecki, P. & Horodecki, R. General teleportation channel, singlet fraction, and quasidistillation. *Physical Review A* **60,** 1888 (1999).

282. Takesue, H. & Shimizu, K. Effects of multiple pairs on visibility measurements of entangled photons generated by spontaneous parametric processes. *Optics Communications* **283,** 276–287 (2010).

283. Schneeloch, J. *et al.* Introduction to the absolute brightness and number statistics in spontaneous parametric down-conversion. *Journal of Optics* **21,** 043501 (2019).

284. Takeoka, M., Jin, R.-B. & Sasaki, M. Full analysis of multi-photon pair effects in spontaneous parametric down conversion based photonic quantum information processing. *New Journal of Physics* **17,** 043030 (2015).

285. Graffitti, F., Barrow, P., Proietti, M., Kundys, D. & Fedrizzi, A. Independent high-purity photons created in domain-engineered crystals. *Optica* **5,** 514–517 (2018).

286. Pittman, T., Jacobs, B. & Franson, J. Single photons on pseudodemand from stored parametric down-conversion. *Physical Review A* **66,** 042303 (2002).

287. Migdall, A. L., Branning, D. & Castelletto, S. Tailoring single-photon and multiphoton probabilities of a single-photon on-demand source. *Physical Review A* **66,** 053805 (2002).

288. Kaneda, F. & Kwiat, P. G. High-efficiency single-photon generation via large-scale active time multiplexing. *Science Advances* **5,** eaaw8586 (2019).

289. Zhu, F., Tyler, M., Valencia, N. H., Malik, M. & Leach, J. Is high-dimensional photonic entanglement robust to noise? *AVS Quantum Science* **3,** 011401 (2021).

290. Xie, Z. *et al.* Efficient C-band single-photon upconversion with chip-scale Ti-indiffused pp-LiNbO 3 waveguides. *Applied optics* **58,** 5910–5915 (2019).

291. Pelc, J. S. *et al.* Long-wavelength-pumped upconversion single-photon detector at 1550 nm: performance and noise analysis. *Optics Express* **19,** 21445–21456 (2011).

292. Kamada, H. *et al.* Efficient and low-noise single-photon detection in 1550 nm communication band by frequency upconversion in periodically poled LiNbO 3 waveguides. *Optics Letters* **33,** 639–641 (2008).

293. Shentu, G.-L. *et al.* Ultralow noise up-conversion detector and spectrometer for the telecom band. *Optics Express* **21,** 13986–13991 (2013).

294. Lunghi, T. *et al.* Free-running single-photon detection based on a negative feedback InGaAs APD. *Journal of Modern Optics* **59,** 1481–1488 (2012).

295. Yan, Z. *et al.* An ultra low noise telecom wavelength free running single photon detector using negative feedback avalanche diode. *Review of Scientific Instruments* **83,** 073105 (2012).

296. http://raicol.com/wp-content/uploads/catalog.pdf.

297. Bennett, C. H. *et al.* Remote State Preparation. *Phys. Rev. Lett.* **87,** 077902. https://link.aps.org/doi/10.1103/PhysRevLett.87.077902 (7 July 2001).

298. Kivshar, Y. All-dielectric meta-optics and non-linear nanophotonics. *National Science Review* **5,** 144–158 (2018).

299. Krenn, M., Malik, M., Fickler, R., Lapkiewicz, R. & Zeilinger, A. Automated search for new quantum experiments. *Physical Review Letters* **116,** 090405 (2016).

300. Ndagano, B. *et al.* A deterministic detector for vector vortex states. *Scientific Reports* **7,** 1–8 (2017).

301. Kwiat, P. G. & Weinfurter, H. Embedded Bell-state analysis. *Physical Review A* **58,** R2623 (1998).

302. Schuck, C., Huber, G., Kurtsiefer, C. & Weinfurter, H. Complete deterministic linear optics Bell state analysis. *Physical Review Letters* **96,** 190501 (2006).

303. Barbieri, M., Vallone, G., Mataloni, P. & De Martini, F. Complete and deterministic discrimination of polarization Bell states assisted by momentum entanglement. *Physical Review A* **75,** 042317 (2007).

304. Wang, C., Chen, Y. & Chen, L. Four-dimensional orbital angular momentum Bell-state measurement assisted by the auxiliary polarization and path degrees of freedom. *Optics Express* **30,** 34468–34478 (2022).

305. Zhang, H. *et al.* Arbitrary two-particle high-dimensional Bell-state measurement by auxiliary entanglement. *Physical Review A* **99,** 052301 (2019).

306. Zeng, Z. General scheme for complete high-dimensional Bell state measurement. *Optics Letters* **47,** 5817–5820 (2022).

307. Kysela, J. High-dimensional quantum Fourier transform of twisted light. *Physical Review A* **104,** 012413 (2021).

308. Sangouard, N. *et al.* Faithful entanglement swapping based on sum-frequency generation. *Physical Review Letters* **106,** 120403 (2011).

309. Ndagano, B. *et al.* Characterizing quantum channels with non-separable states of classical light. *Nature Physics* **13,** 397–402 (2017).

310. Iliyasu, A. M. Towards realising secure and efficient image and video processing applications on quantum computers. *Entropy* **15,** 2874–2974 (2013).

311. Yao, X.-W. *et al.* Quantum image processing and its application to edge detection: theory and experiment. *Physical Review X* **7,** 031041 (2017).

312. Ruan, Y., Xue, X. & Shen, Y. Quantum image processing: opportunities and challenges. *Mathematical Problems in Engineering* **2021,** 1–8 (2021).

313. Mastriani, M. Quantum image processing? *Quantum Information Processing* **16,** 27 (2017).

314. Li, H.-S., Fan, P., Xia, H.-y. & Zhou, R.-G. A comment on "Quantum image processing?" *Quantum Information Processing* **19,** 1–10 (2020).

315. Mastriani, M. Quantum image processing: the pros and cons of the techniques for the internal representation of the image. A reply to: A comment on "Quantum image processing?" *Quantum Information Processing* **19,** 156 (2020).

316. Padgett, M. J. & Boyd, R. W. An introduction to ghost imaging: quantum and classical. *Philosophical Transactions of the Royal Society A: Mathematical, Physical and Engineering Sciences* **375,** 20160233 (2017).

317. Zhang, Y. *et al.* Quantum imaging of biological organisms through spatial and polarization entanglement. *arXiv preprint arXiv:2303.05643* (2023).

318. Rodríguez-Fajardo, V., Pinnell, J. & Forbes, A. Towards time-efficient ghost imaging. *Journal of Modern Optics* **0,** 1–8 (2020).

319. Bornman, N. *et al.* Ghost imaging using entanglement-swapped photons. *npj Quantum Information* **5,** 1–6 (2019).

320. Schneeloch, J. & Howell, J. C. Introduction to the transverse spatial correlations in spontaneous parametric down-conversion through the biphoton birth zone. *Journal of Optics* **18,** 053501 (2016).

321. Jack, B. *et al.* Holographic ghost imaging and the violation of a Bell inequality. *Physical Review Letters* **103,** 083602 (2009).

322. Moreau, P.-A., Toninelli, E., Gregory, T. & Padgett, M. J. Ghost imaging using optical correlations. *Laser & Photonics Reviews* **12,** 1700143 (2018).

323. Tasca, D. *et al.* The influence of non-imaging detector design on heralded ghost-imaging and ghost-diffraction examined using a triggered ICCD camera. *Optics Express* **21,** 30460–30473 (2013).

324. Pittman, T. B., Shih, Y. H., Strekalov, D. V. & Sergienko, A. V. Optical imaging by means of two-photon quantum entanglement. *Physical Review A* **52.** ISSN: 10502947 (1995).

325. Abouraddy, A. F., Saleh, B. E., Sergienko, A. V. & Teich, M. C. Role of entanglement in two-photon imaging. *Physical Review Letters* **87,** 123602 (2001).

326. Bennink, R. S., Bentley, S. J. & Boyd, R. W. "Two-photon" coincidence imaging with a classical source. *Physical Review Letters* **89,** 113601 (2002).

327. Gatti, A., Brambilla, E., Bache, M. & Lugiato, L. A. Ghost imaging with thermal light: comparing entanglement and classical correlation. *Physical Review Letters* **93,** 093602 (2004).

328. Edgar, M. P., Gibson, G. M. & Padgett, M. J. Principles and prospects for single-pixel imaging. *Nature Photonics* **13,** 13–20 (2019).

329. Gibson, G. M., Johnson, S. D. & Padgett, M. J. Single-pixel imaging 12 years on: a review. *Optics Express* **28,** 28190–28208 (2020).

330. Moreau, P.-A., Toninelli, E., Gregory, T. & Padgett, M. J. Imaging with quantum states of light. *Nature Reviews Physics* **1,** 367–380 (2019).

331. Moreau, P.-A. *et al.* Resolution limits of quantum ghost imaging. *Optics Express* **26,** 7528–7536 (2018).

332. Toninelli, E. *et al.* Resolution-enhanced quantum imaging by centroid estimation of biphotons. *Optica* **6,** 347–353 (2019).

333. Aspden, R. S. *et al.* Photon-sparse microscopy: visible light imaging using infrared illumination. *Optica* **2,** 1049–1052 (2015).

334. Morris, P. A., Aspden, R. S., Bell, J. E., Boyd, R. W. & Padgett, M. J. Imaging with a small number of photons. *Nature Communications* **6,** 1–6 (2015).

335. Pelliccia, D., Rack, A., Scheel, M., Cantelli, V. & Paganin, D. M. Experimental X-Ray Ghost Imaging. *Physical Review Letters* **117,** 1–5. ISSN: 10797114. arXiv: 1605.04958 (2016).

336. Yu, H. *et al.* Fourier-Transform Ghost Imaging with Hard X Rays. *Physical Review Letters* **117,** 1–5. ISSN: 10797114. arXiv: 1603.04388 (2016).

337. Li, S. *et al.* Electron ghost imaging. *Physical Review Letters* **121,** 114801 (2018).

338. Trimeche, A., Lopez, C., Comparat, D. & Picard, Y. Ion and electron ghost imaging. *Physical Review Research* **2,** 043295 (2020).

339. Shapiro, J. H. Computational ghost imaging. *Physical Review A - Atomic, Molecular, and Optical Physics* **78,** 1–4. ISSN: 10502947. arXiv: 0807.2614 (2008).

340. Erkmen, B. I. & Shapiro, J. H. Ghost imaging: from quantum to classical to computational. *Advances in Optics and Photonics* **2,** 405. ISSN: 1943-8206 (2010).

341. Katz, O., Bromberg, Y. & Silberberg, Y. Compressive ghost imaging. *Applied Physics Letters* **95,** 93–96. ISSN: 00036951. arXiv: 0905.0321 (2009).

342. Zerom, P., Chan, K. W. C., Howell, J. C. & Boyd, R. W. Entangled-photon compressive ghost imaging. *Physical Review A - Atomic, Molecular, and Optical Physics* **84,** 3–6. ISSN: 10502947 (2011).

343. Lyu, M. *et al.* Deep-learning-based ghost imaging. *Scientific Reports* **7,** 1–6 (2017).

344. Shimobaba, T. *et al.* Computational ghost imaging using deep learning. *Optics Communications* **413,** 147–151 (2018).

345. Komuro, K., Nomura, T. & Barbastathis, G. Deep ghost phase imaging. *Applied Optics* **59,** 3376. ISSN: 1559-128X (2020).

346. Rizvi, S., Cao, J., Zhang, K. & Hao, Q. DeepGhost: real-time computational ghost imaging via deep learning. *Scientific Reports* **10,** 1–9 (2020).

347. Moodley, C., Sephton, B., Fajardo, V. R. & Forbes, A. Deep learning early stopping for non - degenerate ghost imaging. *Scientific Reports,* 1–9 (2021).

348. Duarte, M. F. *et al.* Single-pixel imaging via compressive sampling. *IEEE Signal Processing Magazine* **25,** 83–91. ISSN: 1053-5888 (2008).

349. Nasr, M. B. *et al.* Quantum optical coherence tomography of a biological sample. *Optics Communications* **282,** 1154–1159 (2009).

350. Liu, H.-C. *et al.* Single-pixel computational ghost imaging with helicity-dependent metasurface hologram. *Science Advances* **3,** e1701477 (2017).

351. Altuzarra, C. *et al.* Imaging of polarization-sensitive metasurfaces with quantum entanglement. *Physical Review A* **99,** 020101 (2019).

352. Magdenko, L. V., Sokolov, I. V. & Kolobov, M. I. Quantum teleportation of optical images with frequency conversion. *Optics and Spectroscopy* **103,** 62–66 (2007).

353. Aspden, R. S., Morris, P. A., He, R., Chen, Q. & Padgett, M. J. Heralded phase-contrast imaging using an orbital angular momentum phase-filter. *Journal of Optics (United Kingdom)* **18.** ISSN: 20408986 (2016).

354. Zhang, Y. *et al.* Interaction-free ghost-imaging of structured objects. *Optics Express* **27,** 2212. ISSN: 1094-4087. arXiv: 1711.09171 (2019).

355. Ndagano, B. *et al.* Quantum microscopy based on Hong–Ou–Mandel interference. *Nature Photonics,* 1–6 (2022).

356. Aidukas, T., Konda, P. C., Harvey, A. R., Padgett, M. J. & Moreau, P.-A. Phase and amplitude imaging with quantum correlations through Fourier ptychography. *Scientific Reports* **9,** 1–9 (2019).

357. Defienne, H., Ndagano, B., Lyons, A. & Faccio, D. Polarization entanglement-enabled quantum holography. *Nature Physics* **17,** 591–597 (2021).

358. Malik, M., Shin, H., O'Sullivan, M., Zerom, P. & Boyd, R. W. Quantum ghost image Identification with correlated photon Pairs. *Physical Review Letters* **104,** 1–4. ISSN: 00319007 (2010).

359. Walsh, J. L. A closed set of normal orthogonal functions. *American Journal of Mathematics* **45,** 5–24 (1923).

360. Welsh, S. S., Edgar, M. P., Bowman, R., Sun, B. & Padgett, M. J. Near video-rate linear Stokes imaging with single-pixel detectors. *Journal of Optics* **17,** 025705 (2015).

361. Gong, W. & Han, S. Phase-retrieval ghost imaging of complex-valued objects. *Physical Review A* **82,** 023828 (2010).

362. Hou, H.-Y. *et al.* Complex-amplitude Fourier single-pixel imaging via coherent structured illumination. *Chinese Physics B* (2022).

363. Braunstein, S. L. & Mann, A. Measurement of the Bell operator and quantum teleportation. *Physical Review A* **51,** R1727 (1995).

364. Pavičić, M. Near-deterministic discrimination of all Bell states with linear optics. *Physical Review Letters* **107,** 080403 (2011).

365. Qiu, X., Li, F., Liu, H., Chen, X. & Chen, L. Optical vortex copier and regenerator in the Fourier domain. *Photonics Research* **6,** 641–646 (2018).

366. Deng, F.-G., Ren, B.-C. & Li, X.-H. Quantum hyperentanglement and its applications in quantum information processing. *Science Bulletin* **62,** 46–68 (2017).

367. Wei, H.-R., Deng, F.-G. & Long, G. L. Hyper-parallel Toffoli gate on three-photon system with two degrees of freedom assisted by single-sided optical microcavities. *Optics Express* **24,** 18619–18630 (2016).

368. Simon, D. S. & Sergienko, A. V. High-capacity quantum key distribution via hyperentangled degrees of freedom. *New Journal of Physics* **16,** 063052 (2014).

369. Ali, L., Ikram, M., Abbas, T., Ahmad, I., *et al.* Hyperentanglement teleportation through external momenta states. *Journal of Physics B: Atomic, Molecular and Optical Physics* **54,** 235501 (2022).

370. Gao, S. *et al.* Paraxial skyrmionic beams. *Physical Review A* **102,** 053513 (2020).

371. Ndagano, B. & Forbes, A. Entanglement distillation by hong-ou-mandel interference with orbital angular momentum states. *APL Photonics* **4,** 016103 (2019).

372. Bennett, C. H. *et al.* Purification of noisy entanglement and faithful teleportation via noisy channels. *Physical Review Letters* **76,** 722 (1996).

373. Yao, A. M. Angular momentum decomposition of entangled photons with an arbitrary pump. *New Journal of Physics* **13,** 053048 (2011).

374. Anwar, A., Lal, N., Prabhakar, S. & Singh, R. Selective tuning of Hilbert spaces in states encoded with spatial modes of light. *New Journal of Physics* **22,** 113020 (2020).

375. Vaziri, A., Pan, J.-W., Jennewein, T., Weihs, G. & Zeilinger, A. Concentration of higher dimensional entanglement: qutrits of photon orbital angular momentum. *Physical Review Letters* **91,** 227902 (2003).

376. Bennett, C. H., Bernstein, H. J., Popescu, S. & Schumacher, B. Concentrating partial entanglement by local operations. *Physical Review A* **53,** 2046 (1996).